A Pre-Tensioned, Rocking Bridge System for Accelerated Construction and Enhanced Seismic Performance

Travis Thonstad

A dissertation

submitted in partial fulfillment of the

requirements for the degree of

Doctor of Philosophy

University of Washington

2016

Reading Committee:

John F. Stanton, Chair

Marc O. Eberhard, Chair

Richard Wiebe

Program Authorized to Offer Degree:

Civil and Environmental Engineering

University of Washington

Abstract

A Pre-tensioned, Rocking Bridge System for Accelerated Construction and Enhanced Seismic Performance

Travis Thonstad

Co-Chairs of the Supervisory Committee:

John F. Stanton
Civil and Environmental Engineering

Marc O. Eberhard
Civil and Environmental Engineering

A new bridge bent system has been developed to reduce on-site construction time, minimize residual displacements even after a large earthquake, and reduce seismic damage in comparison with conventional cast-in-place construction. Precast connections used in the system have been tested successfully under quasi-static conditions and found to perform exceptionally well, re-centering with essentially no concrete damage or residual drift after being loaded cyclically to drift ratios of up to 10%.

The seismic performance of the new system was evaluated with shaking table tests of a quarter-scale, two-span bridge. The maximum displacements of the bents were similar to those expected for a conventional bridge through the Design Level event (PGA=0.75g). Damage to the column concrete was negligible; the columns would not need any repair after being subjected to

the Design Level motion. Residual drift ratios never exceeded 0.2% up to the 221% Design Level motion (PGA = 1.66g). The only structural damage to the bridge was the eventual fracture of the column's longitudinal reinforcement and bulging of the column's confining tubes placed at the ends of the columns, both of which occurred at drift ratios of approximately 6%.

Results from the subassembly and shaking table tests were used to develop a design methodology for the new system that aligns with the displacement-based procedure outlined in the *AASHTO Guide Specifications for LRFD Seismic Bridge Design* (2015). The modifications to this procedure necessary to align with the objectives of the new system are straightforward and could be implemented within current design practice. A modeling strategy for the pre-tensioned bent system is also proposed and specific aspects of this approach are validated against the subassembly and shaking table test results.

TABLE OF CONTENTS

ACKNOWLEDGEMENTS

I would first like to express my sincere appreciation for my advisors, Dr. John F. Stanton and Marc O. Eberhard. They have guided my growth as a researcher and an individual in fundamental ways, and I am grateful for it.

I would also like to thank Richard Wiebe for his input as a member of my reading committee, and John Schaufelberger for agreeing to serve as the Graduate School Representative on my committee.

At the University of Nevada Reno, I worked closely with Islam Mantawy and Professor David Sanders. They made me feel welcome while staying in Reno, and for that I am forever grateful. I would also like to thank David Sanders for agreeing to serve on my supervisory committee.

At the University of Washington, I had the privilege to work alongside Bryan Kennedy and Jeff Schaefer who tested the subassembly specimens. Their contributions to the research presented in this thesis cannot be understated.

I would also like to thank my peers in More 236, Olafur Haraldsson, Hung Viet Tran, Jonathan Weigand, Bo-shiuan Wang, Ramona Barber, Andrew Sen, and Nasser Marafi for their valuable input. I would like to extend specific thanks to Max Stephens for being a great friend and source of advice throughout this process.

I would also like to acknowledge the many people who were involved in the construction and testing of the shaking table experiment. The precast columns and cap beams were fabricated at the University of Washington with the assistance of laboratory manager Vince Chaijareon and students Jimmy Au, Lisa Berg, Peter Deng , Monika Keller, Stephanie Kuroda, Spencer

Livermore, Scott Tetzlaff, Kevin Tsuchida, Connor Tsuchida, Lucas Whitesell and Chase Young.

The specimen was assembled and tested at the University of Nevada Reno with the assistance of laboratory manager Patrick Laplace, laboratory technicians Chad Lyttle and Todd Lyttle, and students Osvaldo Arias, Lisa Bryant, Mimi Mungedi, Guillermo Munoz, Taylor Nielsen and Eric Ramirez. The support of all of the research participants is gratefully acknowledged.

Finally, I would like to thank my wife, Sarah Coddington, for her immeasurable patience, support, and understanding throughout my time as a graduate student.

DEDICATION

To Sarah

CHAPTER 1: INTRODUCTION

New bridge systems are needed to meet the needs of the traveling public. Bridges must be built quickly to reduce closures and re-routing, and those in seismically active regions must be able to withstand shaking without significant damage, residual deformations or interruptions to service.

The Federal Highway Administration (FHWA) and many state departments of transportation (DOTs) are actively developing and implementing new methods for accelerating the on-site construction of bridges. These efforts are intended to reduce negative construction impacts; especially in densely urbanized, remote or ecologically sensitive areas. Accelerated bridge construction (ABC) has the additional benefits of higher construction quality and greater work-zone safety [FHWA 2011].

It is particularly challenging to develop bridge systems that can be built quickly in seismically active regions, because the connections between members usually experience large deformation and force demands. The primary goal of the research presented in this thesis is to evaluate the performance of a new precast, pre-tensioned bridge system suitable for ABC in seismic regions through:

- Subassembly tests (Schaefer et al. 2014a, Kennedy 2015),
- Shaking table tests (Thonstad et al. 2016), and
- Comparison with a previously tested cast-in-place bridge (Mantawy et al. 2016).

The work has also led to the development of design recommendations so that the system can be used in practice.

1.1 The Need for Accelerated Bridge Construction

There is no one method for accelerating bridge construction. There are numerous strategies that agencies have employed in the past to shorten project duration, road closures and re-routing. The key feature of these methods is the pre-fabrication of bridge elements, or portions of the bridge, somewhere other than their final location on-site. This could be done in a precasting facility, an off-site construction yard, or on the job site itself.

Prefabrication of superstructure components has been widely adopted throughout the United States. Precast, prestressed girders have been used in the United States for over 50 years. The standardization and mass production of these elements, the high level of quality control and superior material properties have made precast girders a highly economical and practical construction product.

More recently, technologies for prefabricating entire superstructures have become more practical. Self-Propelled Modular Transports (SPMTs) are one alternative. These large transports are capable of moving entire spans into their final alignment. The Utah Department of Transportation (UDOT) has used this technology extensively. In the summer of 2008 their "Innovate 80" project was able to replace 12 bridges in two months on or near the Interstate-80 corridor [Deslis 2014]. Within Washington State, several projects have recently utilized another alternative; "slide-in" technology [e.g. Vanek et al. 2014, Dusenberry 2015]. Bridge spans are constructed on specialized sliders adjacent to their final location on-site, and are pushed, using hydraulic rams, into position in a matter of hours.

Although prefabricated superstructure components (e.g., beams and deck panels) have been used extensively, prefabricated substructure components (columns, cap beams, and foundations) have been used seldomly. Projects supported by the Florida Department of

Transportation and the Texas Department of Transportation are two exceptions. In these low-seismic regions, segmentally constructed precast columns have been used successfully as a means to shorten project duration [e.g. Billington et al. 2001, FHWA 2009]. Some of these columns were post-tensioned to provide a continuous element through the precast segments.

1.2 Accelerated Construction in Seismically Active Regions

Bridge closures for inspection, repair or demolition after an earthquake can significantly impact the resilience of the communities they serve. Conventional reinforced concrete seismic design practice relies on large inelastic deformations in the column plastic hinge regions. During a major earthquake, damage to the column will likely cause spalling of the unconfined cover concrete, yielding of longitudinal and lateral reinforcement and possibly bar buckling and fracture. Although this performance may satisfy life-safety expectations, this level of damage requires either extensive repairs or replacement following the earthquake.

In addition, columns in reinforced concrete bridges may not return to their original plumb positions after an earthquake. These "residual displacements" are an important measure of the condition of the bridge, and the ease with which it can be repaired and brought back into service. As a rule of thumb, Japanese engineers consider a bridge to be beyond repair if it shows more than 1% residual drift in any of its columns [Japan Road Association JRP, part V 2002].

These performance expectations make it challenging to use ABC techniques for substructure components in seismic regions. Agencies are reluctant to use these techniques largely because the most convenient places to join precast substructure components are at the column-to-cap beam and column-to-footing interfaces, and these areas experience the greatest deformation demands during earthquake events. Precast substructure elements could be

connected elsewhere, at the point of contraflexure in the columns for example, but this typically is not done, because it makes the precast components difficult to transport and handle.

The benefits of rapid construction of substructure components can and should be realized nationwide. Thirty-six states have bridges built in a moderate-to-high seismic areas (Seismic Zone 2 and above Seismic Design Category B and above) [Marsh et al. 2011]. Thus, the challenge of developing prefabricated substructure systems suitable for seismic regions is a national issue.

1.3 Previous Research at University of Washington

The system presented in this document is the result of over a decade of research at the University of Washington. This research began with Hieber et al. (2005a), who summarized existing precast concrete technologies for accelerated bridge construction and discussed their application in areas of moderate-to-high seismicity. Hieber et al. (2005b) proposed a precast and a precast, prestressed concrete substructure concept, and performed numerical simulations to determine the feasibility of these concepts under seismic loading. Wacker et al. (2005) used the results of these numerical simulations to develop general design procedures and recommendations using force-based and direct-displacement-based design methodologies.

Steuck et al. (2009) further developed the precast substructure concept by proposing a grouted bar column-to-cap-beam connection using only a few, large diameter bars. They conducted pullout tests to determine if the depth of the superstructure was sufficient to develop the bars. Pang et al. (2010) then tested subassemblies constructed using this precast column-to-cap beam connection, and confirmed that the connection performed as well as cast-in-place construction under cyclic loads. In parallel, Cohagen et al. (2008) tested two post-tensioned column-to-cap beam subassemblies constructed using the large-bar connection.

Haraldsson et al. (2013) refined the precast substructure concept by developing a novel column-to-spread footing connection. The precast column was connected to the cast-in-place spread footing through shear friction only, simplifying construction on-site. Tran (2015) adapted this spread footing connection for drilled shafts. Khaleghi et al. (2012) summarized the design and construction of a bridge over SR-90 in Washington State that utilized the developed grouted-bar and column-to-spread footing connections.

Davis et al. (2012) further developed the prestressed bent concept, by incorporating pre-tensioned rather than post-tensioned strands in the columns. The column-to-cap beam connection of Pang et al. (2010) was modified in order to bond the pre-tensioned strands within the depth of the cap-beam. Finnsson (2013) then improved the pre-tensioned concept by protecting the hinge region by ductile, fiber-reinforced concrete and investigated the use of stainless steel reinforcement to improve column ductility. Haraldsson (2015) then dynamically tested a similar column-to-spread footing subassembly with pre-tensioned columns protected in the hinge region by ductile, fiber reinforced concrete.

These tests demonstrated the excellent restoring properties of the pre-tensioned bent concept, but the columns suffered damage at drifts lower than in comparable reinforced concrete systems, attributed to the increased axial stress due to prestressing and the reduction in longitudinal bar size that resulted from replacing some of the mild steel reinforcement with prestressing strands. The system presented in this thesis is the direct extension of this pre-tensioned concept, aiming to eliminate damage to the column concrete and delay reinforcement fracture in comparison to previously tested pre-tensioned specimens [Davis et al. 2012, Finnsson 2013, Haraldsson 2015].

1.4 Precast, Pre-tensioned Substructure Concept

This research develops and evaluates the performance of a prestressed, high-performance substructure system suitable for accelerated construction in seismic regions. This system is shown schematically in Figure 1.1. This system incorporates precast, pre-tensioned concrete columns and precast cap beams, with cast-in-place footings or drilled shafts. The system includes damage-reducing steel armoring in the connection regions, meant to eliminate the damage observed in subassembly tests of similar pre-tensioned columns [Finnsson 2013, Davis et al. 2012].

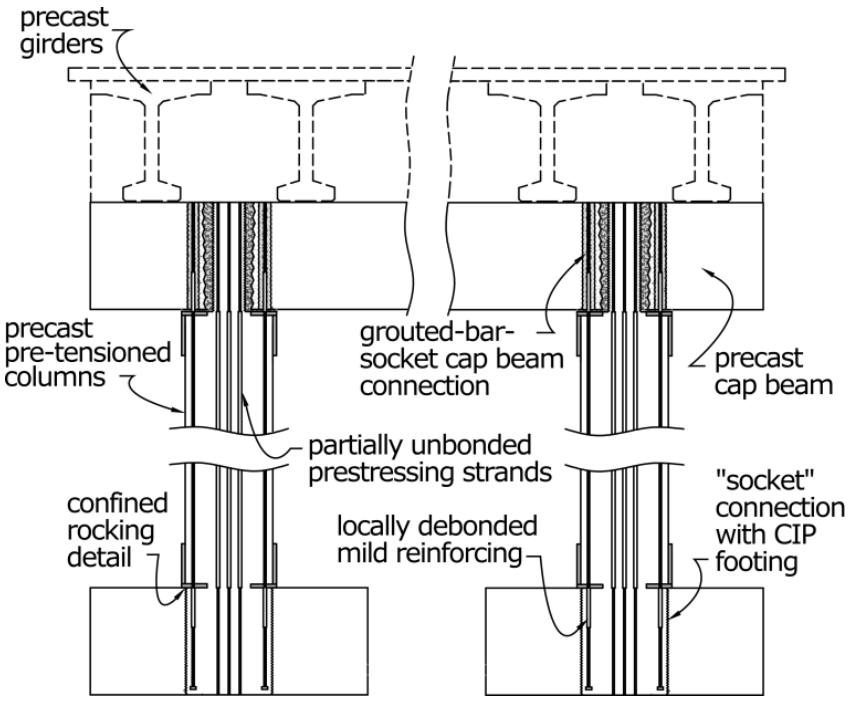

Figure 1.1 Schematic of new bent concept.

This system differs from other high-performance systems for accelerated bridge construction [e.g. Motaref et al. 2014, Trono et al. 2014, Varela and Saiidi 2014, Guerrini et al. 2015, White and Palermo 2016] in that it uses pre- versus post-tensioned columns that are protected at their ends with steel armoring. This is the first time a system has used this

combination of pre-tensioning and steel armoring. As discussed below, the system accelerates construction, minimizes post-earthquake displacements, greatly reduces column damage, and uses only conventional materials.

Accelerated construction is achieved through the use of precast columns and cap beams that can be assembled rapidly on-site. The precast connections for this system have been tested previously [Haraldsson et al. 2013, Pang et al. 2010, Tran 2015, and Davis et al. 2012], and a non-prestressed version of the precast system has been constructed in the field [Khaleghi et al. 2012].

Post-earthquake displacements are minimized, by pre-tensioning the columns with partially unbonded tendons. These tendons are designed to remain elastic during the earthquake and bring the bridge back to its original, plumb position after the shaking has ended.

Column damage is reduced by concentrating flexural deformations to specially detailed regions at the top and bottom of the columns. Because the columns "rock" instead of bend, they do not crack or spall as is typical of a conventional system during an earthquake, and damage to the concrete is effectively eliminated.

1.5 Document Organization

The document is organized as follows:

- Chapter 2 summarizes previous research related to systems for accelerated bridge construction in seismic regions.
- Chapter 3 discusses the specific components of the precast, pre-tensioned, rocking bridge bent concept that are necessary to achieve the performance outlined in Section 1.4
- Chapter 4 describes the subassembly connection tests conducted by Schaefer et al. (2014a) and Kennedy (2015) at the University of Washington.

- Chapter 5 describes the design and construction of a quarter-scale, two-span, bridge specimen with precast, pre-tensioned columns that was tested at the University of Nevada, Reno.
- Chapter 6 presents the observed and measured data from the shaking table tests of the precast, pre-tensioned bridge [Thonstad et al. 2016].
- Chapter 7 compares the shaking-table performance of the precast, pre-tensioned bridge specimen to a bridge constructed using conventional cast-in-place methods with nominally the same geometry and strength that was tested by Johnson et al. (2008) [Mantawy et al. 2016].
- Chapter 8 describes the proposed design methodology for the pre-tensioned bridge system using the displacement-based design procedure outlined in the *AASHTO Guide Specifications for LRFD Seismic Bridge Design* (2015).
- Chapter 9 describes a modeling strategy for the pre-tensioned bent system, and validates specific aspects of the model against the subassembly and shake table tests.
- Chapter 10 concludes with a summary of the results of this investigation..

CHAPTER 2: PRECAST CONCRETE SYSTEMS FOR ACCELERATED CONSTRUCTION IN SEISMIC REGIONS

This chapter summarizes previous research pertaining to precast concrete systems for accelerated construction in seismic regions.

- Section 2.1 describes research pertaining to precast concrete connections.
- Section 2.2 describes research pertaining to prestressed beam-to-column connections for buildings.
- Section 2.3 describes research pertaining to precast, post-tensioned bridge systems.
- Section 2.4 describes research pertaining to precast, pre-tensioned bridge systems.
- Section 2.5 summarizes the major findings of these experimental programs and identifies the key properties of precast, prestressed construction that must be considered when developing new, high-performance bridge systems.

2.1 Precast Concrete Connections

Previous researchers have shown that connections between precast columns and cap beams, spread footings and drilled shafts can be designed achieve similar levels seismic performance as cast-in-place systems. These connections can be grouped into broad categories based on the method whereby the longitudinal column reinforcement is anchored into the joint, which is contained within either the column-to-cap beam or column-to-foundation connection region. These connection types, shown schematically in Figure 2.1, are summarized here. Marsh et al. (2011) provides more details.

The connection types listed are not ordered as a logical progression of ideas, but rather different approaches which could be used to fit the needs of the particular project and agency. This section is meant to show that there are many viable ways to accomplish the same objective, and each strategy has its own strengths and drawbacks.

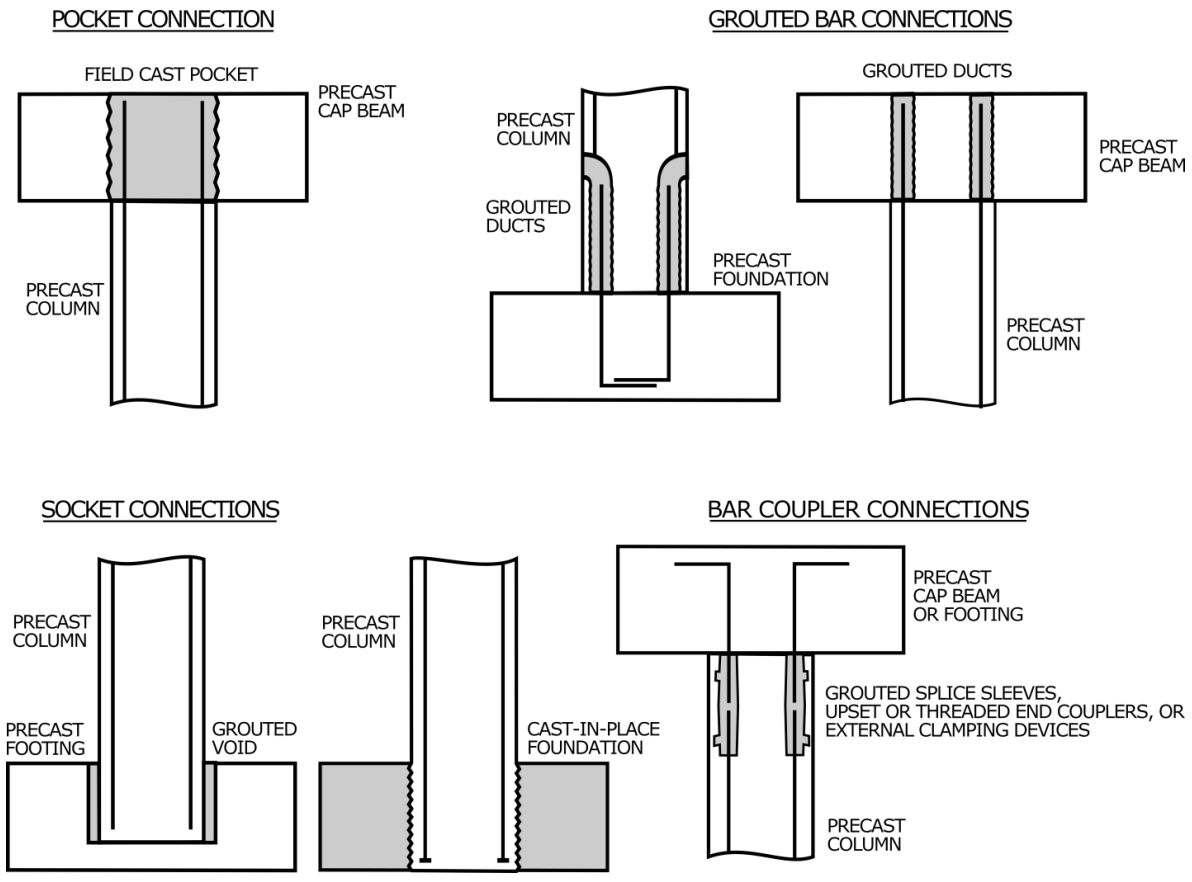

Figure 2.1: Precast connection types (excludes bolted connections).

2.1.1 Bar Coupler Connections

Bar-coupler connections are completed by mechanically splicing or "coupling" the column longitudinal reinforcement to bars within the foundation or the cap beam. These splices can be completed in a number of ways, including grouted splice sleeves, upset or threaded end couplers and external clamping devices. In some bar-coupler connections no cast-in-place concrete is needed, making them convenient from a contractor's perspective. The benefit of this

type of connection is that it can be completed quickly, although these connections typically will require tighter construction tolerances than other methods because the bars must meet end-to-end.

Haber et al. (2013) tested four large-scale, column-to-footing connections using upset headed bar and grouted sleeve couplers, shown in Figure 2.2, spliced within the body of the column. This study showed that both upset headed bar and grouted sleeve connections could achieve ductility ratios comparable to cast-in-place columns, although it was noted that columns with headed couplers outperformed those with grouted sleeves.

Ameli et al. (2015) tested three column-to-cap beam subassemblies constructed using grouted sleeve couplers. The performance of all three subassemblies was adequate, despite varying ductility capacities and failure modes. Placing the coupler within the cap beam, rather than the column, was found to provide superior performance, and locally debonding the reinforcement at the connection interface was found to increase the ductility capacity.

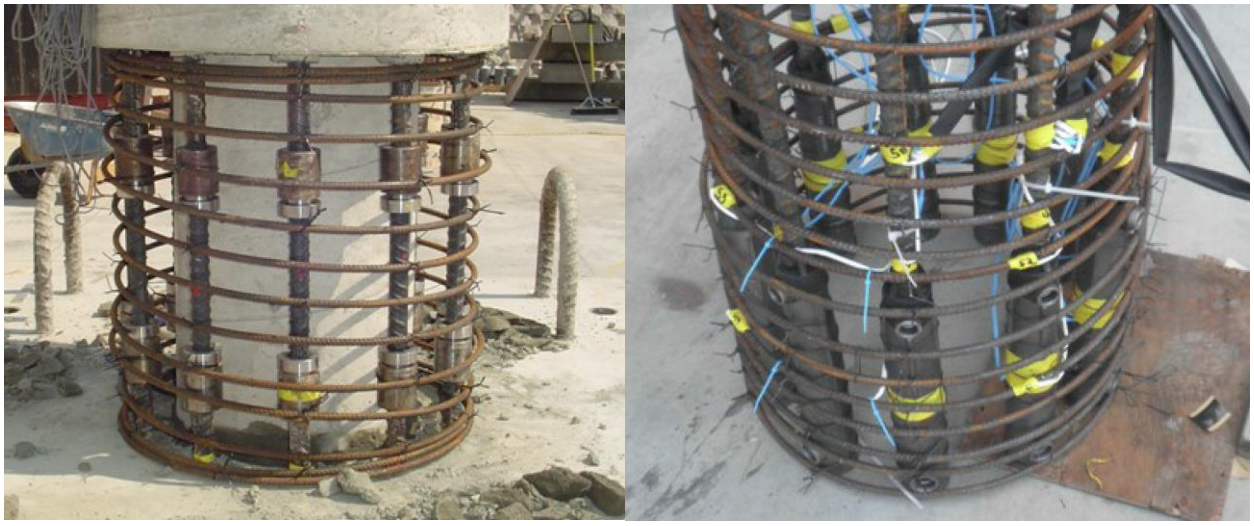

Figure 2.2. Upset headed coupler and grouted sleeve connection (from Haber et al. 2013)

Phillippi and Hegemier (2013) tested a two-column bridge bent under reversed cyclic loading. Couplers were placed in the column and were staggered in an attempt to avoid stress concentrations. The predominant mode of failure was the buckling of longitudinal reinforcement adjacent to couplers within the plastic hinge region.

2.1.2 Pocket Connections

An alternative to mechanically joining the columns longitudinal bars in the connection region is to cast the longitudinal bars from the column directly into the precast cap beam or foundation. This avoids the tighter tolerances associated with splicing the bars using bar couplers, however, since the cap beam and/or footing is likely precast, void(s) must be cast in the connecting member to accept protruding reinforcement from the column. One strategy for accomplishing this is to cast a single void larger in diameter than the columns spiral reinforcing, or a "pocket", into the connecting member to accept all of the protruding bars from the column. The single, large void can then be subsequently filled with either field cast concrete or high strength grout.

Longitudinal and shear reinforcing within the cap beam or footing is either routed around the void or is passed through it, as shown in Figure 2.3. Because the voids in the cap-beam or footing are typically created using steel corrugated tubes, the need for vertical shear steel in the joint region is greatly reduced. However, the time savings from such connections are typically small in comparison to other accelerated construction systems because the voids are usually filled with field cast concrete rather than grout, which requires a longer curing time.

Restrepo et al. (2011), Matsumoto et al. (2008), tested six large-scale column-to-cap beam subassemblies, two of which were constructed using pocket connections, shown in Figure 2.3. The results of these tests showed that the connections were able to achieve the required level

of performance, reaching drift ratios in excess of 5%. However, the tested subassembly where joint reinforcement was not provided (in addition to the corrugated tube) suffered greater joint distress and deformation than the cast-in-place specimen, with over 28% of the deformation of the specimen resulting from joint shear deformations.

Figure 2.3: Pocket connection (from Restrepo et al. 2011)

Pocket connections reduce the required construction accuracy, but may lead to wider cap beam designs than otherwise, due to the large voids for the column bars and the potential for cracking or splitting between the corrugated tube and the exposed face of the beam. This may also be true if the cap beam flexural reinforcement is meant to pass around the pocket rather than through it, to avoid significant congestion. This is less of a concern when dealing with foundation connections.

2.1.3 Grouted Duct Connections

Instead of casting a large, single void within the depth of the cap beam of foundation, one could instead grout each individual bar into its own duct. This approach requires slightly tighter construction tolerances than the pocket connection, but has the advantage of allowing cap beam

or foundation reinforcement to pass around the ducts. Grouted ducts have been shown to exhibit bond properties superior to that of to cast-in-place concrete. This type of connection is relatively easy to complete on-site and requires less curing time than cast-in-place construction, because the grout gains strength quickly.

To determine the capacities of a grouted bar column-to-cap beam connections for precast bridge bent construction, Steuck et al. (2009) conducted pullout tests of large diameter (No. 18) bars grouted into ducts. The results of these tests indicated that very high bond stresses could be achieved in the ducts, and even large diameter bars (e.g., No. 18) could be fully developed within the depth of a typical precast cap beam.

Figure 2.4: Grouted bar connections (from Pang et al. 2010 and Tazarv and Saiidi 2014, respectively).

Building on this work, Pang et al. (2010) tested three column-to-cap beam subassembly specimens constructed using a "large-bar connection", shown in Figure 2.4. These grouted bar connections utilize a small number of large-diameter bars at the column-cap beam interface. Fewer larger bars means fewer larger ducts in the precast cap beam, which reduces congestion and increases construction tolerances.

The precast columns had force-displacement responses nearly identical to those of a reference cast-in-place specimen, however it was noted that a majority of the total cantilever deflection was attributable to rotations at the connection interface rather than curvature in the plastic hinge region as intended of other precast connection systems. Column longitudinal reinforcing was locally debonded in two of the three specimens at the connection interface. This detail was found to have little effect on the force-deformation characteristics and damage progression of the columns. In all four specimens, the concrete column longitudinal bars bucked at a drift ratio of approximately 5.5% and fractured shortly thereafter. Because the bars fractured due to flexural, rather than axial, strains the local debonding had little effect on the drift ratio at first bar fracture.

Restrepo et al. (2011), Mashal and Palermo (2014) and Tazarv and Saiidi (2014) also tested grouted bar cap beam connections with locally debonded mild steel reinforcement. The bars were unbonded at the connection interface to prevent premature fracture. Tazarv and Saiidi (2014) used ultra-high performance concrete (UHPC) instead of grout to anchor the bars.

The experiments in the preceding paragraphs used grouted bar connections consisting of extending column reinforcing into ducts within either the cap beam or foundation. Belleri and Riva (2012) tested three grouted duct connections for buildings under reversed cyclic loading. In this case, bars protruded from the foundation and the connection was completed by grouting these bars into ducts cast within the body of the column. The columns behaved very similarly to a cast-in-place reference specimen. The confining effect of the ducts within the body of the column prevented buckling of the longitudinal reinforcement, and damage to the reinforcement was further reduced by locally debonding the bars in the grouted ducts.

2.1.4 Socket Connections

The bar coupler, pocket, and grouted bar connections all function by joining or anchoring the column longitudinal reinforcement across a cold joint into the connecting member, either a cap beam or foundation. This means that the concrete at the connection interface is not monolithic and cannot be relied on to carry tensile stresses. As an alternative to these "jointed" systems, the precast column could instead be extended into the cap beam or foundation and embedded directly into the connecting member as shown in Figure 2.5.

These extensions contain the columns longitudinal bars and transverse reinforcing; they are either fitted within a partial depth void precast into the connecting member and grouted, a "dry socket" connection, or they are directly embedded into a cast-in-place member like a spread footing by erecting the column prior to casting, a "wet socket" connection.

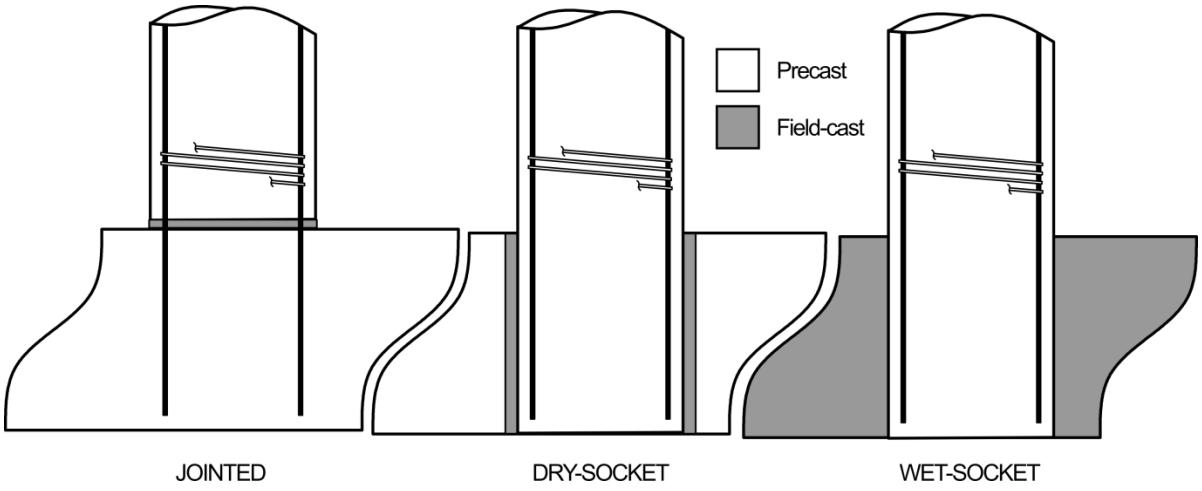

Figure 2.5 Socket connection types

Osanai et al. (1996) tested eight "dry" socket subassemblies with varying embedment depths and socket surface finishes under reversed cyclic loading. The columns with roughened exteriors in the socket region required half of the embedment depth of those without roughened exteriors to reach the ultimate strength of the columns. Belleri and Riva (2012), Mashal and

Palermo (2014) also tested “dry” socket connections following similar recommendations for socket surface roughening and embedment depth. In both experiments, failures were successfully confined to the precast columns.

Haraldsson et al. (2013) tested three “wet” socket column-to-footing connection subassemblies. All three columns had external roughened surfaces, as shown in Figure 2.6; the depth of the footing, and thus the length of the column socket, was varied. In one specimen, some of the foundation’s mat reinforcement was passed underneath the column, whereas in others it was moved to the side. In no case did reinforcing cross the precast cast-in-place interface. All three subassemblies reached their predicted capacities. In the specimens with larger footing depths, failure was confined to the column and damage to the footing was minimal, however the specimen with the shallow foundation depth (only one half of one column diameter) failed in a combined punching shear and moment transfer mechanism. The headed terminators used in the embedded portion of the column were effective at anchoring the longitudinal reinforcement and reduced joint shear demands in the connection region by providing a more direct flow of internal forces.

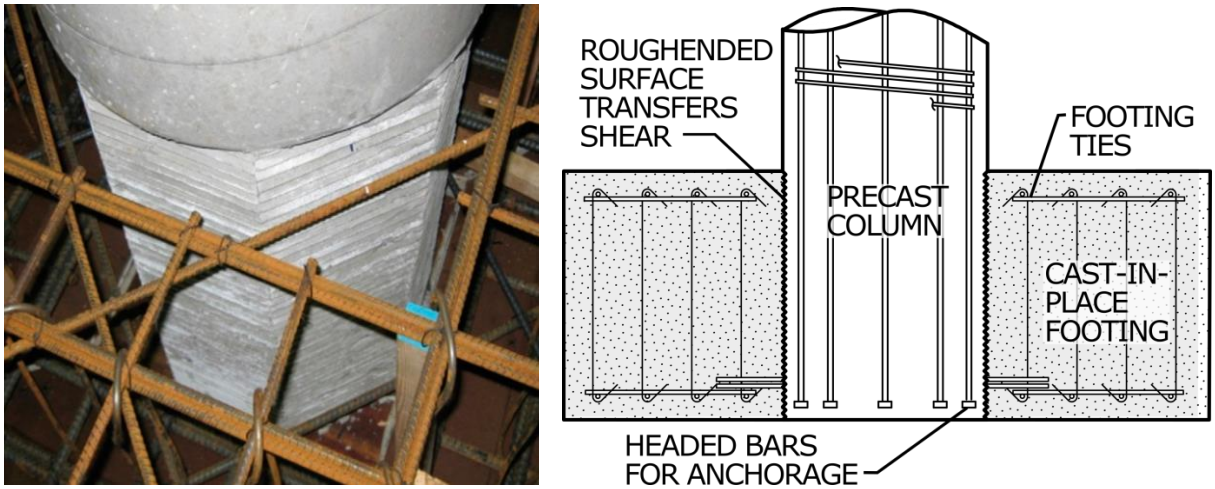

Figure 2.6: Wet-socket spread-footing connection (adapted from Haraldsson et al. 2013).

Tran (2015) tested three column-to-drilled shaft subassemblies joined using “wet” socket connections, shown in Figure 2.7, with varying transverse reinforcing ratios and transition region diameters. Two of the three specimens were detailed with code specified transverse reinforcement in the drilled shaft transition region, and performed like monolithic cast-in-place systems; plastic hinges formed in the columns and little damage was observed in the transition region. The third specimen, which was detailed with half of the code-specified amount of spiral, failed in a prying failure mechanism with the column being relatively undamaged at the end of testing. The two subassemblies with adequate transition region detailing performed similarly to the columns tested by Haraldsson et al. (2013) which had the same nominal strength.

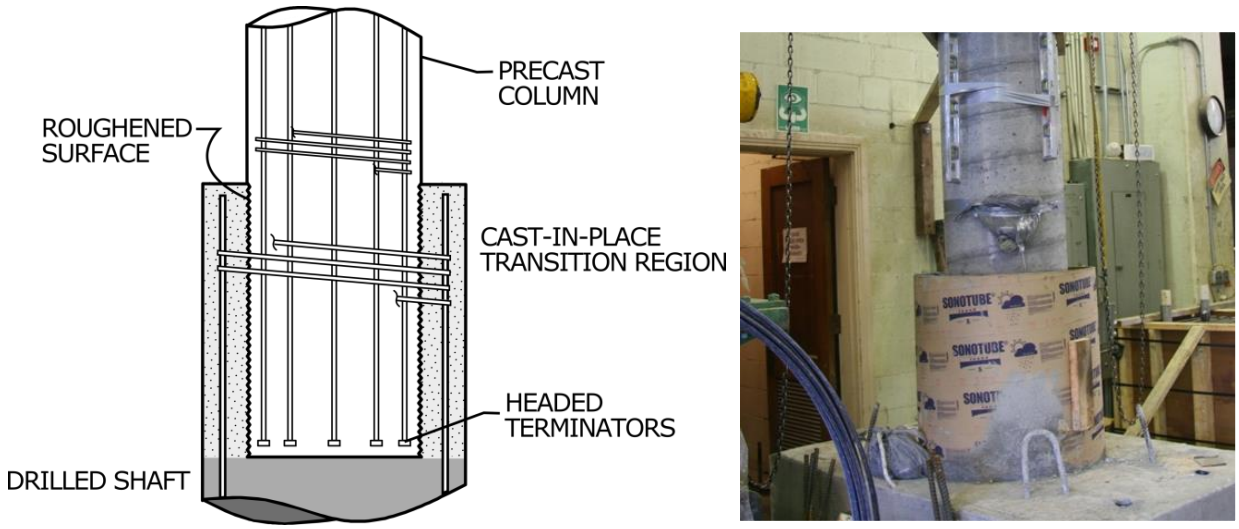

Figure 2.7 Wet-socket drilled shaft connection (adapted from Tran 2015).

2.2 Precast Beam-to-Column Connections with Unbonded Post-tensioned Strands

Non-prestressed precast systems, like those described in Section 2.1, are typically designed so that the inelastic action occurs in the column, although connection rotation also plays a significant role. These systems, as is the case for cast-in-place ones, are prone to earthquake damage and post-earthquake displacements.

As was observed in Section 2.1, for tests of grouted duct connections, rotations concentrated at the end of the columns, rather than distributed column bending, are the predominate deformations observed during experiments [e.g. Pang et al. 2010]. Many researchers have proposed exploiting this property of precast concrete connections, by intentionally concentrating column deformation at the precast connection interfaces, often called "rocking" behavior.

Rocking designs are often combined with unbonded post-tensioning to provide clamping forces that cause any cracks that form to close at the end of an earthquake. Such connection behavior can minimize the residual displacements of a structure following the end of seismic shaking and prevent spalling due to cyclic inelastic hinging. This concept was originally explored for frame buildings by Ishizuka et al. (1984), who proposed using unbonded post-tensioning for seismic resistance in a cast-in-place building. Priestley and Tao (1993) and Mole (1994) then conducted analyses of a version of the system that used post-tensioned, precast elements that were designed to rock at the connections. Stone et al. (1995) and Priestley and MacRae (1996) then conducted tests on a similar system.

Stone et al. (1995) tested ten precast, prestressed concrete beam to column connections with varying amounts of bonded and unbonded mild steel and prestressing steel. The mild steel was added to these connections to increase the amount of energy dissipation which was identified by Cheok and Lew (1993), who tested prestressed beam-to-column connections with bonded strands at NIST, as one potential issue facing prestressed frame design. The results of the tests showed that the frames with partially unbonded prestressing could achieve large drift capacities (6%) with only minimal cover spalling at the corner of the beam and negligible residual displacement.

Priestley and MacRae (1996), as part of the PRESSS program, tested two ungrouted post-tensioned precast beam to column joint connections. The subassemblies were designed with greatly reduced beam and joint shear reinforcement, however they contained spiral confinement of the beam end regions, as shown in Figure 2.8. The two subassemblies performed well with only minor damage up to drift ratios of 3%, energy dissipation was small and residual displacements were negligible.

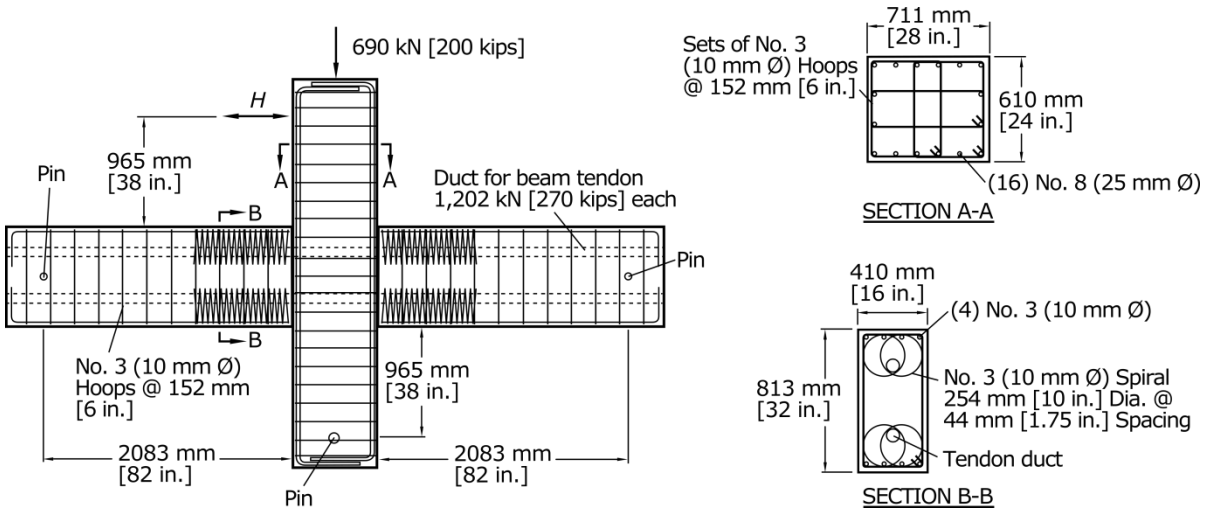

Figure 2.8 Precast, prestressed interior subassembly (adapted from Priesltey and MacRae 1996).

In Phase II of the PRESS program, Palmieri et al. (1996) tested five different precast, prestressed beam-to-column connection details, three of which contained only prestressing steel. The remaining two specimens were detailed with both mild and prestressing steel crossing the beam-to-column interface and had a novel “gap” grouted interface in which only the bottom third of the beam area was in contact with the column face. Several of these specimens, had very short lengths of prestressing strands, which yielded at low drift levels. The results of these tests were mixed; only three of the tested connection details exhibited the desired behavior through 3% drift. Several of these specimens included a corbel underneath the column to aid in erection and

to support the precast beam if interface friction proved insufficient to carry the required shear across the precast joint.

Stanton et al. (1997) summarized the beam-to-column experiments conducted at the NIST testing laboratory [Cheok and Lew (1991), Cheok and Lew (1993) and Stone et al. (1995)] and provided design criteria and code implications resulting from the test program. Their analyses showed that friction could be relied on to carry shear across the joint provided that the beam aspect ratio was sufficiently large, eliminating the need for corbels. They also showed that the hybrid frame system carried shear through a more direct mechanism than conventionally reinforced frames, and the amount of shear steel in the beam could likely be reduced from the code specified value.

These experimental programs demonstrated that precast prestressed frame systems could be designed to have very low residual drifts, large drift capacities and negligible damage even after large earthquakes. The use of mild steel reinforcement was successful at increasing the energy dissipated per cycle of the system, but it came with the tradeoff of increased residual displacements. These tests also demonstrated that the shear in the precast beam was carried through a direct strut mechanism which reduces the demand on, and necessity for, transverse reinforcing in the beam.

2.3 Precast, Post-tensioned Bridge Columns

The principles underlying the design of precast, prestressed frames for buildings are directly transferable to precast, prestressed systems meant for accelerated bridge construction. Research has suggested that the same benefits of precast, prestressed building frame construction (rapid on-site assembly, greater quality control and seismic performance) can be realized in bridges. The major difference is that the columns of the bridge, rather than the beams in a

concrete frame, are the prestressed components of the system. Functionally, the bridge bents behave like one-bay frames turned through 90 degrees.

2.3.1 Segmental Bridge Construction

Post-tensioned bridge systems are especially attractive for segmental column construction, since the strands provide continuity between the precast column sections. Billington et al. (1999, 2001) proposed a precast segmental substructure system concept as an alternative to conventional cast-in-place construction. Figure 2.9 shows schematically the system concept for a single-column pier. The hollow match cast segmental columns are joined by epoxy adhesive, and field-cast construction joints are used at the ends of the columns to provide the required geometric tolerances. Shear keys are provided between segments, and no mild steel reinforcement crosses the precast segment interface.

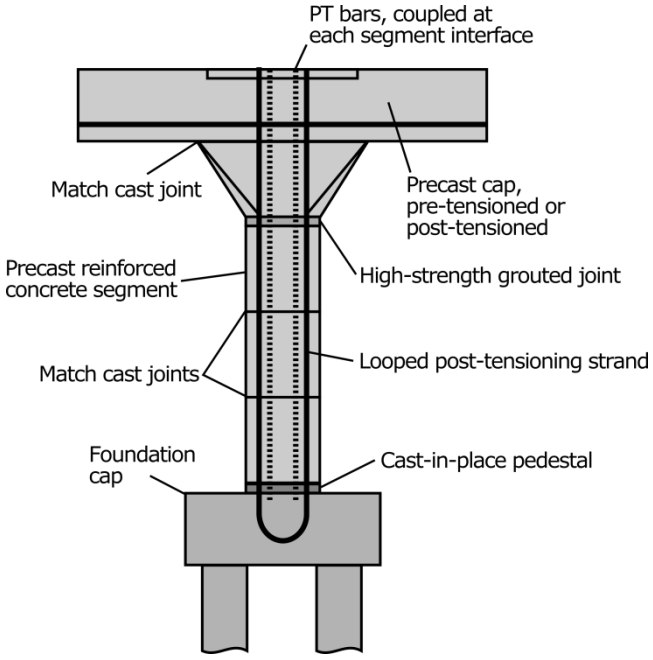

Figure 2.9 Precast segmental substructure system concept (adapted from Billington et al. 1999).

The columns are post-tensioned using bars and strands to provide increased durability. The proposed system was estimated to have higher initial costs than typical cast-in place substructures, but this higher initial investment could be offset by the expected savings in on-site construction time, estimated to be 50%-75% shorter for the precast system over the cast-in-place alternative.

Hewes and Priestly (2002) tested a precast, prestressed segmental substructure system. Four large-scale segmental columns were tested; Figure 2.10 shows the reinforcement details for the specimens. The column segments were connected using epoxy adhesive, and had vertical, unbonded, post-tensioned strands that were anchored in the foundation and in the loading stub. The bottom-most segment included a steel jacket for added confinement. For each aspect ratio, two different jacket thicknesses were tested, 6 mm [0.25 in.] and 2.8 mm [0.11 in.]. These thicknesses represent tubes with diameter-to-thickness ratios of roughly 100 and 200, respectively.

Three of the four specimens were able to achieve drift ratios of 4.0% with little to no degradation in strength; the fourth suffered significant spalling above the steel jacket at a drift ratio of 3%, at which time the test was discontinued. All of the specimens had small residual drift ratios, the maximum being 0.3% at test end. Because no mild steel was included in the columns, the hysteretic energy dissipation of the columns was low, on average the equivalent viscous damping was 5%. Damage to the column consisted of concrete crushing at the jacket toe, spalling in the cover concrete directly above the steel jacket and yielding of some of the steel jackets in hoop tension.

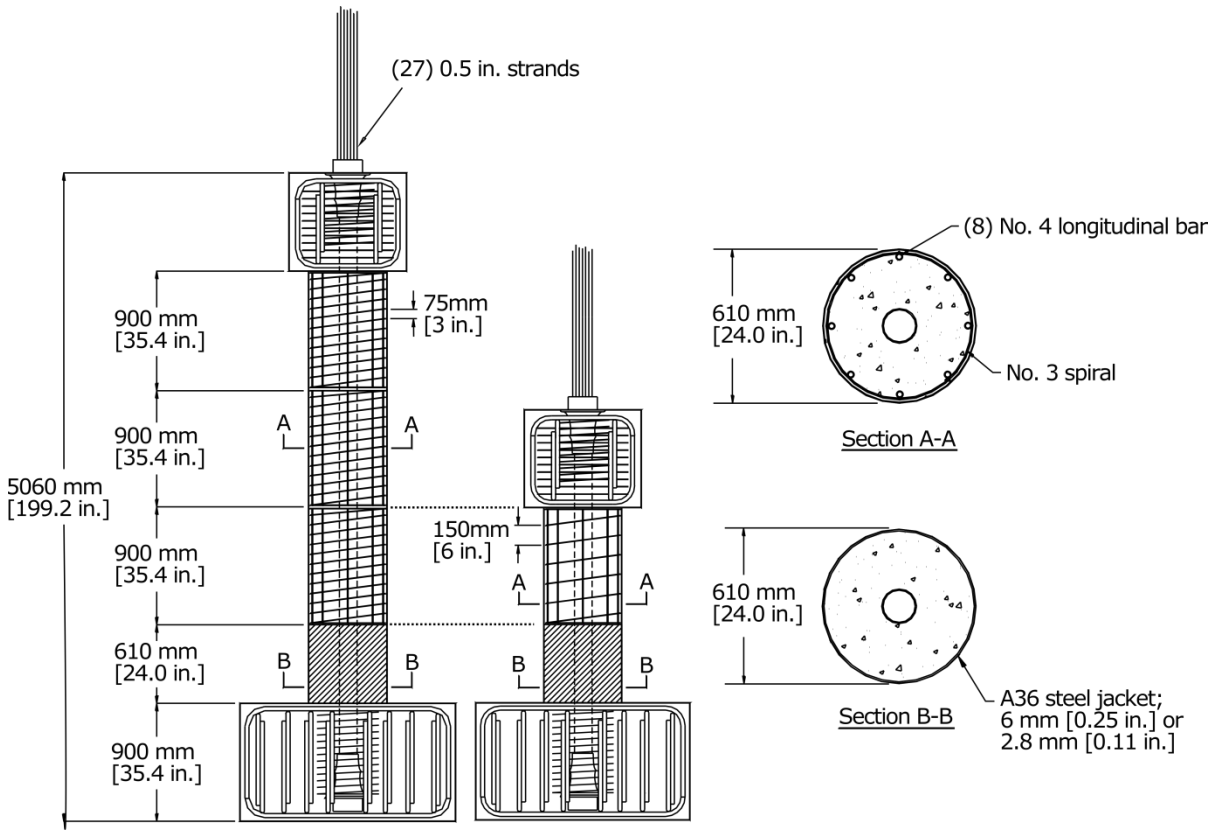

Figure 2.10 Precast, post-tensioned segmental subassembly (adapted from *Hewes and Priestly 2001).*

Similar segmental systems have been tested by other researchers. Billington et al. (2004) tested seven precast, segmental, post-tensioned cantilever subassemblies. The end segment of five of these specimens was constructed using a ductile fiber-reinforced cement-based composite (DFRCC). Chou and Chen (2006) tested two segmental, post-tensioned, precast concrete filled tube (CFT) column-to-footing subassemblies. One specimen contained energy dissipating devices at the base of the column to increase its hysteretic damping. Yamashita and Sanders (2009) conducted shaking table testes of a quarter-scale, match cast, segmental, post-tensioned column. ElGawady et al. (2010) tested three segmental post-tensioned, concrete-filled fiber tube (CFFT) column-to-footing subassemblies. Bonded neoprene was used in one segmental specimen to connect the segments at the first two precast interfaces, and steel angles were added

to the column-to-footing interface in another. Ou. et al. (2010) tested four segmental, post-tensioned, single column bents under reversed cyclic loading. These specimens contained varying amounts of locally debonded energy dissipating deformed bars that crossed column-to-footing interfaces ($0\% \leq \rho \leq 1\%$). Motaref et al. (2014) tested post-tensioned segmental precast columns with different details for the first precast segment. One subassembly utilized an engineered cementitious composite material, one had an elastomeric bearing at its base and one was wrapped in a carbon fiber reinforced polymer tube. Sideris et al. (2015) conducted shaking table tests of a single span bridge specimen, which had single column bents and post-tensioned, segmental columns with hybrid sliding-rocking joints. The sliding joints were meant to dissipate energy in lieu of mild steel reinforcement.

These experiments demonstrated that segmental bridge columns with unbonded post-tensioning could be designed to reach very large drift ratios with little strength degradation, residual drift and damage. They also re-iterated the tradeoff between the system's ability to re-center and dissipate energy.

2.3.2 Non-segmental Construction

Precast columns with unbonded post-tensioning have also been suggested for non-segmental construction. Cohagen et al. (2008) tested two post-tensioned column-to-cap beam connection subassemblies. These subassemblies, shown in Figure 2.11, were constructed to represent a precast column-to-cap beam connection completed using a grouted bar connection (the large diameter bar concept developed by Pang et al. 2010). The specimens' geometry and test program were identical to the cast-in-place subassembly tested by Pang et al. (2010) which served as the reference. The relationship between re-centering behavior and the initial force and

proportioning of prestressed and mild steel reinforcement was investigated. Both columns showed a better re- centering capability after 2% drift than the comparable non-prestressed

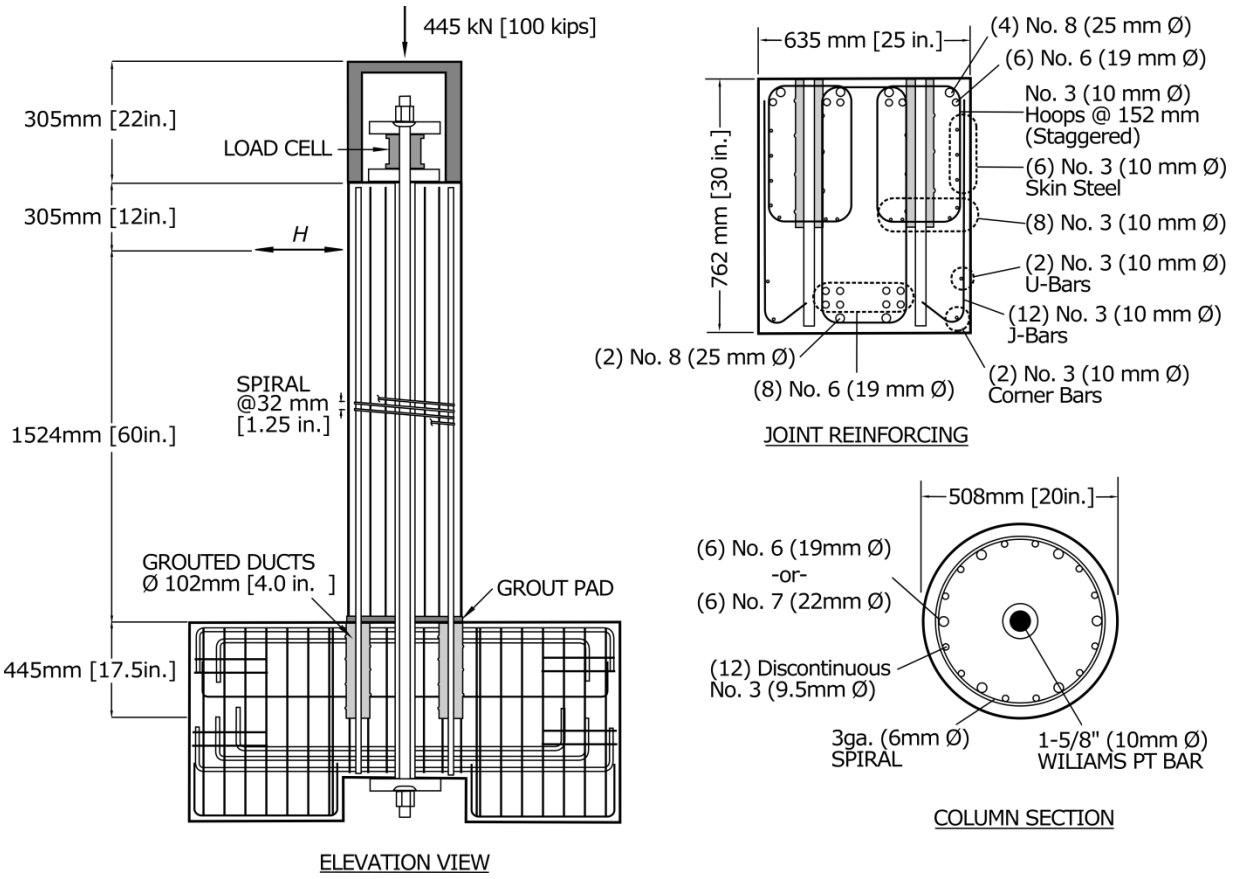

Figure 2.11 Precast, post-tensioned subassembly (adapted from Cohagen et al. 2009).

reference column, and the column with the higher initial prestressing force re-centered better than its more lightly prestressed counterpart. Both specimens had more damage at the interface than the reference specimen tested by Pang et al (2008), which was attributed to the increase in axial stress due to post-tensioning.

Similar systems have been tested by other researchers. Palermo et al. (2007) tested four precast, post-tensioned column-to-footing subassemblies with mild steel energy dissipating bars, a baseplate on the top of the foundation, and steel angles embedded into the column to protect

the column edges. These connections were completed with grouted bar connections within the body of the column.

Solberg et al. (2009) tested two columns, one of which included unbonded post-tensioning, steel plates at the bottom of the column and the top of the foundation, and replaceable energy dissipaters that were cast into a "shoe block" at the end of the column, above the footing.

Restrepo et al. (2011) tested three precast, post-tensioned column-to-cap beam subassemblies completed using a grouted bar connections. The specimens included a precast column, a precast concrete-filled tube column and a precast "dual-shell" column, consisting of two steel tubes with cast-in-place concrete infill between them.

Trono et al. (2014) conducted shaking table tests on a post-tensioned, rocking column-to-footing subassembly with hybrid fiber reinforced concrete (HyFRC) at the column-footing interface.

White and Palermo (2016) tested two armored, post-tensioned columns. One featured replaceable dissipaters located within the body of the column, and used a bar coupler connection similar to those tested by Haber et al. (2013). The other, included interior energy dissipaters, a dry socket connection, and threaded inserts for post-earthquake retrofit.

The specimens were all able to achieve large ductility levels with minimal damage and improved re-centering in comparison to cast-in-place reference specimens. The columns that were also reinforced with mild steel crossing the column-to-footing interface had both higher energy dissipation and residual displacements.

2.4 Precast, Pre-tensioned Bridge Columns

Recently, researchers have investigated the use of pre-tensioned (as opposed to post-tensioned) precast columns to achieve re-centering. Pre-tensioning with strands provides several

advantages. Such columns can be prestressed in a fabrication plant, thus eliminating the need for anchorages and field post-tensioning, which is time-consuming and requires specialized labor. The elimination of anchorages is a second benefit, because they can be susceptible to corrosion, and stress concentrations at the wedges can limit the fatigue strength of the tendon [Walsh and Kurama 2012].

Davis et al (2012) tested two precast, pre-tensioned subassemblies, one column-to-footing connection and one column-to-cap beam connection. The columns included both prestressing and mild steel, proportioned so that the strands contributed 60% of the columns moment capacity. The column-to-footing connection was completed using a "wet socket" connection, nearly identical to those used in Haraldsson et al. (2013), but were provided with no special confinement reinforcement other than standard spiral. The column-to-cap beam connection was completed using a modified "large-bar" connection, as shown in Figure 2.12. In it, a reduced-diameter extension of the column was grouted into a large central duct, and bars, arranged in a circle around the column extension, were grouted into individual ducts. The column extension contained the strands, and allowed them to be anchored within the depth of the cap beam.

These specimens demonstrated the excellent restoring properties of the pre-tensioned column concept, but the columns suffered damage at drifts lower than in comparable precast reinforced concrete systems without pre-tensioning [Haraldsson et al. 2013]. This difference was again attributed to the increased axial stress due to prestressing and, more importantly, to the reduction in longitudinal bar size and the attendant tendency to buckle that resulted from replacing some of the mild steel reinforcement with prestressing strands.

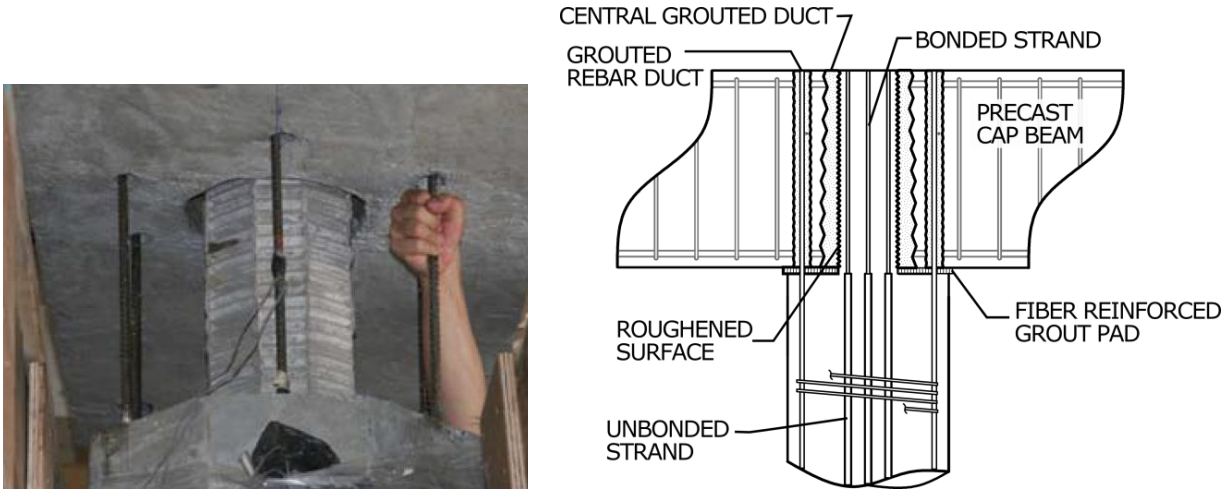

Figure 2.12 Modified grouted bar connection (adapted from Davis et al. 2015).

Building on this research, Finnsson (2013) tested two precast, pre-tensioned column-to-footing subassemblies connected using "wet" socket connections suitable for footings. These columns contained Hybrid Fiber Reinforced Concrete (HyFRC) shells in the plastic hinge regions; it was hoped that the superior tensile strength and toughness of the HyFRC over traditional concrete [Kumar et al. 2011] would control the spalling and damage observed in the previously tested pre-tensioned column specimens. One specimen also contained stainless steel longitudinal reinforcement to investigate the benefits of its higher ductility.

The columns were both able to maintain over 80% of their peak lateral load to drift ratios of approximately 10%, much further than the comparable pre-tensioned specimens without HyFRC [Davis et al. 2012]. Both specimens eventually formed dominant crack planes, as shown in Figure 2.13, causing localized inelastic deformation and premature failure in the mild steel reinforcement. Bar buckling and fracture still occurred at drift ratios lower than the previously tested system without pre-tensioning [Haraldsson et al. 2013], although the use of stainless steel reinforcing increased the drift ratio at first bar fracture.

Figure 2.13 Dominant crack planes formed in columns made with fiber reinforced concrete shells (from Finnsson 2013).

Haraldsson (2015) conducted shaking table tests of a column-to-footing subassembly constructed using similar details to Finnsson et al. (2013) but at 25%, rather than 42%, scale. The specimen was designed to have strength and geometry similar to those of a subassembly constructed using conventional detailing [Schoettler et al. 2013] that served as the reference. The pre-tensioned specimen showed superior re-centering capability compared to reference column, but the shaking table tests revealed the same propensity that had been observed during Finnsson's quasi-static tests. A single, large crack formed in the HyFRC shell, the column rocked about this plane, and because cracking did not distribute up the height of the column, strains in the column mild steel reinforcement were concentrated there, leading to premature bar fracture.

Schaefer et al. (2014a) and Kennedy (2015) tested three precast, pre-tensioned subassemblies using armored column end details, two column-to-footing and one column-to-cap beam connection. The column reinforcement near the precast connection interface was locally debonded and a confined rocking detail was provided in the column end region to confine the column concrete there, preventing spalling and bar buckling. These specimens represented the

culmination of a long sequence of developments at the University of Washington [Stuek et al. 2009, Pang et al. 2010, Cohagen et al. 2008, Davis et al. 2012, Finnson 2013, Schaefer et al. 2014a, Kennedy 2015]. They provided excellent performance, which is discussed in detail in Chapter 4.

2.5 Summary and Lessons Learned

This chapter summarized previous research pertaining to precast concrete systems for accelerated construction in seismic regions. These precast connections can be broadly divided by the way the precast components are meant to behave, into "emulative" and "jointed" connections, as shown in Figure 2.14.

Emulative Connections. Emulative connections are intended to emulate cast-in-place construction and its performance. Distributed curvature occurs within the columns, which produces flexural cracking, spalling and potentially transverse reinforcement fracture and longitudinal reinforcement buckling.

Jointed systems. These systems consist of precast elements joined, across field-cast joints, through the members longitudinal reinforcement. These connections are typically meant to emulate the performance of cast-in-place construction, however, flexural deformations in these systems are shared by curvature within the column and concentrated rotations at the connection interface. These connection rotations lead to strain concentrations in the longitudinal reinforcement. These strain concentrations may be exacerbated if strain penetration into the bond region is prevented, as is the case in rigid grout sleeve connections. This results in reduced drift capacity unless the reinforcement in locally debonded to compensate [Marsh et al. 2011].

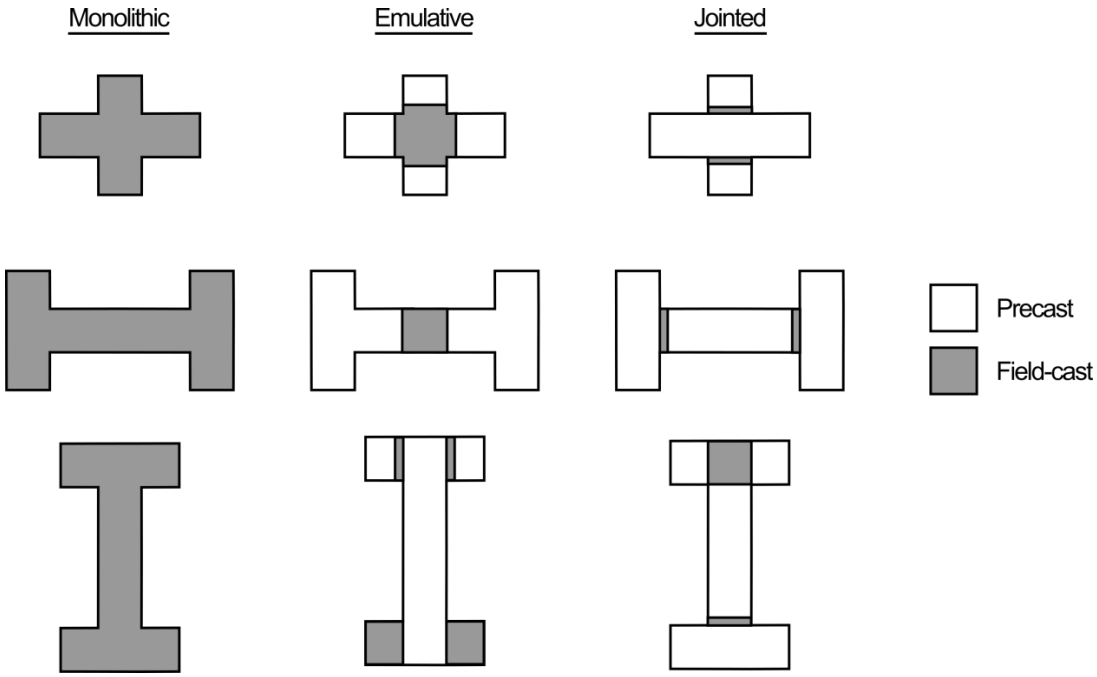

Figure 2.14 Precast component connection types

Jointed Prestressed Systems. Jointed column connections may be prestressed to minimize residual displacements. This concept has been tested and used in buildings [e.g. Englekirk 2002], where the beams, rather than the columns were prestressed. It has been tested for bridge columns, but not yet implemented.

Pre-tensioned Systems. Prestressed, jointed systems may be either post-tensioned or pre-tensioned. Most studies to date have focused on post-tensioning, but pre-tensioning appears to offer advantages for construction speed, quality and life-cycle durability.

Mild-steel reinforcement. The addition of mild steel to prestressed jointed systems increases hysteretic energy dissipation, but also leads to larger residual displacements than those without.

Connection region confinement. The use of ductile concrete or confining jackets in the connection region of prestressed jointed systems reduces spalling and improves ductility

capacity. However, the use of fiber reinforced concrete is not effective at delaying bar buckling and fracture when compared to cast-in-place columns.

Partially Unbonded Reinforcement. In jointed precast systems, locally debonding longitudinal reinforcement at the precast connection interface is necessary to prevent premature bar fracture and was shown to have little effect on the force-displacement response of the system [e.g. Pang et al. 2010].

CHAPTER 3: PRE-TENSIONED, ROCKING BRIDGE SYSTEM

This chapter describes the key features of the pre-tensioned rocking bridge system and how it meets the performance goals outlined in Chapter 1 (reiterated here). The new system was developed to:

1) accelerate bridge construction,

2) minimize post-earthquake residual displacements; and

3) eliminate damage to the column concrete during an earthquake.

This chapter describes how the proposed system achieves these objectives.

- Section 3.1 describes the precast connections used in the proposed system, and presents field experience with a similar non-prestressed bent system which utilized similar connections.
- Section 3.2 discusses the proportioning of mild and prestressing steel to achieve re-centering, and defines several metrics to quantify both the ability of the system to re-center and how re-centering can be assessed through quasi-static experiments.
- Section 3.3 presents the plastic hinge detailing strategies in the proposed system that are meant to confine and protect the column concrete, prevent bar buckling, and delay bar fracture.

3.1 Prefabricated Components for Accelerated Construction

The pre-tensioned bent system is built on proven connections that have been experimentally validated and field verified. A non-prestressed bent system that used similar connections was used to construct an overpass in Washington State [Khaleghi et al. 2012], see

Figure 3.1. The bridge consisted of two tall abutments and a center four-column bent. The precast columns were connected to the spread footings using “wet” socket connections [Haraldsson et al. 2013], and the cap beam was connected to the tops of the columns using “large-bar” connections [Pang et al. 2010].

Figure 3.1 Construction of a non-prestressed, precast bridge bent (from Khaleghi et al. 2012).

No major problems were encountered during construction and the alignment was straightforward. The columns were constructed segmentally, and the cap beam, due to weight limitations, consisted of two separate pieces; the placement of each took less than 30 minutes. Dividing the columns into segments was not necessary for the project, but the owner elected to do it in order to verify that it could be done for future cases.

This project demonstrated that the proposed pre-tensioned system could be constructed rapidly. The proposed precast, pre-tensioned system has construction details similar to those of the non-prestressed system and could be assembled similarly as shown in Figure 3.1, although the columns would be non-segmental. The bottom connection is identical; the precast columns are cast directly into spread footings [Haraldsson 2013] or drilled shafts [Tran 2015] using a “wet socket” connection, as shown in Figure 3.2a. The top connection in the proposed system differs only slightly from the one used in Khaleghi et al. (2012) since it must also contain a

central reduced-diameter column section, where the pre-stressing tendons are bonded, that must be fitted into a large duct in the cap beam. The precast cap-beams are connected to the columns using grouted "hybrid-bar-socket" connections [Davis et al. 2012], as shown in Figure 3.2b.

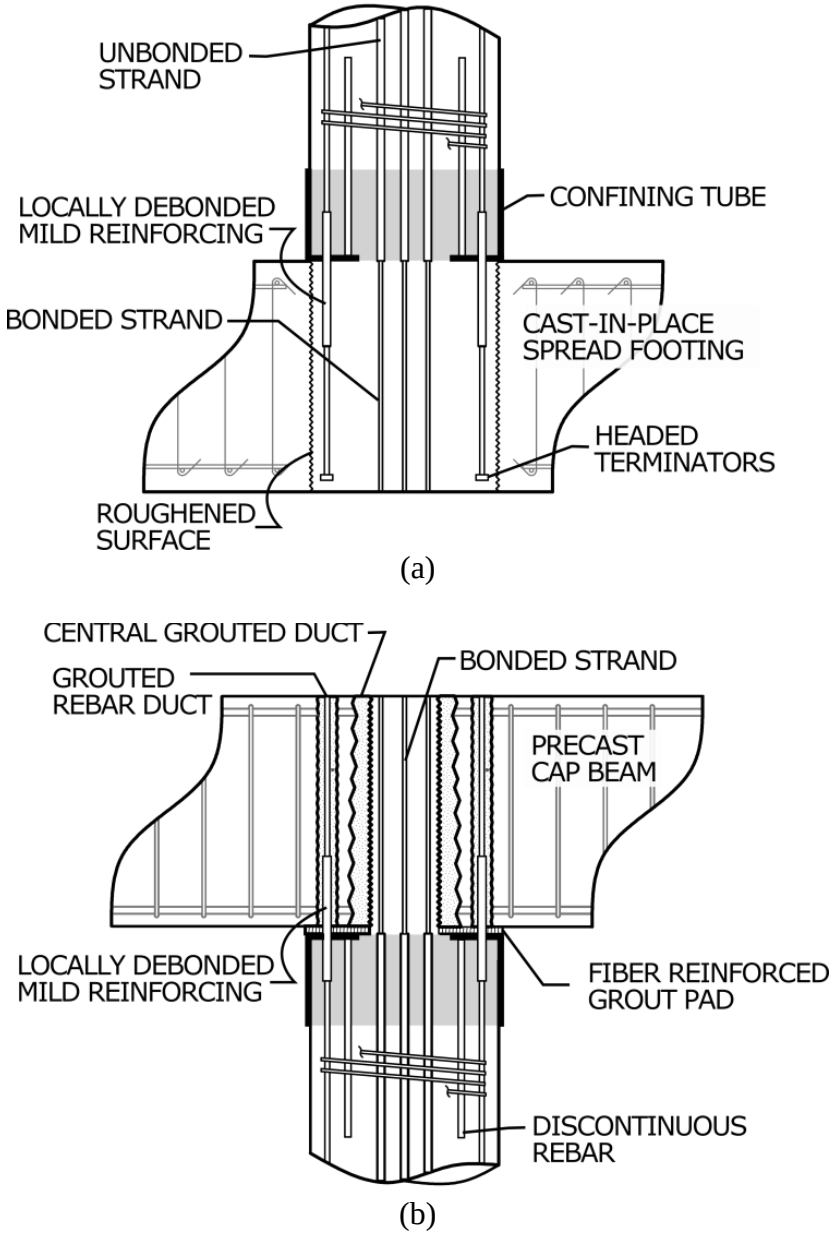

Figure 3.2 Precast connections for the proposed pre-tensioned bridge system. (a) "Wet" socket footing connection (b) "Hybrid-bar-socket" cap beam connection.

Figure 3.3 compares the construction sequence of the proposed precast system with that of a traditional cast-in-place system. The columns and cap beams are fabricated off-site and

assembled rapidly on-site. The largest time savings in on-site construction are realized by precasting the cap beam, which eliminates a casting and curing cycle [Weinert 2011, Marsh et al. 2011].

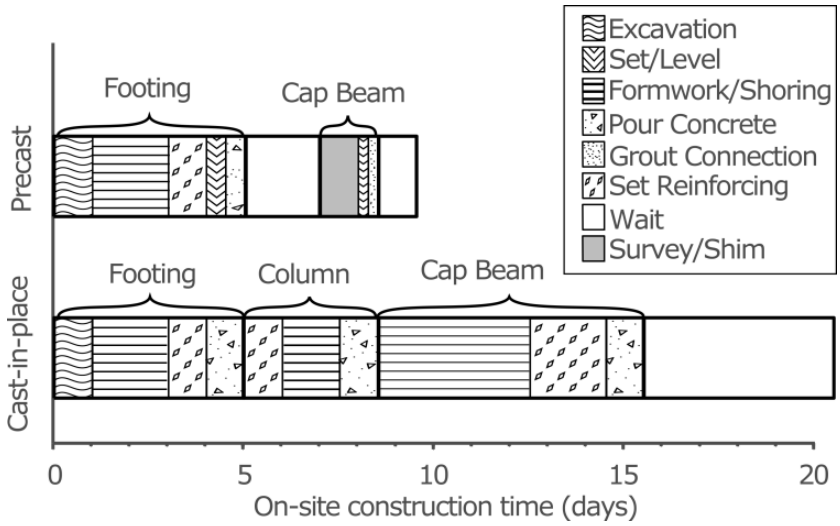

Figure 3.3 Comparison of bridge bent construction sequence (data from Marsh et al. 2011).

3.2 Prestressed Columns to Minimize Residual Displacements

The proposed system reduces post-earthquake residual displacements by reinforcing the column with partially unbonded prestressing strands. In order to maximize the seismic drift reached before the strands yield, the strands are unbonded over the greatest height possible and bonded only at the ends of the columns. At the bottom, this is simple; the strands are bonded in the part of the column that is embedded in the cast-in-place footing. At the top, the strands are developed within the reduced-diameter region of the column that extends into the cap beam. This configuration has an added benefit of providing a column "shoulder" on which to support the cap beam during erection.

In order to discuss how one would design a system to have a desired re-centering performance, two quantities are needed;

1) a measure of re-centering performance, which is a consequence of the constructed system; and

2) a property of the of the system, which is determined during the design process.

The following paragraphs describe two such parameters, and the relationship that exists between them based on experimental results.

The re-centering characteristics of a precast, prestressed column tested quasi-statically can be quantified using the measured displacements at zero applied force, as shown in Figure 3.4.

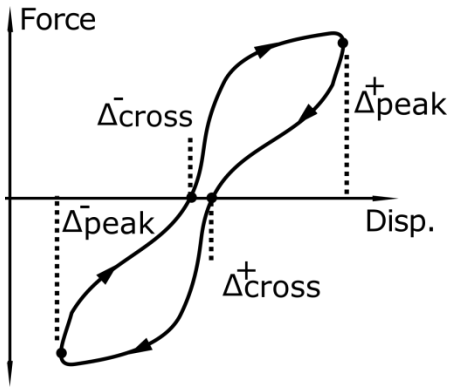

Figure 3.4 Definition of the cross-over displacements

A dimensionless form of this measure is given by the normalized cross-over displacement (NCOD), defined in Equation 3.1.

$$\text{NCOD} = \frac{\Delta^{+}_{\text{cross}} - \Delta^{-}_{\text{cross}}}{\Delta^{+}_{\text{peak}} - \Delta^{-}_{\text{peak}}} \qquad [3.1]$$

where $\Delta^{+}_{\text{cross}}$ and $\Delta^{-}_{\text{cross}}$ are defined as the displacements in a particular cycle of the specimen's moment-drift response at which the moment passes through zero, and Δ^{+}_{peak} and Δ^{-}_{peak} are the maximum and minimum imposed displacements in that same cycle. A NCOD value of 0.0 would correspond to perfect re-centering, whereas a value of 1.0 would imply a residual displacement equal to the peak displacement.

The re-centering capability of a prestressed column in closely related to its flexural strength, which consists of contributions from both mild and prestressing steel. These steel areas must be carefully proportioned in order to provide the desired re-centering characteristics. As seen in the experiments described in Chapter 2, this proportioning has a noticeable effect on the level of re-centering achieved by the specimens. Recommendations for the relative proportions of mild and prestressing steel have been made for frame buildings [e.g. Stanton et al. 1997, Ozden and Ertas 2007] and for bridge columns [e.g. Davis et al. 2013, Ou et al. 2010]. In general, the recommended values for the mild steel contribution ranges from 20-50% of the overall flexural strength.

To describe why this proportioning has such a drastic effect on the recentering behavior of prestressed precast systems, consider the idealized column shown in Figure 3.5. At this point, the column has been displaced sufficiently to fully yield the mild steel reinforcing, but not enough to yield the prestressing strands. If the column is released, the stress in the prestressing strands and the axial load acting on the column would both cause moments which would tend to reduce the rotation at the precast joint, while the mild steel reinforcing will resist these moments, since the bars must be forced to yield in compression.

When the rotation at the joint is close to zero, if the area of mild steel (and hence its flexural strength contribution) is too large, the axial load and initial force in the prestressing steel will not be able to overcome the resisting moment caused by the deformed bar reinforcement, and the column will fail to re-center. The ratio of these moments, assuming that the resultants all act at the center of the column, can be described by the re-centering ratio, defined in Equation 3.2.

$$\lambda = \left(A_p f_{pe} + P\right) / A_s f_{sy}, \qquad [3.2]$$

where A_s is the gross area of the reinforcing steel, A_p is the gross area of the prestressing steel, f_{sy} is the yield stress of the mild steel reinforcing, f_{pe} is the initial stress of the strand, and P is the vertical load acting on the column.

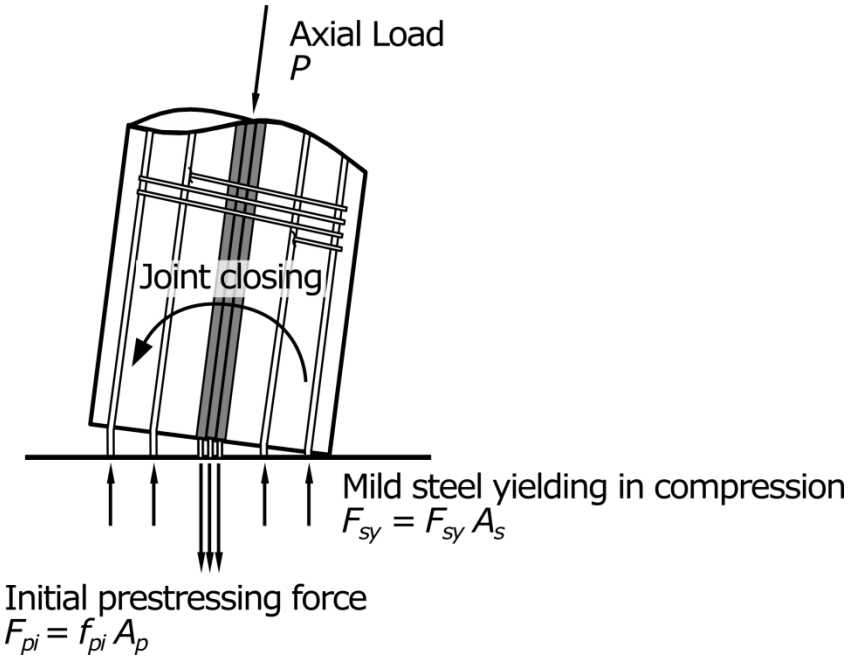

Figure 3.5 Idealized prestressed, precast concrete column joint.

A column's re-centering ratio, λ, is an important design quantity for hybrid prestressed systems. The system's residual displacements after an earthquake are inversely related to its design λ value, and for λ values less than unity, the system should be expected to exhibit the poor re-centering typified by conventional cast-in-place construction.

Ozden and Ertas (2007) tested five precast post-tensioned building frame subassemblies with varying proportions of mild and prestressing steel. The specimens were labeled by the percentage of the beam's flexural strength attributable to mild steel reinforcement (i.e. specimen PTM30 was designed so that 30% of the flexural strength was attributable to the mild steel reinforcement).

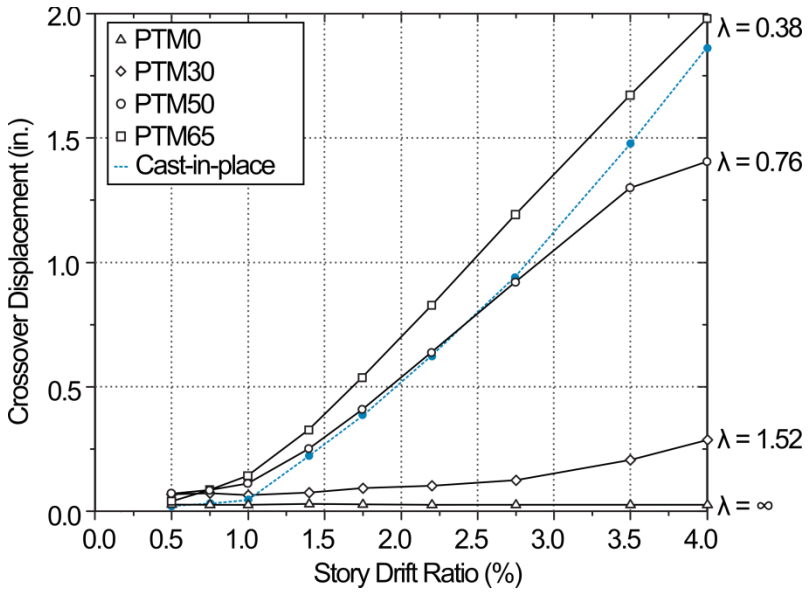

Figure 3.6 Crossover displacement as a function of story drift ratio for frame buildings (adapted from Ozden and Ertas 2007). Note: the subassembly story height was 75.6 in.

Figure 3.6 shows the crossover displacements of the force displacement response of the post-tensioned subassemblies versus the maximum drift achieved in the same cycle. Each specimen's computed dimensionless re-centering ratio (with P=0) are also shown. The crossovers of the reference cast-in-place specimen are shown for comparison. Specimen PTM10, with mild steel contributing 10% of the beams flexural strength (λ=5.73) is omitted, its behavior was nearly identical to specimen PTM0.

For those specimens with $\lambda > 1.0$, the frame subassembly had crossover drift ratios less than 0.5%. In contrast, the specimens with $\lambda < 1.0$ had crossover displacements similar to those of the monolithic reference specimen (λ=0).

Figure 3.7 shows the relationship between normalized cross-over displacement and peak drift ratio for the prestressed columns tested by Cohagen et al. (2008), Schaefer et al. (2014a) and a non-prestressed column tested by Haraldsson et al. (2013). The specimens' re-centering ratios are also shown for reference.

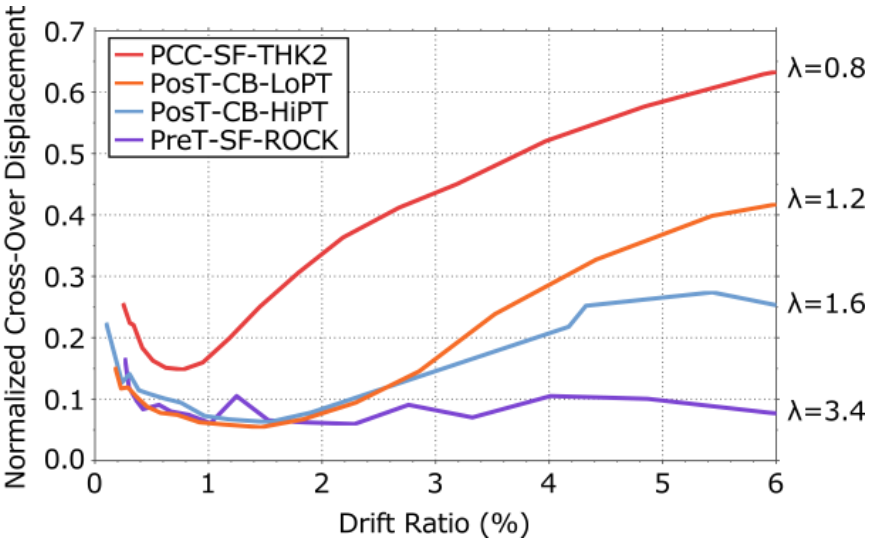

Figure 3.7 Normalized cross-over displacement drift ratio relationship for reinforced concrete and prestressed bridge column specimens.

For columns with $\lambda > 1.0$, the measured NCOD values are greatly reduced from the reference precast, non-prestressed column (λ=0.8), especially for drift ratios less than 2%. Furthermore, the column with λ=3.4, performed better (lower NCOD values) than those with smaller re-centering ratios at higher drift ratios. These results suggest that the system can be designed with nearly any desired level of re-centering. The proportioning of deformed bar and prestressing steel, and how to design the proposed system for specific re-centering performance will be discussed more in Chapter 8.

3.3 Column End Detailing to Eliminate Concrete Damage

The proposed system reduces seismic damage by designing the columns to concentrate rotations at their ends, so that the bodies of the columns undergo little deformation. The concrete in the columns' end regions are protected by steel confining tubes, to which annular baseplates are welded, as shown in Figure 3.8. These baseplates create natural crack planes to encourage rocking and stiffen the tube at its base.

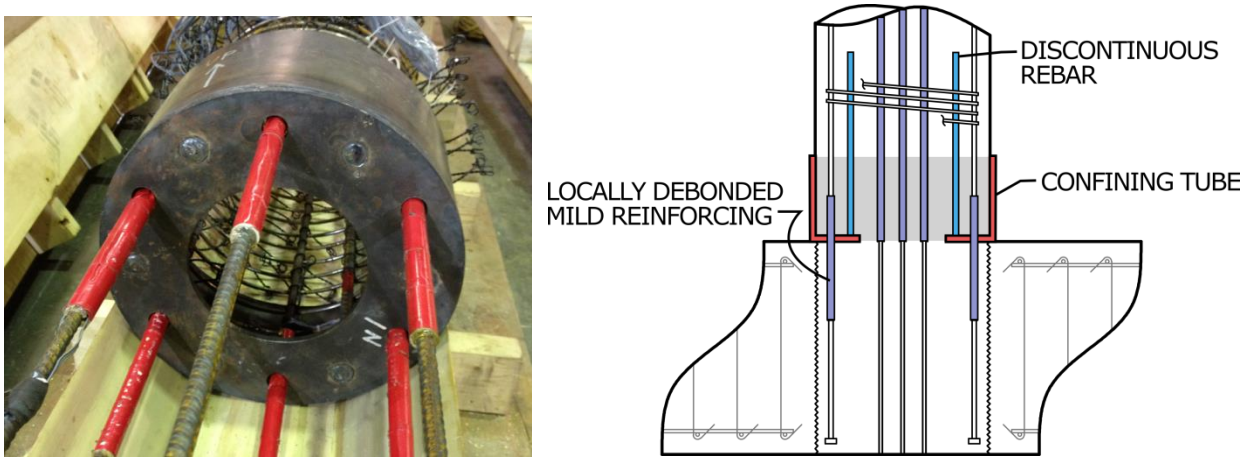

Figure 3.8 Confined rocking detail.

Discontinuous reinforcement is welded to the annular end plate, extending partially into the clear span of the column. This reinforcement is meant to help distribute the forces from the base plate into the column on the compression face of the column and to prevent cracks from occurring just beyond the confining jacket on the tension face. This detailing only extends over a short length of the column and is identical at both top and bottom.

The prestressing strands are passed through the central hole of the annular end plate and the longitudinal reinforcing passes through smaller holes, orbiting the central one. The longitudinal reinforcement is locally debonded to distribute the concentrated elongations caused by rocking over a sufficient length to prevent fracture at the design deformation.

Jacketing prestressed columns has been shown to be an effective method to reduce concrete spalling and increase the systems ductility capacity [Hewes and Priestly 2002, Chou and Chen 2005 and Jeong et al. 2008]. These tests are summarized in Table 3.1.

In Table 3.1, a is the cantilever length, D the column diamter, t the thickness of the steel tube, f'_c the compressive strenght of the column concrete, and f_{yt} *is* the yield stress of the steel jacket. In these tests, the bases of the columns bore directly on grout interfaces at the foundation; a gap was left between the bottom of the steel jacket and the top of the foundation. Because of

this, the steel jackets were primarily activated in hoop tension. This is different than in the proposed pre-tensioned system, where the annular end plate bears directly on the foundation or cap beam and compressive stresses are transferred up into the tube wall. This combined loading was not present in the steel jacketed columns, until large rotations caused direct bearing of the tube on the foundation.

Table 3.1 Steel-jacketed, prestressed column specimens

Researcher	Specimen	a/D	D (in)	t (in)	f'_c (ksi)	f_{yt} (ksi)	D/t
Hewes and Priestly (2002)	JH1	6.0	24.0	0.236	7.1	41.1	102
	JH2	6.0	24.0	0.110	7.4	44.0	218
	JH3	3.0	24.0	0.236	8.3	42.1	102
	JH4	3.0	24.0	0.110	8.4	46.0	218
Chou and Chen (2006)	1	4.9	19.7	0.197	7.7	36.0*	100
	2	4.9	19.7	0.197	7.8	36.0*	100
Jeong et al. (2008)	PRC-UJ	6.2	16.0	0.060	4.7	42.3	267
Mashal and Palermo (2014)	ABC LD		19.7	0.394			50

*Indicates nominal values

Figure 3.10 shows the distribution of the recorded hoop strains in the steel jackets on the extreme compressive face of the columns tested by Hewes and Priestly (2002). The dashed horizontal lines in this figure correspond to half of one column diameter up the height of the steel jacket (305 mm), which extended to one full column diameter (610 mm).

Strains in the steel jackets were larger for those columns outfitted with the thinner walled tube (D/t = 218) and were largely confined to the bottom half of the segment. Larger hoop strains were recorded at the top of the jacket than at its mid-height, likely attributable to rocking about the second precast segment interface and the concentrated compressive forces associated with this behavior.

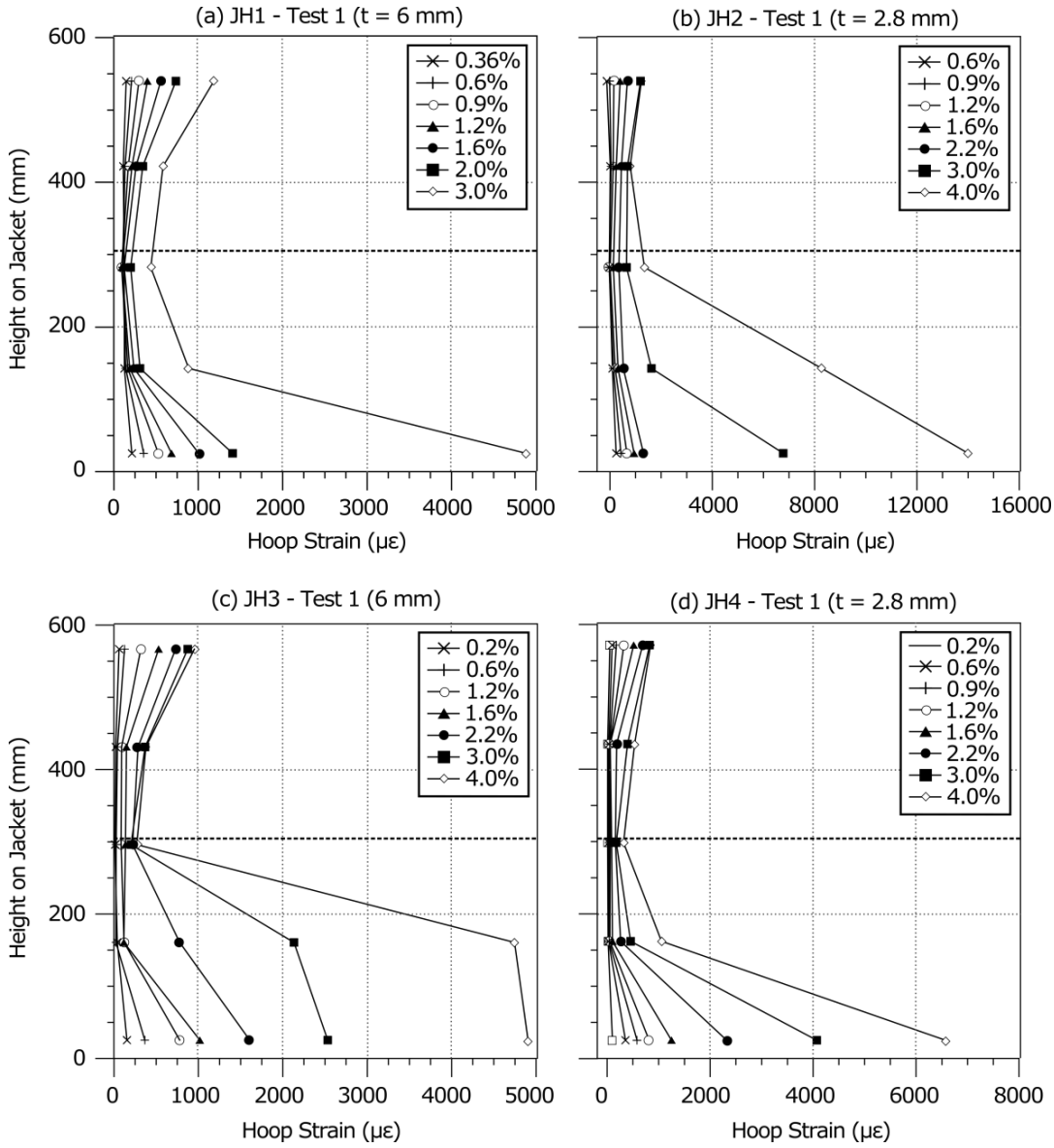

Figure 3.10 Hoop strains in the steel confining jacket (adapted from Hewes and Priestly 2002)

Damage to the confining jackets was minimal. When the columns were re-tested with higher prestressing forces after repairing the damaged non-jacketed segments, the high aspect ratio specimen with the thinner walled tube experienced "bulging" of the jacket at a drift ratio of 4%, as shown in Figure 3.11. This type of damage has been observed in many tests of concrete filled tubes (CFTs) [e.g. Lehman and Roeder 2012]; it is controlled primarily by the tube's diameter to thickness ratio (D/t). In tests of CFT specimens, this damage usually precedes failure

of the tube. This type of damage is less of an issue in the case of jacketed columns, since large strain reversals are not felt by the confining jacket.

Figure 3.11 Bulging of the steel confining jacket (from Hewes and Priestly 2002)

In precast systems where large rotations occur at the precast connection interface, large localized elongations of the longitudinal reinforcement may lead to premature bar fracture. Locally debonding the reinforcing bars at the connection interface has been shown to be effective at distributing these concentrated deformations and to have little effect on the force displacement response [e.g Pang et al 2010, Bellerini and Riva 2012]. These experiments are summarized in Table 3.2. Methods for computing the strain in the reinforcing bars, and thus the required debonded length, at a pre-designated drift limit have been proposed [e.g. Bellerini and Riva 2012], predominately these methods use column-curvature idealizations or rigid-body mechanics to relate drift ratios to strains in the longitudinal reinforcement.

Table 3.2 Precast column tests with partially unbonded longitudinal reinforcement.

Researcher	Specimen	Prestressed	Debonding method	lunb (db)	Drift ratio at Bar fracture
Jeong et al. (2008)	PRC-U	Yes	Wax	85	>8.9%
	PRC-U2	Yes	Wax	85	> 8.2%
	PRC-UJ	Yes	Wax	85	> 7.9%
Palermo et al. (2007)	HBD1	Yes	Unknown	3	> 4.5%
	HBD2	Yes	Unknown	4	> 4.5%
Cohagen et al. (2008)	PosT-CB-LoPT	Yes	PVC	9	6.75%
	PosT-CB-HiPT	Yes	PVC	11	6.75%
Trono et al. (2014)	PT-HyFRC	Yes	PVC	32	8.8%
Guerrini et al. (2015)	1B	Yes	Tape	14	7.5%
Pang et al. (2010)	PCC-CB-DB01	No	PVC	8	7%
	PCC-CB-DB02	No	PVC	8	7%
Ou et al. (2010)	C5C	No	Tape	25	6%
	C8C	No	Tape	4	6%
	C5C-1	No	Tape	25	6%
Belleri and Riva (2012)	GS4U	No	Tape	12	> 5%
Tazarv and Saiidi (2014)	PNC	No	Tape	8	10%

Table 3.2 suggests that the drift ratio at first bar fracture is not sensitive to the amount of local debonding. This is likely because bar buckling and subsequent re-straightening during the next half cycle, rather than excessive tension strain, are the events that most commonly trigger bar fracture [Moyer and Kowalsky 2003], and they are in turn promoted by loss of concrete cover and yielding and kinking of the spiral. In specimens where spalling of the cover concrete is not prevented, bar buckling and spiral fracture will occur regardless of the locally debonded length, and thus the absence of a clear pattern in these experimental results is unsurprising.

For systems where spalling of the cover concrete in the plastic hinge region is prevented, fracture of the longitudinal reinforcement will likely be due to low-cycle fatigue rather than bar buckling, and the locally debonded length of the bars is likely to play a more significant role in the drift ratio at first bar fracture.

CHAPTER 4: TESTS OF PRE-TENSIONED, ROCKING SUBASSEMBLIES

This chapter summarizes subassembly tests of two critical regions of the pre-tensioned bent system, one representing a column-to-footing connection [Schaefer et al. 2014a] and another a column-to-cap beam connection [Kennedy 2015]. The subassemblies were subjected to cyclic horizontal displacements of increasing amplitude under a constant vertical load. The chapter also compares the performance of these specimens to a previously tested precast, non-prestressed column.

- Section 4.1 describes the design of the subassembly specimens.
- Section 4.2 describes the experimental setup and instrumentation for the tests.
- Section 4.3 discusses the moment-drift response of the specimens.
- Section 4.4 summarizes the damage to the column observed during the tests.
- Section 4.5 discusses the performance of the confined rocking detail.
- Section 4.6 discusses the strains in the mild steel reinforcing.
- Section 4.7 discusses the strains in the prestressing strands.
- Section 4.8 summarizes the experiments and the draws several conclusions from the test results.

4.1 Design of Test Specimens

The cantilever columns for both specimens were designed to have geometries and strengths similar to those of a non-prestressed subassembly, PCC-SF-THK2 (Precast Concrete-

Spread Footing-Thick Footing 2), tested by Haraldsson et al. (2013). The PreT-SF-ROCK subassembly (Pre-Tensioned-Spread Footing-Rocking Column) tested represented the connection between a column and a spread footing. The companion PreT-CB-ROCK subassembly (Pre-Tensioned-Cap Beam-Rocking Column) represented the connection between a column and a precast cap beam.

Column elevations and critical sections for the two, 42%-scale cantilever subassemblies are shown in Figure 4.1. Pre-tensioning required horizontal casting, so the columns were octagonal to facilitate finishing. They had inscribed diameters (flat-to-flat) of 508 mm (20 in.) and cantilever heights of 1524 mm (60 in.). Schaefer et al. (2014a) and Kennedy (2015) provide details of these tests.

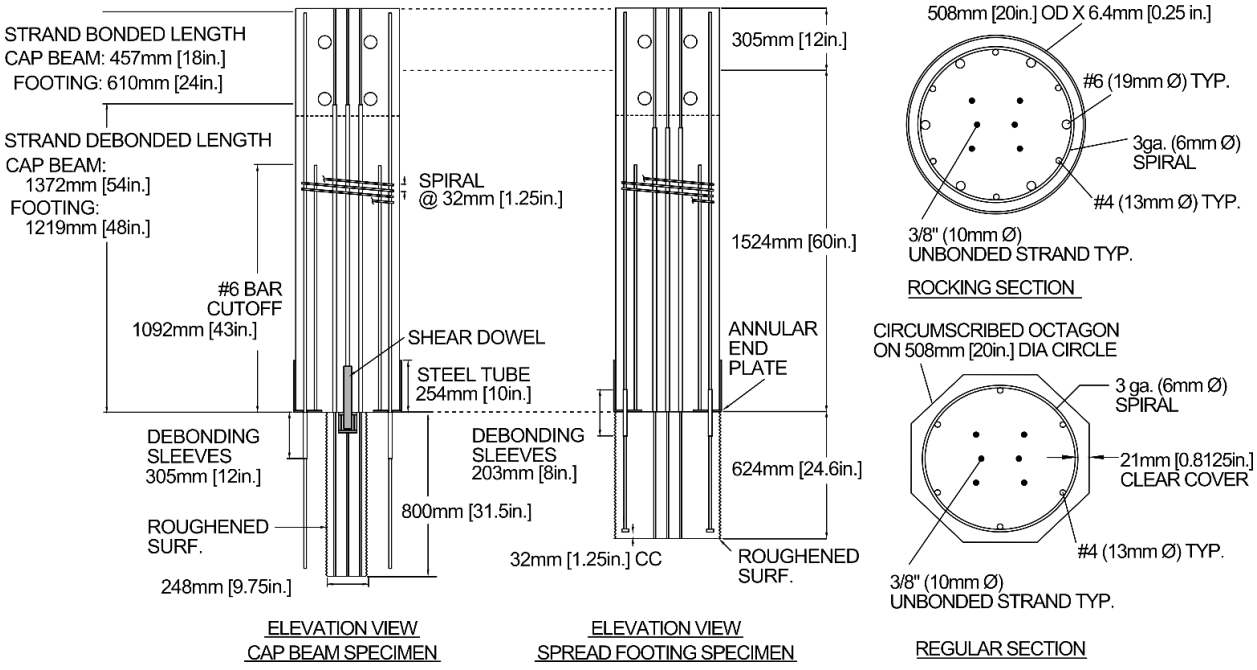

Figure 4.1 Column elevations and critical sections.

4.1.1 Column Reinforcement

The column reinforcement was designed so that the columns would have the same nominal flexural strength as a conventional reinforced concrete column with 1% longitudinal reinforcement. To promote re-centering, the column reinforcing was proportioned such that 60% of the column's flexural strength would be provided by the prestressing strand, and the remaining 40% by the mild steel reinforcing bars. This strategy resulted in target reinforcing ratios of ρ_{pg} = 0.6 (f_{sy}/f_{py})*1% = 0.15% for the strand and ρ_{sg} = 0.4% for the mild reinforcing steel, where f_{sy} is the yield stress of the mild steel reinforcing (413 MPa or 60 ksi), and f_{py} is the yield stress of the strand (taken as 1654 MPa or 240 ksi). Each column was reinforced with six No.4 (A_s = 774mm^2) A706 reinforcing bars and six 3/8 in. (A_p = 329mm^2) epoxy coated strands, which together, provided an equivalent reinforcing ratio of 0.98%.

The longitudinal reinforcing bars were locally debonded near the column-spread footing or column-cap beam interfaces. Some of the debonding details differed between the two specimens. In the spread-footing subassembly, the bars were debonded using PVC sleeves for a total of 203 mm (8 in.), half within the body of the column and half within the spread footing. In the cap beam subassembly, the bars' debonded lengths were increased to 305 mm (12 in.), and the debonded length was located entirely within grouted ducts in the cap beam. To evaluate the effect of the sleeve material, three reinforcing bars (on one side of the section's centerline) were sheathed in steel tubes, and the remaining three were debonded with PVC sleeves, as was done in the spread footing subassembly.

The strands were epoxy coated and placed near the center of the cross section. They were unbonded over most of the column height and were bonded only at the ends of the precast column members. Details can be seen in Figure 4.1.

At laboratory scale (42%), the diameter of the 13 mm (1/2-in.) prototype strands would have scaled to 5 mm (0.21 in), and in that case, there would have been 117 and 150 strand diameters (d_b) available to anchor the strands within the footing and cap beam respectively. Since the smallest, commercially available, epoxy-coated strands had a diameter of 10 mm (3/8in.), the resulting bonded lengths (66 and 84 d_b) did not meet the current AASHTO guidelines for strand development [AASHTO 2016]. To address this scaling artifact, additional anchorage was supplied in the form of strands vices at the tops and bottoms of the columns, and load cells were used to monitor potential strand slip. Load cells were only placed at the top of the column, where the bonded lengths were shortest.

The prestressing strands were stressed to 1,240 MPa (180ksi) before casting. Their average stress on the testing dates was estimated to be 1,137 MPa (165ksi) for both subassemblies, after accounting for losses due to elastic shortening, relaxation, creep and shrinkage.

4.1.2 Column Rocking Detail

The columns were protected with a confined rocking detail at their interfaces with the footing or the cap beam. This detail consisted of a short section of steel tube 254 mm (10 in.) in height, 508 mm (20 in.) in diameter with a wall thickness of 6 mm (0.25 in.). Welded to the tube was an annular, steel end plate, 13 mm (0.5 in.) thick, with holes to accommodate the continuous reinforcing bars. Together, the confining tube and the annular end plate created a steel shoe on which the column could rock. Discontinuous reinforcing bars (six No. 6 bars - 19mm diameter), welded to the annular end plate, extended 1092 mm (43 in.) into the body of the column. This reinforcement was added to distribute up the height of the column the high end compressive

forces caused by the rocking behavior, and to control the width of cracks just above the confining tube.

Because of concerns that the rocking detail might permit shear sliding across the connection interface, a cup-and-dowel system was used in the cap beam specimen to allow free rotation and vertical movements but to prevent horizontal translation. A high-strength, 51 mm (2 in.) diameter steel dowel was cast into the column with a paired housing cast into the portion of the column that extended into the cap beam.

4.1.3 Column-to-Spread-Footing Connection

As shown in Figure 4.2a, the column in the PreT-SF-ROCK specimen was anchored to the cast-in-place spread footing using a "wet-socket" connection [Haraldsson et al. 2013]. In this connection, both the precast column and the footing reinforcement are placed in the excavation, and the footing concrete is cast in place around them. No reinforcement crosses the interface between footing and column; instead the column surface is roughened to facilitate the transfer of forces to the surrounding concrete.

4.1.4 Column-to-Cap-Beam Connection

The column in the PreT-CB-ROCK subassembly was connected to the precast cap beam, as shown in Figure 4.2b, using a "hybrid-bar-socket" connection [Davis el al. 2012]. This connection consisted of fitting a reduced diameter section of the column and protruding

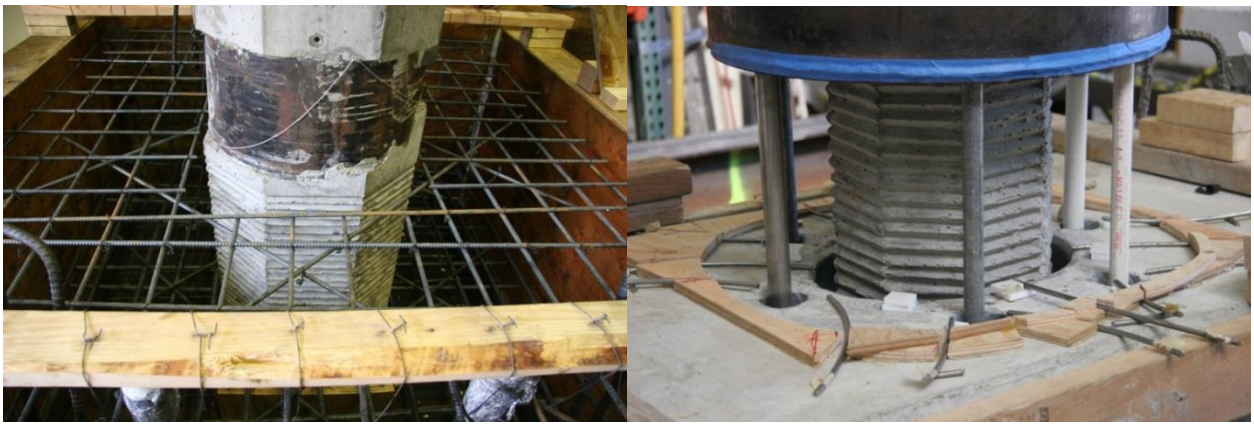

(a) (b)

Figure 4.2 Precast connections. (a) “Wet socket” connection. (b) “Hybrid-bar-socket” connection. (Note the photos show the connections in the orientation used for testing).

longitudinal reinforcing bars into a set of vertical ducts cast into the precast cap beam. One central duct, made from 305-mm (12-in.) diameter corrugated steel pipe, accepted the reduced diameter section of the column used to bond the strands. Around this central duct, six 51-mm (2 in.) diameter steel ducts accepted the column longitudinal bars. Grout was used to anchor the bars and reduced section into the cap beam. A bedding layer of fiber reinforced grout, nominally 13-mm (0.5-in) thick at laboratory scale, was used to provide a seat between the baseplate of the precast column and cap beam.

4.2 Test Setup and Instrumentation

The experimental setup is shown schematically in Figure 4.3. The columns were subjected to a constant vertical load of 708 kN (159 kips) and identical lateral displacement histories, consisting of ten, four-cycle sets, as shown in Figure 4.4. The displacement history is a modified version of the NEHRP recommendation for precast structural walls [Building Seismic Safety Council 2004].

Electrical resistance strain gages, potentiometers, and inclinometers were used to measure deformations of the column as well as strains in the strands, mild steel reinforcing, and

components of the confined rocking detail. A detailed sensor list and experimental data can be found on the Network for Earthquake Engineering Simulation Data Repository [Schaefer et al. 2014b, Kennedy et al. 2014].

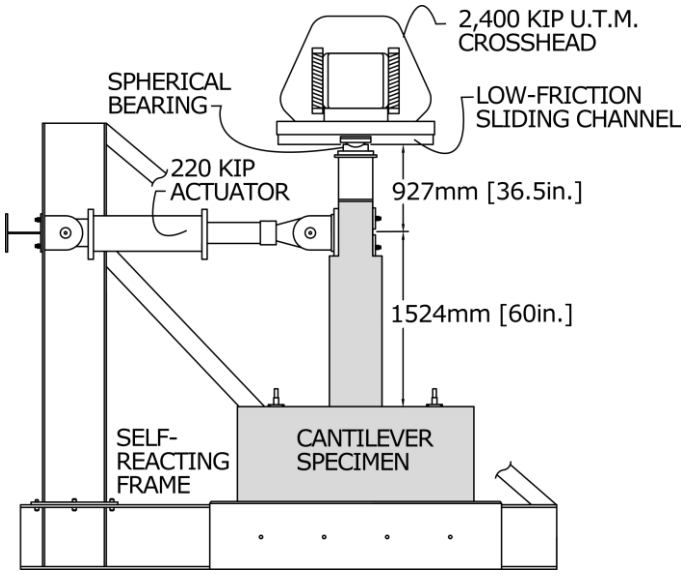

Figure 4.3 Test configuration

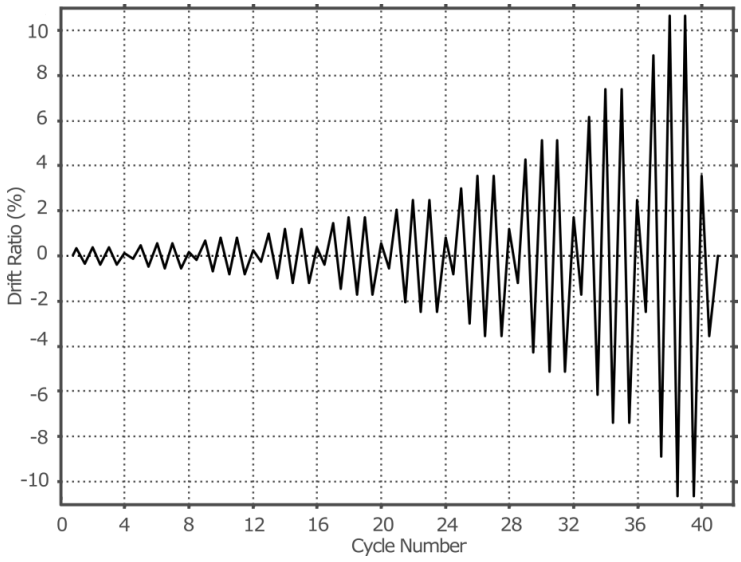

Figure 4.4 Target drift ratio history

4.3 Moment-Drift Response

Figure 4.5 shows the moment-drift responses of the subassembly specimens. These moments were computed by summing the contributions from the applied lateral load, the applied vertical load (P-delta), and the estimated friction forces present in the test configuration. The coefficient of kinetic friction present in the test configuration was taken as 1.6%, following recommendations by Brown (2008), for the setup shown in Figure 4.3. The resulting friction force, 11.1 kN (2.5 kips), was less than 5% of the maximum lateral force. The responses of the PreT-SF-ROCK and PreT-CB-ROCK subassemblies were nearly identical, exhibiting little strength degradation and little residual drift following the removal of lateral loading.

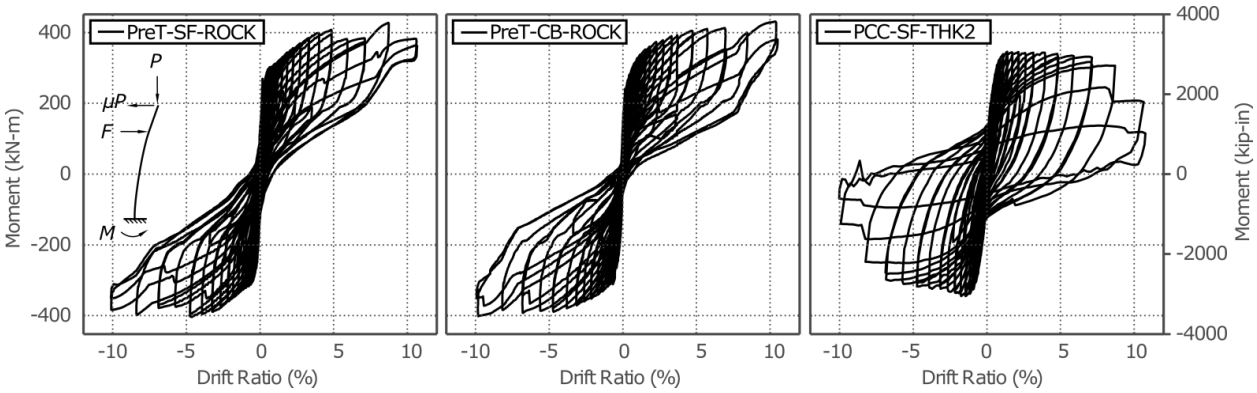

Figure 4.5 Corrected moment-drift relationships.

4.3.1 Flexural Strength

The pre-tensioned columns maintained nearly 100% of their peak flexural strengths up to the maximum drift ratio of 10.4%, despite the fracture of some of the longitudinal reinforcing bars. In comparison, the reference reinforced concrete column (PCC-SF-THK2) had lost 20% of its strength by a drift ratio of 6.9%.

The normalized moment envelopes of the pre-tensioned, rocking specimens (PreT-SF-ROCK and PreT-CB-ROCK) and the reference specimen (PCC-SF-THK2) are compared in

Figure 4.6. They are shown in normalized form to facilitate comparison among columns with different reinforcement arrangements. For each column, the measured moments were divided by the ideal moment capacity given by Equation 4.1, which represents the strength of a column made with concrete of infinite compressive strength and with steel that does not strain harden.

$$M_{\text{ideal}} = \left(f_{sy}\rho_{\text{equiv.}}A_g + P\right) D/2 \qquad [4.1]$$

where f_{sy} the nominal yield stress of the longitudinal reinforcing, ρ_{equiv} the equivalent reinforcing ratio (given in Equation 1), P the applied vertical load and D the column diameter In the absence of strain hardening, the normalized moment will always be less than 1.0, because the lever arm will be less than $D/2$.

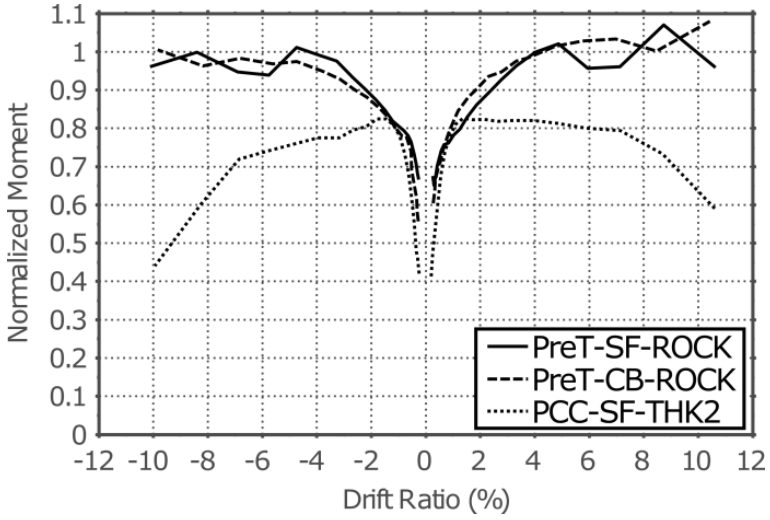

Figure 4.6 Normalized moment drift envelopes.

The prestressed columns had higher maximum normalized moments than the reference specimen. This difference was attributed to the confining tube's suppression of concrete spalling, which maintained the section's full lever arm.

4.3.2 Re-centering

For peak drift ratios up to approximately 6%, the pre-tensioned columns returned to essentially their undeformed configuration upon unloading. For peak drift ratios of up to 10% the columns had residual drift ratios of less than 1%. In comparison, the conventionally reinforced concrete column displayed noticeable residual deformations after being displaced to a drift ratio of 1%.

Figure 4.7 shows the NCOD for the first and second cycles in each of the four-cycle sets versus each cycle's maximum drift ratio. For each of the ten sets, only these two cycles are shown, because they represent the first excursions to larger drift ratios. The first set is omitted, because the drift ratios were below the columns' yield drifts. As can be seen from the figure, pre-tensioning radically improved the column's re-centering performance.

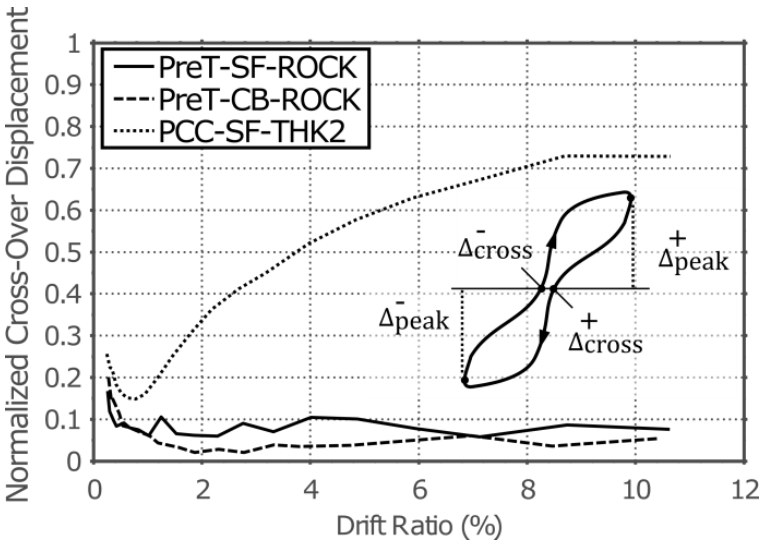

Figure 4.7 Normalized cross-over displacements.

4.4 Observed Damage

Figure 4.8 compares the PreT-SF-ROCK and PreT-CB-ROCK pre-tensioned specimens with the non-prestressed reference column (PCC-SF-THK2) at the end of testing. In the

reference specimen, the first open residual crack was observed after an excursion to a drift ratio of 0.88%. Spalling was first observed at a drift ratio of 1.10%. The column was fully

(a) (b) (c)

Figure 4.8 Columns at end of testing. (a) PreT-SF-ROCK (b) PreT-CB-ROCK (c) PCC-SF-THK2.

spalled by a drift ratio of 4.0%, and the longitudinal reinforcement became visible at a drift ratio of 6.9%.

In contrast, concrete damage in the prestressed specimens was nearly eliminated; cosmetic cracks and minor flaking formed at the change in column geometry between the steel tube and the octagonal concrete section. If desired, this minor damage could likely be eliminated by smoothing the transition in column section from circular to octagonal. During testing, the grout pad in the top connection suffered only minor damage. No damage was observed in either the cap beam of the footing. Throughout the tests, neither of the pre-tensioned columns developed cracks greater than 0.5-mm in width in the concrete, even at peak displacements.

No buckling of the longitudinal reinforcement was observed. The longitudinal reinforcing bars in the pre-tensioned column-to-spread footing connections fractured after experiencing a drift ratio of 5.9%. The column-to-cap-beam connection bars, which had a 50%-longer debonded length, fractured after experiencing a drift ratio of 7.0%. No significant difference in the drift at

first fracture was observed for reinforcing debonded using steel tubes (North side) and PVC sleeves (South side); they fractured in the same cycle. No evidence of bar buckling was seen in the pre-tensioned specimens.

4.5 Performance of Rocking Detail

The performance of the rocking detail can be evaluated in terms of the extent to which it concentrated rotations at the column connections, the strains in the column tube, and the strains in the shear dowel rod assembly.

4.5.1 Concentrated Rotations at Column Connections

Potentiometer pairs at the base of the columns were used to determine local rotations at the connection interfaces. Figure 4.9 shows the rotations at the connection interface expressed as a percentage contribution to the overall drift ratio. Deformations in the pre-tensioned columns (PreT-SF-ROCK and PreT-CB-ROCK) were dominated by concentrated rotations at the connections, as opposed to flexural deformations along the column height. For the spread footing and cap beam subassemblies, respectively, the base rotation was responsible for 88% and 80% of the overall drift of the column at a drift ratio of 1%. By a drift ratio of 3%, these values increased to 96% and 90%. In comparison, the deformations in the reference specimen (PCC-SF-THK2), which was designed to perform similar to cast-in-place construction, were much more distributed; at a drift ratio of 1%, the rotation in the first 45 mm (1.75 in.) of the column contributed only 38% of the overall deformation. By a drift ratio of 3%, this number decreased to 30% as the plastic hinge spread above the elevation of the instrument. These results demonstrate that rocking detail was effective in concentrating the rotation at the connection interface.

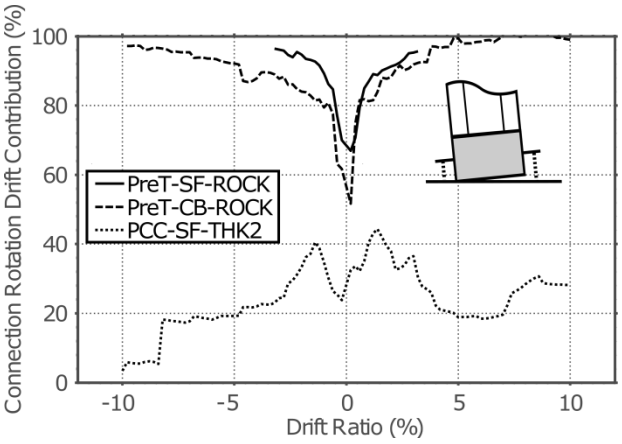

Figure 4.9 Percentage contribution of connection rotation to drift.

4.5.2 Neutral Axis Depth

Potentiometer pairs at the base of the columns were also used to estimate the neutral axis depths as a function of drift at the connection interfaces. Figure 8.7 shows the envelopes of the computed neutral axis depths for both subassembly specimens.

The neutral axis depth converged to a small fraction of the column diameter (roughly 10%) rapidly and remained at this value throughout larger drift ratios (>3%).

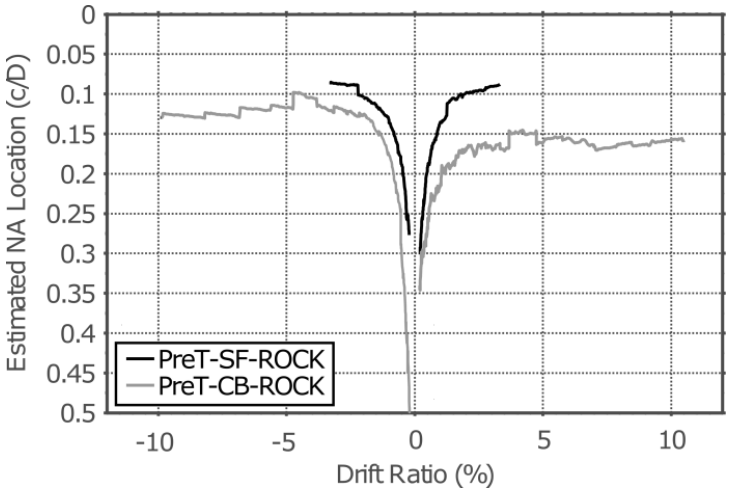

Figure 8.7 Neutral axis depth drift ratio relationship

4.5.3 Strains in the Confining Tube

In the column-to-cap beam subassembly test (PreT-CB-ROCK), two-dimensional strains in the steel confining tube were measured with strain-gage rosettes on the north face of the column at elevations 51 mm (2 in.) and 152 mm (6 in.) above the rocking interface. The normalized strain envelopes for the longitudinal and hoop strains at these locations are shown in Figure 4.10. The longitudinal and transverse strains at both locations were small when the north face was in tension (positive drift ratio in the figure). Significant longitudinal and hoop strains developed only when the north face of the tube, where the gages were affixed, was in compression (during negative drift ratios).

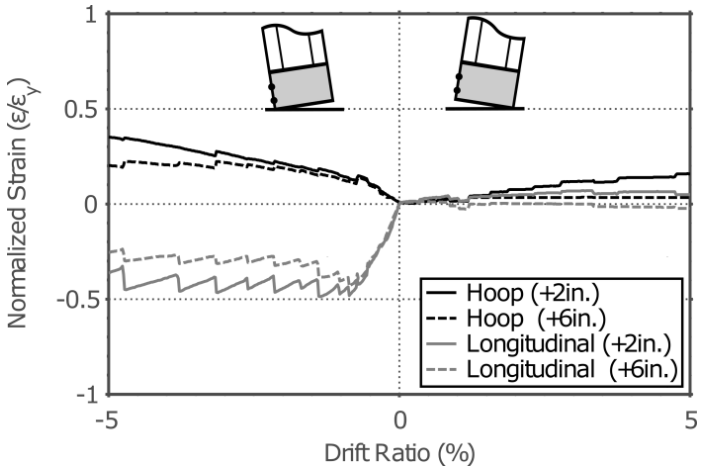

Figure 4.10 Confined rocking detail strain envelopes for PreT-CB-ROCK.

The strains measured 51 mm (2 in.) above the rocking interface were always the higher of the two locations. At a drift ratio of 5%, the longitudinal compression strains at elevations 51 mm (2 in.) and 152 mm (6 in.) above the rocking interface were 726 and 511 microstrain respectively. The reduction of strain with elevation is likely attributable to the increase in the effective area of the tube resisting the concentrated, compressive bearing force due to rocking.

The radial confining pressure between the steel tube and concrete can be estimated using the recorded hoop strains. At a drift ratio of 5%, the hoop strain at an elevation 51 mm (2 in.) above the rocking interface was 703 microstrain. This strain implies an average lateral confining pressure of 3.5 MPa (510 psi).

4.5.4 Strains in the Shear Dowel Rod Assembly

Vertical strains in the shear dowel, which was included only in the cap beam subassembly (PreT-CB-ROCK), were monitored directly above the rocking interface. The vertical strains in the steel dowel never exceeded 30% of the yield strain. Assuming flexural behavior, it appears that the dowel carried less than 15% of the shear force on the column. More importantly, no horizontal sliding was measured for the spread footing column (without a shear dowel), indicating that friction alone was sufficient to transfer shear forces across the connection interface.

4.6 Strains in Deformed Bar Reinforcement

Axial strains in the outermost longitudinal reinforcing bars were measured at three elevations: in the middle of the debonded region of the bars (near the rocking interface), as well as at distances of 76 mm (3 in.) above and below the ends of the debonded region.

Figure 4.11 shows the strain distribution in the column reinforcement for the spread-footing (PreT-SF-ROCK) and reference (PCC-SF-THK2) specimens at a drift ratio of 1%. For plotting purposes, the bar strains in the pre-tensioned column were assumed to be constant throughout the locally debonded region, and the strains were assumed to vary linearly within the bonded region.

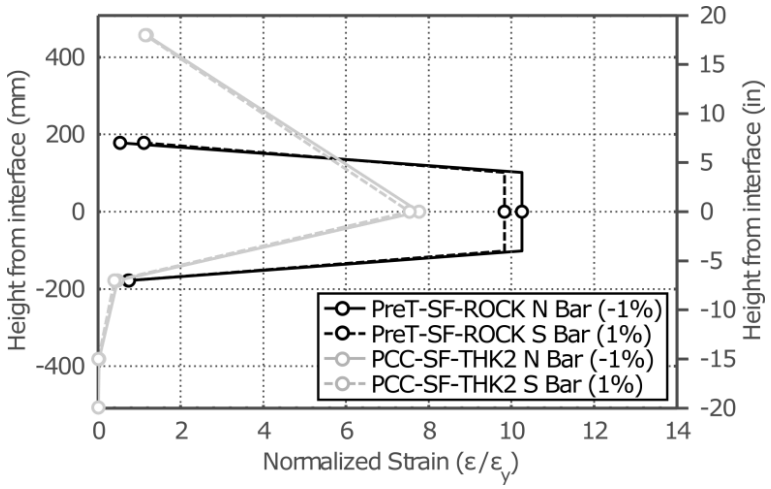

Figure 4.11 Longitudinal reinforcing strain distributions at a drift ratio of 1%.

As shown in the figure, the strains in the pre-tensioned specimen were concentrated at the rocking interface, and they decreased quickly within the bonded region, such that the bars were fully developed within the confined rocking detail (above the interface) and the portion of the column cast into the spread footing (below the interface). In the reference specimen, reinforcing strains were more evenly distributed between the gages at and above the column-to-spread footing interface.

Figure 4.12 shows the measured strain envelopes for the extreme tension reinforcement at the interface for both the pre-tensioned spread footing specimen (PreT-SF-ROCK) and the reference specimen (PCC-SF-THK2). Strains in the pre-tensioned column consistently exceeded those in the reference specimen. The reinforcing bars remained elastic until a drift ratio of nearly 0.3% in the pre-tensioned specimen versus 0.5% in the non-prestressed reference column. The drift at which yielding occurs depends on the unbonded length; yielding could be delayed by increasing this length.

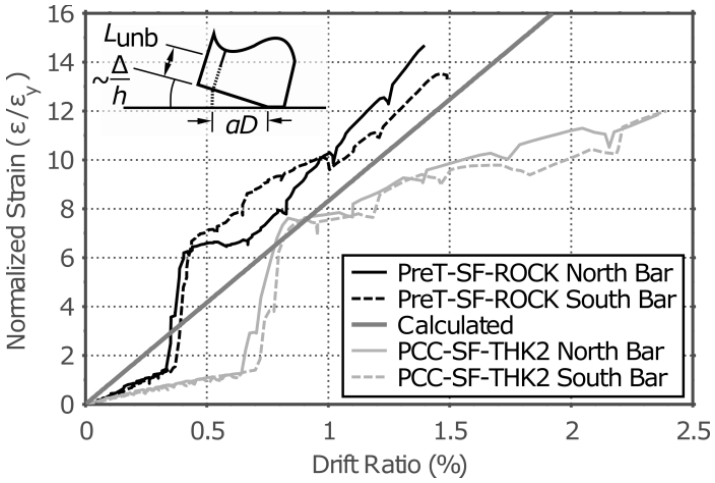

Figure 4.12 Longitudinal reinforcing strain envelopes at column-to-spread footing interfaces.

For both specimens, the abrupt jump in strain (Figure 4.12) after first yield is likely attributable to a reduction in bar cross-sectional area at the gage locations, which had been milled in order to apply the strain gages. This reduction in area was negligible before yield and in the strain-hardening region, but it led to some strain concentration within the yield plateau.

The strain in the extreme tension reinforcement can be approximated by assuming rigid-body kinematics, which lead to Equation 4.2:

$$\varepsilon = \left(\frac{\Delta}{h}\right)\left(\frac{\alpha D}{L_{\text{unb}}}\right) \qquad [4.2]$$

where the rotation at the joint is assumed to be equal to the drift ratio, Δ/h; the distance from the reinforcement to the neutral axis, αD, is expressed as a fraction of the column diameter; and the effective unbonded length of the reinforcement is denoted as L_{unb}.

In computing α, the neutral axis depth was assumed to be located 0.1D from the compressive face of the column, based on data from rotation potentiometers affixed to the base of the confining tube. The effective unbonded length was estimated by transforming the assumed trapezoidal strain distribution, shown in Figure 4.11, into an equivalent rectangular region with the same area, and the same strain as measured by the interface gage. Using the two available

sets of strain data (North and South bars) for the spread footing specimen, the effective debonded length was found to be equal to the intentionally debonded length ($16d_b$) plus an additional $2d_b$ at each end. As shown in Figure 4.12, Equation 4.4 overestimates the measured strains initially, because the joint has not yet opened. After yield and opening of the joint (above 0.5%), the slopes of the computed and measured strain-drift-ratio relationship are the same.

4.7 Changes in Prestressing Strand Strains

Changes in strand strain were measured at approximately mid-height of the unbonded region with gage pairs (for redundancy) and are shown in Figure 4.13 The strands are grouped based on their location within the section parallel to the direction of applied load. The changes in strain in the strands were similar for the spread footing prestressed column.

The strain increments in the strands can be approximated with rigid-body kinematics using Equation 4. For positive drift ratios, the depths from the south face of the column to the prestressing were 328 mm (12.9 in.), 254 mm (10.0 in.) and 180 mm (7.1 in.) for the North, Middle and South strand groups respectively (α = 0.54, 0.40 and 0.26). The effective unbonded length was taken as the length of the debonded region, plus the flexural bond length (47 d_b) for the strands to reach their ultimate stress, one half added to each end of the debonded region. Since no strain measurements were available for the bonded region, the flexural bond length was computed following the recommendations of Cousins et al. (1990) for the plastic bond stress coefficient for low-grit, epoxy coated strands. As shown in Figure 4.13, the measured changes in strains agreed well with the calculated ones.

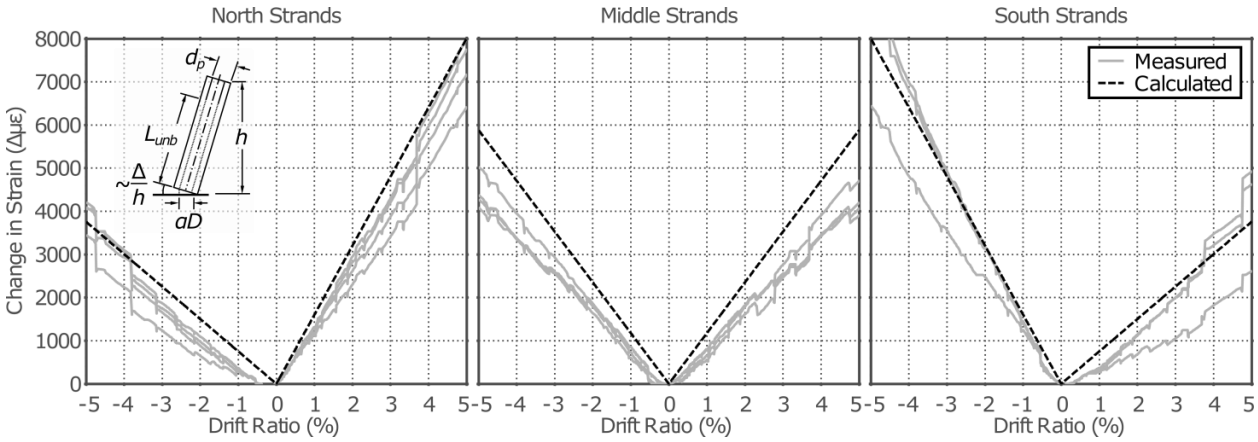

Figure 4.13 Strand strain increment envelopes for PreT-CB-ROCK.

The data acquisition system was disconnected from the strand strain gages during final assembly of the specimens. Assuming that there were no significant changes in the strand strains during the assembly process, it is estimated that the North and South strand groups remained essentially elastic to drift ratios of approximately 3%. Because the columns would rock at both top and bottom of a multi-column prototype structure, the change in strain in the strands would be most closely represented by the Middle strand group, which did not yield until drift ratios of nearly 5%.

4.8 Summary and Conclusions

Two subassembly tests were performed [Schaefer et al. (2014a). Kennedy (2015)] representing a column-to-spread footing and a column-to-cap beam connection. The new system's performance was compared with that of a previously tested precast, non-prestressed column-to-spread footing subassembly of similar design strength [Haraldsson et al. 2013]. The specimens were subjected to increasing cyclic lateral displacements under a constant vertical load.

Elimination of Residual Displacements. The column exhibited good re-centering when the transverse load was removed, returning to within 1% of vertical even after excursions to drift ratios exceeding 10%.

Reduction of Concrete Damage. The steel confining tube eliminated structural concrete spalling. The only damage to the concrete was cosmetic and could likely be avoided by a minor change in geometry. Neither the cap beam nor the spread footing sustained noticeable damage during testing. The confining detail remained elastic for the entire test.

Exceptional Ductility. The moment-drift responses of the spread footing and cap beam subassemblies were remarkably similar. No significant reduction in lateral strength was observed even to drift ratios exceeding 10%.

Effect of Debonded Length of Deformed Bar Reinforcement. The first reinforcing bar fractured at drift ratios of roughly 6% and 7% for the column-to-spread footing and column-to-cap beam subassemblies, respectively. This difference was consistent with the debonded lengths of the longitudinal reinforcing, which was 50% greater in the column-to-cap beam subassembly. To further delay bar fracture, the debonded length could be increased further.

Effect of Debonding Material. The material (steel vs PVC tubes) used to debond the longitudinal reinforcing bars did not affect the drift ratio at bar fracture.

Effect of Initial Prestress in the Strands. The strands remained essentially elastic until a drift ratio of roughly 3%. This drift ratio is largely determined by the initial stress in the strands, which in this case was 1,137 MPa (165 ksi). Because re-centering is promoted by the total prestressing force rather than the stress in any one individual strand, using a larger number of strands each with a lower initial stress would have delayed strand yielding further.

Effectiveness of Dowel Bar. The dowel bar that was included to transfer shear forces from the column to the cap beam proved to be unnecessary. Friction was sufficient to transfer all of the column shear force to the spread footing.

Design Models. For a design target drift ratio, the strains in the longitudinal reinforcing bars and the prestressing strands can be estimated well using rigid body kinematics (i.e., with Equation 4.2).

CHAPTER 5: SHAKING TABLE TEST PROGRAM

The performance of the precast, pre-tensioned rocking bridge column concept was investigated with a multi-shaking table test of a two-span, quarter-scale bridge. The bridge was constructed to have similar geometry and strength to a previously tested conventional cast-in-place bridge specimen tested by Johnson et al. (2008).

This chapter describes the design and construction of the bridge specimen as well as the experimental program. Chapter 6 presents the observed and measured results of experiment, and Chapter 7 compares the shaking table performance of the new system with that of the conventional cast-in-place bridge.

- Section 5.1 introduces the purpose and scope of the experiment.
- Section 5.2 describes the geometry of the specimen, the column and connection details.
- Section 5.2 describes the construction process at the University of Nevada Reno.
- Section 5.2 summarizes the types and locations of instruments used in tests.
- Section 5.2 summarizes the ground motions used in the experiment.

5.1 Introduction

Shaking table tests were conducted on a two-span, three-bent bridge constructed at quarter scale and tested at the University of Nevada NEES Site, as shown in Figure 5.1. The main purpose of the test was to demonstrate the improved performance of the new system and to evaluate the effects of dynamic loading on a highly indeterminate bridge system with bents of different heights.

The specimen geometry, column strengths, and experimental motions were all chosen to replicate a cast-in-place bridge that had been tested by Johnson et al. (2008), so that the performance of the new system could be compared with that of conventional construction. The prototype bridge was intended to represent a typical, continuous, post-tensioned, box-girder bridge in the western United States.

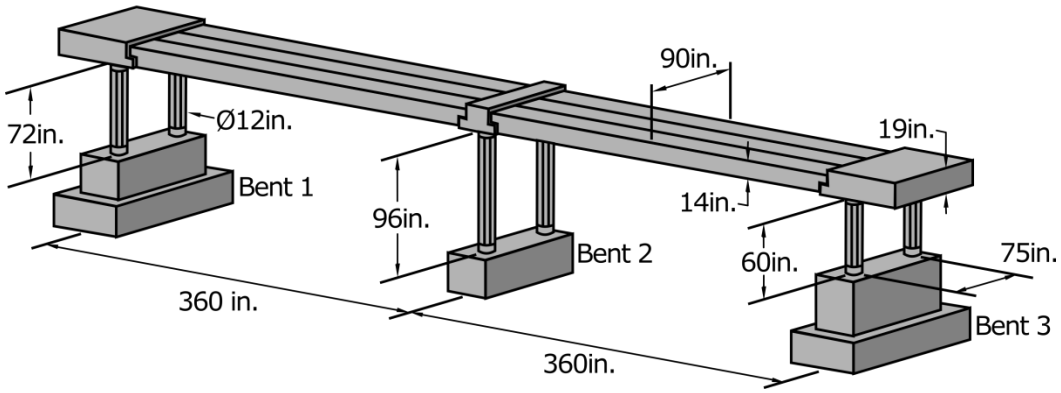

Figure 5.1: Illustration of the shaking table specimen.

The testing consisted primarily of transverse motions, since the purpose of this test was to investigate the behavior of the new pre-tensioned system, rather than bridge-abutment interactions. The ground motions used were a combination of the motions used by Johnson et al. (2008) and near-field, pulse-type motions, which were added to the experimental schedule in an attempt to induce large residual displacements in the new system.

5.2 Design

The precast, pre-tensioned bridge specimen was designed so that the overall bridge geometry, superimposed mass and column flexural capacity resembled closely those of the bridge tested by Johnson et al. (2008). The geometric similarities of the two specimens were

intended to permit direct comparison of their seismic performance (e.g., damage progression and re-centering).

The bridge specimen had three bents and two spans of 9.1 m (30 ft) each, with overhangs at the outer bents to support a portion of the superimposed dead load, as shown in Figure 5.2. Each bent contained two 305-mm (12-in.) diameter columns with a center-to-center spacing of 1905 mm (75 in.). The clear column heights (from the tops of the footings to the bottoms of the bent caps) were 1.8 m, 2.4 m and 1.5 m (6 ft, 8 ft and 5 ft) for bents 1, 2 and 3, respectively. The exterior bents, which had the shorter columns, were placed on spacer blocks in order to maintain a level superstructure.

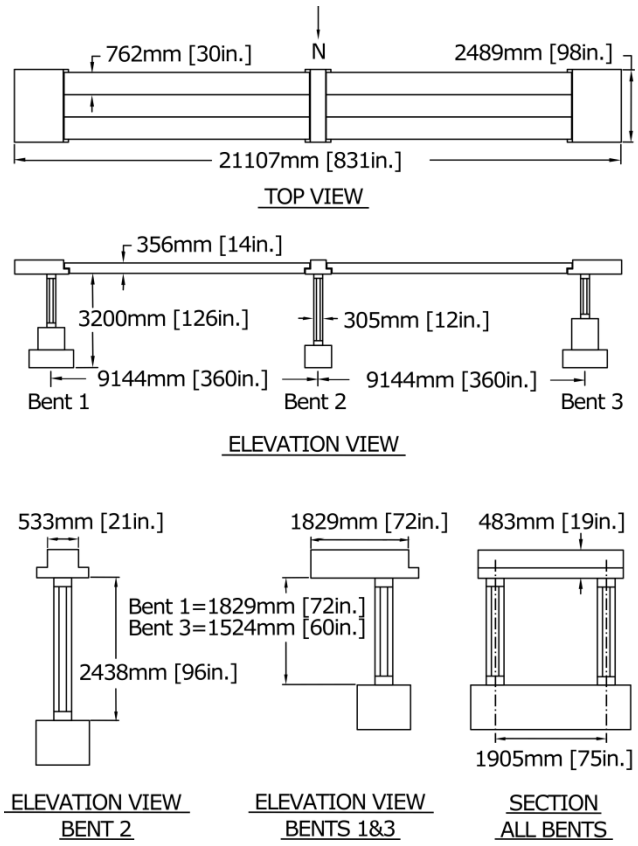

Figure 5.2: Specimen geometry.

5.2.1 Columns

The column details of the pre-tensioned bridge are shown in Figure 5.3. The reinforcement in the columns was selected so that 60% of the columns' flexural strength was provided by the prestressing strand, and 40% was provided by the mild reinforcing steel. Since the reinforcing ratio used in the cast-in-place specimen was ρ=1.56%, target reinforcing ratios of ρ_p = 0.6 (f_{sy}/f_{py})*1.56% = 0.23% and ρ_s = 0.62 % were chosen for the strand and the mild reinforcement respectively, where f_{sy} is the yield stress of the mild steel reinforcing and f_{py} is the yield stress of the strand.

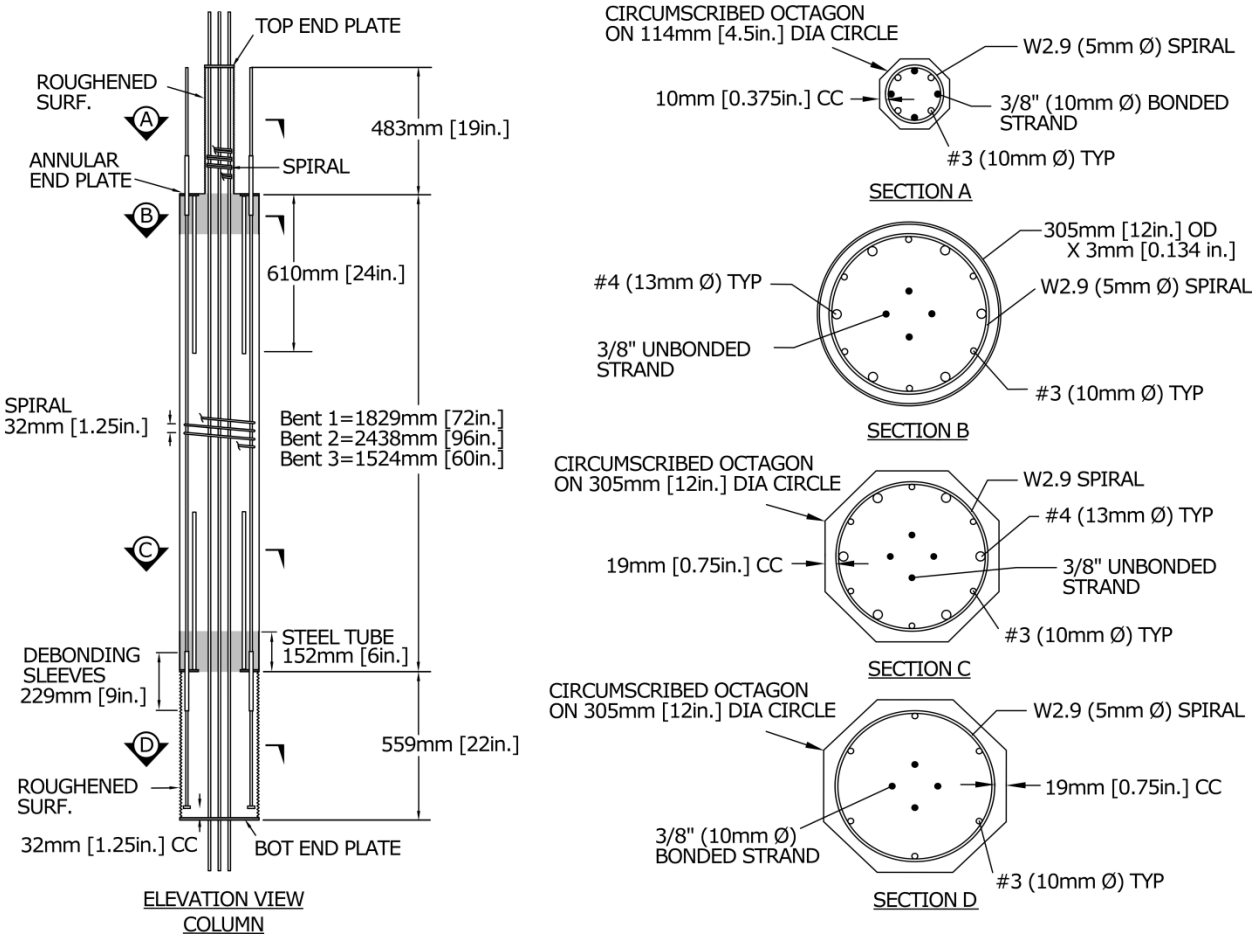

Figure 5.3: Column elevation and critical sections.

The resulting longitudinal steel areas were provided by six No.3 (A_s = 426mm^2) bars and four 3/8 in. (A_p = 219mm^2) epoxy coated strands; this resulted in an equivalent reinforcing ratio (accounting for the higher yield strength in the prestressing strands) of 1.7 %. This value, slightly higher than that used by Johnson et al. (2008), was used in order to have a symmetric column section with six reinforcing bars around the perimeter. The longitudinal reinforcing bars were bonded over most of their length, but they were locally debonded at the rocking interfaces with PVC sleeves for a total length of 24 bar diameters (228 mm or 9 in.). A transverse volumetric steel ratio of 0.9% was provided by W2.9 (4.9 mm dia.) smooth spiral spaced longitudinally at 32mm (1.25 in.). This reinforcing detail matched the previous experiment, although the spacing exceeds that permitted by the current AASHTO guidelines for confinement [AASHTO 2015], as was noted in Johnson et al. (2008).

The strengths of the precast, pre-tensioned columns and previously tested reinforced concrete column can be compared analytically. The pre-tensioned columns were analyzed using moment-rotation analyses to account for the strain incompatibilities at the connection interface. To compare these moment-rotation behaviors to the reinforced concrete columns, the moment-curvature response of the reinforced concrete section was multiplied by an analytic plastic hinge length, computed using Equation 5.1 [Priestley et al. 1996].

$$L_p = 0.08\left(\frac{H}{2}\right) + 0.15 f_{ye} d_b \qquad [5.1]$$

where H is the height of the column, f_{ye} is the expected yield strength of the longitudinal reinforcement and d_b is the longitudinal bar diameter.

Figure 5.4 shows the moment-rotation response for the columns of Bent 1. Both the chosen, symmetric design ($\rho_{equiv} = 1.7$ %) and one with three strands ($\rho_{equiv} = 1.4$ %) are shown. All of the analyses assumed nominal material properties, an axial load of 207 kN (46.5

kips) and a concrete compressive strength of 41 MPa (6000 psi), the measured strength of the column concrete in Johnson et al. (2006). For the moment-rotation analyses, the effective unbonded length of the mild steel reinforcement was taken as the deliberately debonded length plus 8 d_b, the effective unbonded lengths of the strands were taken as half the column height plus half of one flexural bond length (24 d_b), and the effective stress in the strands was taken as 1068 MPa [155 ksi]. Both the bars and the strands were modeled as bi-linear with post yield stiffness ratios of 1% and 4%, respectively. Mander's confined concrete model used for all three sections [Mander et al. 1988].

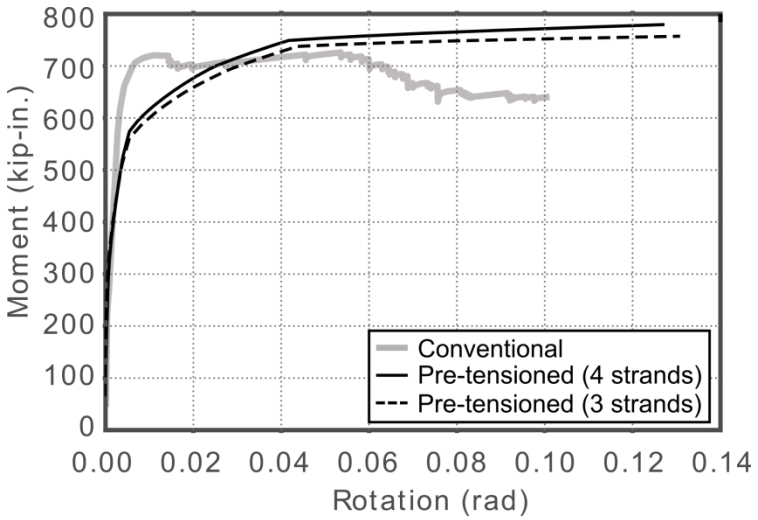

Figure 5.4 Moment rotation response of Bent 1 columns

Both pre-tensioned sections have a calculated moment capacity that is less than 10% larger than that of the reinforced concrete section. Additionally, the strength increase from using four versus three strands is small, and results in a symmetric section and a 15% increase to the columns re-centering ratio.

The confinement detail at the ends of each column consisted of a 152 mm (6in.) long piece of steel tube that was 305mm (12in.) in diameter and 3.4mm (0.134in.) thick, welded to a

6.4 mm (0.25in.) thick annular steel plate. Together they formed a steel can on which the column could rock. Discontinuous No. 4 (D12) longitudinal bars, extending 610 mm (24in.) into the body of the column, were welded to the annular plate. These bars were added to the column to arrest any cracks at the end of the tube where the column section changed and to distribute the high local compressive forces from rocking up into the body of the column.

The strands were unbonded over the clear height of the column. They were bonded for 559 mm (22in.) at the bottom of the column (within the footing) and 483 mm (19in.) at the top of the column (within the column extension). At quarter scale, the diameters of the strands would have been 3mm (0.13 in), and a length equal to 152 strand diameters would have been available to anchor the strands. However, such small strands were not available commercially, so unlike the prototype, the provided bonded lengths of 50 and 60 strand diameters did not meet the AASHTO guidelines for development [AASHTO 2016]. Instead, strand vices were provided at both the top and bottom of the column to prevent slipping if the bond proved inadequate. Load cells were placed at the cap beam end, which had the shorter bonded length, between the column and the strand vices to indicate any loss of bond.

The prestressing strands were stressed to 1,240 MPa (180ksi) before casting. Their average stress on the day of testing was estimated to be 1,068 MPa (155ksi), after accounting for losses due to elastic shortening, relaxation, creep and shrinkage.

5.2.2 Column Connections

A “wet socket” connection was used to anchor the columns into the cast-in-place footings [Haraldsson et al. 2013]. It was made by placing the footing steel in the formwork with openings in the cage to accommodate the columns, setting and bracing the precast columns, then casting the footing concrete around the columns. The socket depth of 559mm (22 in.) was the same in

the three bents. This depth was larger, and therefore more conservative, than the one used in the previous cyclic tests, but it was used because the seismic performance of the embedment was not the focus of the shake-table experiment. The final footing depth was 762 mm (30in.) in bents 1 and 2, and 1067 mm (42in.) in Bent 3, which was cast deeper to accommodate the varying lengths of the columns.

A "hybrid-bar-socket" connection was used to connect the precast cap beams to the precast columns [Davis et al. 2012], as shown in Figure 5.5c. The connection uses a set of vertical ducts cast into the cap beam. One central duct, made from 152mm (6in.) diameter corrugated pipe, accepted the reduced diameter column section that was used to bond the prestressing tendons, while six smaller 32mm (1.25in.) ducts accepted the individual longitudinal reinforcing bars that were positioned around the perimeter of the column and protruded from it. Fiber-reinforced grout was used between the shoulders of the precast columns and the precast cap beam to accommodate differences in column height and level and to seal the joint. The nominal grout pad thickness was specified as 6.4mm (0.25in.) at laboratory scale. Once the cap beam was placed, the reduced diameter sections of the columns and the longitudinal reinforcement were grouted into the cap beam ducts.

5.2.3 Cap Beams

The cap beams' longitudinal and shear reinforcement were designed, at scale, according to the *AASHTO Guide Specifications for LRFD Seismic Bridge Design* (2015). The ledges and anchor regions, for the longitudinal superstructure post-tensioning, were designed according to the *AASHTO LRFD Bridge Design Specifications* (2016).

Because much of the columns reinforcement was replaced with prestressing strands, only the minimum joint shear reinforcement was required. This observation was also made by

Tobolski (2010), who investigated a similar post-tensioned rocking system. The longitudinal and shear reinforcement included in the cap beam, provided twice the required steel areas to resist the columns' overstrength moments. Since the test was meant to investigate the performance of the columns, this was done to prevent superfluous failures in the essentially elastic elements. This was also done to replicate the procedure performed by Johnson et al. (2008).

5.2.4 Superstructure

Each span consisted of three longitudinal dapped, precast slabs, transversely post-tensioned prior to the assembly. The slabs from the previous cast-in-place experiment were reused after minor repairs.

The target axial-load ratio for the columns was 8%. Because the specimen was only quarter-scale, it was necessary to add mass to the top of the superstructure to compensate for the dead load and dynamic mass lost by scaling. This superimposed mass consisted of eight 89kN (20kip) concrete blocks and two 22.7kN (5.1kip) stacks of steel plates. At the two end bents (1 and 3), the slab cantilevered outwards to accommodate a portion of the superimposed load and to balance the gravity moments at the columns.

5.3 Construction

Figure 5.5 shows key stages of the construction process. Mantawy and Sanders (2016) provides a detailed account of the assembly process at the University of Nevada, Reno NEES Site. Six precast, pre-tensioned columns and three cap beams were fabricated at the University of Washington (Figure 5.5a) and shipped to the University of Nevada, Reno (Figure 5.5b). Columns were then erected and aligned in the footing formwork and the cap beams were dry fitted over timber shoring before casting the spread footings. This was done because of the tighter

tolerances associated with constructing specimens at this scale. After the footings cured sufficiently, the cap beams were removed, and the partially constructed bents, consisting of a footing and two columns, were installed on the shake tables. Because of the varying column heights, spacer blocks were first installed on the tables to maintain a level superstructure. The cap beams were then placed on the columns (Figure 5.5c).

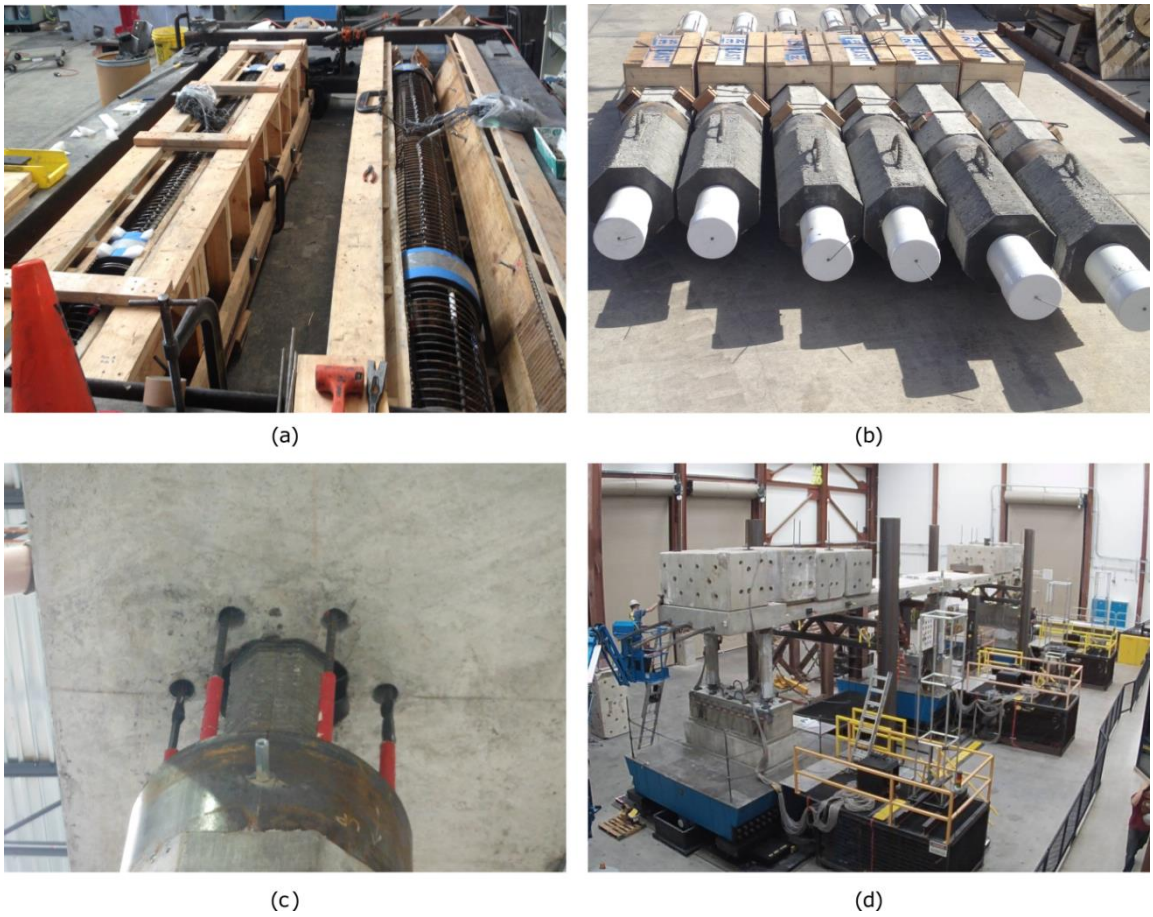

Figure 5.5: Construction photos. (a) column construction, (b) precast, pre-tensioned columns after arriving at UNR, (c) hybrid-bar-socket connection, (d) completed bridge prior to testing.

The column longitudinal bars and reduced diameter section of the middle bent (Bent 2) were first grouted into the cap beam to provide stability during beam placement. Then, while the vertical ducts in the cap beams of the end bents (bents 1 and 3) were still ungrouted, the longitudinal slabs were installed and their interfaces with the cap beams were filled with a high-

strength gypsum grout. Next, the bridge was post-tensioned longitudinally in stages, during which time the superimposed masses were added, in order to reduce the effect of secondary moments on the columns. Last, the cap beam connections at the end bents were grouted and the added weights were bolted down to the specimen. Figure 5.5d shows the completed bridge specimen prior to testing.

5.3.1 Implications for Full-Scale Construction

In order for the precast components to be connected on-site, the protruding elements of the precast columns, the reduced diameter extension and longitudinal reinforcement, must fit within the ducts that are precast into the cap beams. There are two potential alignment issues. The local configuration of the ducts to accept the protruding elements from a single column, and the global alignment of the columns in a multicolumn bent to match the spacing and rotation of sets of ducts cast within a single cap beam.

Local alignment issues can be reduced by minimizing the number of deformed bars that must be grouted into the cap beam. This means that larger ducts can be used and tolerances increase. The global alignment of the columns requires careful surveying and may lead to the use of segmental cap beams, which may be preferred anyway due to crane weight limitations.

While the construction of a scaled experiment is different than the construction of a full-scale bridge, the methods used to prevent these alignment issues in the pre-tensioned bridge experiment are likely similar to those that would be used in practice.

Local Configurations of the Ducts. In the pre-tensioned bridge experiment, column reinforcement cages were constructed using steel jigs to ensure the correct longitudinal bar spacing, and the confining shoes were slid onto the rebar cage after it was constructed. Steel jigs were also used to align the discontinuous reinforcement prior to plug welding them to the

annular end plate. The ducts in the cap beam were held in place by a set of wooden jigs during casting to ensure that they remained parallel through the depth of the cap beam. Reinforcement that was passed between the ducts was used to anchor the ducts against translation and rotation during casting. The use of these jigs ensured that the ducts in the cap beams and the protruding elements of the columns had consistent patterns. In a precasting facility, this level of precision could easily be achieved. In the pre-tensioned bridge experiment, these jigs were reused for six columns and three cap beams. To be economical in practice, the up-front cost of producing these jigs must be spread out over large production orders.

Global Alignment of the Columns. The different heights of the columns were accounted for both in the foundation and at the cap beam interface, based on their as-built dimensions. The spacing and rotation of the columns within the shared footings were determined from the as-built measurements of the cap beams. The column spacing was adjusted through turnbuckles on the column bracing. Because tolerances do not scale, the cap beams were dry fit to ensure spacing/rotation were correct prior to casting the foundation. This operation was possible at scale, but would likely not be possible on a typical construction site. However, a template with the same duct pattern as the cap beam may potentially serve the same purpose.

In addition to these considerations, contractors have also expressed additional concerns which must be addressed in full-scale precast substructure construction. These include; the weight of the columns and cap beams, and the implication on crane rental and mobilization costs; the required curing time of the cast-in-place foundation prior to placing the cap beams, and the required grout strength prior to placing the girders; the bracing of the columns prior to casting the foundation with limited construction footprints; and the additional cost and risk versus the perceived time savings.

5.4 Instrumentation

The specimen was instrumented with 395 sensors to capture the motion of the superstructure and to assess the column performance. Details of instrumentation, and all of the recorded data for each of the experimental motions, can be found in the Network for Earthquake Engineering Simulation data repository [Thonstad et al. 2015]. Detailed sensor locations are also provided in Appendix B. Additional information on sensor types and locations can be found in Mantawy and Sanders. (2016).

Slab displacements and accelerations (longitudinal, transverse and vertical) were measured at five locations: at each of the three bents and within both spans. Column rotations were measured using potentiometers at the rocking interface of each column, in both the transverse and longitudinal directions. Strain gauges were used to measure the strains in the longitudinal and transverse reinforcement, as well as the strand within critical column sections and in the confined rocking detail of the shortest bent (Bent 3).

5.5 Experimental motions

In order to replicate in the pre-tensioned system the same structural demands as in the previously tested cast-in-place specimen, some of the low-amplitude motions and all of the high amplitude motions from Johnson et al. (2008) were repeated. These motions were derived from the E-W and N-S components of the Century City Country Club North (CCN) record from the 1994 Northridge, California earthquake [Johnson et al. 2008].

The bridge was not designed using a particular earthquake spectrum, but rather was designed to match the strength of the previously tested structure. Thus, as a baseline indicator of the approximate level of shaking caused by each motion, the design level event was defined as the first motion that caused a drift ratio of 3% in the exterior bents in the previous experimental

program of the conventional reinforced concrete bridge. The motion derived from the Century City County Club North (CCN) record scaled to a peak ground acceleration (PGA) of 0.75g (Motion 16) represented the 100% Design Level motion.

5.5.1 Low-level motions

The test schedule for the low and high-amplitude tests is shown in Table 5.1. White noise and square wave excitations were run throughout the testing program to determine the period and damping of the bridge specimen. The low-amplitude tests were composed of coherent, incoherent, biaxial and sinusoidal excitations, all designed to create bent responses smaller than the estimated bent yield displacements; the maximum drift ratio in all of the bents for these motions was less than 0.1%. Motions 1A and 1B were coherent excitations used to create a baseline structure response to compare with the incoherent excitations. Motions 4-6 were used to investigate the effects of motion incoherency on the response of the structure. Motions 9A, 9B and 9C were used to investigate the effects of biaxial motions and Motions S1-S5 were added to the motion schedule of Johnson et al. (2008) to investigate the response of the rocking structure to simple harmonic inputs of varying periods and intensities.

Several motions were added to investigate the behavior of the structure under near-field, pulse-type and harmonic motions. The N-S component recorded at the Sylmar Olive View Medical Center (SYL) during the 1994 Northridge earthquake and the N-S component recorded at the Takatori Station (TAK) during the 1995 Kobe, Japan earthquake [PEER NGA] were selected for this investigation based on the responses of preliminary computational models.

Table 5.1 Experimental test schedule

Test Date	Significance	Motion	Description	Target Max. Table Accel. (g)
Jul. 11, 2014	Low level coherent motions	WN0001 / SQ0001		
		1A	CCN	0.08
		1B	CCN	0.15
		WN0104 / SQ0104		
	Low level incoherent motions	4	CCN	0.07/0.18/0.18
		5	CCN	0.18/0.07/0.18
		6	CCN	0.18/0.18/0.07
		WN0609 / SQ0609		
	Low level biaxial motions	9A	CCN	0.08
		9B	CCN	0.15
		WN0912 / SQ0912		
	High level coherent motions	12	CCN	0.08
		13	CCN	0.15
		14A	CCN	0.25
Jul. 14, 2014		WN1414A / SQ1414A		
	Low level sinusoidal motions	S1	Td = 0.25sec	0.05
		S2	Td = 0.25sec	0.1
		S3	Td = 0.25sec	0.15
	Low level biaxial motions	9C	CCN	0.25
		WN1414B / SQ1414B		
	Low level sinusoidal motions	S4	Td = 0.30sec	0.15
		S5	Td = 0.30sec	0.2
	High level coherent motions	14B1	SYL	0.2
		14B2	SYL	0.4
		14C	TAK	0.2
		WN1415 / SQ1415		
		15	CCN (67% DL)	0.5
		WN1516		
		16	CCN (100% DL)	0.75
		WN1617		
		17	CCN (133% DL)	1
Jul. 15, 2014		WN1718 / SQ1718		
		18	CCN (177% DL)	1.33
		WN1819 / SQ1819		
		19	CCN (221% DL)	1.66
		WN1920 / SQ1920		
		20A	CCN (100% DL)	0.75
		WN2020 / SQ2020		
		20B	SYL	0.84
		WN2021 / SQ2021		
		21A	TAK	0.4
		WN2121A / SQ2121A		
		21B	TAK	0.6
		WN2121B / SQ2121B		
		21C	TAK	0.8
		WN2100 / SQ2100		

Figure 5.6 shows the target spectra for the 33% Design Level motions derived from the Century City record (Motion 14A), the Sylmar record (Motion 14B2) and the Takatori record (Motion 14C). These motions were meant to induce similar levels of demand in the structure. The figure shows that the Sylmar and particularly the Takatori records had higher displacement demands than the Century City motion at longer periods. The other high-amplitude motions were scaled linearly from this set.

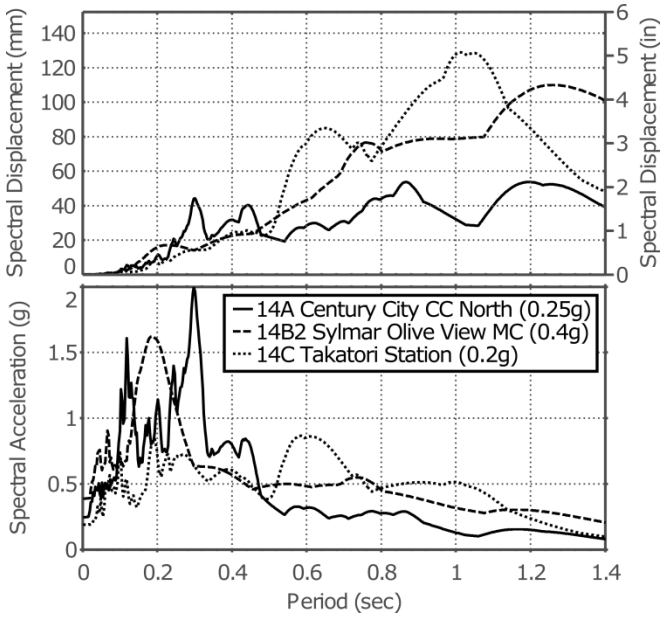

Figure 5.6: Spectral displacements and accelerations for motions 14A, 14B2 and 14C.

CHAPTER 6: SHAKING TABLE TEST RESULTS

This chapter presents the observed and measured data from the shaking table test of the two-span bridge specimen with precast, pre-tensioned rocking columns.

- Section 6.1 presents the damage to the specimen observed during testing.
- Section 6.2 presents the measured response of the system, including: maximum and residual displacements; computed base shear response; rotations at the precast interfaces; as well as strains in the longitudinal reinforcement, strands and steel confining tube.
- Section 6.3 summarizes the performance of the shaking table specimen. The system is evaluated in terms of whether it met the primary objectives of the proposed. It also discusses some test observations that have important implications for the design of the system in practice.

6.1 Observed Damage

No damage to the bridge (superstructure, columns and footings) was observed in the low-amplitude tests. For these tests, the maximum column moment in each of three bents was estimated (from the bent base shear) to be 62.8 kN-m (556 kip-in.), 57.5 kN-m (509 kip-in.) and 76.2 kN-m (674 kip-in.) for bents 1, 2 and 3 respectively. These moments are near the average nominal yield moment of the three bents of 67.4 kN-m (596 kip-in).

Table 6.1 summarizes the six major types of damage observed during the test and includes the ground motion number and peak drift ratio that preceded the time when the damage was first witnessed in each of the three bents. Figure 6.1 shows the worst case occurrences of

these damage states in Bent 1 after the after the 100% (or 133%) Design Level motion (Motion 16 or Motion 17) and at the end of testing. The damage in Bent 3 was similar. The damage experienced by the bridge after the 100% Design Level motion was minimal and would not need any repair.

Table 6.1: Maximum column drift ratios that preceded reaching key damage states

Damage State	Bent 1	Bent 2	Bent 3
First yield of mild reinforcement	0.47% (14A)	0.55% (14A)	0.48% (14A)
Minor spalling at octagonal corners	2.1% (15)	3.5% (17)	4.3% (17)
Crushing of grout pad	9.2% (18)	7.6% (19)	6.0% (18)
Bulging of confined rocking detail	9.2% (18)	N/A	6.0% (18)
Residual horizontal cracks in column	11.8% (19)	N/A	13.2% (19)
First bar fracture	5.7% (17)	7.6% (19)	6.0% (18)

Throughout testing, the masses remained rigidly attached to the bridge superstructure, and no slip was observed between the footings and shake table platens.

6.1.1 Damage to column concrete

Limited spalling was observed in the column concrete, where the confining tube ended and the cross-section changed from circular to octagonal, in Bent 1 during the 67% Design Level motion (Motion 15), and in Bents 2 and 3 during the 133% Design Level motion (Motion 17). It was similar to that seen during the quasi-static tests at the University of Washington. Because this type of spalling does not affect column performance and could be eliminated by tapering the transition in column geometry, it was deemed cosmetic. Once the corner of the octagon was spalled, no further damage occurred at that location.

Grout crushing, defined as a loss of material from the main body of the grout pad between the column and cap beam, began along the north and south edges of the pads in bents 1 and 3 during the 177% Design Level motion (Motion 18) at drift ratios of 9.2% and 6.0%

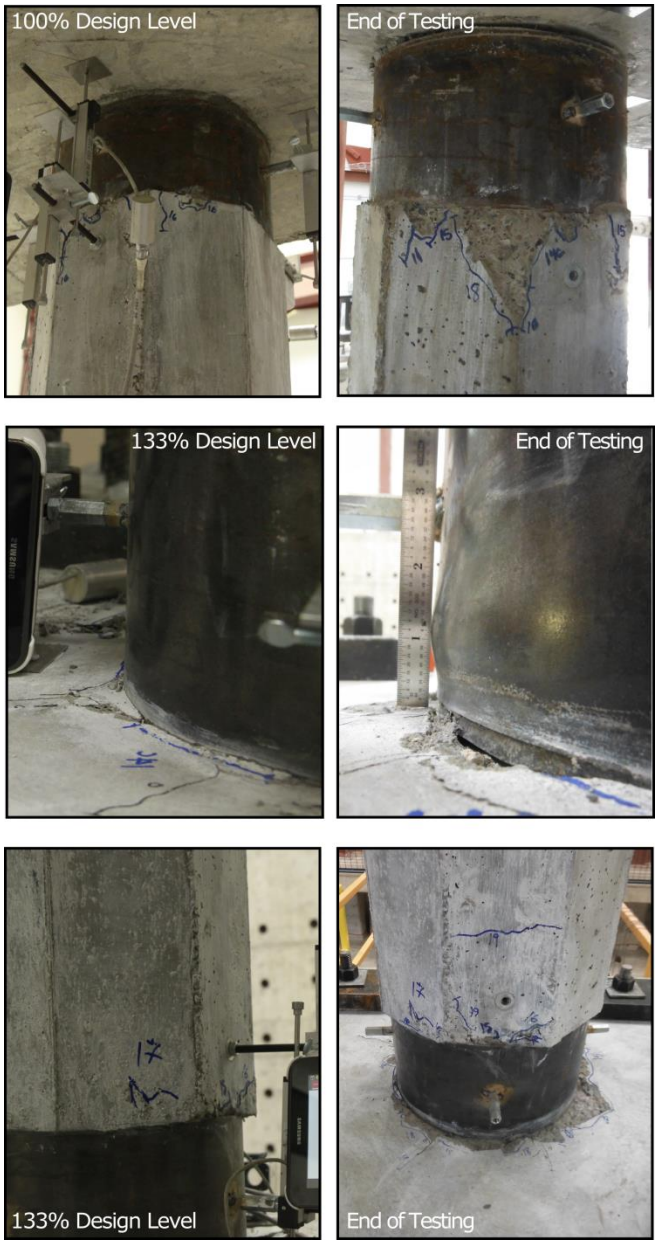

Figure 6.1: Observed damage in Bent 1 near Design Level motion and at end of testing.

respectively, and in Bent 2 during the 221% Design Level motion (Motion 19) at a drift ratio of 7.6%. After the 221% Design Level motion (Motion 19) between 30% and 40% of the grout pads in bents 1 and 3 had crushed and fallen from the column shoulder. Despite this damage the columns continued to carry the axial load and to rock, bearing on the remainder of the grout pad or the underside of the cap beam under extreme cases. There were no signs that the cap beam

was damaged by these concentrated stresses. Upon unloading, the columns returned to vertical and the central, undamaged portion of the grout pad and the reduced column section continued to carry the full vertical load of the structure.

A total of three residual flexural cracks formed in the six columns during testing. They occurred in bents 1 and 3 after the 221% Design Level motion (Motion 19). They were horizontal, located roughly 305mm (12in.) into the clear span of the columns and never exceeded hairline width. They did not propagate in any of the near–field motions (Motion 20B through Motion 21C).

6.1.2 Damage to longitudinal reinforcement

Longitudinal reinforcement fracture was first heard during the 133% Design Level motion (Motion 17) in Bent 1, which experienced a maximum drift ratio of 5.7%. This was earlier than expected from the results of the quasi-static specimens which were able to achieve a drift of 7% before bar fracture [Kennedy 2015]. Additional fractures were heard during the 177% Design Level motion (Motion 18), corresponding to 9.2% and 6.0% maximum drifts in bents 1and 3 respectively, and in the 222% Design Motion (Motion19). The fractures could not be detected with the strain gauges, because they were beyond their deformation capacity.

6.1.3 Damage to confining detail

The confining tube bulged on the north and south sides of the columns in bents 1 and 3 during the 177% Design Level motion (Motion 18) with maximum drift ratios of 9.2% and 6.0% respectively. Although the tube bulged and the annular end plate warped slightly, the rocking detailing continued to protect the column concrete. Because the tube was only activated in compression and not subject to reversed cyclic strains, it did not fracture. In the earlier quasi-

static tests, the tube had a slightly lower diameter-to-thickness ratio (governed by commercial availability) and never bulged, even at drifts ratios in excess of 10%.

6.2 Measured Response

The displacements of the deck were largely characterized in terms a transverse rigid body displacement and a twist rotation (about a vertical axis), which was caused by the asymmetric geometry. The measured distributions of column deformation were consistent with expectations; the columns largely rocked as rigid bodies between the footings and cap beams, and strains increases in both the strands and the mild steel reinforcement were largely attributable to the concentrated rotations that existed at the ends of the columns.

Table 6.2 shows the achieved table accelerations and maximum drifts in each of the bents for the high-amplitude coherent, unidirectional motions, as well as some of the low-level biaxial and sinusoidal motions that took place after the first high-level motion. In the high-amplitude motions, only transverse excitations were applied because the specimen lacked abutments, and thus the longitudinal boundary conditions did not replicate those that would be found in the prototype bridge.

6.2.1 Displacement Response

Figure 6.2 shows the maximum and residual drift ratios in each of the three bents for the high-amplitude motions. Prior to the 221% Design Level motion (Motion 19) the maximum drifts in Bent 1 were always higher than in bents 2 and 3. This behavior was attributed to the tendency of the structure to twist about Bent 3 because its columns were shorter, and therefore stiffer. The residual drift ratios for bents 1 and 2 remained below 0.1% for all of the experimental

motions and below 0.1% for Bent 3 through the 177% Design Level motion (18). No column was ever more than 6 mm (0.25 in.) out of true over its height at the end of a motion.

Table 6.2: Achieved peak table accelerations and maximum bent drift ratios

Motion	Description	Max. Table Accel. (g)			Max Drift Ratio (%)		
		Bent 1	Bent 2	Bent 3	Bent 1	Bent 2	Bent 3
High Amplitude Coherent Motions							
12	CCN	0.09	0.08	0.11	0.14	0.11	0.12
13	CCN	0.16	0.15	0.20	0.41	0.27	0.34
14A	CCN	0.32	0.23	0.24	1.08	0.61	0.75
Low Amplitude Sinusoidal Motions							
S1	Td = 0.25sec	0.04	0.04	0.04	0.07	0.06	0.07
S2	Td = 0.25sec	0.08	0.07	0.06	0.16	0.13	0.20
S3	Td = 0.25sec	0.12	0.10	0.09	0.23	0.21	0.33
Low Amplitude Biaxial Motions							
9C	CCN (d/3)	0.23	0.23	0.23	0.19	0.15	0.17
Sinusoidal Motions							
S4	Td = 0.30sec	0.23	0.12	0.13	0.54	0.41	0.63
S5	Td = 0.30sec	0.15	0.08	0.1	0.36	0.26	0.36
High Amplitude Coherent Motions							
14B1	SYL	0.24	0.20	0.19	0.46	0.34	0.44
14B2	SYL	0.43	0.39	0.42	1.10	0.80	1.03
14C	TAK	0.31	0.28	0.27	1.27	0.72	0.55
15	CCN (67% Design)	0.46	0.48	0.52	2.07	1.46	2.13
16	CCN (100% Design)	0.93	0.81	0.77	3.25	2.01	3.13
17	CCN (133% Design)	1.07	1.09	1.12	5.72	3.48	4.28
18	CCN (177% Design)	1.37	1.41	1.50	9.24	4.29	5.98
19	CCN (221% Design)	1.77	1.83	1.96	11.81	7.62	13.18
20A	CCN (100% Design)	0.79	0.77	0.85	6.46	5.18	9.49
20B	SYL	0.94	0.92	0.97	10.83	7.89	12.41
21A	TAK	0.4	0.39	0.4	5.92	4.38	7.56
21B	TAK	0.61	0.62	0.65	8.61	5.83	9.68
21C	TAK	0.8	0.89	0.83	11.99	7.72	12.87

The fracture of some of the longitudinal reinforcing bars during the 177% and 221% Design Level motions (Motion 18 and Motion 19), as well as yielding of the prestressing strands, lengthened the period of the structure. The reduced stiffness and strength of the specimen can be observed by comparing the response of the structure during the first and second 100% Design

Level motions (Motion16 and Motion 20A). Despite the eventual fracture of the longitudinal bars, the structure returned to vertical after the shaking ended.

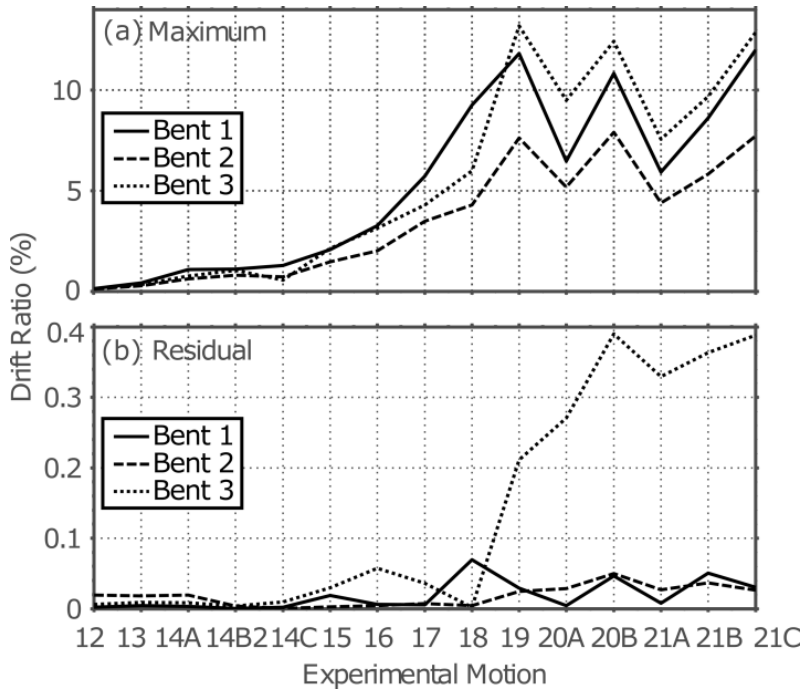

Figure 6.2: Maximum and residual drifts for high-amplitude motions.

The maximum center-of-mass (COM) and twist displacements of the structure during the high-level coherent motions was compared to those of an elastic-perfectly-plastic (EPP), single degree-of-freedom (SDOF) oscillator with similar stiffness, mass and strength of the undamaged shake-table specimen. Twist displacement in this context is defined as the relative displacement between Bent 1 and Bent 3. The SDOF system was subjected to the average of the three achieved table accelerations for each of the motions. The maximum displacement of the oscillator, defined here as $S_{di,}$ was recorded for each of these motions. Figure 6.3 shows the COM and twist displacements of the specimen versus the corresponding displacement of the oscillator (S_{di}).

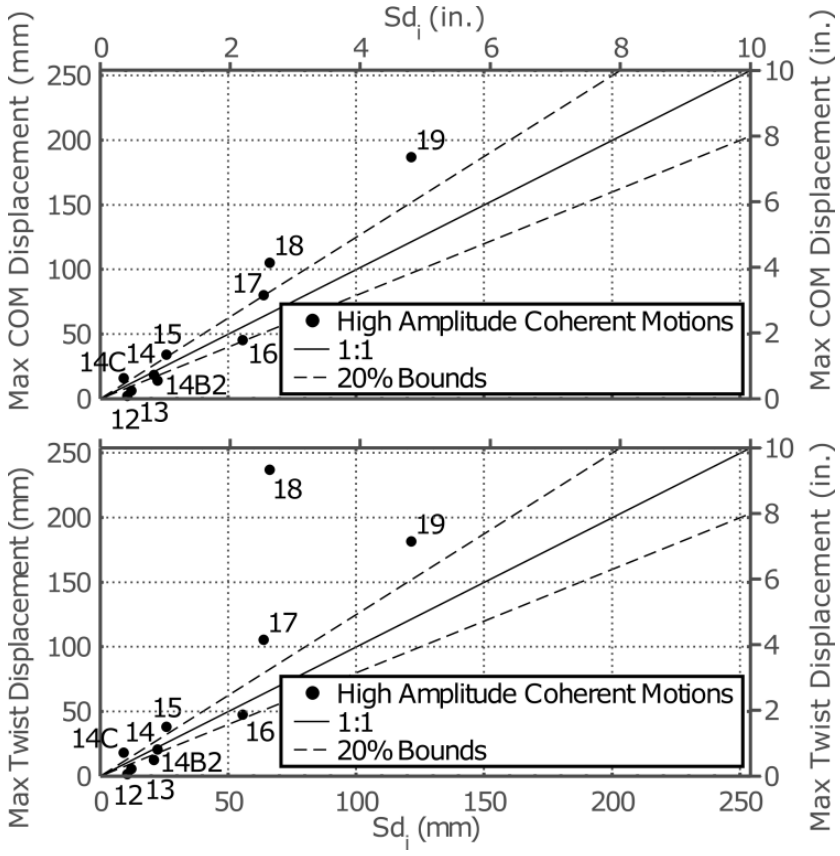

Figure 6.3: Maximum center of mass displacement versus Sdi for high-amplitude motions.

Up to the 177% Design Level motion (Motion 18), the SDOF model predicted the COM displacement of the specimen within 20%. Because of bar fracture in bents 1 and 3 during that motion, the properties of the bridge specimen changed. Thereafter the response of the bridge was no longer approximated well by the SDOF model, which did not degrade in strength or stiffness. The twist displacement of the structure did not increase linearly with S_{di}. The irregular geometry of the bridge specimen, the variation in damage among the bents, and the accidental incoherency of the table motions increased twisting of the superstructure, which contributed significantly to the recorded drifts in the exterior bents.

6.2.2 Base Shear Response

Two independent methods were employed to estimate the total base shear of the bridge during shaking. The first method was based on the inertial resistance of the deck and was computed by multiplying the accelerations of the superstructure by the tributary mass of each accelerometer location. The second method was based on the forces recorded in the table actuators and the accelerations of the shake tables. This second estimate was computed by subtracting from the actuator forces the inertial resistances of the table platens, footings and spacer blocks. The estimates calculated using this method are an upper bounds to the true value, since the recorded actuator forces include some table friction, which was not considered in the calculation.

Figure 6.4 shows the estimated base shear envelope for the bridge specimen, normalized by the sum of the idealized base shear capacities of the individual columns, each calculated using Equation 6.1:

$$V_{column} = \frac{(f_{sy}A_s + f_{py}A_p + P)D}{h} \quad [6.1]$$

where f_{sy} is the yield stress of the reinforcing, f_{py} is the yield stress of the prestressing strands, A_s is the total area of column longitudinal reinforcing, A_p is the total area of prestressing strand, P is the nominal axial load acting on the column, D is the column diameter, and h is the clear column height.

The maximum center of mass displacements for 100% and133% Design Level motions (Motion 16 and Motion 17) are also plotted for reference. The agreement between the two sets of measurements suggests that the forces measured by the load cells in the actuators could be used to estimate the individual bent response. The system continued to maintain over 50% of its base shear capacity through the end of testing.

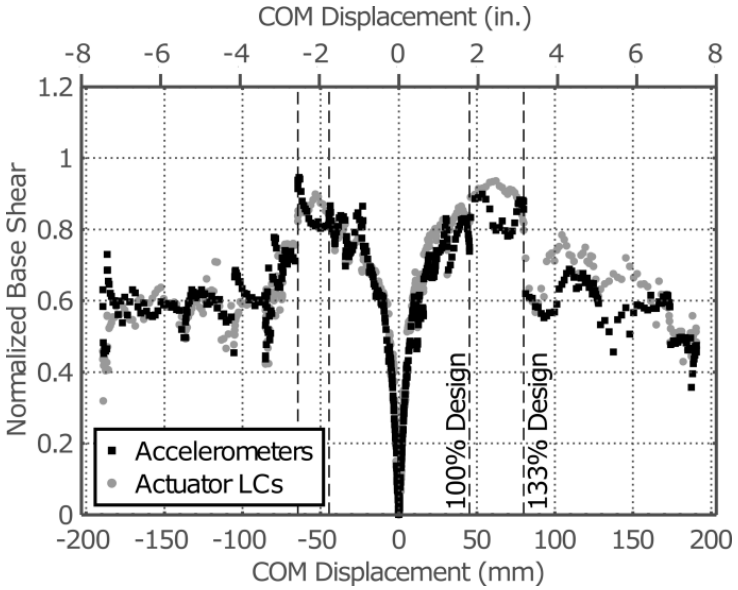

Figure 6.4: Specimen base shear envelope calculated using data from accelerometers and actuator load cells.

Figure 6.5a shows the base shear response for each of the three bents computed from the actuator load cells for the 100% Design Level motion (Motion 16). The maximum base shear computed for each bent is consistent with the variation in column heights. Bent 3, with the shortest columns, had a maximum base shear of 267 kN (60 kips), 14% higher than Bent 1 and 60 % higher than Bent 2. The ductility demands during the Design Level motion were 7.0, 3.7 and 6.5 for bents 1, 2 and 3 respectively. The system re-centered well; the maximum drift ratio at zero force was 0.6%.

Figure 6.5b shows the base shear envelopes for each of the three bents computed from the actuator load cells, normalized using Equation 4.1. The maximum drift ratio experienced by each bent during the 100% and 133% Design Level motions (Motion 16 and Motion 17) are again plotted for reference. The effective stiffness of each bent was calculated based on the point on the measured force-displacement curve corresponding to first yield in the mild steel reinforcing. The measured values of 17.3 kN/mm (98.8 kip/in.), 8.0 kN/mm (45.7 kip/in.) and 24.5 kN/mm (139.8 kip/in.) for bents 1, 2 and 3 respectively were 16%, 21% and 23% lower than the values

predicted by Elwood and Eberhard (2009) for non-prestressed, reinforced concrete columns with equivalent reinforcing ratios and axial loads. The bents reached their peak strength at drift ratios of 3.4%, 4.3%, and 3.5% and maintained over 80% of this value until drift ratios of 5.0 %, 6.4 %, and 5.9 % for bents 1, 2 and 3 respectively.

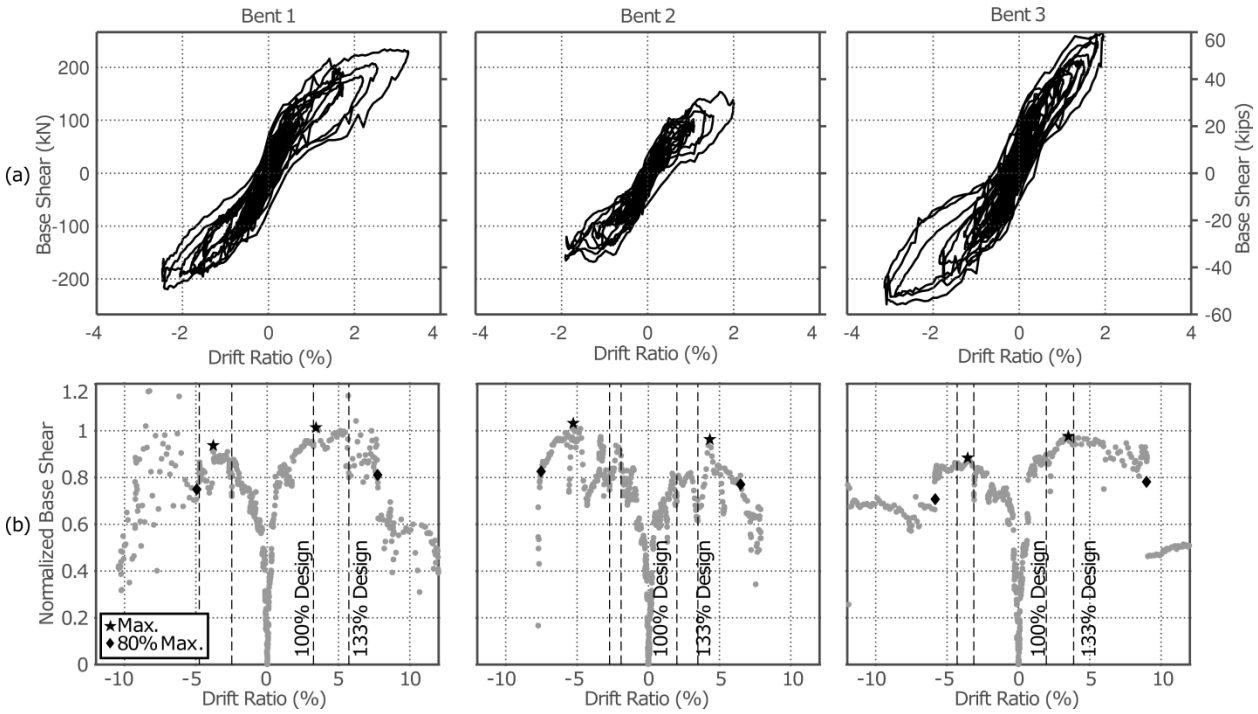

Figure 6.5: Bent base shear, calculated using data from actuator load cells. (a) for the 100% Design Level motion, (b). envelope for all motions.

6.2.3 Concentrated Rotations at Column Connections

Potentiometer pairs at either end of each column were used to compute local rotations over the first 76 mm (3 in.) of the column (at the precast connection interface) and over the next 152 mm (6 in.) of the column (at the interface directly above the confining tube). The average rotation for each of the four connections of each bent was compared to the measured drift. The rotations over the first 229 mm (9 in.) of the column, expressed as a percentage contribution to the overall bent drift, are shown in Figure 6.6.

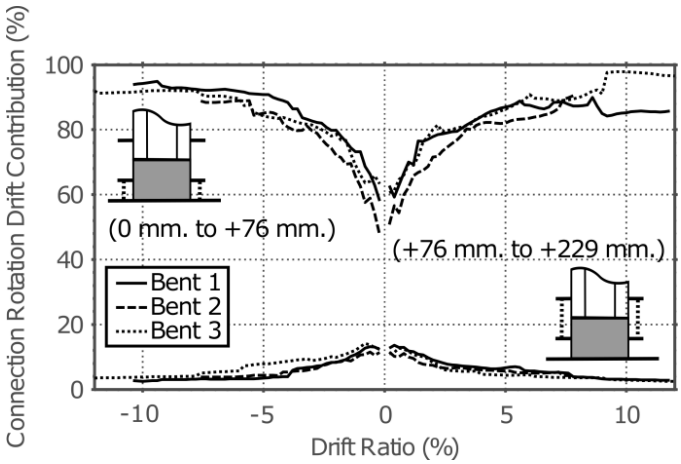

Figure 6.6: Percentage contribution of connection rotation to drift for each bent.

The deformation of the system was dominated by connection rotation. For example, at a drift ratio of 1%, rotations within the first 229 mm (9 in.) of the column accounted for 84%, 73%, and 80% of the total deformation of the system for bents 1, 2, and 3 respectively. At a drift ratio of 5%, these values increased to 94%, 89% and 91% for bents 1, 2 and 3 respectively. Because the columns had limited curvature, cracks which would be seen in a traditional cast-in-place system were nearly eliminated.

6.2.4 Neutral Axis Depth

The potentiometers at the ends of each column were also used to estimate the location of the neutral axis during testing. A plane was fit to the four displacement measurements, and the line which corresponded to zero displacement was defined as the neutral axis. The envelopes of the computed neutral axis in the transverse direction of the bridge for the twelve connections are shown in Figure 6.7.

All twelve measurements (four per column) showed good agreement. The neutral axis depth asymptotically approached a value of 10% of the column diameter, reaching this value by a drift ratio of roughly 2%. For larger drifts very little change in neutral axis depth occurred,

especially in the bottom connections. In the top connections the value appears to increase slightly for larger drifts, this is likely attributable to the loss of material from the grout pad and thus the decrease in available bearing area.

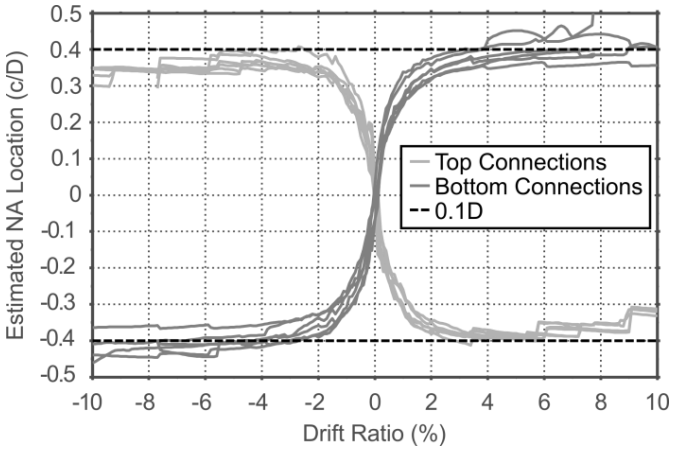

Figure 6.7: Percentage contribution of connection rotation to drift for each bent.

6.2.5 Strains in the Steel Confining Tube

Figure 6.8 shows the recorded envelopes of the strains in the confining tube, which were monitored 38mm (1.5 in.) above the column-footing interface on the north side of both columns of Bent 3. Strains were recorded using strain gauge rosettes to capture the two-dimensional state of strain. In the previous quasi-static tests, the strains had been measured in two locations, one near the top and one near the bottom of the tube. The strains near the interface, comparable to the ones measured here, were the larger of the two.

Both longitudinal and hoop strains developed when the north side of the tube was in compression. The strains in the south column were consistently larger than those in the north column. This difference is the opposite of what was expected based on the additional axial forces from overturning, and the reasons for it are unknown. The tubes remained elastic until

approximately 3.0% drift and bulged near the location of the gauges during the 177% Design Level motion (Motion 18 with 6.0% max drift ratio in Bent 3).

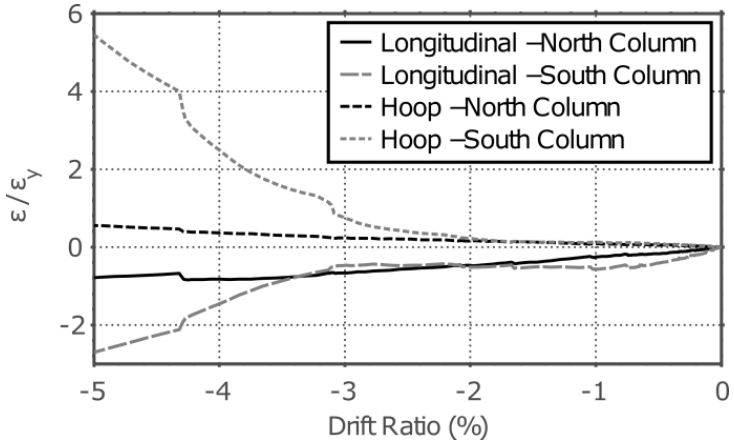

Figure 6.8: Confined rocking detail strain envelopes for Bent 3 columns.

6.2.6 Strains in the Mild Steel Reinforcement

Figure 6.9 shows the average strain envelopes for the longitudinal reinforcement in Bent 3 at three locations; at the rocking interface; 152 mm (6 in.) above or below the interface within the clear height of the column; and 229 mm (9 in.) above or below the interface within the anchorage region in either the cap-beam or the spread footing. The strains in the longitudinal reinforcement were measured in the north and south bars of each column at six elevations: at both rocking interfaces, and between 51mm (2in.) and 102mm (4in.) above and below each debonded region at each location. Gauge pairs were used to provide redundancy in measuring axial strain as well as to observe any bar buckling.

The strains were highly localized within the debonded region. The bond in the footing and within the steel confining tube was sufficient to prevent significant bar slip. The rebar remained elastic until roughly 0.5% drift.

The strain in the extreme tension reinforcing, located 277mm (10.9 in.) from the compression face of the column, at the interface was estimated based on rigid-body kinematics with Equation 4.2 (reprinted here as Equation 6.2),

$$\varepsilon = \left(\frac{\Delta}{h}\right)\left(\frac{\alpha D}{L_{\text{unb}}}\right) \qquad [6.2]$$

where the rotation at the joint is assumed to be equal to the drift ratio, Δ/h, αD is the distance from the neutral axis to the reinforcing bar, and L_{unb} is the effective unbonded length of the reinforcement. The neutral axis was assumed to be located 0.10D from the compressive face of the column, leading to α = 0.81. The effective unbonded length was estimated by transforming an assumed trapezoidal strain distribution between the three gauge locations (anchorage, interface, and column) into an equivalent rectangular region with the same area, and with the same strain as the interface gauge. Using the 35 available sets of strain data, this value was found to be the debonded length ($24d_b$) plus an additional $4d_b$ on either end of the unbonded region.

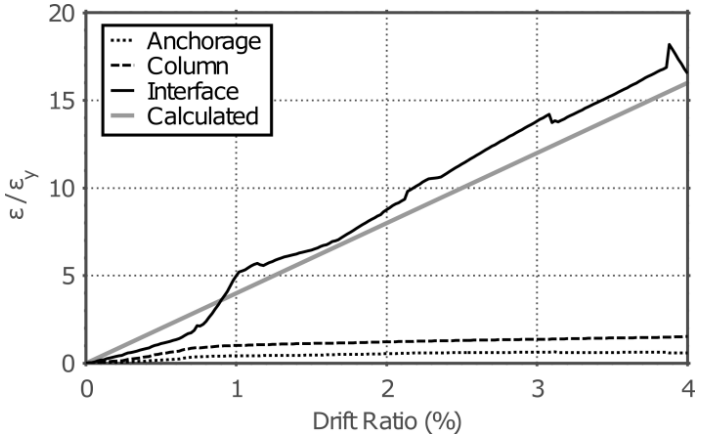

Figure 6.9: Average longitudinal reinforcing strain envelopes for Bent 3 columns.

The strain values calculated using Equation 6.2, shown in Figure 6.9, were similar to the measured strains in the reinforcing through apart from the initial portion of the curve. Longitudinal reinforcement first fractured in Bent 1 during the 133% Design Level motion

(Motion 17) with a maximum drift ratio of 5.7% and later during the 177% Design Level motion (Motion 18) in Bent 3 with a maximum drift ratio 6.0%. The computed strain in the longitudinal reinforcement at 6% drift using Eq. 2 was 0.049. This value is 30% lower than the calculated strain at fracture in the quasi-static specimens. Because the longitudinal bar strain for a given drift level is inversely proportional to the locally debonded length, the drift at bar fracture could likely be increased by providing a longer PVC sleeve.

6.2.7 Strains in the Strand

Strain increases were measured at mid-height of each of the columns' vertical prestressing strands. The average normalized strand strain envelope for each of the three bents is shown in Figure 6.10. To account for the variability in column height, the strains in this figure were normalized as follows,

$$\varepsilon_{\text{norm}} = \Delta\varepsilon \left(L_{\text{p, unb}}\right)/D \qquad [6.3]$$

where $\Delta\varepsilon$ is the recorded strain increment, D is the column diameter, and $L_{\text{p, unb}}$ is the effective unbonded length of the prestressing strand. The effective unbonded length is used here, in order to capture the effects of bond slip in the measured strain values. The unbonded length of the strand was taken as the clear height of the column plus half of the flexural bond length required for the strand to reach its ultimate stress on either end of the debonded region. The flexural bond length ($48d_b$) was computed based on the work of Cousins et al. (1990) using their recommendations for the plastic bond stress coefficient for low-grit, epoxy coated strands.

The normalized strain increments in the strands were estimated based on rigid-body kinematics. Assuming that the neutral axis was located 0.10D from the compression face of the column, the strand strains increments were estimated using Equation 6.2 (replacing $L_{\text{s, unb}}$ with $L_{\text{p, unb}}$). Because the strands experienced elongations from rocking at both the top and bottom of

the column, they acted as if located at the center of the section (α = (0.5-0.1)*(2 interfaces) = 0.8). The calculated normalized strain increments, shown in Figure 6.10, are slightly higher than the measured values particularly at low drift levels, where the deformation is largely attributed to column bending rather than rocking, which does not cause significant elongation of the strand. The slope of the calculated normalized strain versus drift relationship (0.008) was 18%, 31% and 7% higher than the measured values for bents 1, 2 and 3 respectively. The rank order of the percentage differences in slope (largest to smallest) is the same as the span-to-depth ratio. This order was expected, because longer column would be expected to have a large contribution from column bending.

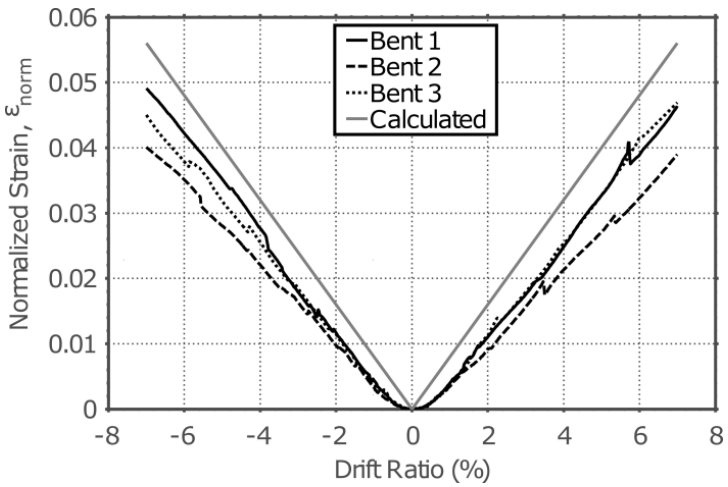

Figure 6.10: Average strand strain increment envelopes for each bent.

Because the instruments had to be disconnected when the columns were shipped from Seattle to Reno, the absolute strains at the start of testing were unknown. By adding the last recorded value to the strain increments recorded during testing, (i.e. assuming no change during shipping) it is estimated that the strands remained below the essentially elastic strain limit (0.0086) until roughly 3% drift in each of the six columns.

6.3 Summary and Conclusions

A quarter-scale, shake table specimen, consisting of three, two-column bents, was subjected to a suite of simulated ground motions to assess the seismic performance of the proposed system under dynamic loading.

Elimination of Residual Displacements. The partially unbonded, pre-tensioned strand in the columns almost completely eliminated residual displacements. The largest recorded residual drift ratio for all of the experimental motions was less than 0.1% in bents 1 and 2 and less than 0.4% in Bent 3 despite peak drifts of over 13%, rebar fracture (first occurring at drift ratios of roughly 6%) and yielding of many of the strands (first occurring at drift ratios of roughly 3%).

Reduction of Concrete Damage. Damage to the column concrete was effectively eliminated by allowing the columns to rock on specially detailed ends. Only three residual flexural cracks were observed during testing, none exceeding hairline in width.

Effect of Debonded Length of Deformed Bar Reinforcement. The reinforcement was debonded for a total of 24 bar diameters. Rebar fracture, first occurred during the 133% Design Level motion (with a maximum drift ratio of 5.7% in Bent 1). Rebar fracture could be further delayed by additional debonding of the longitudinal reinforcing.

Concentration of Column Deformations at the Connection Interface. The behavior of the specimen was dominated by the rigid body rotation of the columns as evidenced by the rotations measured at the precast joints, and the strains in the prestressing tendons and mild steel.

Effect of Steel Confining Tube Thickness. The steel tubes used in the shake table test had D/t ratios of 90. Bulging of the steel confining tube was first observed during the 177% Design Level motion (with maximum drift ratios of 9.2% and 6.0% in bents 1 and 3 respectively). Bulging could be delayed by using a thicker walled tube.

Design Models. For a design target drift ratio, the strains in the longitudinal reinforcing bars and the prestressing strands can be estimated well using rigid body kinematics (i.e., with Equation 6.2). For assessing performance objectives for design, this procedure will lead to conservative estimates (i.e. overestimate the strain in the reinforcement).

CHAPTER 7: COMPARISON OF RESULTS OF TWO SHAKING TABLE TESTS

As described in Chapter 5, the precast, pre-tensioned bridge specimen was designed to have similar geometry and column strengths to a cast-in-place bridge that was tested by Johnson et al. (2008). The experimental program and instrumentation were also replicated as closely as possible. This was done so that the performance of the new precast, pre-tensioned system could be compared with that of conventional cast-in-place construction. Chapter 6 summarized the results of the tests of the precast, pre-tensioned specimen.

This chapter compares the two tests, including the experimental programs, as well as the observed and measured responses of the two specimens.

- Section 7.1 compares the designs of the two bridge specimens.
- Section 7.2 compares the time required to construct the two specimens in the laboratory.
- Section 7.3 compares the base motions used in the experiments.
- Section 7.4 compares the damage observed during testing in the two experimental programs.
- Section 7.5 compares the measured global displacement response.
- Section 7.6 compares the calculated base shear response.
- Section 7.7 compares the distribution of column deformation in the two bridges.
- Section 7.8 compares the strains in the column longitudinal reinforcement.
- Section 7.9 compares the changes in the fundamental periods of the specimens.
- Section 7.10 summarizes the conclusions that can be drawn from the comparison of these two experiments.

7.1 Test Specimens

The two bridge specimens were similar in many ways. Both bridges contained two spans of 9.1 m (30 ft.) with overhangs at the end bents to accept a portion of the superimposed dead load. Each bent contained two 305-mm (12 in.) diameter columns spaced at 1905 mm (75 in.). The clear column heights (from the top of the footings to the bottom of bent caps) were 1.8 m , 2.4 m and 1.5 m (6 ft, 8 ft and 5 ft) for bents 1, 2 and 3 respectively.

The target axial load ratio (ALR) for the columns in both specimens was 8%. In addition to the dead load of the structural components, 793 kN (178.2 kips) of total added mass was placed on the superstructure to match the scaled prototype bridge mass. Although the distribution of these masses varied slightly between the two specimens, the total weight of the superstructure from the mid height of each of the columns was the same:1193 kN (268 kips).

The design parameters for the columns of the cast-in-place bridge specimen tested by Johnson et al. 2008 and the pre-tensioned bridge are summarized in Table 7.1.

Table 7.1 Column overview.

Bridge Specimen	***D*** **(in.)**	A_s **(in.^{2})**	A_p **(in.^{2})**	ρ_{equiv} **(%)**	ρ_v **(%)**	f'_c **(ksi)***	f_y **(ksi)***	***cc*** **(in)**	***ALR*** **(%)**
Pre-tensioned	12	0.66	0.34	1.7	4.5	9.9	70.5	0.75	8
Cast-in-place	12	1.76	0.00	1.6	0.9	5.9	69.7	0.75	8

*Average measured material properties between the three bents

Figure 7.1 compares the typical column details for two bridge specimens. The column longitudinal reinforcement for the cast-in-place bridge consisted of sixteen 10-mm bars (No. 3), corresponding to a reinforcement ratio of 1.56%. At the top of the columns, those bars were anchored in the cast-in-place cap beam by embedment of the projecting column bars. Because the scaled depth of the cap beam was inadequate for properly anchoring the longitudinal

reinforcement, steel bars were welded across the ends of adjacent longitudinal bars to provide the needed anchorage. Transverse confinement was provided by spirals made from 5-mm (W2.9) diameter wire spaced at 32 mm (1.25 in.), corresponding to a volumetric transverse reinforcement ratio of 0.9%.

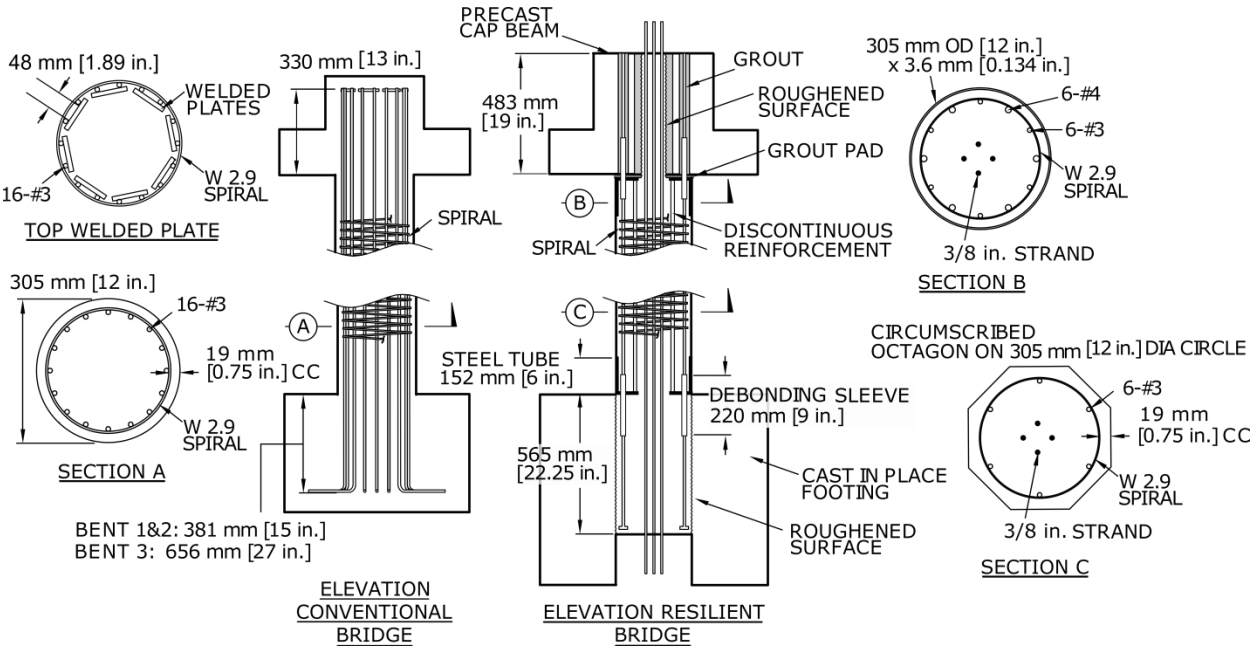

Figure 7.1 Column details at the top and bottom connections of both bridges

In the pre-tensioned bridge, the column longitudinal reinforcement consisted of six 10-mm (No.3) diameter bars and four 10 mm (3/8 in) diameter epoxy coated pretension strands, leading to an equivalent reinforcing ratio (accounting for the higher strength of the prestressing strands) of 1.7%.

7.2 Construction Times

Figure 7.2 compares the on-site construction time for both bridge systems in the laboratory environment. Although the laboratory is not a typical construction site, and many parameters, including lab technician experience, affected the scheduling of each bridge, the

construction times can still be compared. The bents of the precast, pre-tensioned bridge were built in one week, compared with five weeks for the bents of the conventional reinforced concrete bridge.

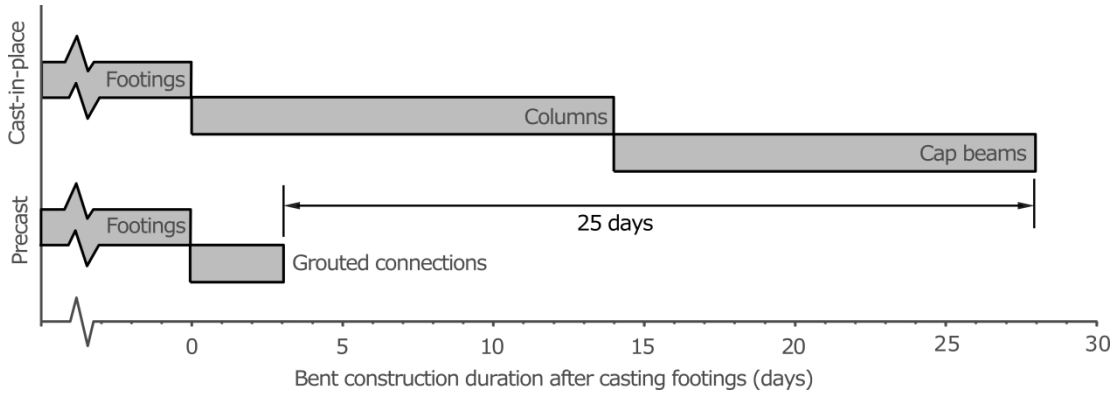

Figure 7.2 On-Site bent construction time for both bridges.

The precast column-to-cap beam connection needed only three days of curing before installing the superstructure beams. This is in contrast to the conventional reinforced concrete bridge, where 14 days were needed between casting the column and the bent cap, and another 14 days were required after casting the bent cap before placing the superstructure beams. The time savings was therefore largely attributed to precasting the bent cap and columns, which eliminated two casting and curing cycles.

7.3 Base Motions

Both bridges were subjected to a series of low-level coherent, incoherent and biaxial coherent motions, none of which caused damage to either bridge. The bridges were then subjected to a series of high-level coherent motions. In the precast pre-tensioned bridge experiment, this series of ground motions included the same high-level motions at the cast-in-place bridge, supplemented by the addition of high-level near-field motions. In this Chapter, only motions common to the two bridges are discussed.

Although the common ground motions were nominally identical, the experimental motions varied slightly due to differences in shaking table performance, which occurred because of upgrades to the table control software, and because the two systems provided different inertial resistances. To evaluate possible differences in motion intensity, the input motions for the two systems were compared using a two-degree-of-freedom (2DOF) nonlinear model of the conventional cast-in-place bridge, which could capture both the transverse motion of the structure as well as the twisting behavior caused by the varying column heights among the three bents. The same 2DOF model was used to characterize the intensity of all of the motions applied to both bridges, so that the effects of differences in the achieved ground motions could be distinguished from differences between the characteristics of the two bridges.

To create the 2DOF model, the bridge was idealized as a rigid beam excited by the three table motions through nonlinear springs, which represented the resistances of the individual bents. For each column, the spring strength and stiffness were taken as the pre-test values for the conventional cast-in-place bridge based on pushover analyses presented in Johnson (2006). The individual bent stiffness of 384 kN/mm (67.3 kips/in.), 178 kN/mm (31.2 kips/in.) and 629 kN/mm (110.2 kips/in.) for Bent 1, 2 and 3, respectively, were on average 95% of those computed for the given column section using the recommendations presented in Elwood and Eberhard (2009). The strengths of the bents were taken as 180 kN (40.4 kips), 138 kN (30.9 kips) and 257 kN (57.8 kips) for Bent 1, 2 and 3 respectively. The bents were modeled using elastic-perfectly-plastic (EPP) hysteretic elements. Each motion was run independently of previous motions; residual displacements from previous motions were ignored, so that the idealized system would start in the un-deformed configuration for each motion.

The maximum drift ratios for each of the three springs are compared in Figure 7.3 for each of the common motions. Prior to Motion 16 (100%), the two maximum calculated responses of the 2DOF model were higher in Bent 1 for the 2014 motions and higher in Bent 3 for the 2005 motions. During the Motion 16 (100%), the peak responses of bents 1 and 2 were nearly the same for the two experimental motions. However, at Bent 3, the calculated drift ratio for the 2005 motions (drift ratio of 4.2%) was higher than for the 2014 motions (drift ratio of 3.0%). For Motion 17 (133%) and Motion 19 (221%), the effects of the motions were again nearly identical. Motion 18 (177%) had similar maximum displacements for Bent 2, but the calculated maxima were higher in bents 1 and 3 under the 2014 motions.

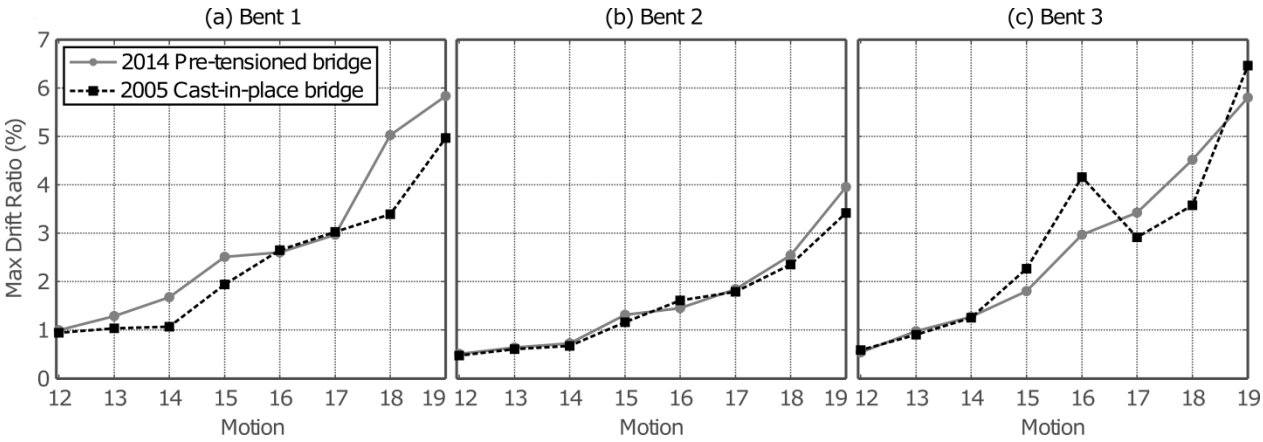

Figure 7.3 Maximum drift ratios for a 2 DOF model subjected to the two sets of ground motions

7.4 Observed Damage

Table 7.2 lists the first occurrence of the different damage stages for both bridges. Figure 7.4 shows a side-by-side comparison of the damage for both bridges. Direct comparison of the damage in the two systems is not possible for all damage states, because the key damage states in the two systems were different. However, the precast, pre-tensioned bridge generally suffered less damage than did the conventional cast-in-place bridge, and damage that would cause similar performance reductions occurred at higher drift ratios for the precast, pre-tensioned bridge.

Table 7.2 First occurrence of damage states for both bridges

Damage State	Bent 1		Bent 2		Bent 3	
	Cast-in-place	Pre-tensioned	Cast-in-place	Pre-tensioned	Cast-in-place	Pre-tensioned
Flexural Cracking	2.2%(15)	11.8%(19)	1.3%(15)	-	2.4%(15)	13.2%(19)
Cosmetic Spalling	3.7%(16)	2.1%(15)	3.5%(18)	3.5%(17)	2.4%(15)	4.3%(17)
Grout pad Crushing	-	9.2%(18)	-	7.6%(19)	-	6.0%(18)
Bar yielding	0.9%(13)	0.5%(14)	0.6%(14)	0.6%(14)	0.5%(13)	0.5%(14)
Bar Exposure	3.1%(20)	-	5.5%(22)	-	5.5%(18)	-
Bar Buckling	3.1%(20)	-	5.5%(22)	-	7.9%(19)	-
Bar Fracture	-	5.7%(17)	-	7.6%(19)	7.9%(19)	6.0%(18)
Spiral Yielding	3.7%(16)	-	3.5%(18)	-	0.5%(13)	-
Spiral Fracture	-	-	-	-	7.9%(19)	-
Strand Yielding	-	3.3%(16)	-	4.3%(18)	-	3.1%(16)
Tube Yielding	-	unavailable	-	unavailable	-	3.1%(16)
Tube Bulging	-	9.2%(18)	-	-	-	6.0%(18)

7.4.1 Concrete and Grout

Damage to the column concrete was extensive in the cast-in-place bridge, and followed the pattern seen in most tests of conventional reinforced concrete columns. It consisted primarily of flexural cracking followed by spalling. Flexural cracks first occurred during Motion 15 (67%) in all three bents and progressed in subsequent motions as shown in Figure 7.4. By the end of Motion 19 (221%), every column was severely cracked, with residual crack widths on the order of 2 mm (0.08 in.). The cover first spalled in Bent 3 during Motion 15 (67%), when the spalling extended over a length of 100 mm (4 in.) from the end of the column. Its progression thereafter can be seen in Fig. 10. The longitudinal and transverse reinforcement was first exposed by the concrete spalling during Motion 17 (133%). By the end of Motion 19 (221%), the cover in every column had spalled, with an average length of 150 mm (6 in.), or half the column diameter (the plastic hinge length).

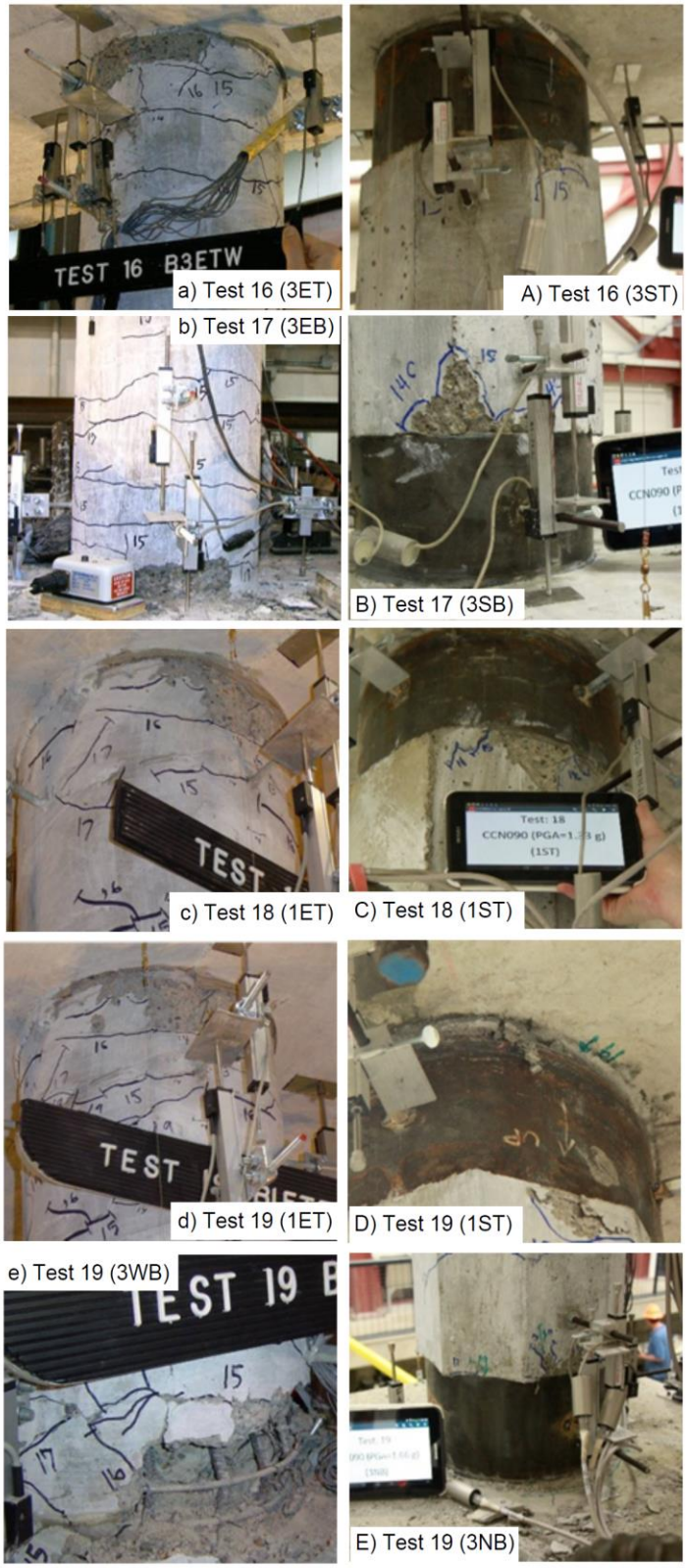

Figure 7.4 Damage progression comparison during motions 16 through 19 (from Mantawy et al 2016)

In contrast, damage to the column concrete in the precast, pre-tensioned bridge was minimal. The flexural cracking consisted of a total of six hairline cracks in three of the columns; the other three columns remained uncracked throughout the entire test program. The spalling was limited to the corners of the octagonal columns; it had no effect on the column strength, and can be considered as cosmetic damage. It was first seen during Motion 15 (67%).

The grout pads at the tops of the columns suffered some crushing, as shown in Figure 7.4D. It was first observed in both columns of Bent 1 and Bent 3 during Motion 19 (221%), but this damage did not compromise the columns' ability to carry gravity load. The grout pad could be easily repaired by injecting it with new grout without the need to close the bridge.

7.4.2 Longitudinal Reinforcement

In the cast-in-place bridge, the longitudinal reinforcement yielded, buckled then fractured during the motions listed in Table 7.3. This table also provides the comparable values for the precast, pre-tensioned bridge.

In the cast-in-place bridge, bar fracture was promoted and preceded by bar buckling, whereas the bars in the precast, pre-tensioned bridge never buckled. This illustrates the different behaviors of the reinforcement in the two systems. In a conventional, cast-in-place bridge column, bar buckling and subsequent re-straightening during the next half cycle, rather than excessive tension strain, are the events that most commonly trigger bar fracture [Moyer and Kowalsky 2003], and they are in turn promoted by loss of concrete cover and yielding and kinking of the spiral.

By contrast, in the pre-tensioned bridge columns, bar buckling is inhibited by the rigid confinement provided by the tube detail, in which case bar fracture does not occur until the

tension strain becomes excessive. However, the confinement provided by the tube detail also improves the local bond capacity, so the bar experiences less progressive strain penetration, and the deliberately debonded length must therefore be great enough to keep the tension strains to a tolerable level. The distribution of bar strains measured in the tests are discussed in more detail in Section 7.6. One consequence of these different behaviors is that increasing the debonded length to delay bar fracture is likely to be a more successful strategy in the precast, pre-tensioned column than in a conventional one.

7.4.3 Transverse Reinforcement

In the conventional cast-in-place bridge, strains were monitored in the spiral 152 mm (6 in.) away from the interfaces, near the end of the calculated plastic hinge. For the conventional cast-in-place bridge, the spiral first yielded in Bent 3 during Motion 13 (20%), and fractured in Bent 3 during Motion 19 (221%) at 7.9% drift ratio, as shown in Figure 7.4e**.** In the precast, pre-tensioned bridge, strains were monitored in the spiral 76 mm (3 in.) beyond the end of the confining tube. The spiral remained elastic at all times, and the maximum strain recorded was 85% of the yield strain.

Bulging of the steel tube first occurred during Motion 18 (177%) at the bottom connections of Bents 1 and 3. The bulging increased during the subsequent motions. The tube detail was successful in preventing spalling damage at the ends of the columns, although its wall thickness and length (D/90 and D/2 respectively) were chosen empirically. This damage state could be delayed or eliminated by using a tube with a thicker wall. In the earlier quasi-static tests [Schaefer et al. 2014a and Kennedy 2015] the thickness of the tube wall was D/80 and no bulging occurred.

Strains in the confining tube were monitored using strain rosettes located 38 mm (1.5 in.) above the column-footing interface on the north side of both columns of Bent 3. The tubes remained elastic until approximately 3.0% drift then yielded and, bulged in Bents 1 and 3 at drifts of approximately 9.2% and 6.0%, respectively.

7.5 Displacement Response

In both shaking table tests, the deformations of the deck were much smaller than its rigid-body motions, so the response could be characterized in terms of two degrees of freedom. These DOFs corresponded to transverse displacement and twist rotation (about a vertical axis), which were caused by the asymmetric geometry.

Under the low-level excitations, the Center of Mass (COM) displacements, approximated as the average of the three relative displacements between the tables and superstructure, were within the elastic range of response. They were nearly the same for both systems, and the residual drift ratios were small (less than 0.1%).

For the high-level excitations, the peak drift ratios are summarized in Table 7.3. Figure 7.5 shows the maximum and residual drift ratios for both bridges for the high-level motions (Motion 14 (33%) through Motion 19 (221%)), plotted against the computed maximum spring displacements for the previously described 2DOF model subjected to the same measured motions. As shown in Figure 7.4, the maximum drift ratios for large excitations were generally higher for the precast, pre-tensioned bridge, however the residual drift ratios were generally lower.

For all motions up to Motion 18 (177%), the residual drifts in both systems were less than 0.2%, and even in Motion 19 (221%), they were less than 0.5%. This is in part due to the choice of ground motion. The Century City record is a far-field motion. Typically, these motions

produce smaller residuals than near-field, pulse-type excitations. The residual drift ratios were consistently lower for the pre-tensioned bridge than for the cast-in-place bridge.

Table 7.3: Maximum bent drift ratios for the shared high-amplitude experimental motions.

Motion	Design Level (%)	Bent 1 (%)		Bent 2 (%)		Bent 3 (%)	
		Cast-in-place	Pre-tensioned	Cast-in-place	Pre-tensioned	Cast-in-place	Pre-tensioned
12	10.6	0.32	0.14	0.18	0.11	0.21	0.12
13	20	0.88	0.41	0.45	0.27	0.52	0.34
14	33	1.05	1.08	0.58	0.61	0.82	0.75
15	67	2.17	2.07	1.30	1.46	2.44	2.13
16	100	3.66	3.25	2.39	2.01	3.14	3.13
17	133	2.75	5.72	2.03	3.48	2.37	4.28
18	177	3.86	9.24	3.51	4.29	5.50	5.98
19	221	4.89	11.81	4.45	7.62	7.85	13.18

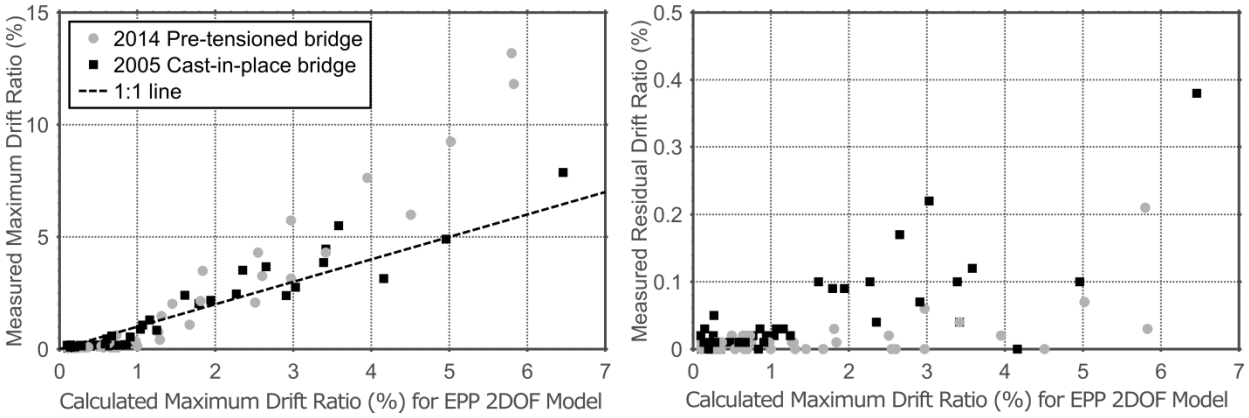

Figure 7.5 Maximum and residual drift comparison for both bridges.

For excitations applied after the 221% Design Level motion (Motion 19), direct comparisons are not possible, because the conditions in the tests differed. In the conventional cast-in-place bridge experiments, the damage induced by 221% Design Level motion (Motion 19) was so extensive that a lower level motion (The 133% Design Level motion) was re-run and then the supplementary masses over Bent 3 were removed in the interests of safety before

running two more scaled CCN motions. After these three "post-peak" motions, the maximum residual drift ratio was 0.4% for Bent 1 and 1.7% for Bent 3, with significant damage occurring in all three bents. In the precast, pre-tensioned bridge experiment, all the masses were kept in place after the common motions had been completed, and near-field motions of increasing intensity, using the Sylmar and Takatori records, were applied to produce more damage and larger residual displacements. Despite the high peak drifts that these motions induced (more than 12%), the residual drifts increased little or not at all over those induced by the previous far-field motions applied earlier. The largest residual drift ratio for all of the motions was 0.07% for Bent 1 and 0.4% for Bent 3.

7.6 Base-Shear Response

Figure 7.6 shows the peak total base shear vs the COM displacement for the two bridge systems. The maximum COM displacement from each motion is also shown for reference.

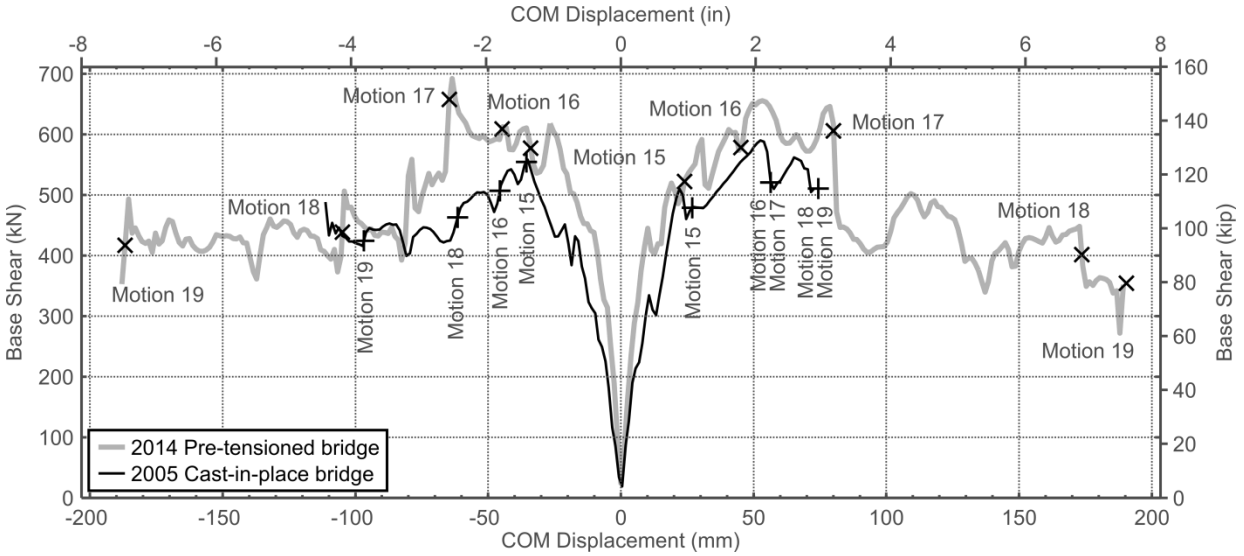

Figure 7.6 Total base shear envelopes. (Maximum displacements during each motion are identified by vertical text for the cast-in-place bridge)

The plot shows that, after the 67% Design Level motion (Motion 15), the peak base shear was approximately constant, because by then the bridges had reached their lateral capacities, controlled by the flexural strengths of the columns. Up to the 221% Design Level motion (Motion 19), the last motion common to both systems, the precast, pre-tensioned bridge had somewhat higher base shears, reflecting its slightly greater column strengths. Through the 133% Design Level motion (Motion 17), the peak drifts of the two systems were nearly the same, but the peak base shears were higher in the precast, pre-tensioned bridge, indicating that it was generally stiffer. Variations within that general trend existed, and they were attributed to the fact that the two systems have different force-displacement characteristics, which induced different dynamic responses under the same excitation.

7.7 Distribution of Column Deformations

The measured distributions of column deformation were consistent with expectations; in the conventional cast-in-place bridge, curvatures were more distributed over the height of the columns, whereas, in the precast, pre-tensioned bridge columns, the rotations were at their ends. Potentiometer pairs at each end of each column were used to compute local rotations over the first 76 mm (3 in.) of the column (at the precast connection interface) and over the next 152 mm (6 in.) of the column (at the interface directly above the confining tube in the precast, pre-tensioned bridge). The locations of the instruments were the same in both bridges.

At each bent, the average of the four individual connection rotations over the first 229 mm (9 in.) of the column was divided by the bent drift ratio, and this ratio was used as a measure of the distribution of the column rotation. The values are shown in Figure 7.7. At all drifts, but particularly at larger drifts, the concentration of the deformations at the ends of the columns was greater in the precast, pre-tensioned bridge than in the conventional cast-in-place bridge.

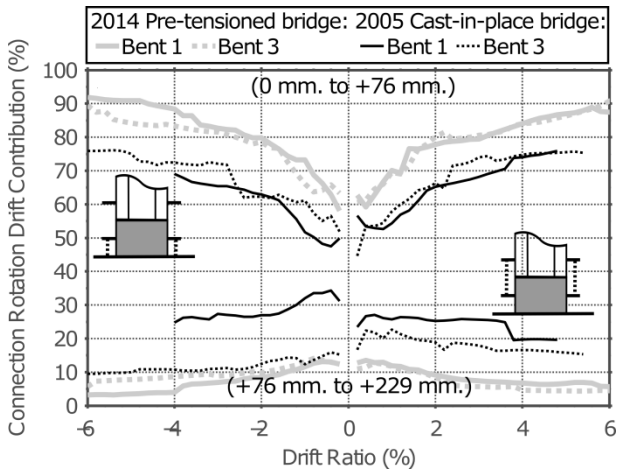

Figure 7.7 Contribution of drift to total connection rotation for bents 1 and 3.

7.8 Distribution of Strains in the Longitudinal Reinforcement

The distribution of strains in the reinforcement was consistent with the manner in which each specimen deformed. In the conventional cast-in-place bridge columns, in which the bars were not debonded, the strains in the reinforcement were distributed throughout the plastic hinge regions. In the precast, pre-tensioned bridge columns, strains were distributed along the debonded region at the connection interface, and dropped rapidly outside it. Despite this difference, longitudinal reinforcement yielding was first recorded during the 20% Design Level (Motion 13) and the 33% Design Level motions (Motion 14) in both bridges. This similarity is attributable to the fact that the debonded length in the precast, pre-tensioned bridge was chosen to be nearly equal to the calculated plastic hinge length of the conventional cast-in-place bridge.

Figure 7.8 shows the distribution of the measured strain in the extreme tensile reinforcement at the top connection of the north column of Bent 1 in the precast, pre-tensioned bridge and the corresponding location in the conventional cast-in-place bridge. Strains are shown for drift ratios of 1% and 2%. In both bridges, the reinforcement was instrumented in three locations: below, at, and above the interface. Due to the use of debonding sleeves in the precast, pre-tensioned bridge, the locations of the gauges are similar but not identical between the two

specimens. For the given drift ratios, strains at the rocking interface for Bent 1 of the precast, pre-tensioned bridge were lower than the interface strains of Bent 1 for the conventional cast-in-place bridge. The distribution of strain in the reinforcement of the precast, pre-tensioned bridge was highly localized at the interface and demonstrated that the bar achieved excellent bond within the confined rocking detail.

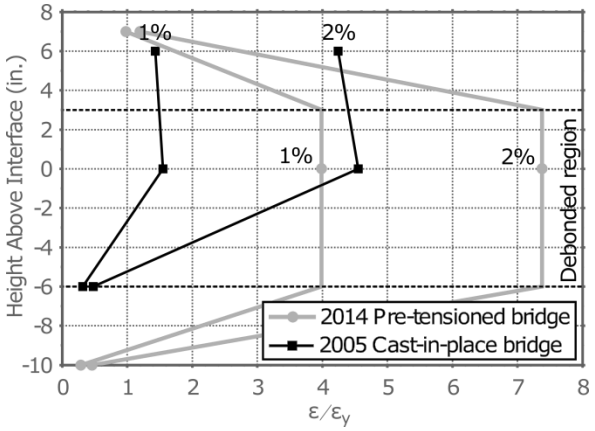

Figure 7.8 Typical strain distributions for both bridges.

Figure 7.9 shows the strain envelopes for the extreme tensile reinforcement at the bottom connection of the north column of Bent 3 in the precast, pre-tensioned bridge and the corresponding location in the conventional cast-in-place bridge. The strains at the interface and in the anchorage region (in either the cap beam or footing) were elastic and quite similar for both bridges. However, the strains within the plastic hinge location were inelastic and much higher for the conventional cast-in-place bridge (up to four times at 1.6% drift ratio). This difference is consistent with the formation of a plastic hinge in the conventional column, and the associated progressive debonding, near the location of the column strain gauge, located 152 mm (6 in.) above the interface. The approximate plastic hinge length was 147 mm (5.8 in.), computed according to the recommendation of Priestly and Park (1987).

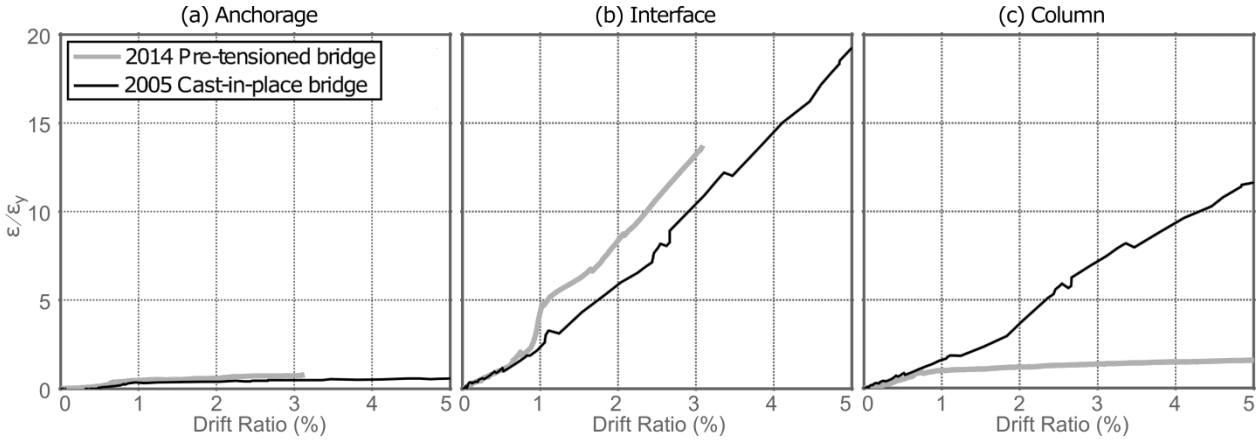

Figure 7.9 Typical longitudinal reinforcement strain envelopes for both bridges.

7.9 Fundamental Periods

Both specimens were subjected to low-intensity "white-noise" excitations between simulated earthquake motions so that changes in their low-strain dynamic characteristics could be estimated. During these motions, the transverse, accelerations of the superstructure of either bridge was measured at five locations; at each bent and at the middle of each span.

The period of the first mode of vibration for both bridges was estimated using two methods. The first method, the peak-picking method [Johnson et al. 2006], uses the power spectral densities of the recorded superstructure accelerations. The largest period which corresponds to a local maximum value of the power spectral density is deemed to be the first-mode period of vibration. The second method, the Successive Linear Programming (SLP) algorithm [Ranf 2007], optimizes a simple 5-DOF model of the bridge structure, excited by the measured acceleration records, to match the measured superstructure accelerations.

Figure 7.10a compares the identified periods for the reinforced concrete bridge using both the peak-picking (PP) and SLP methods, as well as the periods identified by Ranf (2007) and Johnson et al. (2008). Figure 7.10b shows the estimated first-mode period of the pre-tensioned bridge.

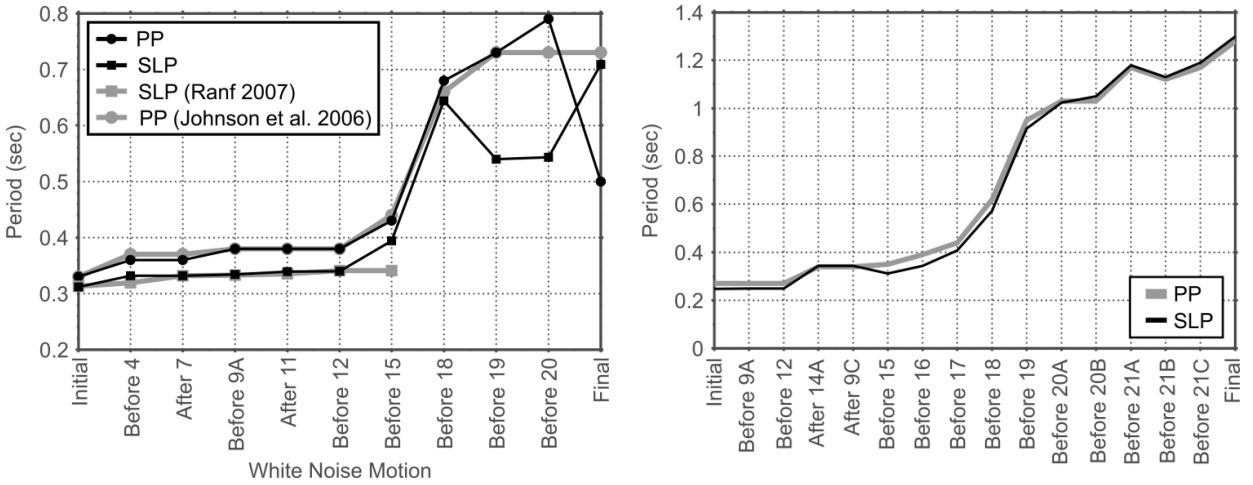

Figure 7.10 Estimated first-mode period of vibration for the (a) cast-in-place and (b) the pre-tensioned bridges.

The computed values agree reasonably well with one another and the previously reported values, until the white noise motion run before the 221% Design Level motion (Motion 19). The agreement between the estimates gives confidence that these values represent the dynamic properties of the structure. Figure 7.11 compares the identified first-mode periods of both bridges throughout the high-amplitude motions.

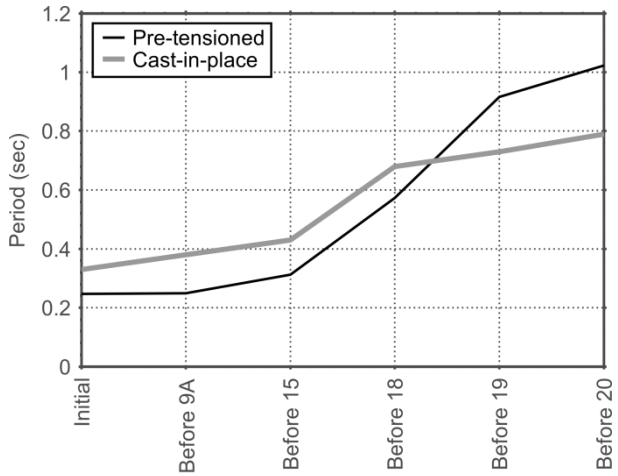

Figure 7.11 Comparison of the estimated first-mode period of vibration for both bridges

The initial, first-mode period of vibration of the pre-tensioned bridge was found to be approximately 15% lower than the cast-in-place bridge. This is likely because the columns were prestressed and therefore uncracked, prior to testing. Up to the 177% Design Level motion (Motion 18), the period for the precast, pre-tensioned bridge was shorter than for the conventional cast-in-place bridge, but was longer thereafter. This difference is attributed to the fracture of the longitudinal bars and yielding of the prestressing strands, which reduced the stiffness of the pre-tensioned bridge.

7.10 Summary and Conclusions

In order to evaluate the seismic performance of the new system, the shaking table performance of the new system and a conventional reinforced concrete bridge system were compared. Both bridges had the same overall geometry and added mass, they had approximately the same lateral strength. The cast-in-place bridge was tested in 2005, and the new precast, pre-tensioned bridge was tested in 2014.

The two bridges were subjected to a suite of nominally identical seismic excitations. In the conventional cast-in-place bridge, the motions (up to the 221% Design Level motion) caused considerable damage to the structure, the masses were removed over a portion of the bridge and the test was stopped shortly thereafter. In the precast, pre-tensioned bridge, the damage was considerably less, and further excitations, using near-fault motions of increasing amplitude, were applied.

The two experiments made it possible to compare the two systems in terms of the speed of construction, maximum displacement demands, residual displacements and development of damage in the concrete and steel.

Accelerated Construction. The use of precast components and new connection details in the precast, pre-tensioned bridge allowed the bents to be constructed in 20% of the time needed for the conventional cast-in-place bridge.

Elimination of Residual Displacements. The residual drifts, after the ground motion had stopped, were consistently smaller in the precast, pre-tensioned bridge than in the conventional cast-in-place bridge. During the 221% Design Level motion (Motion 19), the residual drift ratio in the conventional cast-in-place bridge reached, 0.5% and the extensive damage required removal of the added inertial mass blocks, by end of testing the maximum residual drift was 1.7% in Bent 3. In contrast, the residual drift in the Precast, pre-tensioned bridge never exceeded 0.4% despite its being subjected to an additional series of high-intensity near-field ground motions that caused peak drifts of more than 12%.

Reduction of Concrete Damage. Damage to the column concrete was effectively eliminated in the precast, pre-tensioned bridge. Every column in the conventional cast-in-place bridge sustained both extensive cracking and major spalling, which started during the Motion 15 (67%). In contrast, the only cracks that formed in the precast, pre-tensioned bridge were during the 221% Design Level motion (Motion 19); they were few in number (half of the columns never cracked) and never exceeded hairline width. In the precast, pre-tensioned bridge, the grout at the interface suffered some crushing, but it could be repaired by injection without the need to close the bridge.

Damage to the Deformed Bar Reinforcement. Bar buckling first occurred in the conventional cast-in-place bridge at a drift ratio of 5.5% in Bent 3, but never occurred in the precast, pre-tensioned bridge, owing to the stiff confinement provided by the steel tube detail. The first bar fractures occurred at 7.8% and 5.6% drift ratio in the conventional and precast, pre-

tensioned bridges respectively. It is likely that bar fracture in the precast, pre-tensioned bridge could be delayed by increasing the length of the deliberately debonded region of the bars.

Maximum Displacement Demands. The maximum drift ratios of the two bridges were essentially identical through the 100% Design Level motion (Motion 16). After this motion, the peak drift ratios were higher in the precast, pre-tensioned bridge due to the fracture of longitudinal reinforcement and the yielding of prestressing strands.

CHAPTER 8: DESIGN OF HIGH-PERFORMANCE, HYBRID BRIDGE COLUMNS

This chapter summarizes the seismic design methodology outlined in the *AASHTO Guide Specifications for LRFD Seismic Bridge Design* (2015), and proposes a strategy for using this methodology to design precast, pre-tensioned rocking columns. The chapter is divided into six sections

- Section 8.1 summarizes the seismic design methodology outlined in the *AASHTO Guide Specifications for LRFD Seismic Bridge Design* (2015).
- Section 8.2 discusses the performance criteria for prestressed, rocking columns, and the implications for the deformation capacity of the columns for seismic design.
- Section 8.3 outlines a procedure for developing a permissible column design space that is based on service load requirements and seismic performance criteria.
- Section 8.4 presents a method to analyze the rocking columns using moment-rotation analysis and the modifications that must be made to account for the strain incompatibilities that exist at the rocking interface.
- Section 8.5 presents detailing recommendations for the confining shoe, based on the limited data available.
- Section 8.6 discusses several aspects the proposed methodology.

8.1 Summary of Existing Method

Figure 8.1 summarizes the displacement based procedure outlined in *AASHTO Guide Specifications for LRFD Seismic Bridge Design* (2015). This procedure relies on a force-based design to satisfy service load criteria. The non-seismic forces and moments acting on the columns are used to estimate the diameter and flexural reinforcement of the columns. The suitability of this initial design is then assessed under the design level seismic hazard.

The *AASHTO Guide Specifications for LRFD Seismic Bridge Design* (2015) define the design level hazard as the 5% damped spectral acceleration with a 7% probability of exceedance in 75 years. The damping ratio of 5% is assumed for all designs, regardless of structural system; higher levels of damping are permissible at the discretion of the owner, but are limited to 10%.

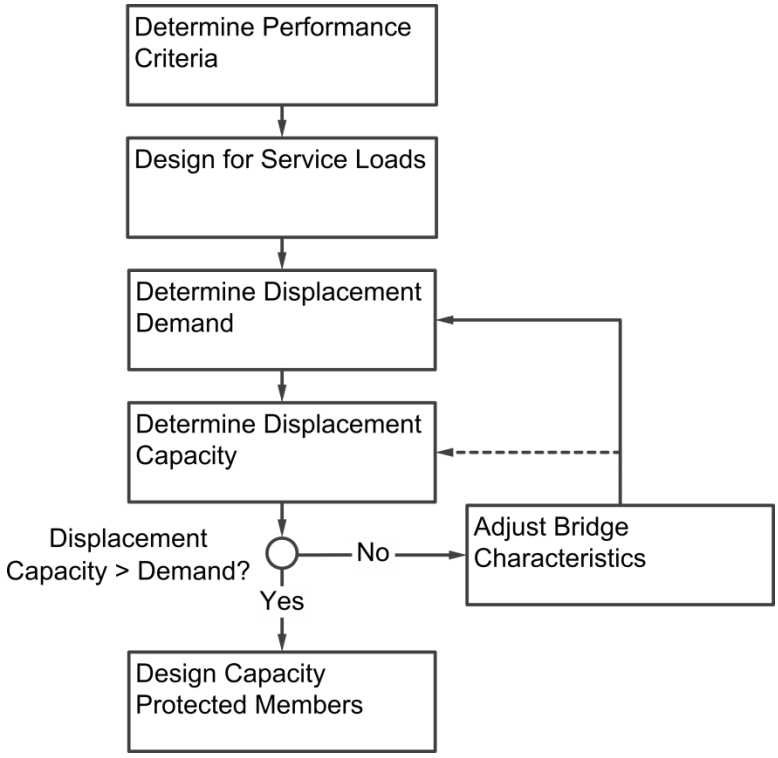

Figure 8.1 AASHTO Seismic Design Procedure for SDC D (adapted from AASHTO 2015)

Short period considerations are handled by a response modification coefficient, which amplifies the elastic displacement demand for frames whose period falls within the equal energy region of the design spectrum.

For bridges in Seismic Design Category (SDC) D, displacement demands are determined using multi-modal response spectrum analysis using the effective section properties of the ductile elements.

Once the seismic displacement demand is established based on the elastic modal analysis, frames of the bridge are then analyzed inelastically to ensure that they possess the required displacement capacity. This is done using the inelastic properties of the bridge members, which in SDC D requires an incremental static, "push-over", analysis. If the displacement demand exceeds the capacity, bridge characteristics (i.e. bridge geometry or column section properties) are adjusted, and the displacement demand and/or the capacity of the structure are recomputed. This process is repeated until a satisfactory design is found. Once the ductile members are designed and their plastic capacities established, the other members are designed to remain elastic under the magnified inelastic action of these ductile members, using the principles of capacity design.

8.1.1 Performance Criteria

The *AASHTO Guide Specifications for LRFD Seismic Bridge Design* (2015) require that under the design level hazard, all bridges should meet life safety performance objectives, with a low probability of collapse during the design level motion. This performance objective defines the criteria against which the displacement capacities of the ductile members of the bridge are assessed. However, it implies that the bridge may suffer significant damage, leading to disruptions to service and partial or complete replacement after an earthquake. In this context,

significant damage is taken to include permanent offsets (residual drifts), cracking and spalling of concrete and reinforcement yielding [AASHTO 2015].

These performance objectives lead to deformation limits for the ductile elements based on strains in the concrete and reinforcement, specifically the crushing strain of the confined concrete core and the fracture strain of the mild steel reinforcement.

8.1.2 Design for Service Loads

In order to determine preliminary member sizes and strengths, the ductile elements of the bridge are first designed according to *AASHTO LRFD Bridge Design Specifications* (2016) under the combined action of self-weight, live and time-dependent loads, including thermal effects.

For bridges with three or more spans, where the bridge girders are integrally connected to the cap beams, forces arising from a uniform temperature distribution over the depth of the superstructure can potentially govern the required moment strength of the columns. Thermal expansion imposes longitudinal displacements rather than forces on the columns. If the induced moment is too large, and the column is strengthened by increasing the diameter or the reinforcement ratio, the column stiffness and the induced moments both rise, assuming that the deck is much stiffer and stronger than the columns. This is particularly problematic for prestressed columns with unbonded strands which must meet more stringent service level requirements.

8.1.3 Displacement Demand Analysis

The displacement demand on the structure is determined using response spectrum analysis. For structures in SDC B and C or for single span bridges, single mode analyses are sufficient. However, for SDC D, multi-modal analysis is required.

Effective section properties, assuming that the response of the bridge is governed by the cracked member properties, are determined via empirical relationships or through moment-curvature analyses of the ductile members. The effective stiffnesses of each of the ductile members are computed as the secant stiffness of the section's moment-curvature response at first bar yield, as shown in Figure 8.2.

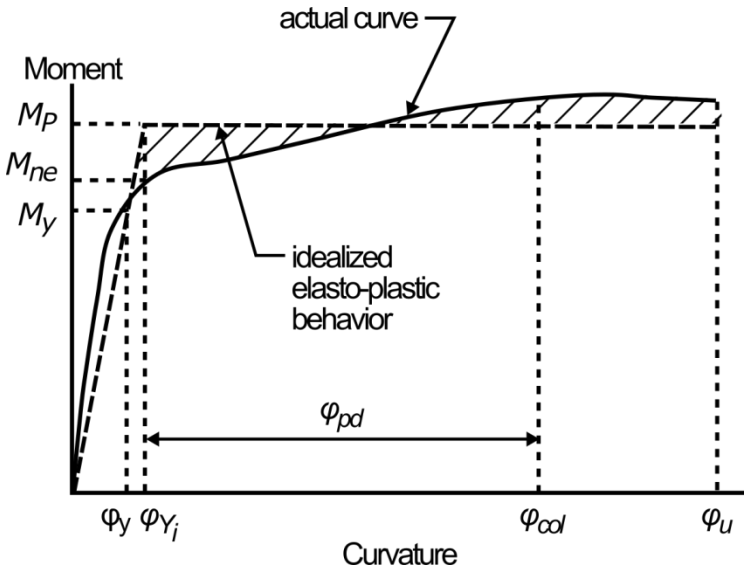

Figure 8.2 Idealized moment-curvature response (adapted from AASHTO 2015)

Response spectrum analyses are conducted in two orthogonal directions, typically the longitudinal and transverse directions of the bridge. The resulting displacement demands are combined using a 100%-30% rule to determine the overall displacement demand on each of the ductile elements.

8.1.4 Displacement Capacity Analysis

The capacity of the structure must be determined considering the inelastic action of the ductile elements. For SDC B and C, this may be done using empirical equations, which determine the approximate ultimate curvature of the ductile element. For SDC D, this is done through incremental static, "push-over", analysis or time-history analysis. The plastic capacity of

each of the ductile members is found through moment-curvature analysis by balancing the areas above and below the computed and idealized elasto-plastic curves, as shown in Figure 8.2. The ultimate curvature in Figure 8.2 is computed as the curvature to first cause reinforcement fracture or crushing of the confined concrete core. In lieu of specific data, AASHTO provides strain limits for reinforcement fracture of 0.12 for No. 10 bars and smaller and 0.09 for No. 11 bars and larger. The ultimate strain limit for the confined concrete core is determined using Mander's confinement model [Mander et al. 1988] based on the provided transverse confinement reinforcement. Typical values range from 0.008 to 0.025.

Moment-curvature analyses are conducted for a number of axial loads, until an interaction surface is established, including both the plastic moment as well as the plastic rotation capacity. The plastic rotation capacity at each axial load is computed by multiplying the plastic curvature capacity by an estimated plastic hinge length.

Each bent is analyzed individually in the transverse direction, and frames or larger portions of the bridge are analyzed together in the longitudinal direction. Ductile elements in the model are assigned non-linear hinge properties at their assumed plastic hinge locations. Each analysis is terminated when the first ductile element reaches its plastic rotation capacity; the displacement at which this occurs is described as the displacement capacity of the bridge subassembly.

The static push-over curves can then be used to determine member forces at the design level drift, to check for shear capacity and axial load limits. The requirements are intended to ensure that the response is small enough that P-Delta effects can be ignored. This is achieved by ensuring that the displacement induced moments arising from the axial load are less than 25% of the columns plastic moment capacity.

8.1.5 Adjust Bridge Characteristics

If the computed displacement capacity is smaller than the demand, the design of the bridge must be modified. The *AASHTO Guide Specifications for LRFD Seismic Bridge Design* (2015) suggest adding longitudinal reinforcement, reducing the dead load acting on the column, or adjusting the dynamic properties of the bridge. Suggestions for adjusting the dynamic properties of the bridge include modifying foundation/abutment flexibility, column heights or locations, and joint layout [AASHTO 2015].

8.2 Modifications for Pre-tensioned rocking columns

The preceding methodology was devised considering typical design procedures for reinforced concrete and steel bridge structures, with the intention of satisfying life-safety objectives during the design level event. In this procedure the size, strength and ductility of the columns are determined under non-seismic loads, and the seismic performance of the resulting design is checked in terms of displacements under seismic forces. For the seismic design of pre-tensioned rocking columns, the following modifications to this procedure are proposed (also shown in Figure 8.3);

1) The performance objectives should be revised to include higher performance levels and their corresponding deformations limits;

2) In addition to service level requirements, the size of the columns and the proportioning of column reinforcement should be constrained by seismic performance criteria;

3) The effective stiffness and plastic rotation capacity of the columns should be determined through moment-rotation analysis, since strain compatibility does not hold; and

4) The specific detailing requirements for the column's confined ends should be developed.

These four modifications are highlighted in Figure 8.3 and outlined in subsequent sections.

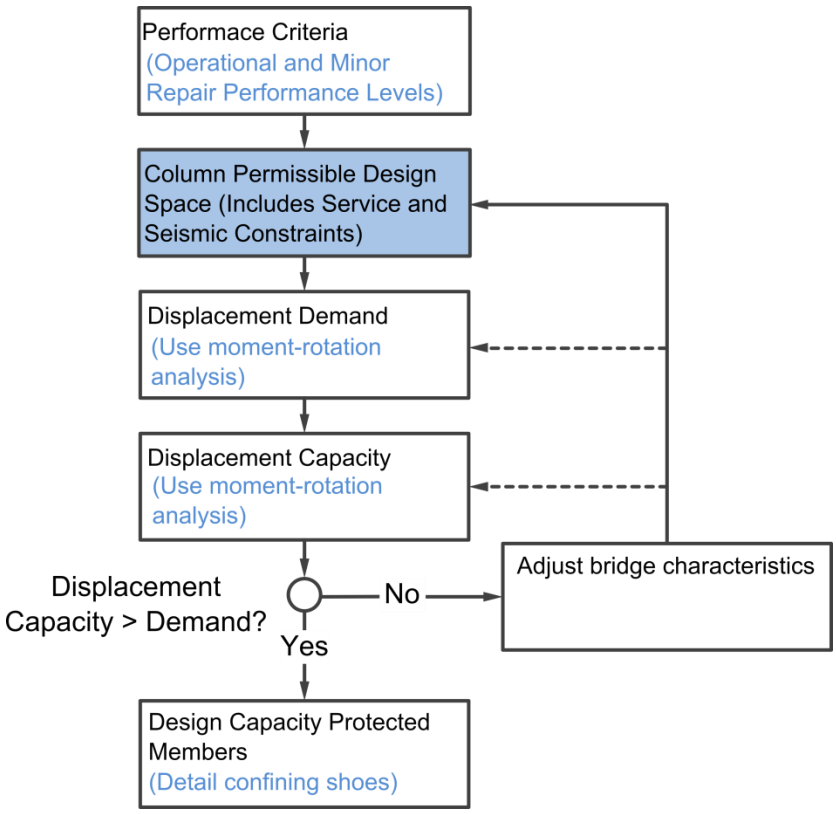

Figure 8.3 Modified design procedure (modifications highlighted in blue)

8.3 Performance Objectives

The performance objectives outlined in the *AASHTO Guide Specifications for LRFD Seismic Bridge Design* (2015) are meant to ensure life safety, while permitting significant damage to the column concrete, residual deformations, and disruptions to service after an earthquake. This level of performance falls well below the philosophy of the precast, pre-tensioned, rocking system concept, which aims to eliminate residual drifts and concrete damage in order to minimize disruptions to service after a seismic event. Both the performance objectives of the bridge and the plastic rotation capacity of the columns must be re-envisioned.

For reinforced concrete columns, failure of the column is typically defined by crushing of the concrete core or fracture of longitudinal reinforcement. Reinforcing bar fracture leads to

rapid loss of strength, and is usually preceded by significant spalling of the cover concrete, transverse reinforcing fracture and longitudinal bar buckling.

In prestressed rocking columns, strain (and therefore deformation) limits relating to crushing of the concrete core are unlikely to limit the ultimate displacement capacity of the columns. The high degree of both confinement and localization of concrete strain in the steel shoe result in very little damage to the column concrete, despite the high contact forces present at the base of the column. This has been supported by experimental observations in both the subassembly and shaking table tests presented in previous chapters.

In prestressed, rocking columns the mild steel reinforcement acts primarily to dissipate energy through hysteresis. If the columns are effectively proportioned to ensure good re-centering performance, fracture of the mild steel reinforcing bars has been found to lead to very little strength degradation; in the subassembly experiments, the full strength of the strands had not been mobilized at the time of bar fracture. However, fracture of longitudinal reinforcing decreases the rotational stiffness of the rocking joint and changes the dynamic properties of the bridge. It might also lead to disruptions in service and partial or full replacement of the bridge after the earthquake. Because of this, bar fracture must be prevented during the design level hazard, just as it is in conventional reinforced concrete systems.

Proposed performance levels, aligned with current performance based methodologies, are presented in Figure 8.4, along with the strain limits that delineate each performance level. Performance levels for conventional cast-in-place system, based on the work of Marsh and Stringer (2013), are also shown for reference.

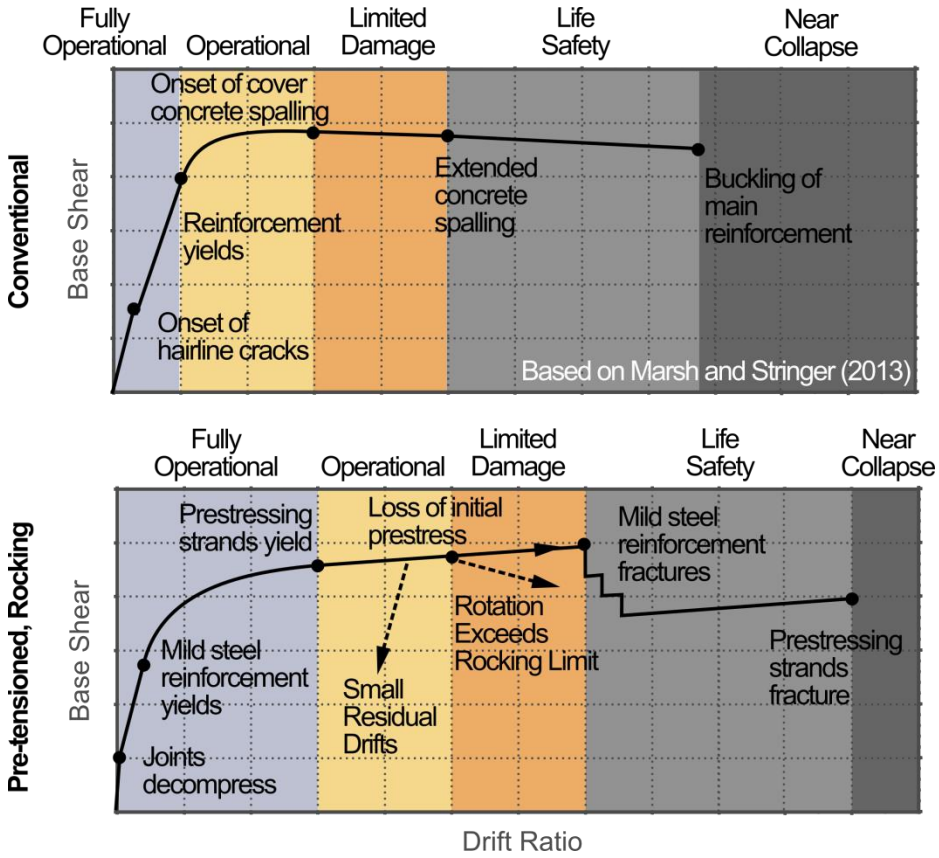

Figure 8.4 Proposed performance categories and corresponding strain limits.

If the pre-tensioned columns are designed to meet the operational requirement, it is expected that during the design level motion, both the strands and mild-steel reinforcement may yield, however neither will fracture and some prestress will remain in the columns to re-center the bridge. In this case, the deformation capacity of the column will be controlled by the fracture strain of the longitudinal reinforcement and the strain which corresponds to a loss of prestress in the strands. This limit state implies that the structural properties of the bridge will be impacted due to the earthquake, however, no repair will be necessary and the bridge will still be able to withstand subsequent earthquakes without a significant loss of performance.

Additional performance objectives are also possible. For structures with greater importance, it may be desirable to avoid strand yielding during the design level event. These

structures would be fully operational after the earthquake; the strength and capacity of the system would remain unchanged and no repair would be necessary. In this case, the deformation capacity of the column will be limited by the yield strain of the strand or the fracture of longitudinal reinforcement.

The strains in strands should be limited to one of the values in Equation 8.1, depending on the desired performance. For high importance structures, the strain in the strands should not exceed the essentially elastic limit during the design event to ensure immediate serviceability.

Strand yield: $$\varepsilon_p < \varepsilon_{EE} \quad [8.1a]$$

Loss of prestress $$\varepsilon_p < \varepsilon_{EE} + f_{pe}/E_p \quad [8.1b]$$

Strand fracture $$\varepsilon_p < \varepsilon_{pu} \quad [8.1c]$$

where ε_{EE}, is the essentially elastic strain limit (0.0086), f_{pe} the effective prestress in the strands, E_p the elastic modulus of the strands, and ε_{pu} the ultimate strain in the strands (0.03) [AASHTO 2015].

The strains in the mild steel reinforcement should be limited by the reduced ultimate strain, given in Table 8.4.2-1 in the *AASHTO Guide Specifications for LRFD Seismic Bridge Design* (2015).

Bar Fracture $$\varepsilon_s < {\varepsilon_{su}}^R \quad [8.2]$$

For high aspect ratio columns, or those with long debonded lengths of reinforcement, a third criterion may be applicable, shown schematically in Figure 8.5.

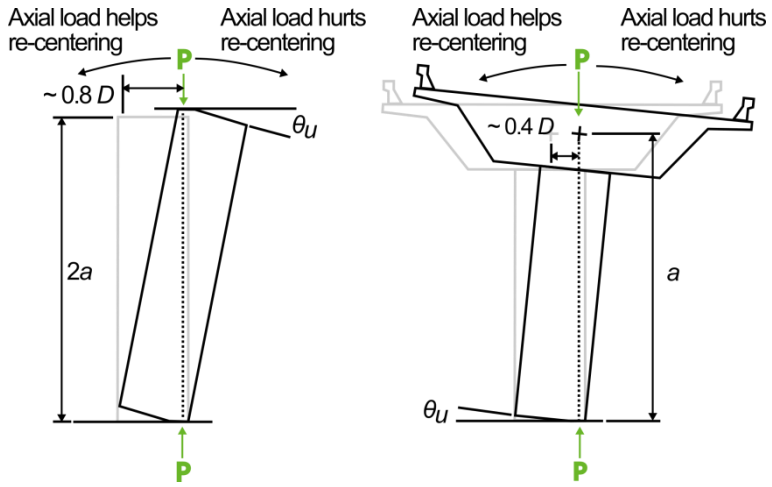

Figure 8.5 Rocking limit state

If the rotation of the bent is large enough, the axial force acting on the column may no longer help to re-center it. Since this scenario might lead to excessive residual deformations, this limit should be included in addition to AASHTO's P-Delta provisions. The rotation to cause this "rocking limit" can be approximated using Equation 8.3, assuming that the concrete compressive force acts a distance 0.1D from the face of the column.

$$\theta_r = \frac{0.4D}{a} \qquad [8.3]$$

This limit state does not imply a lack of stability, but should be avoided if possible. If the strands have not fractured at this level of rotation, and they are sufficiently stressed, the re-centering moment from the prestressing strands will be larger than the destabilizing moment caused by the axial loads and the column will still re-center if transverse loads are removed.

8.4 Column Permissible Design Space

In order to estimate the column diameter and to proportion the column reinforcement, both service and seismic design criteria should be considered. These criteria lead to a feasible design space for the column; the procedure for developing this design space is outlined in the following sections.

8.4.1 Service Criteria

In addition to the typical service level requirements for reinforced concrete columns, including maximum and minimum reinforcing ratios, AASTHO imposes an additional constraint on prestressed columns with unbonded prestressing strands, namely:

1) The effective prestressing forces must be sufficient to prevent decompression of the columns under Service IV loads,

This imposed criterion will likely produce designs that automatically satisfy other service level load cases.

8.4.2 Seismic Criteria

For the pre-tensioned rocking substructure system, the proportioning of the column reinforcement should also be constrained by two specific seismic performance criteria. These criteria are meant to meet specific seismic performance goals, and constrain the feasible design space to a region where the desired seismic performance is achieved. These additional constraints are meant to ensure that

2) The columns are sufficiently prestressed to re-center after an earthquake and

3) The columns' hysteretic energy dissipation is sufficient to prevent excessive displacements during an earthquake

8.4.3 Design variables (DV's)

The design variables for the initial design of a pre-tensioned rocking column are:

- D, the diameter of the column;
- ρ_s, the mild steel reinforcing ratio;
- ρ_p, the prestressing strand reinforcing ratio; and

- f_{pe}, the effective stress of the prestressing strands.

These properties should be determined based on the three objectives outlined in the previous section.

In addition to the three performance criteria, Section 8.8 the *AASHTO Guide Specifications for LRFD Seismic Bridge Design (2015)*, defines prescriptive maximum and minimum reinforcing ratios. These provisions are intended for conventional reinforced concrete systems, and are meant to control time-dependent cracking, prevent congestion and ensure ductile performance [AASHTO 2015]. Pre-tensioning the columns and allowing them to rock eliminates many of these concerns. However, these limits are valuable from a constructability standpoint regardless of system type, and are included in the proposed initial design process. To meet these requirements, the equivalent reinforcing ratio defined in Equation 8.4, should be used.

$$\rho_{equiv} = \rho_s + \rho_p f_{py}/f_{sy} = A_s/A_g + f_{py}/f_{sy}\left(A_p/A_g\right) \quad [8.4]$$

where ρ_{equiv} is the equivalent reinforcing ratio, $A_g$the gross area of the columns, $A_s$the total area of deformed bar reinforcement, f_{py} the yield stress of the prestressing strands, f_{sy} the yield stress of the deformed bar reinforcement, $A_p$the total area of prestressing strand, $\rho_s = A_s/A_g$ the mild steel reinforcing ratio, and $\rho_p = A_p/A_g$ the prestressing strand reinforcing ratio.

The proposed procedure for developing the feasible column design space is shown schematically in Figure 8.6. This process consists of selecting values for the column diameter and effective strand stress in order to develop a two-dimensional design space consisting of the mild steel and prestressing strand reinforcing ratios. If the assumptions for the column diameter and effective stress lead to an unsatisfactory design space, the process is restarted with new values for these parameters.

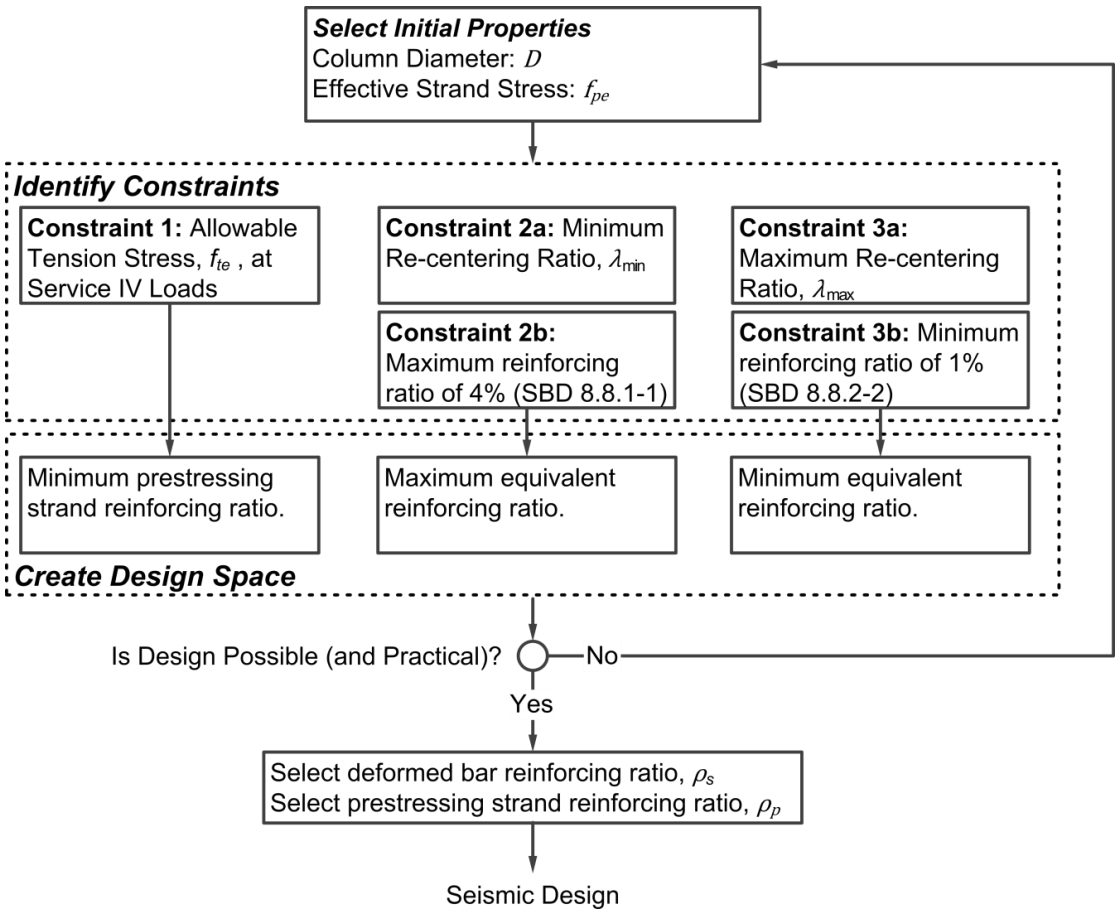

Figure 8.6 Service Load design flowchart

If the assumptions for the column diameter and effective stress lead to a satisfactory design space (i.e. non-zero), the initial design can be optimized for minimum reinforcement, maximum damping, maximum re-centering, etc.

8.4.4 Select Initial Properties

The column diameter should be estimated based on the service axial load, although additional axial stresses will be present in the columns due to prestressing. Because the diameter of the columns determines the moment in the column due to uniform temperature expansion of the deck, selecting a smaller column size may produce a more efficient design in terms of prestressing strand and deformed bar reinforcement.

The effective stress in the prestressing strands, f_{pe}, should be estimated at the start of the design process. This value has implications for the column's seismic performance, and should be kept as low as possible, given the number of strands required to meet service load requirements. If this parameter is set too low, the number of strands needed to meet service level constraints will be excessive. Therefore a balance must be struck between seismic performance and constructability.

8.4.5 Identify Constraints

Three sets of constraints must be determined at the start of the procedure. These constraints should be chosen to meet the three performance goals;

1) Allowable tension stress at service loads, $f_{te} = 0$;

2a) Minimum re-centering ratio, λ_{min} ;

2b) Maximum equivalent reinforcing ratio $\rho_{equiv} \leq 4\%$;

3a) Maximum re-centering ratio, λ_{max} ; and

3b) Minimum equivalent reinforcing ratio $\rho_{equiv} \geq 1\%$.

These constraints are described in the following paragraphs.

Allowable Tension Stress. The allowable tension stress at service loads is prescribed by Article 5.9.4.2.2 the *AASHTO LRFD Bridge Design Specifications* (2016). For components with unbonded prestressing tendons, no tensile stress in the concrete at service loads is permitted. This is independent of corrosion conditions. The load combinations in Article 3.4.1 specify that Service IV loads, "relating only to tension in prestressed concrete columns with the objective of crack control" [AASHTO 2016] should be used to check this criterion.

Maximum and Minimum Re-centering Ratio. The re-centering ratio, λ, can be described as the ratio of moments helping re-center the column to those moments preventing re-centering.

In an idealized system (See Figure 3.5) these moments are all caused by forces whose resultants act at the centroid of the column section. Its definition is reprinted here as Equation 8.5.

$$\lambda = \left(A_p f_{pe} + P\right) / A_s f_{sy}, \qquad [8.5]$$

where A_s is the gross area of the reinforcing steel, A_p is the gross area of the prestressing steel, f_{sy} is the yield stress of the mild steel reinforcing, f_{pe} is the initial stress of the strand, and P is the vertical load acting on the column.

Figure 8.7 shows, schematically, the force-displacement relationships for columns with different values of the re-centering ratio. The re-centering ratio determines both the re-centering performance of the column and also the amount of hysteretic damping provided by it.

For the design of pre-tensioned rocking columns, suitable minimum and maximum limits for this parameter must be selected to ensure both adequate re-centering and hysteretic energy dissipation during an earthquake.

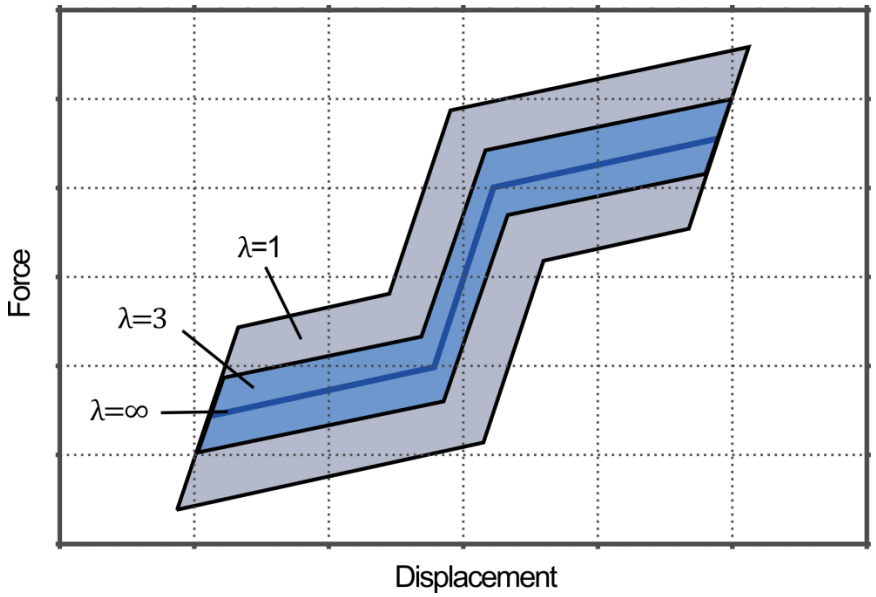

Figure 8.7 Schematic force-displacement behaviors of columns with different re-centering ratios.

The minimum re-centering ratio, λ_{min}, should be determined based on the desired re-centering performance and potential design drift level. Values of $\lambda_{min} < 1$, should not be permitted. Cohagen et al. (2008) tested two post-tensioned subassemblies with re-centering ratios of 1.2 and 1.6. At 2% drift, these subassemblies had essentially the same re-centering performance as the subassembly tested by Schaefer et al. (2014) with a re-centering ratio of 3.4. However, at a 6% drift ratio, the re-centering performance of the column with $\lambda = 3.4$ was unchanged, while the columns with $\lambda = 1.2$ and 1.6 were significantly worse.

The maximum re-centering ratio, λ_{max}, determines the minimum level of hysteretic energy dissipation that should be provided by the system. Prestressed rocking systems by definition dissipate less energy than conventional reinforced concrete ones, and the amount of hysteretic energy dissipation in the system has implications for the maximum drift ratio during an earthquake. The maximum re-centering ratio should be chosen to prevent excessive deformations during the design level motion.

Figure 8.8 schematically shows these two limits on the re-centering ratio and their implications on column performance. In the figure, each value of the re-centering ratio determines both a maximum and residual displacement during an earthquake. This relationship is probabilistic and the solid and dashed lines are meant to represent the median and confidence interval, respectively.

The choice of the limits on the re-entering ratio value must be carefully selected with desired seismic performance in mind. Choosing the right limits for λ ensures that the system will have adequate damping to prevent excessive deformations and also sufficient re-centering to prevent large residual deformations. This further emphasizes the need to design for seismic conditions first, then to check service conditions.

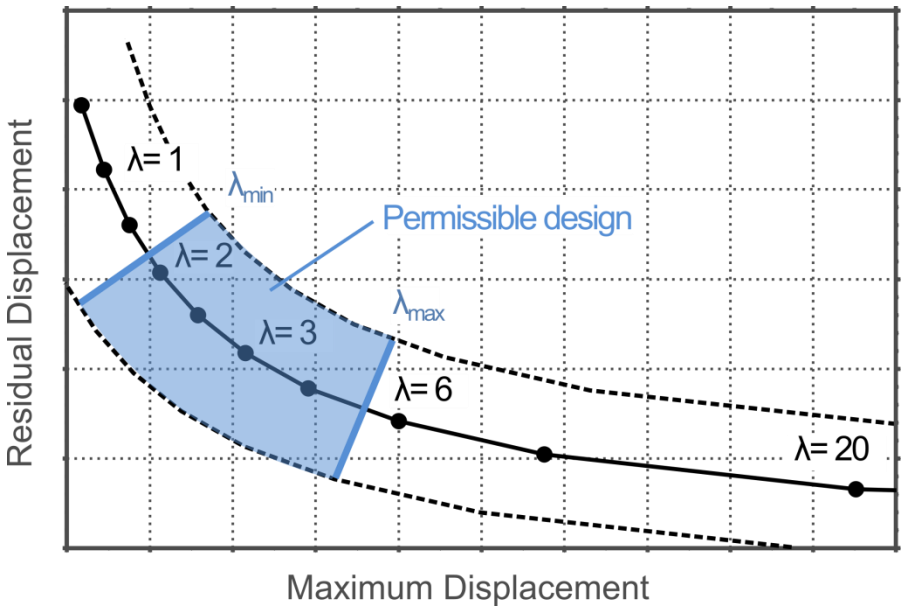

Figure 8.8 Relationship between re-centering ratio and the maximum and residual displacement.

Research on precast systems has resulted in very few recommendations for maximum values for λ. Typically, minimum values of the re-centering ratio are given, without much consideration for what the maximum value of λ should be. Ozden and Ertas (2007) suggested a reasonable upper bound of $\lambda \approx 5$, although values closer to 10 are likely also acceptable. Typically design recommendations have instead proposed minimizing λ, while providing adequate re-centering performance [e.g Stanton and Nakaki 2002]. In this design process, no maximum λ is needed, since the optimal design will always contain the minimum λ value. Stanton and Nakkaki (2002) proposed a minimum re-centering ratio of 1.0, although more recent research has shown this value may be too small.

8.4.6 Define Design Space

1) Minimum Prestressing Strand Reinforcing Ratio

For a concrete member with unbonded prestressed tendons, stress limits must be checked under Service IV loads with the maximum tensile stress, f_{te}, equal to zero. The maximum

compressive stress limit, $0.6f'_c$, is unlikely to control, unless the axial load ratio is greater than 30%.

The minimum prestressing strand reinforcing ratio ($\rho_p = A_p/A_g$), given the effective stress in the prestressing strands to prevent decompression at service loads can be determined by Equation 8.6.

$$\rho_p \, f_{pe} \geq \, M_s \, /S \, - P_s/A \qquad [8.6]$$

where f_{pe} is the effective stress in the strands, M_s the Service IV moment, P_s the Service IV axial load, S the section modulus for the column, and A the gross area of the column.

At this point the effective stress of the strands can be adjusted to reach a particular reinforcing ratio based on constructability or other considerations.

2) Maximum Deformed Bar Reinforcing Ratio

In order to ensure re-centering performance, the re-centering ratio should be limited to a minimum value of 1.0. Given the minimum re-centering ratio, the maximum deformed bar reinforcing ratio ($\rho_s = A_s/A_g$), given the prestressing strand reinforcing ratio can be determined using Equation 8.7.

$$\rho_s \, \lambda_{min} f_{sy} \leq \rho_p f_{pe} + P_s/A \qquad [8.7]$$

In addition, *AASHTO Guide Specifications for LRFD Seismic Bridge Design* specifies a maximum reinforcing ratio, interpreted here to mean the equivalent reinforcing ratio.

$$\rho_{equiv} \leq 4\% \qquad [8.8]$$

This requirement is partially meant to prevent congestion in the joint region of the cap beam. This is true of both cast-in-place and pre-tensioned columns. This requirement leads to the additional constraint, given the number of prestressing strands given in Equation 8.9.

$$\rho_s \leq 0.04 - f_{py}/f_{sy} \; \rho_p \qquad [8.9]$$

This requirement should be met at the connection interface. Because the discontinuous bars in the pre-tensioned system stop short of the precast cap, where congestion issues often arise, they should not be included in this calculation.

3) Minimum Deformed Bar Reinforcing Ratio

The maximum re-centering ratio is meant to ensure adequate damping characteristics of the column The resulting minimum deformed bar reinforcing ratio is given by Equation 8.10.

$$\rho_s \lambda_{max} f_{sy} \leq \rho_p f_{pe} + P_s/A \quad [8.10]$$

The *AASHTO Guide Specifications for LRFD Seismic Bridge Design* (2015) prescribes an additional constraint for bridges in Seismic Design Category D. It specifies a minimum reinforcing ratio, interpreted here as the effective reinforcing ratio.

$$\rho_{equiv} \geq 1\% \quad [8.11]$$

which leads to the constraint given in Equation 8.12.

$$\rho_s \geq 0.01 - f_{py}/f_{sy}\ \rho_p \quad [8.12]$$

These constraints define a bounded design space, like the one shown in Figure 8.9.

The designer can then choose to optimize particular characteristics of the system by choosing a design point lying on one of the constraints. For example, if the designer wanted to maximize re-centering, he or she would select a point lying on the maximum re-centering ratio line.

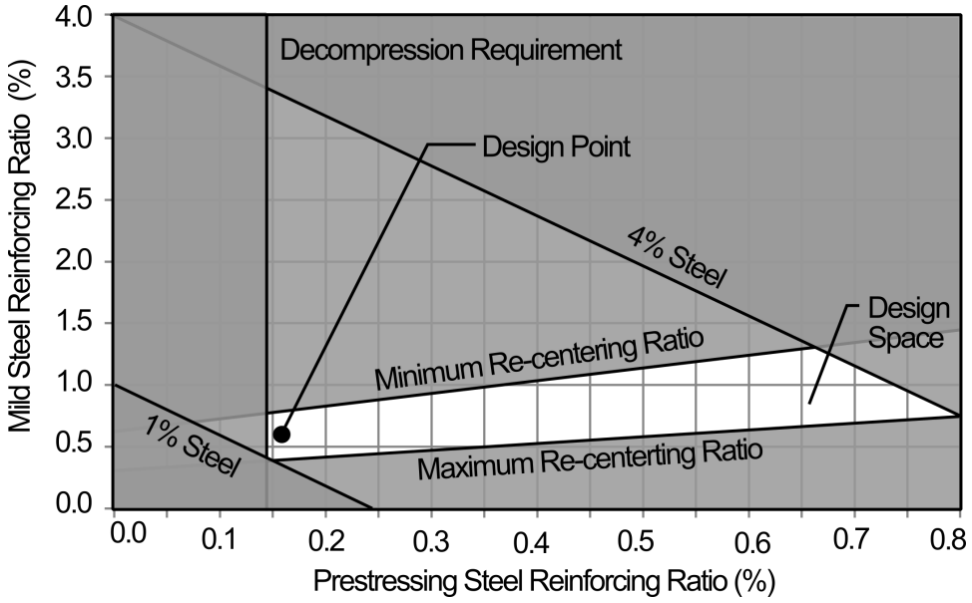

Figure 8.9 Initial design space based on service and seismic criteria

8.5 Moment Rotation Analysis

Moment rotation analysis should be used to determine the effective elastic stiffness of the columns for response spectrum analysis (demand) and the inelastic hinge properties of the columns for use in pushover analysis (capacity). Unlike conventional reinforced concrete which deforms through distributed plasticity in plastic hinge regions, the pre-tensioned, rocking columns deform primarily through concentrated rotations at the ends of the columns. Thus, moment-rotation analysis is warranted, rather than the more typical moment-curvature analysis. This can be accomplished using commercial moment curvature software or subroutines; however the material properties must be modified.

The effective rotational stiffness of the rocking section should be determined using Equation 8.13, and the plastic moment capacity using the AASHTO (or Caltrans) equal area method as shown in Figure 8.10.

$$k_r = \frac{M_y}{\theta_y} \qquad [8.13]$$

where M_y and θ_y are defined in Figure 8.10.

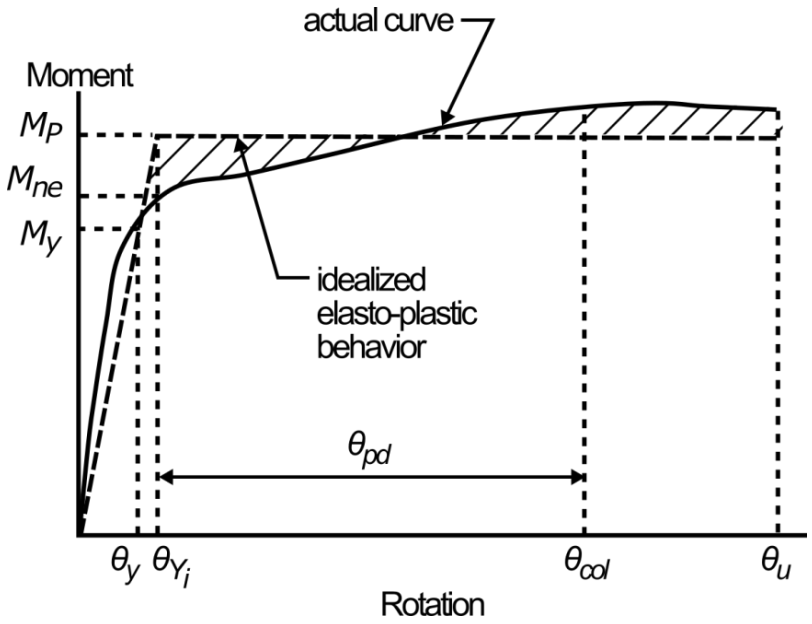

Figure 8.10 Moment rotation curve

The major departure from traditional moment-curvature analyses is that the material models must be specified in stress-displacement space, to account for the strain incompatibilities that exist at the rocking interface. The following sections describe how this can be implemented in current software packages or subroutines.

8.5.1 Mild Steel Reinforcement

At the connection interface, the mild steel reinforcement will undergo concentrated deformations due to the rigid body rotation of the column. These concentrated deformations are spread over an effective unbonded length, which should account for strain penetration into the surrounding concrete. Strain penetration will act to reduce the peak strain in the reinforcement, and thus can be considered to increase the effective unbonded length.

For the pre-tensioned columns tested by Schaefer et al. (2014a), strains in the mild steel reinforcing were reasonably well estimated by assuming an additional debonded length of $2.0d_b$

(per end). For the pre-tensioned bridge discussed in Chapters 5, 6 and 7, the additional debonded length was found to nearly $4.0d_b$ (per end).

It should be noted that the exact value in practice will depend on bar size, surface condition, strength of the surrounding concrete or grout and other factors. For design, a value of $4.0d_b$ (per end) is a reasonable estimate in lieu of more sophisticated analysis, and in light of the limited data available.

8.5.2 Unbonded Length of the Mild Steel Reinforcement

The effective unbonded length of the mild steel reinforcement should be computed according to Equation 8.14:

$$L_{s,unb} = L_s + \alpha d_b \qquad [8.14]$$

where $L_{s,unb}$ is the effective unbonded length of the reinforcement, L_s is the intentionally debonded length, α is the strain penetration correction factor ($\alpha \approx 8$) and d_b is the bar diameter

8.5.3 Reinforcing Steel Model

The stress-deformation relationship for the mild steel reinforcement is shown in Figure 8.11. The strain values provided in *AASHTO Guide Specifications for LRFD Seismic Bridge Design* (2015) Table 8.4.2-1 should be multiplied by the effective unbonded length of the mild steel reinforcement. The modulus of elasticity, Es = 29,000 ksi, should be divided by the unbonded length of the mild steel reinforcement.

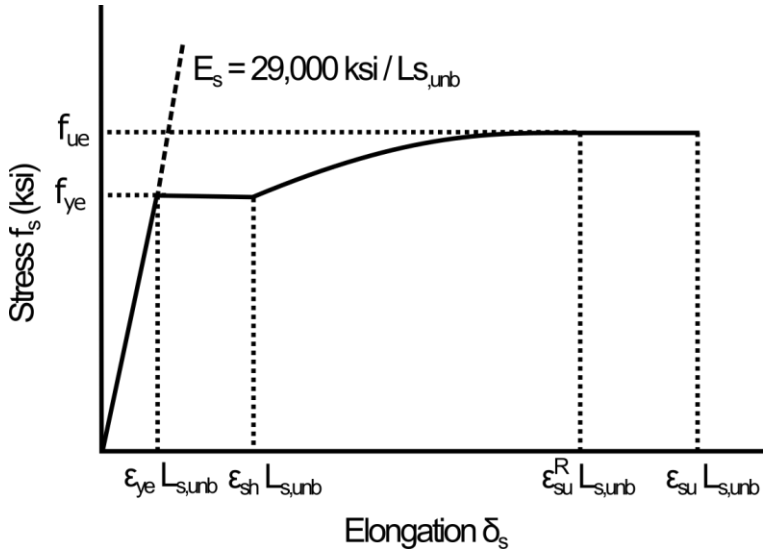

Figure 8.11 Stress-deformation relationship for the mild steel bars

8.5.4 Prestressing Strands

The prestressing strands are deliberately debonded for the clear height of the column. They will elongate due to both concentrated rotations at the column ends, as well as distributed curvature over the height of the column.

While column bending will contribute to the strain increments in the strands, since the strands are near the center of the section and the curvatures in the column are small, these contributions are only noticeable at very small drift levels. At high drift ratios, rotations at the ends of the column will likely account for over 90% of the columns transverse deformation and the effect of column bending is negligible. It is recommended to ignore the effects of column curvature except in the case of very slender columns, where bending deformations may be significant.

For moment-rotation analysis, it is sufficient to model the strands as a single fiber or element at the centroid of the strand group with the total area of the prestressing strands. If modeling a multi-column bent or a single column bent with a torsionally rigid superstructure,

where the columns are meant to rock at both the top of the foundation and underside of the cap beam, the change in strains in the strands will be uniform regardless of the strands' locations within the section. For columns that are meant to rock only at the top of the foundation, the change in strains in the strands will differ across the cross section, however the average strain at the centroid of the strand group will still be a reasonable approximation to the correct overall change in prestressing force.

When determining the rotation capacity of columns intended to rock at only one interface (e.g. cantilever columns), it is important to note that the strands furthest from the compressive face of the column will yield earlier, and the rotation limits computed based on the strands should be adjusted accordingly.

8.5.5 Unbonded Length of the Prestressing Strands

The effective unbonded length of the strands should be computed according to Equation 8.15.

$$L_{p,unb} = L_p + L_{fb} \quad [8.15]$$

Where $L_{p,unb}$ is the effective unbonded length of the pre-stressing strands, $L_p$the intentionally debonded length, and L_{fb} the flexural bond length required to reach the ultimate stress in the strands, determined by Article 5.11.4.2 of *AASHTO LRFD Bridge Design Specifications* (2016) by subtracting the transfer length from the development length of the strand at the ultimate stress or other methods [e.g. Cousins et al. 1990]. This length corresponds to the deliberately debonded length of the strands plus one-half of one flexural bond length on either end of the debonded region. The factor of one half reflects the assumption that the bond stress is constant and the strand stress is linearly distributed in the regions adjacent to the ends of the deliberately unbonded length.

8.5.6 Prestressing Strand Model

Figure 8.12 shows the stress-deformation relationship for the strand. The strain values provided in *AASHTO Guide Specifications for LRFD Seismic Bridge Design (2015)* Article 8.4.3 should be multiplied by the effective unbonded length of the prestressing strands. The modulus of elasticity should be divided by the effective unbonded length of the prestressing strands.

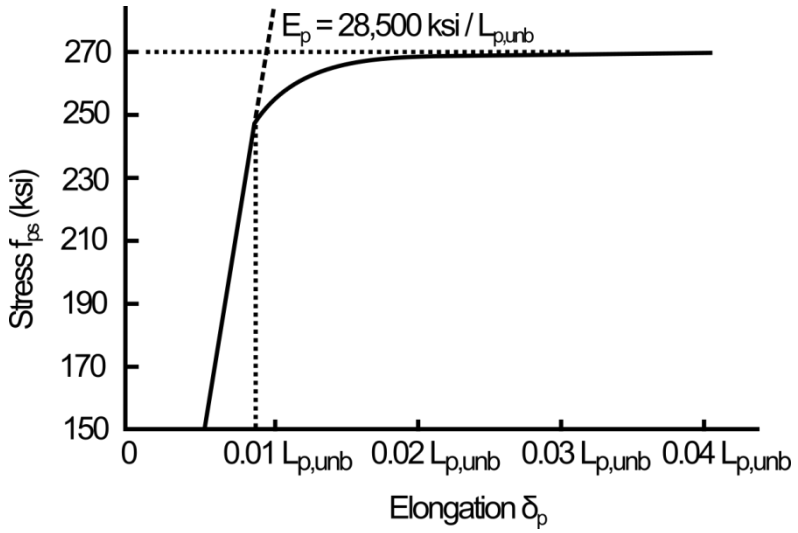

Figure 8.12 Stress-deformation relationship for the strand

8.5.7 Compressive Depth of the Concrete

As the column rocks, the concrete deforms in the compressed region. The deformation, with units of length, is defined by the rotation multiplied by the lever arm, and the corresponding strain is obtained by dividing the deformation by an effective compressive depth. However, that compressive depth cannot be derived simply from the principles of mechanics. Based on previous work [e.g. Stanton and Nakaki 2002, Restrepo and Rahman 2007, Tobolski 2010], it is assumed that there is approximately uniform strain vertically into the column a distance equal to the neutral axis depth, as shown in Figure 8.13.

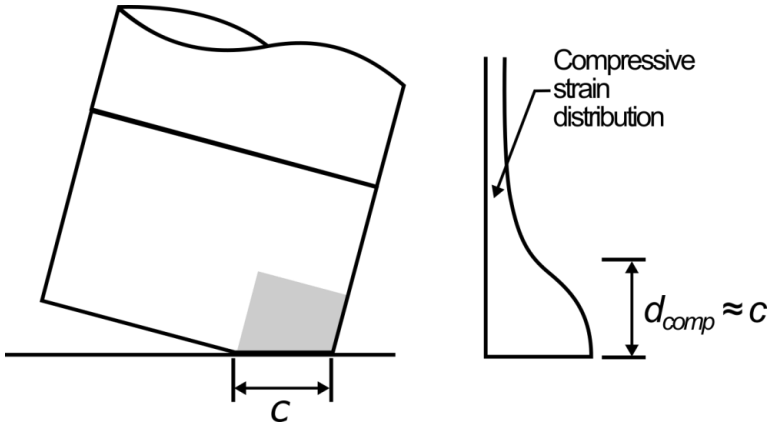

Figure 8.13 Concrete compressive depth (adapted from Tobolski 2010)

Since this compressive depth changes as function of rotation, this is likely not implementable in most commercial moment curvature software packages. If this is so, the compressive depth can be assumed as the neutral axis depth at the first yield in the mild-steel reinforcing. This will ensure that the effective rotational stiffness of the section will be correctly identified, and will lead to only a small reduction in plastic moment capacity for the inelastic pushover analysis.

The neutral axis depth at first yield in the reinforcing must be estimated at the start of the analysis. In lieu of more sophisticated methods a good initial estimate is near 25% of the column diameter based on limited experimental evidence. Once the analysis is completed, a new neutral axis depth reflecting the results of the previous analysis should be used, until the proper depth is found. This process usually converges to within 10% of the assumed value rapidly.

8.5.8 Concrete Model

The *AASHTO Guide Specifications for LRFD Seismic Bridge Design* (2015) Article 8.4.4 specifies Mander's stress-strain model for confined concrete (Mander et. al 1988), shown in Figure 8.14. This model was originally developed for concrete confined with hoops or spirals and is included in many commercial moment curvature programs or subroutines. Often the

parameters for the confined model are found automatically based on the section geometry, bar configuration, size and spacing. For concrete confined by a steel tube, slight modifications to this model are needed:

The confinement effectiveness coefficient should be taken as unity (i.e. the confinement is perfectly effective):

$$k_e = \frac{A_e}{A_{cc}} = \frac{A_g}{A_g} = 1 \qquad [8.16]$$

Where k_e is the confinement effectiveness coefficient, A_e the area of effectively confined concrete core, A_{cc} the area of confined concrete, and A_g the gross area of the column.

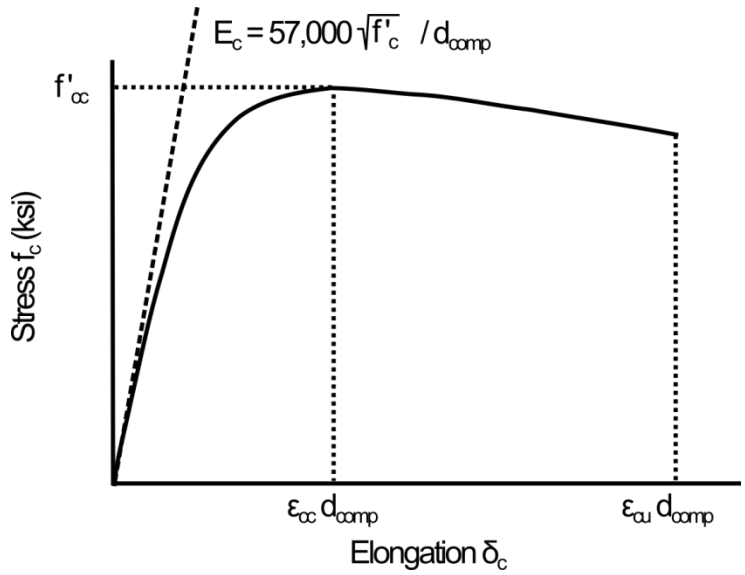

Figure 8.14. Stress-deformation relationship for confined concrete

The (effective) lateral confining pressure, found by considering equilibrium of the half body confined by the tube, is given by:

$$f_l' = k_e f_l = \frac{2 f_{yh} t}{D} \qquad [8.17]$$

Where f_l' is the effective lateral confining stress, f_l the lateral confining pressure on concrete, f_{yh} the yield stress of the confining tube, t the confining tube thickness, and D the diameter of the column.

The lateral confining pressure determines the confined concrete strength. However, it should be noted that the lateral confining stress, and hence actual confined strength of the concrete, in the highly stressed toe of the confining shoe is likely much higher due to the highly localized nature of the strains in that region and the presence of the annular end plate and confining tube. Equation 8.17 accounts only for the radial stress provided by the tube. The base plate will also provide radial confinement to the concrete close to it.

The ultimate deformation of the concrete model should be selected so that concrete failure is avoided prior to the fracture of the mild steel reinforcement.

8.5.9 Effective Stiffness for ESA/EDA Analysis

The rotational stiffness, k_r, obtained via moment rotation analysis must be combined with the gross moment of inertia of the column to get the effective moment of inertia, converting the rocking column into an equivalent elastic one as shown in Figure 8.15, for use in the multimodal analysis.

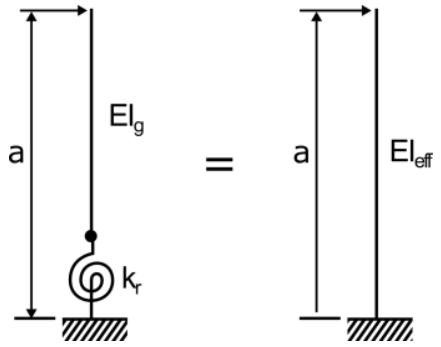

Figure 8.15 Equivalent I_{eff} for a rocking column

For the two cantilever columns to displace equally under a given lateral load at the top, the ratio of the effective to the gross moment of inertia is given by:

$$\frac{I_{eff}}{I_g} = \frac{1}{1+(3\,E_c\,I_g)/(a\,k_r)} \qquad [8.18]$$

where I_{eff} is the effective moment of inertia of the column section, I_g the gross moment of inertia of the column section, E_c the elastic modulus of the column concrete, a the cantilever length (See Figure 8.16), and k_r the rotation stiffness determined using moment-rotation analysis.

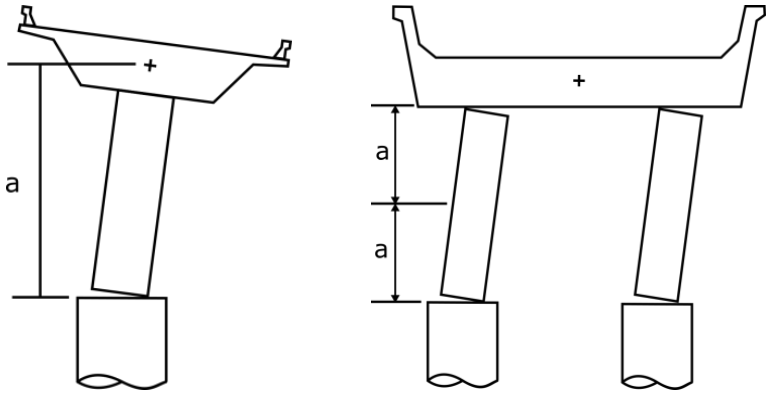

Figure 8.16 Definition of the cantilever length, a, for single and multicolumn bents

For the subassembly tests described in Chapter 4, this procedure has been found to produce good agreement (within 10%) with the measured values as shown in Table 8.1 and Figure 8.17.

Table 8.1 Effective stiffness of cantilever subassemblies

Specimen	Calculated			Measured	Calculated/Measured
	k_r (kip-in/rad)	E_cI_g (kip-in^2)	E_cI_{eff} (kip-in^2)	E_cI_{eff} (kip-in^2)	
PreT-SF-ROCK	1.27×10^6	44.1×10^6	16.2×10^6	15.2×10^6	1.065
PreT-CB-ROCK	0.922×10^6	38.7×10^6	12.5×10^6	12.2×10^6	1.024

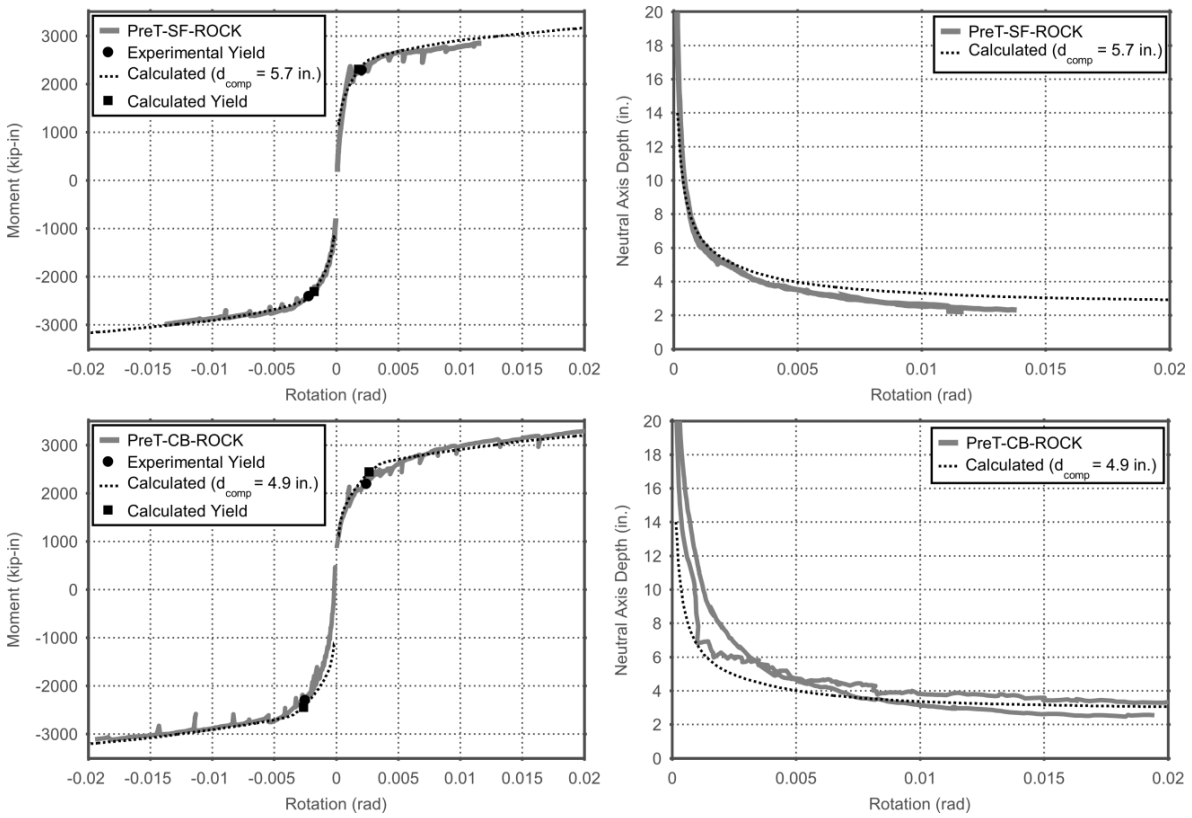

Figure 8.17 Moment-rotation relationship for cantilever subassemblies

8.6 Detailing

In order to ensure minimal damage to the column concrete under the design level hazard, specific detailing requirements are needed for the confining shoe at the ends of the columns. Utilizing the limited amount of test data, detailing recommendations for the precast, pre-tensioned rocking system are presented.

8.6.1 Confining Tube

Hewes and Priestley (2002) tested four rocking segmental columns with steel jackets around the first segment, which was one column diameter in height. The columns were tested twice under different levels of prestress. The extent of the jacket was "determined through moment curvature analysis of the non-jacketed section, to prevent concrete crushing directly

above the jacket" [Hewes and Priestley 2002]. Activation of the confining tube in hoop tension was found to extend approximately half of one column diameter up the height of the column as discussed in Chapter 3.

Mashal and Palermo (2014) independently tested a precast post-tensioned rocking system with end detailing similar to that proposed here. The steel tube used in this experiment extended one column diameter. The effectiveness of the tube was not directly reported, but from photographs, there appeared to be no damage to drift ratios of 2.2%, when the test was discontinued.

In the subassembly and shake table experiments, the confining tubes at the ends of the columns extended up the height of the column one-half column diameter. Given that the purpose of the tubes were for confinement of the highly stressed end region, and the rocking specimens tested by Hewes and Priestley (2002) showed that hoop strains largely dissipated by mid height of the first segment, this choice seemed sensible. This choice also aided in the construction of the scaled experiments, where the steel shoe constrained access to the reinforcement, including prestressing strands at the column end.

It is recommended that the extent of the confining tube into the clear column height should be greater than or equal to one half column diameter:

$$h_{tube} \geq D/2 \qquad [8.19]$$

The required diameter-to-thickness ratio (D/t) of the tube is a critical parameter when discussing the behavior of concrete filled steel tubes (CFSTs). The *AASHTO Guide Specifications for LRFD Seismic Bridge Design* (2015) recommendation for the D/t ratio for CFSTs columns is given in Equation 8.20. For typical line pipe, $f_{ty} \approx 44$ ksi , in which case this equation limits the D/t ratio to less than 100.

$$(D/t)_{CFST} \leq 0.15 \frac{E_t}{f_{ty}} \quad \text{(AASHTO 2015)} \qquad [8.20]$$

This criterion is meant to prevent, or delay, longitudinal buckling of the tube during an earthquake due to compressive stresses. In CFSTs, the tube serves as both the longitudinal and transverse reinforcement for the section, and the required thickness is meant to ensure adequate performance for the combined stress state that occurs in the plastic hinge region. In jacketed concrete columns, this provision is not suitable since the steel tubes are used primarily as transverse reinforcement for confinement, and are not subjected to large longitudinal stresses.

For jacketed, precast columns designed to rock, the jacket needs no axial strength or stiffness, so it is reasonable to assume that higher D/t ratios may be used. Tube bulging was observed in one of the four specimens tested by Hewes and Priestly (2002) at a drift ratio of roughly 3%. This specimen had an aspect ratio of approximately 6 and had a steel jacket with a D/t ratio of 218. The nominally identical column with a D/t ratio of 102 suffered no such bulging. In these specimens, no annular end plate was used and the tube did not bear directly on the foundation prior to tube bulging.

For the precast, pre-tensioned columns, the steel confining tube is welded to an annular end plate, which inevitably transfers some axial compression forces into the steel tube. In the shaking table tests of the precast, pre-tensioned, rocking column system, the confining tubes had a D/t ratio of 90 and suffered bulging at a drift ratio of approximately 6%. This bulging was attributed to the added compressive stresses in the tube caused by bearing of the annular end plate, and the dynamic amplification of forces caused by the impact between the end plate and the foundation or cap beam. In the subassembly tests of the pre-tensioned rocking columns, which had tubes with D/t of 80, no such bulging was observed and the tubes did not yield until

the column drift ratios exceeded 10%. Given that the steel tube is activated in both hoop tension and axial compression, it is recommended to limit the D/t ratio to 80.

$$(D/t)_{tube} \leq 80 \quad [8.21]$$

8.6.2 Annular End Plate

The design of the annular end plate for the subassembly and shake table specimens used the same proportioning strategy, and the specimens all exhibited the desired performance. The specific proportioning choices, given in Equation 8.22, were made based on engineering judgment. These values should be considered as a starting point rather than specific design recommendations.

$$t_{endPL} = 2t_{tube} \quad [8.22a]$$

$$d_{inner,endPL} = D/2 \quad [8.22b]$$

$$d_{hole,endPL} = 1.5d_b \quad [8.22c]$$

The thickness of the plate was twice the thickness of the confining tube. The inner diameter for the strands and hole diameter for the continuous mild steel reinforcement were designed to be as small as possible, while allowing adequate space between the edge of the hole and the reinforcement. In both the subassembly and shaking table test specimens, debonding sleeves for the continuous reinforcement passed through the holes in the annular end place and the diameter of the hole was largely determined by the diameter of the debonding material.

8.6.3 Discontinuous Reinforcement:

Discontinuous column reinforcement was included in both the subassembly and shake table experiments. This reinforcement was intended to arrest cracks at the end of the steel tube on the tension side of the column and to distribute, up the height of the column, the concentrated

forces on the compression side of the column at the rocking interface. In the subassembly tests, strains in the discontinuous bars within the steel shoe were less than the yield strain, even up to drift ratios exceeding 10%. Minor cracking did occur in the column directly above the above the steel shoe as observed in Schaefer et al. (2014) and Kennedy (2015), but these cracks closed upon unloading the column. The amount and extent of the discontinuous reinforcement warrants further refinement,

The total area of discontinuous reinforcement in both experiments was chosen to be greater than the continuous reinforcement; the discontinuous bars were selected to be equal in number, but one size larger than the continuous ones. The discontinuous bars extended the entire height of the column in the subassembly tests, but were terminated at a distance of 1.5 times the development length of the bar above the steel shoe in the shaking table tests. The discontinuous reinforcement was welded to the annular end plate in order to develop the full strength of the reinforcement in tension. In the shake table experiment, plug welds were used for constructability. Both specimens achieved the desired level of performance.

8.6.4 Spiral Reinforcement

Stone et al. (1995) and Priestley and MacRae (1996) showed that jointed, precast, rocking beams carry shear in a more direct mechanism than conventional reinforced concrete ones. The pre-tensioned, rocking columns in the proposed bridge system behave similarly, except turned through 90 degrees. Both the beams in the precast frame and the columns of the precast bridge carry shear through a direct compression strut running diagonally though the member from end to end, shown schematically in Figure 8.18b. High levels of confinement are necessary at the column ends to prevent crushing of the concrete at the column toe, which the steel shoes at the

ends of the column provide. It is therefore likely that only the minimum required spiral is needed through the body of the columns.

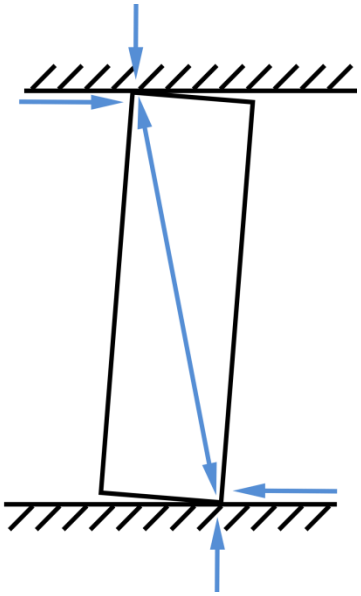

Figure 8.18 Direct compression strut mechanism for shear in rocking columns

This assertion is supported by measured strains in the spiral during the subassembly and shaking table tests. Strains measured in the spiral within the body of the column where the confining tube terminated were found to less than the yield strain (< 0.002) throughout testing, even to drift ratios of 10%. This indicated that the designs were overly conservative, and the minimum code required spiral would likely have been sufficient.

8.7 Discussion

The major departures from conventional cast-in-place column design for pre-tensioned, rocking columns are:

- the performance objectives and hence the strain limits used to in determining column deformation capacity;
- the use of a permissible design space to proportion column reinforcement;

- the use of moment-rotation analyses to determine the effective stiffness, strength and plastic capacity of the columns; and
- the end region detailing.

8.7.1 Seismic Performance

Modifications to the current procedure are reasonably straightforward; however, the outlined procedure has some perceived drawbacks. Chiefly, the designer determines the strength and stiffness of the columns under non-seismic loads and then checks the seismic performance of the system. This process seems backwards if a specific seismic performance, such as those presented in Figure 8.4, is desired. Specific performance goals cannot be chosen by the designer, unless he or she is lucky or diligent enough to arrive at this level of performance through successive iterations.

Additionally, specific choices for the design parameters are largely decided by service level requirements. Specifically, columns designed with unbonded tendons must not decompress under Service IV loads, which include uniform thermal expansion. This criterion, rather than ensuring adequate re-centering performance, may dictate the number of prestressing strands required in the columns.

The restriction that the columns must not decompress is imposed to prevent cracking of the columns, presumably to prevent the ingress of moisture and corrosion of the strands. Logically, that is why larger restrictions are imposed for unbonded strands. If the columns were, instead, allowed to decompress under service loads, protection at the bottom of the column, where rotation would likely occur, could be provided to prevent corrosion of the strands. These protection strategies would, philosophically, serve the same purpose as the current stress limit, which is to ensure the long term durability of the columns. Removing this restriction in the

proposed design procedure would lead to more efficient designs that are specifically optimized for seismic performance.

An alternative approach to the AASHTO methodology, essentially the reverse of this procedure, has been developed for bridges by others [e.g. Kowalsky 2002, Priestley, Calvi and Kowalsky 2007, Calvi and Kowalsky 2013]. This "Direct Displacement Based Design" procedure starts with the desired seismic performance, and works forwards to arrive at a design that meets this performance level. Service load design then becomes a check of the seismic design procedure. This approach may be more suitable from a performance based design standpoint.

8.7.2 Ductility Limits

Article 4.9 of the *AASHTO Guide Specifications for LRFD Seismic Bridge Design* (2015) specifies ductility limits for the columns during the design hazard. These limits are based on the ductility capacity of reinforced concrete columns under modest levels of axial load. The ductility capacity for rocking columns with unbonded prestressing is influenced by two major factors;

First, rocking prestressed systems typically yield at lower drift ratios than conventional systems [e.g. Priestley, Calvi and Kowalski 2007]. Second, prestressed, precast columns without protective detailing were able to achieve ductilties of 11 [Davis et al. 2012] before dropping to 80% of their peak moment capacity, and columns with protective end detailing were able to achieve ductilities in excess of 20 with minimal damage, while maintaining over 80% of their peak moment capacity despite fractured deformed bar reinforcement, [Kennedy 2015, Schaefer et al. 2014a]. These values are well in excess of the typical value of 6.0 accepted for well-detailed reinforced concrete columns.

8.7.3 Damping and Displacement Demand

The *AASHTO Guide Specifications for LRFD Seismic Bridge Design* (2015) defines a dynamic amplification factor for short period systems where T < 1.25Ts. This factor amplifies the elastic displacement found using multi-modal response spectrum analysis which assumes that structures with different plastic capacities will displace the same amount under the same ground motion if their initial stiffnesses are the same. The *AASHTO Guide Specifications for LRFD Seismic Bridge Design* (2015) also prescribes a set level of damping (5%) to all structures regardless of their construction type.

While hybrid (or "flag-shaped") hysteresis curves, typical of precast, prestressed concrete systems, dissipate less hysteretic energy than the Q-shaped (or elastic-perfectly-plastic) curves on which the specifications are based, research has suggested that the displacement ductility demands for the three hysteretic rules are similar, despite the difference in hysteretic energy dissipation [e.g. Christopoulos et al. 2002]. These studies used far-field motions, with relatively short significant durations.

It is therefore reasonable to use Articles 4.3.2 and 4.3.3 of the *AASHTO Guide Specifications for LRFD Seismic Bridge Design* (2015) for hybrid pre-tensioned systems, although further analyses are needed to support this assertion, especially for near field, pulse-type, motions and long duration subduction motions.

CHAPTER 9: NUMERICAL MODELING

This chapter presents a column modeling approach for pre-tensioned, rocking columns, implemented in the analytical platform Open System for Earthquake Engineering Simulation (OpenSees v2.5.0 2016). This modeling approach was used to simulate the response of both the subassembly and shaking table test specimens. Critical parameters for these models were calibrated to the experimental results, and the sensitivity of these models to slight variations in input parameters was investigated.

- Section 9.1 describes the modeling approach for the pre-tensioned columns.
- Section 9.2 describes the nonlinear material models that were used in the numerical simulations.
- Section 9.3 discusses aspects of the modeling approach specific to the subassembly column models.
- Section 9.4 compares the force-displacement response of the subassembly specimen models with the responses measured during the tests.
- Section 9.5 discusses aspects of the modeling approach specific to the shaking table specimen model.
- Section 9.6 compares the dynamic behavior of the shaking table specimen model with the measured response of the experimental specimen.
- Section 9.7 presents an investigation of the fatigue parameters used in the shaking table test specimen for the deformed bar reinforcement.
- Section 9.8 summarizes the conclusions that can be drawn from these numerical simulations.

9.1 Column Modeling Approach

The pre-tensioned columns were modeled using a combination of linear-elastic and nonlinear elements, as shown in Figure 9.1. The rocking behavior at the top and bottom of the column, where the majority of the inelastic displacement occurs, was modeled using a fiber section element with zero length. The axial, flexural, shear and torsional deformations of the column were captured using a linear elastic beam-column element that connected to each of the rocking elements. A co-rotational truss element was used to model the strand.

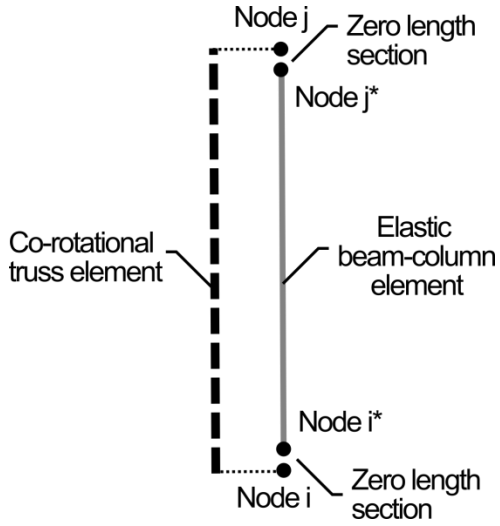

Figure 9.1 Column modeling approach

The elastic axial, flexural, shear and torsional flexibilities of the column were estimated using the gross-section properties. The shear modulus of the concrete was calculated using a Poisson's ratio of 0.2 and the measured elastic modulus of the column concrete on the day of the test. Measured material properties for the experimental specimens can be found in Appendix A.

The zero-length, rocking element cross-section discretization is depicted in Figure 9.2. The cross-section of the column at each rocking interface was modeled in OpenSees with a collection of fiber elements, each fiber having one of the nonlinear constitutive relationships

described in Section 9.2. The column cross-section was divided uniformly in both the radial and circumferential directions. The number of divisions in the radial and circumferential directions was based on the recommendations of Berry (2006) in order to balance convergence and computational efficiency. However, an even number of divisions (12) were used in the radial direction.

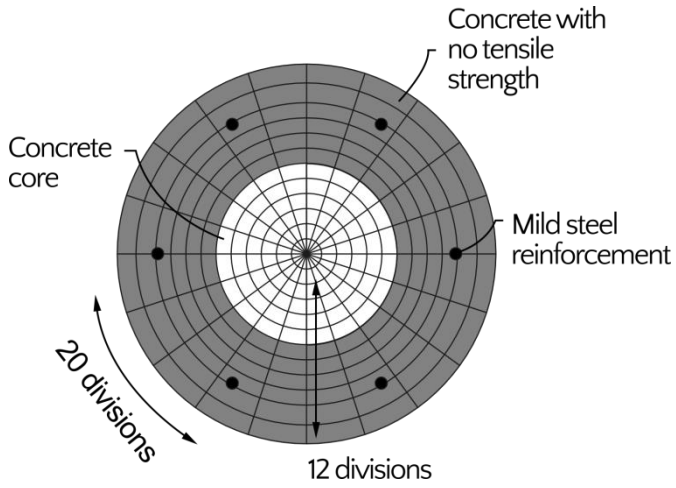

Figure 9.2 Zero-length, rocking element cross-section discretization

9.2 Nonlinear Material Models

The properties for the material models were derived from the measured concrete and steel material properties whenever available. The compressive strength, elastic modulus and tensile strength of the concrete were determined from material tests, as were the yield and ultimate stress and strain of the reinforcement (See Appendix A). Table 9.1 provides an overview of the material formulations implemented in OpenSees.

Table 9.1 OpenSees Material Definitions

Material	Confined concrete	Confined concrete	Deformed bar reinforcement	Strand
OpenSees Material	ConcreteCM	Concrete04	Hysteretic	ElasticPPGap
Yield Stress	n/a	n/a	s1p $= f_y$ s1n $= f_y$	Fy =245 ksi
Deformation at yield	n/a	n/a	s2p $= f_u$ s3p $= f_u$ s2n $= -f_u$ s3n $= -f_u$	n/a
Peak stress	fpcc $= f'_{cc}$	fc $= f'_{cc}$	e1p $= e_y l_{s,unb} + slip_{yld}$ e1n $= -e_y l_{s,unb} - slip_{yld}$	n/a
Deformation at peak stress	epcc $= e_{cc} E_{depth}$	ec $= e_{cc} E_{depth}$	e2p $= e^R_{su} l_{s,unb} + slip_{ult}$ e3p $= e_{su} l_{s,unb} + slip_{ult}$ e2p $= -e^R_{su} l_{s,unb} - slip_{ult}$ e3p $= -e_{su} l_{s,unb} - slip_{ult}$	n/a
Miscellaneous	rc $= \frac{f'_{cc}/e_{cc}}{(E_c - f'_{cc}/e_{cc})}$ xcrn $= 1.2$ ft $= f_t$ et $= 0.0002$ rt $= \frac{f_t/e_t}{(E_c - f_t/e_t)}$ xcrp $= 1.2$ gap $= 1$	ecu $= e_{cu} E_{depth}$ Ec $= E_c / E_{depth}$ fct $= f_t$ et $= 0.0002$ beta $= 0.0$	pinchX $= 0.05$ pinchY $= 0.95$ damage1 $= 0.0$ damage2 $= 0.0$ beta $= 0.0$	E = 28500 ksi gap = 0.0 eta = 0.04 damage = “damage”
Hysteretic Response	Figure 9.4	Figure 9.4	Figure 9.7	Figure 9.8

9.2.1 Concrete

The concrete was modeled in OpenSees using one of two concrete constitutive models, *Concrete04* or *ConcreteCM*. This was done in order to assess the effect of early concrete reloading in compression, which is included in the *ConcreteCM* material, but not in *Concrete04*. The confined properties of the concrete in both material formulations were determined using the confining model proposed by Mander et al. (1988). The effective depth of the concrete was calibrated to the tests to match the force-displacement behavior of the columns. This effective depth determines the relationship between relative displacement and strain, which is needed to compute the stress at a particular level of deformation for the zero-length, rocking section element.

Concrete04 uses the backbone compression envelope proposed by Popovics (1973) given in Equation 9.1, and a linear strain response in tension up to the cracking strain. Beyond the cracking strain the tensile stress decreases exponentially.

$$y(x) = \frac{r\,x}{r-1+x^r} \quad [9.1]$$

where $y = f_c/f'_{cc}$ is the non-dimensional stress, $x = \varepsilon/\varepsilon_{cc}$ the non-dimensional strain, f'_{cc} is the confined compressive strength of the concrete, ε_{cc} the strain at maximum stress, and r a shape parameter that effects the descending branch of the material model.

ConcreteCM uses the envelope proposed by Tsai (1988) in both tension and compression, given in Equation 9.2.

$$y(x) = \frac{m\,x}{1+\left(m-\frac{r}{r-1}\right)x+\frac{x^r}{r-1}} \quad [9.2]$$

where $m = E_c/E_{sec}$ the ratio of the initial tangent modulus to the secant modulus at peak strength and $E_{sec} = f'_{cc}/\varepsilon_{cc}$ the secant modulus at peak strength.

Based on preliminary models, the shape parameter, r, was found to have little influence on the global force-displacement behavior of the columns. If $r = E_c/(E_c - E_{sec})$ as proposed by Mander et al. (1988), the curve proposed by Popovics (1973) and the one proposed by Tsai (1988) are identical. Thus, the value proposed by Mander et al. (1988) was selected to allow a direct comparison between the two constitutive models.

The *ConcreteCM* backbone curves in tension and compression are shown in Figure 9.3, along with the definition of the concrete modeling parameters identified in Table 9.1.

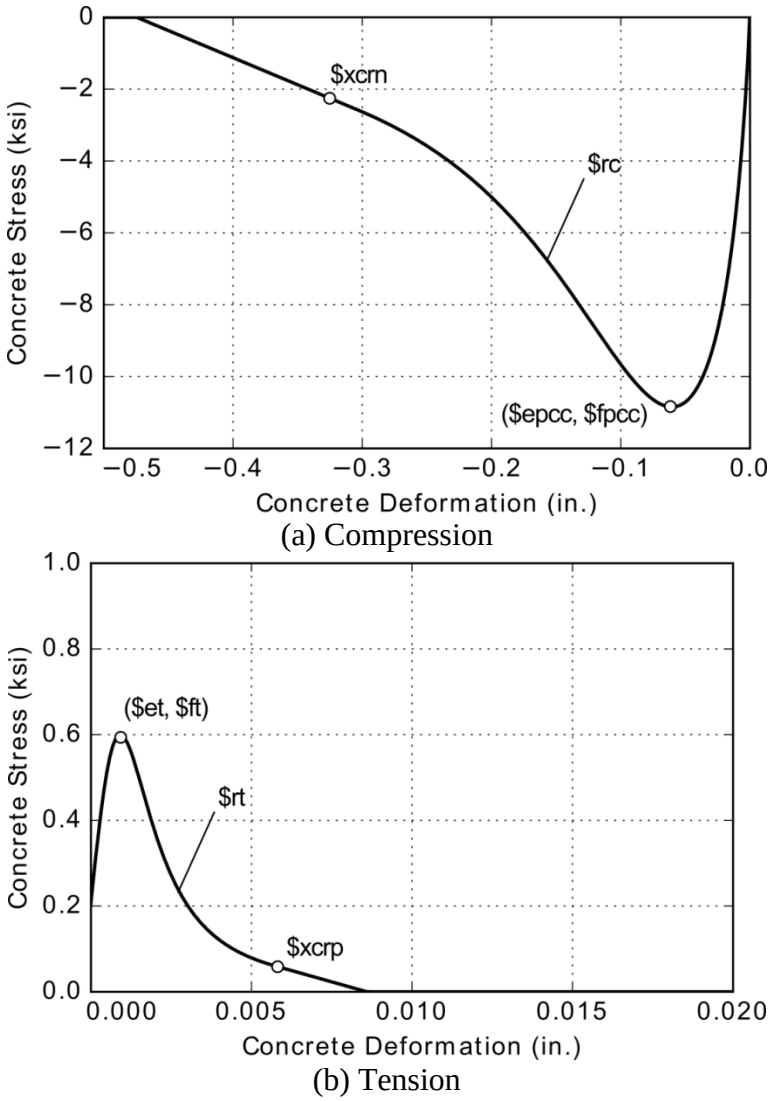

Figure 9.3 Backbone definitions for ConcreteCM material model.

Figure 9.4 compares the cyclic behavior of the *ConcreteCM* and *Concrete04* material models. One key feature of the *ConcreteCM* model is the smooth, cubic transition curve between tension and compression. *Concrete04* returns along the unloading path until it reaches the specified backbone curve.

This early reloading in compression simulates imperfect crack closure when loading from tension to compression. Other material models in OpenSees have features that also account for this phenomenon [e.g. Berry and Eberhard 2007, Lee and Billington 2010, Haraldsson 2015], based on the work of Stanton and McNiven (1979). However, unlike the *ConreteCM* material model, these do not produce smooth transition curves from tension to compression.

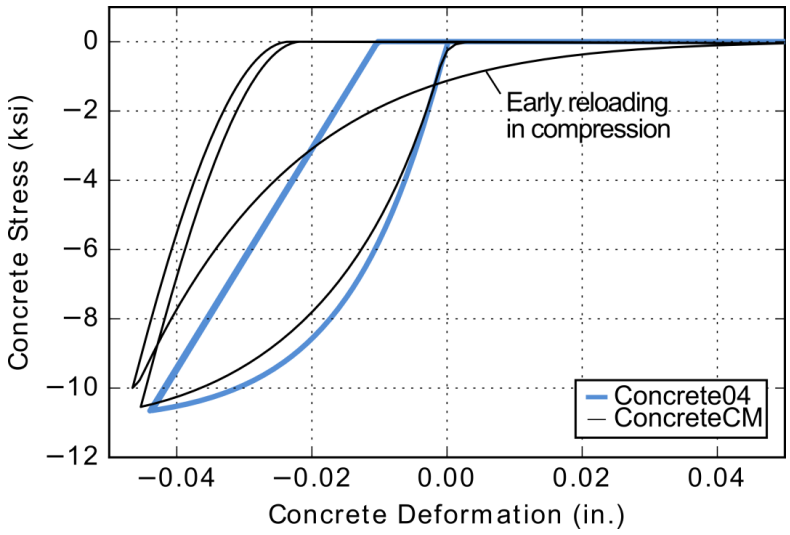

Figure 9.4 Early reloading behavior in concrete constitutive models

Figure 9.5 shows the moment-drift ratio behavior of a rocking, cantilever column using either the *Concrete04* or the *ConcreteCM* material models at the rocking interface. Using the *ConcreteCM* material significantly increases the cross-over drift ratio of the column; this behavior is closer to what is observed in experimental tests.

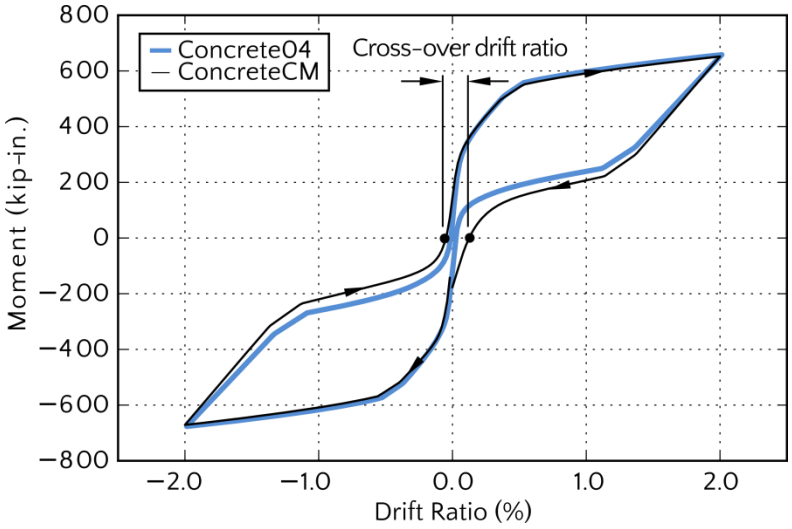

Figure 9.5 Influence of concrete constitutive model on moment-drift ratio response of a cantilever column.

9.2.2 Deformed Bar Reinforcement and Bar Slip

The deformed bar reinforcement was modeled using the *Hysteretic* material model. The backbone curve for the *Hysteretic* model in tension is shown in Figure 9.6, along with the definition of the steel modeling parameters identified in Table 9.1. The cyclic behavior is shown in Figure 9.7. More sophisticated material models for deformed bar reinforcement are available in OpenSees, however many do not function properly in a stress-displacement space. Because only a small amount of deformed bar reinforcement was used ($\rho_s \cong 0.5\%$) in the pre-tensioned columns, the exact shape of the steel constitutive model did not significantly affect their overall force-displacement behavior.

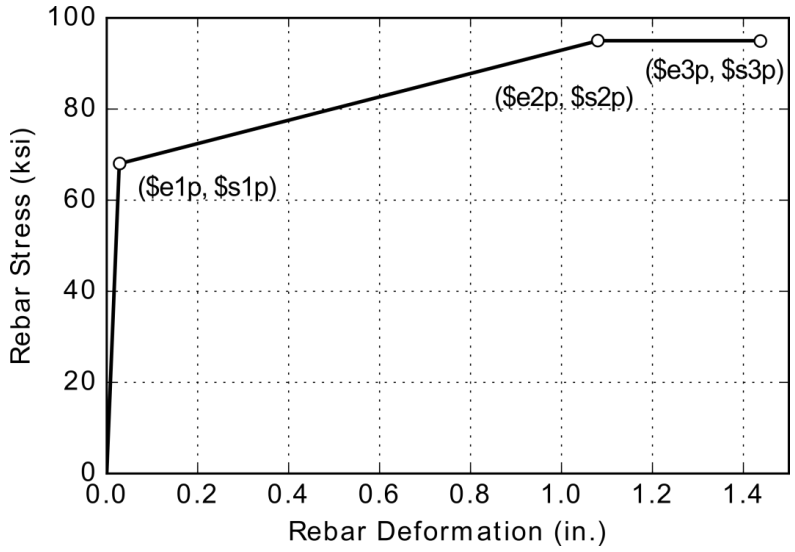

Figure 9.6 Backbone definition for Hysteretic material model.

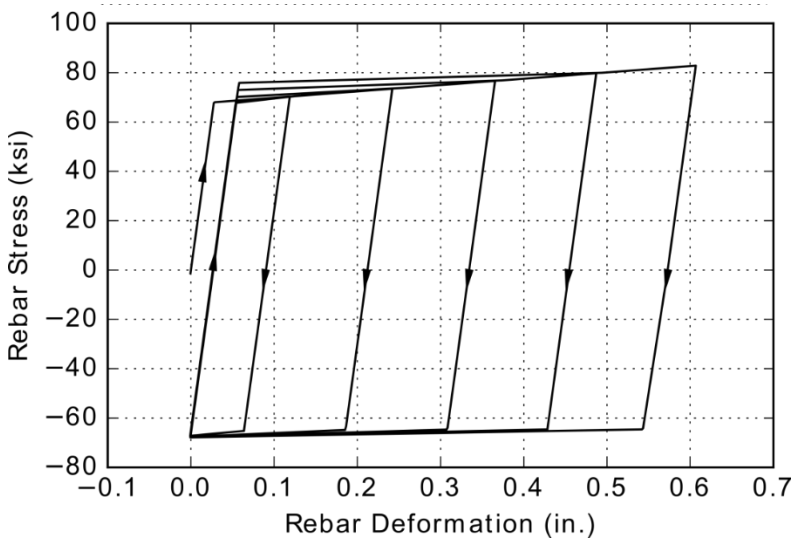

Figure 9.7 Cyclic behavior of Hysteretic material model.

This model was used because the effects of strain penetration can be directly applied to the model, without the need to chain multiple materials in series. The slip at both the yield and ultimate stress in the reinforcement was calculated using the two-component bond model proposed by Lehman and Moehle (1998). These slip deformations were added to the yield and ultimate deformations of the reinforcement for the given deliberately debonded length.

An additional material wrapper (*FatigueMaterial*) was used to model low-cycle fatigue of the deformed bars during the shaking table tests. This material wrapper assesses the fatigue life of the bars using a Coffin-Manson fatigue life relationship [Manson 1954], and uses a Palmgren-Miner linear strain accumulation rule [Miner 1945]. A modified rain flow cycle counter is used to track strain amplitudes throughout the irregular strain history imposed by the dynamic displacements of the structure. The shape parameters for the Coffin-Manson curve were taken as those suggested by Mander et al. (1994) for A615 reinforcing bars. This approach is consistent with the modeling approach of Mantawy (2016) who investigated the fracture of the deformed bar reinforcement during the shaking table tests of the pre-tensioned bridge.

9.2.3 Prestressing Strands

The strands were modeled using an elastic-perfectly-plastic material (*ElasticPPGap*), as shown in Figure 9.8. This material formulation was used, because it can only carry either tension or compression, but not both. This makes it ideal for the unbonded strands, which cannot carry significant compressive forces without buckling. An additional material wrapper (*InitStrainMaterial*) was used to apply the average of the last recorded strains in the strands prior to final specimen assembly. The elastic modulus of the strands was adjusted to account for the effects of strain penetration, using the bond coefficient for low-grit epoxy coated strands recommended by Cousins et al. (1990).

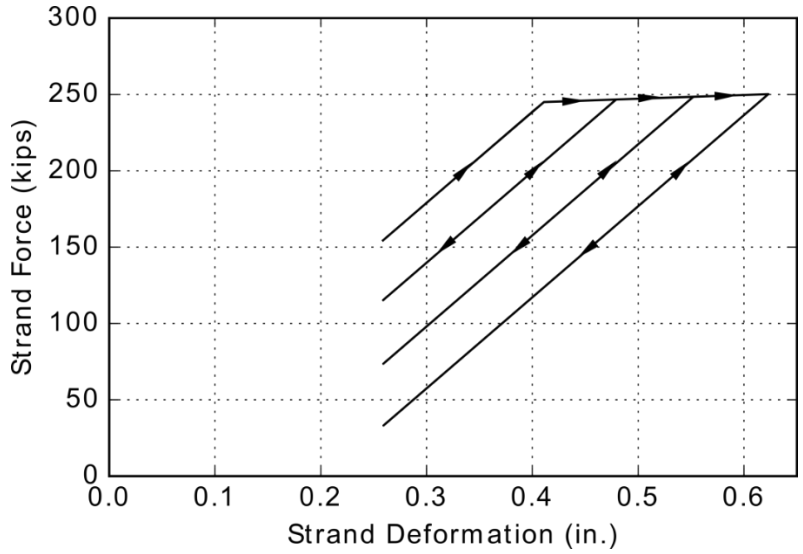

Figure 9.8 Cyclic behavior of ElasticPPGap material

Although some elastic shortening of the column occurred to reach internal equilibrium, the overall change in stress in the strands due to it was small (<5 ksi). This stress change was ignored, given that the initial strain in the strands at the start of each experiment was unknown, and could only be estimated based on strain readings prior to the final assembly of the specimens.

9.3 Subassembly Test Model

The subassembly test model is shown in Figure 9.9. This model was used to simulate the behavior of both the PreT-SF-ROCK [Schaefer et al 2014a] and the PreT-CB-ROCK [Kennedy 2015] subassemblies. The tested columns were cantilevers, therefore only a single zero length rocking section was needed. The offset between the point of the application of the vertical load and lateral displacements was modeled using an elastic beam column element, with 100 times the flexural, shear and torsional stiffness as the elastic column element. In Fig 9.9 it is shown as a “Rigid link”.

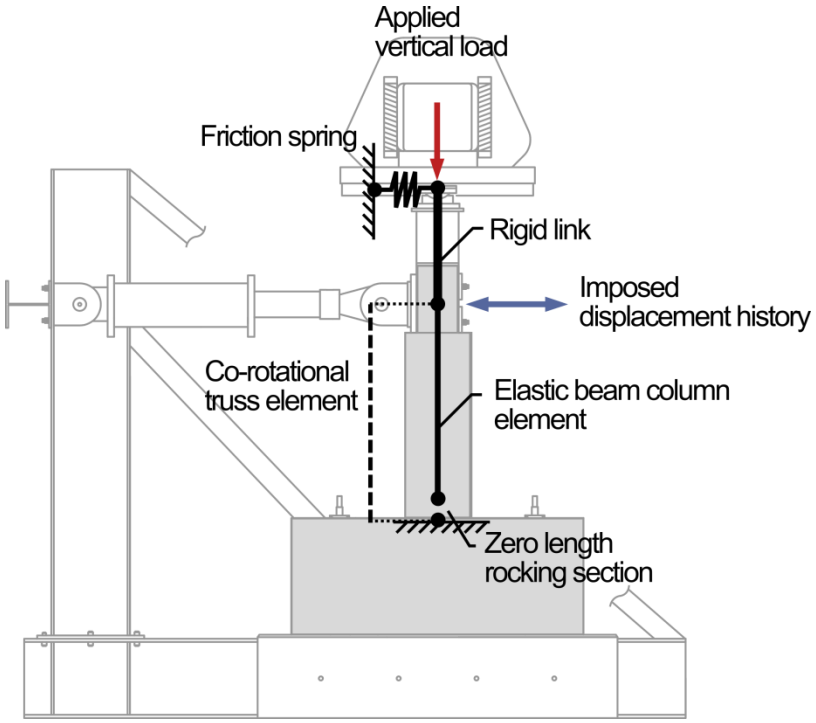

Figure 9.9 Subassembly model components.

An elastic-perfectly-plastic spring was connected to the top of the rigid link to simulate the friction between the universal testing machine's crosshead and the smooth sliding interface. The behavior of the friction element during the imposed displacement history is shown in Figure 9.10. The friction coefficient (1.6%) and elastic stiffness used for the friction element were those suggested by Brown (2008) for this particular testing configuration. Given the axial load and height of the specimen, this leads to a maximum friction force of 2.5kips.

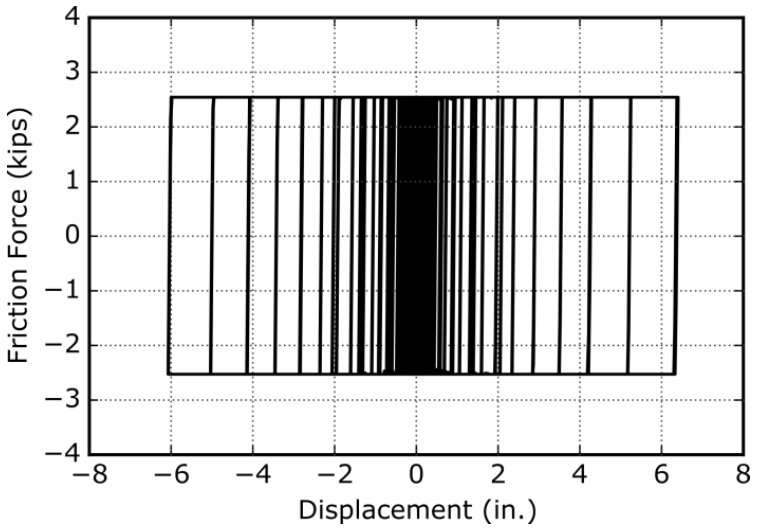

Figure 9.10 Friction element force-displacement behavior.

This friction element was added to the model to correct for the measured non-zero crossover displacements during elastic cycles of the test protocol. Figure 9.11 shows the measured force-displacement response during the second elastic cycle of the PreT-SF-ROCK test as well as the simulated response, both with and without the friction element.

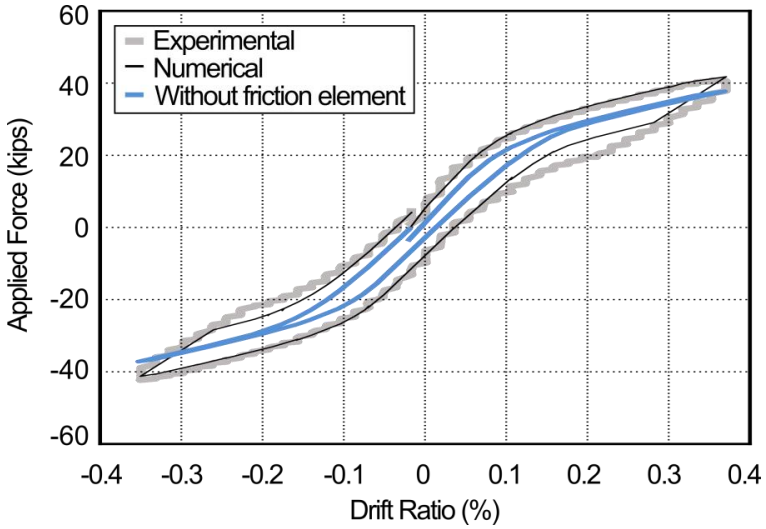

Figure 9.11 Effect of friction element on numerical force displacement response.

The addition of the friction element more accurately captures the energy dissipated during elastic cycles by the testing configuration. In addition, the values recommended by Brown (2008) are consistent with the measured friction within the testing configuration.

9.3.1 Model Calibration

One of the critical parameters for accurately capturing the response of rocking prestressed systems is the effective depth of the concrete at the rocking interface. This parameter determines the strain to the deformation in the concrete, and thus allows the stress to be computed for a particular level of deformation, and therefore the neutral axis depth and the moment-rotation characteristics of the section.

The effective depth of the concrete used in the subassembly models was calibrated using the envelope of the force displacement response measured in the experiments. The objective function used was adapted from Haraldsson (2015), and given in Equation 9.3.

$$min\, f\left(E_{depth}\right) = \sqrt{\frac{\sum_i^N \left(F_{meas}^i - F_{calc}^i\right)^2}{N\, max\left({F_{meas}}^2\right)}} \qquad [9.3]$$

where N is the number of data points and F^i is the measured or calculated force at a given displacement.

Figure 9.12 shows the value of the objective function versus the effective depth. The most optimal value for the effective depth was found to be on average roughly half of one column diameter (0.5D).

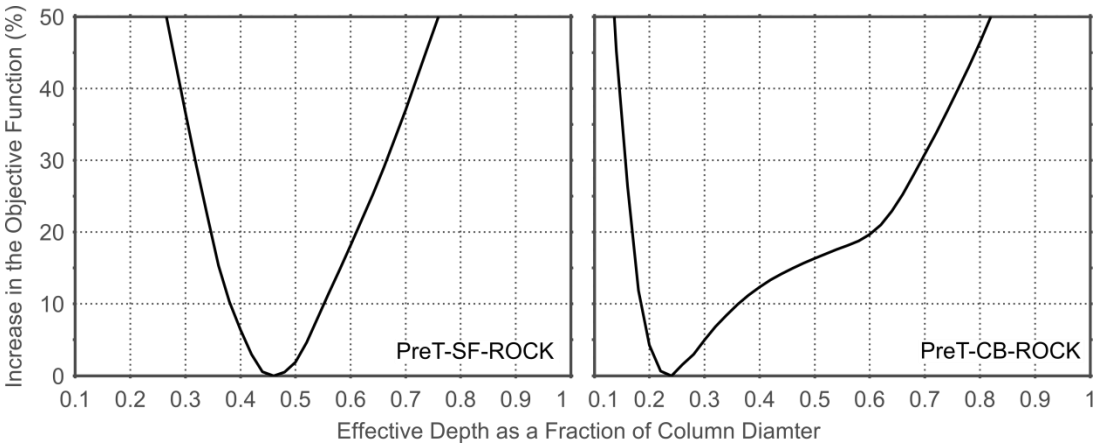

Figure 9.12 Optimal value of the effective depth for the subassembly models.

The numerical force-displacement envelope for the PreT-CB-ROCK subassembly is shown in Figure 9.13 with the optimal value of the concrete's effective depth. The measured force-displacement response is also shown for comparison.

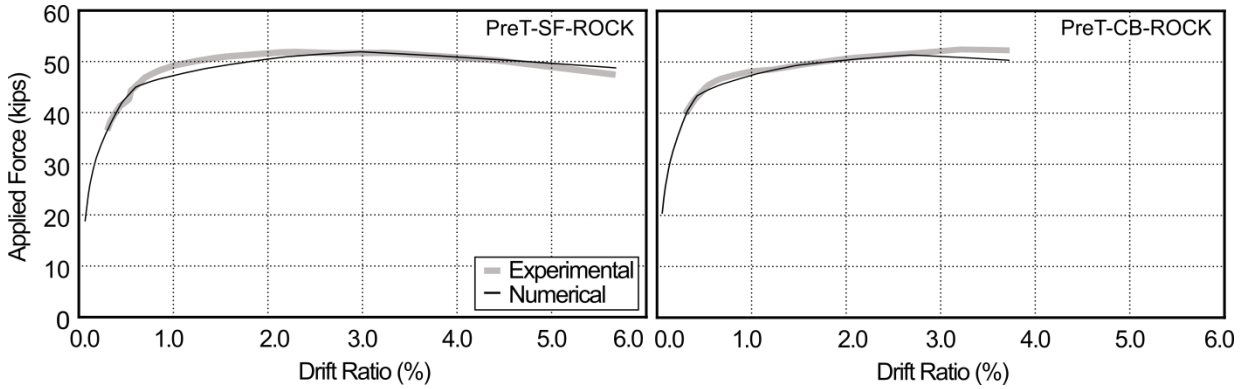

Figure 9.13 PreT-CB-ROCK Force-displacement envelope with calibrated material parameters.

9.4 Comparison to Measured Subassembly Response

A comparison of the experimental and numerical force displacement responses at four drift levels are shown in Figure 9.14 and Figure 9.15 for the PreT-SF-ROCK and PreT-CB-ROCK subassemblies, respectively. These plots are shown for columns modeled using the *ConcreteCM* concrete material model with early reloading in compression. In general, the

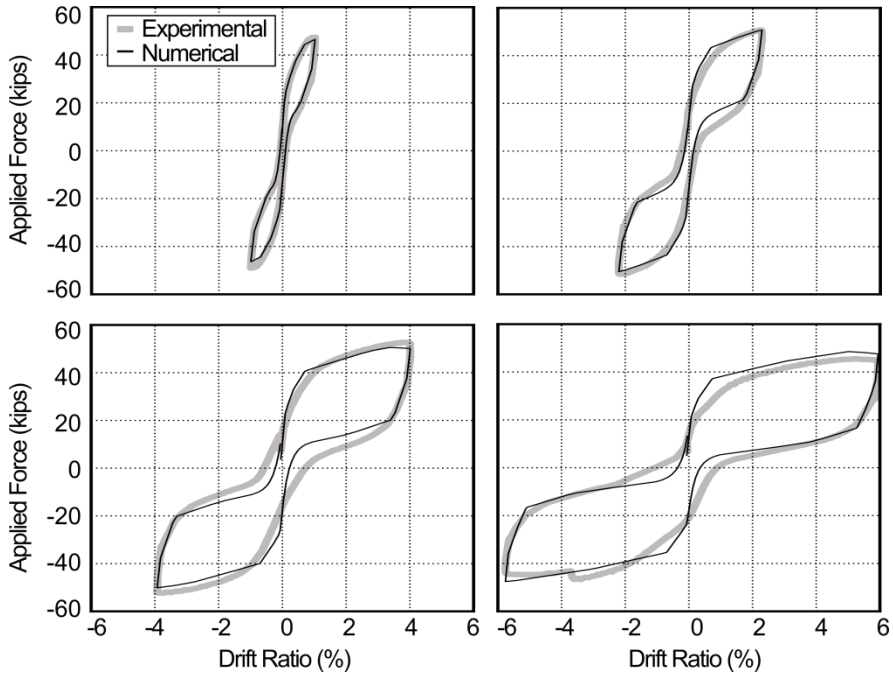

Figure 9.14 PreT-SF-ROCK Force-displacement behavior at drift levels of 1.0%, 2.0%, 4.0% and 6.0%

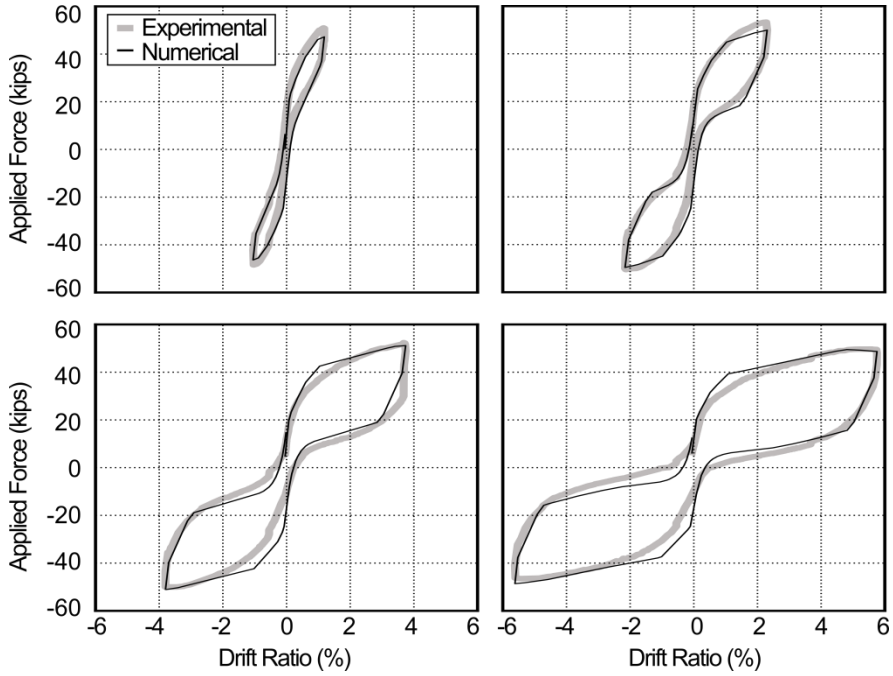

Figure 9.15 PreT-CB-ROCK Force-displacement behavior at drift levels of 1.0%, 2.0%, 4.0% and 6.0%

numerical model accurately predicted the force displacement response of the experimental specimens.

A comparison of the experimental and numerical force displacement responses at four drift levels are shown in Figure 9.14 and Figure 9.15 for the PreT-SF-ROCK and PreT-CB-ROCK subassemblies, respectively. These plots are shown for columns modeled using the *Concrete04* concrete material model without early reloading in compression. The numerical models accurately predicted the maximums of the force displacement response, however the cross-over drift ratios were much smaller than the measured ones.

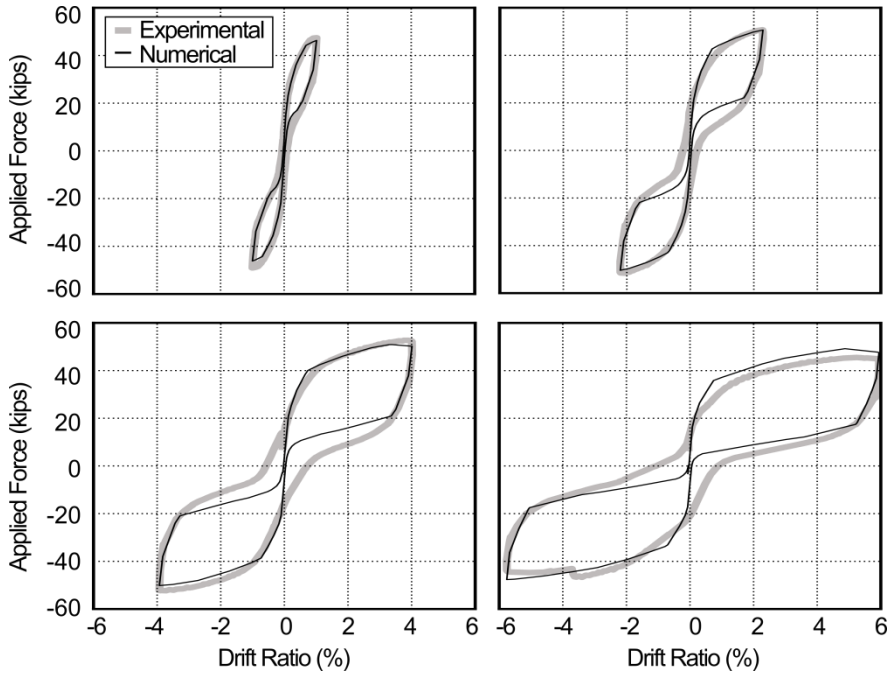

Figure 9.16 PreT-SF-ROCK Force-displacement behavior at drift levels of 1.0%, 2.0%, 4.0% and 6.0% using the *Concrete04* material model

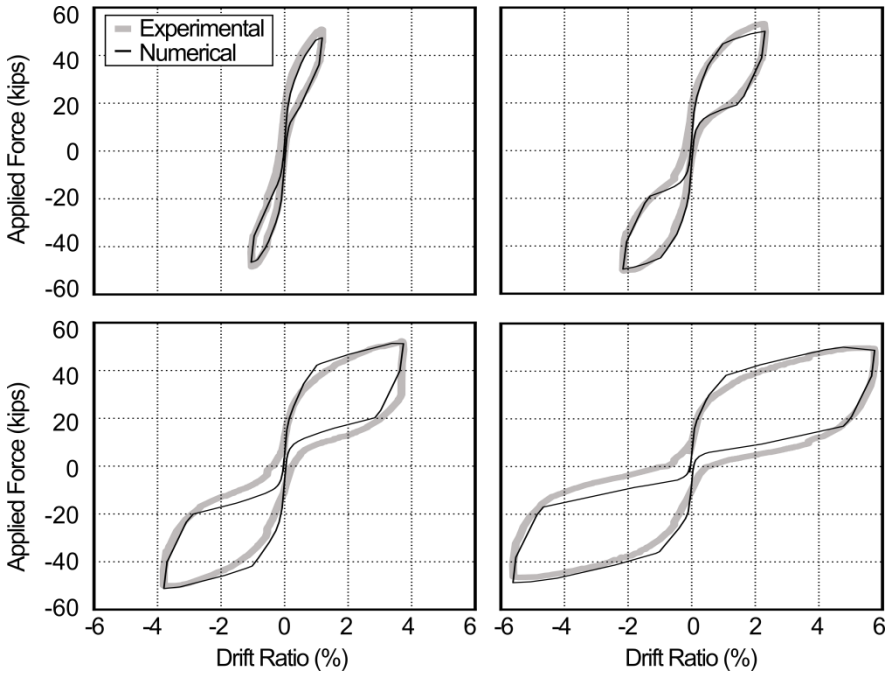

Figure 9.14 PreT-CB-ROCK Force-displacement behavior at drift levels of 1.0%, 2.0%, 4.0% and 6.0% using the *Concrete04* material model

Figure 9.16 shows the numerical cross over drift ratios, defined in Figure 9.5, for each displacement cycle plotted against the measured crossover drift ratios. The models of the subassemblies that included the *ConcreteCM* material model with early reloading in compression more accurately predicted the cross-over drift ratios than those which included the *Concrete04* model.

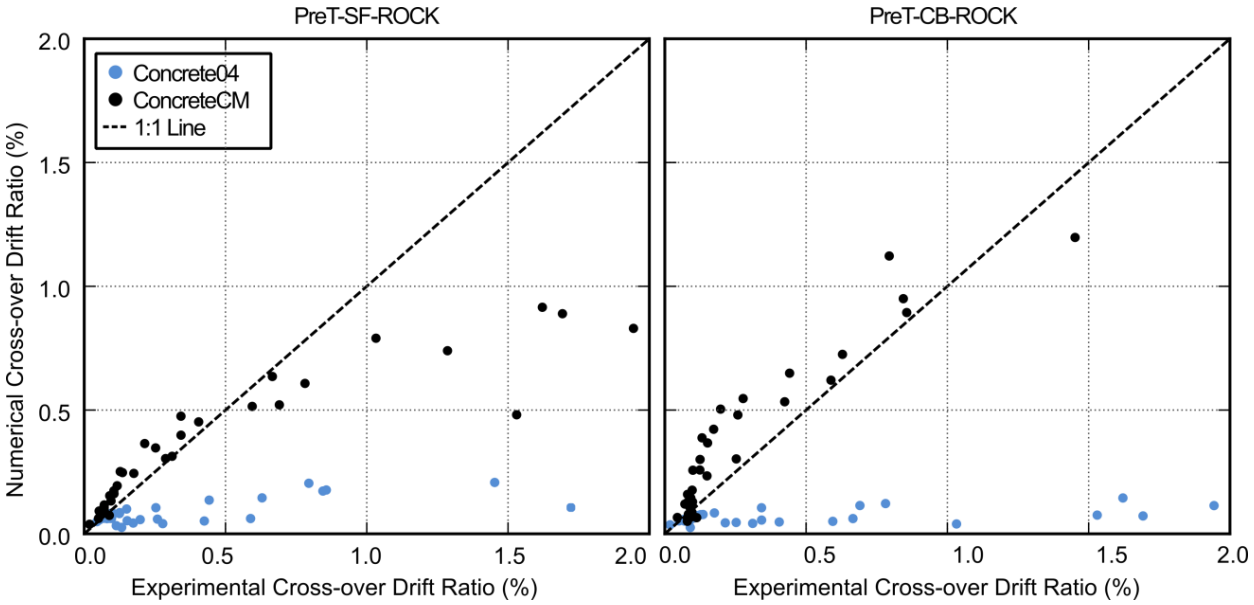

Figure 9.16 Cross over drift ratios for the subassembly models.

9.5 Shaking Table Test Model

Figure 9.17 shows the model of the shaking table test specimen. Many aspects of the bridge model are based on previous calibration of a similar model by Ranf (2007) for the conventional cast-in-place bridge tested by Johnson et al (2008).

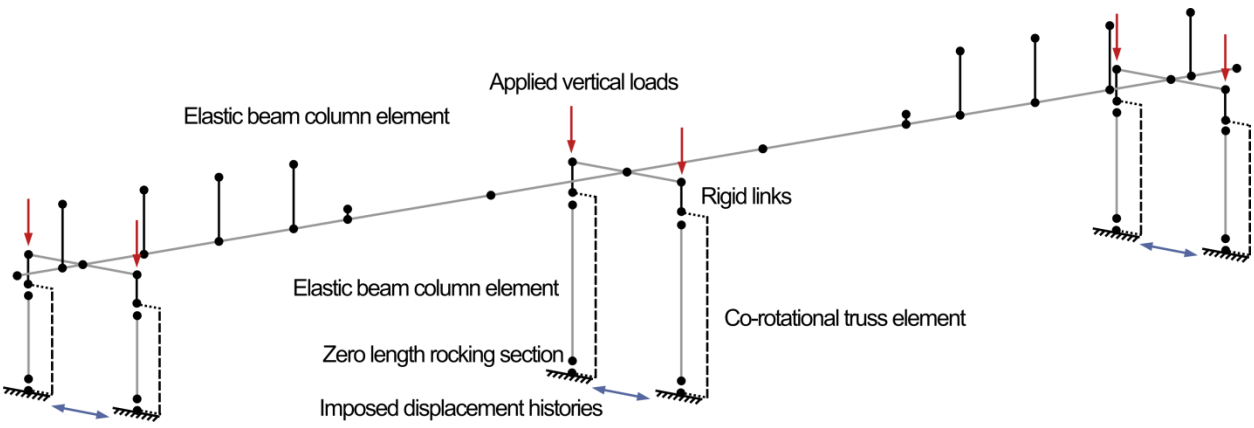

Figure 9.17 Shake table model overview

9.5.1 Superstructure

For the shaking table specimen, both the bridge superstructure and cap beams were modeled using elastic beam column elements, following the recommendation made by Ranf (2007). The cap beams were assigned stiff (100 times nominal) flexural properties about the vertical axis and rigid torsional properties, to simulate the restraint caused by the longitudinal girders in the actual structure.

The superstructure planks were assumed to act compositely with one another, since they were post-tensioned in both the longitudinal and transverse directions. An elastic beam column element with the gross section properties of the full width of the superstructure was used to capture the flexural, shear and torsional deformations of the deck.

Mass nodes, attached to the superstructure beam through ridged links, were used to simulate the superimposed dead load, i.e. the concrete blocks, which were added to the bridge specimen to account for the dead load lost through scaling. The offsets between the center of mass of the blocks and the centerline of the superstructure planks were modeled using elastic beam column elements, with 100 times the flexural, shear and torsional stiffness of the elastic column elements. Similar elastic elements were also used to connect the centerline of the superstructure to the ends of the rocking columns.

The inertial mass of the superstructure and cap beams was assigned to the nodes, based on their tributary area. Mass was not assigned to the nodes in the vertical direction to avoid numerical instabilities described by Ranf (2007).

9.5.2 Model Calibration

The effective depth of the concrete in the zero length rocking elements was calibrated using the measured force-displacement envelope of the bents during the shaking table tests. Each

bent was modeled separately and subjected to incremental lateral displacements. The optimization was performed using the objective function given in Equation 9.3.

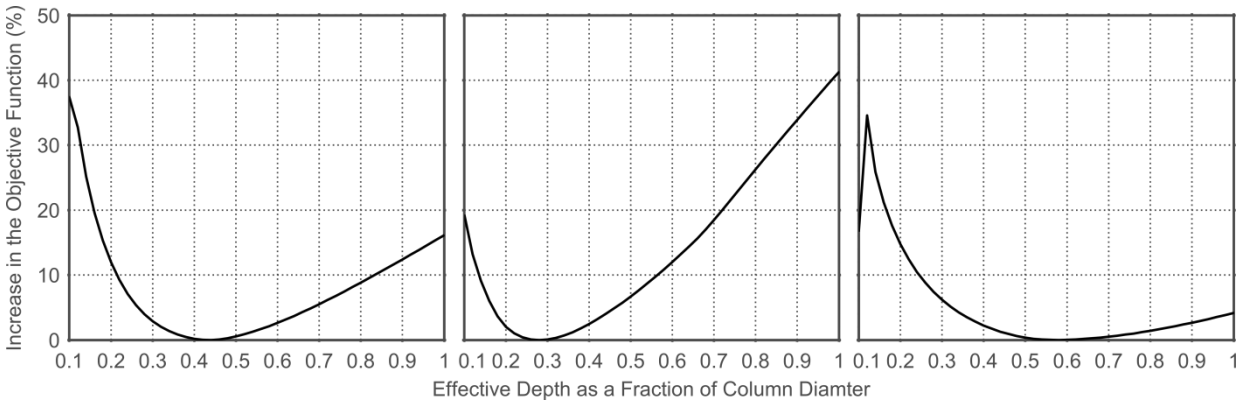

Figure 9.18 Optimal value of the effective depth for the shaking table specimen model.

Figure 9.18 shows the value of the objective functions versus the effective depth. On average, the most suitable value for the effective depth was found to be roughly half of one column diameter (0.5D). This effective depth is the same as was determined from the subassembly tests.

The resulting numerical force-displacement envelopes are shown in Figure 9.19. The numerical force-displacement envelopes have lower peak values than the experimental ones. One reason for this discrepancy is the presence of friction in the shaking tables. The shaking tables move over a thin layer of pressurized hydraulic fluid, and the friction forces created by this configuration are complex and hard to estimate. This friction adds to the structural response and the leads to larger measured forces. These friction forces are included in the measured envelopes but not the numerical ones.

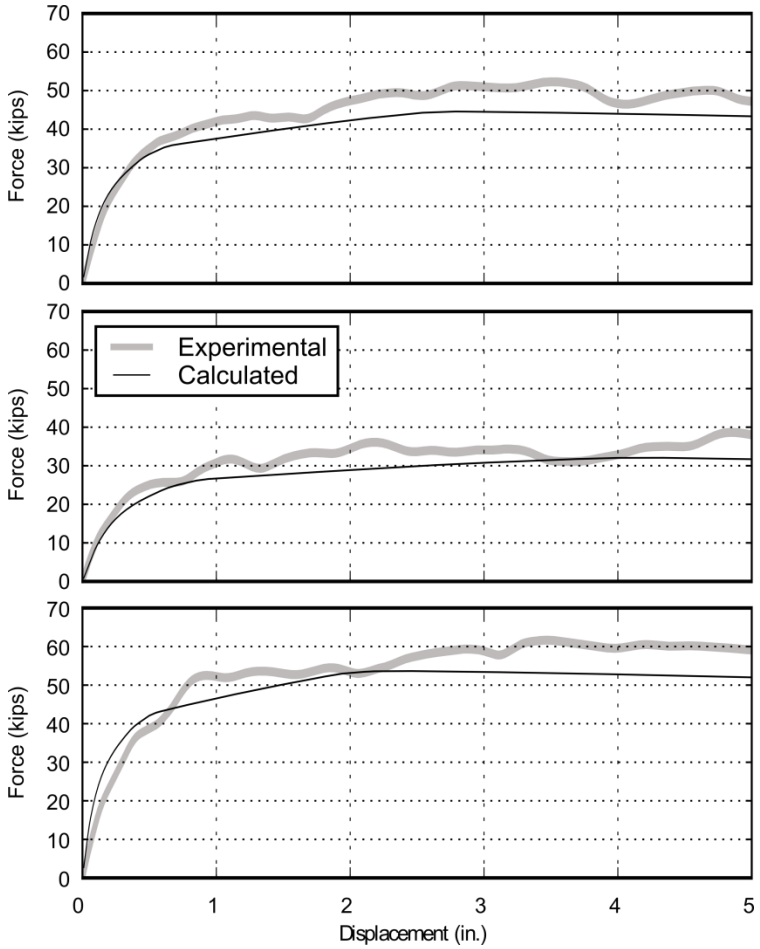

Figure 9.19 Bent base shears with calibrated material properties.

9.6 Comparison to Measured Bridge Response

The center of mass and twist-displacement time histories for three of the high-amplitude coherent motions are shown in figures 9.20, 9.21 and 9.22. The twist displacement is taken here as the difference between the displacement of bents 1 and 3. Prior to roughly 14 seconds in each of the motions, the center-of-mass (COM) and twist displacements are well predicted by the model. After this point, during the 100% and 221% Design Level motions (motions 16 and 19) both the twist displacement and the COM displacements are generally over-predicted by the model. The twist displacements of the bridge are highly dependent on the progression of

reinforcement fracture during the experimental program, and this is highly sensitive to input fatigue parameters. This will be discussed more in Section 9.7.

During the 221% Design Level motion, the bridge model oscillates at longer period than in the experimental specimen. At this point in the test schedule, deformed bar reinforcement had fractured in both the model and the experimental specimen. The observed discrepancies in displacement, particularly in the later motions, are largely influenced by the cyclic degradation of the non-linear material models and the fatigue, and ultimate fracture of, the deformed bar reinforcement in the model. Capturing the stiffness and strength degradation of the columns throughout the testing protocol is crucial to accurately predicting the response of the bridge for the motions after first fracture of the reinforcement.

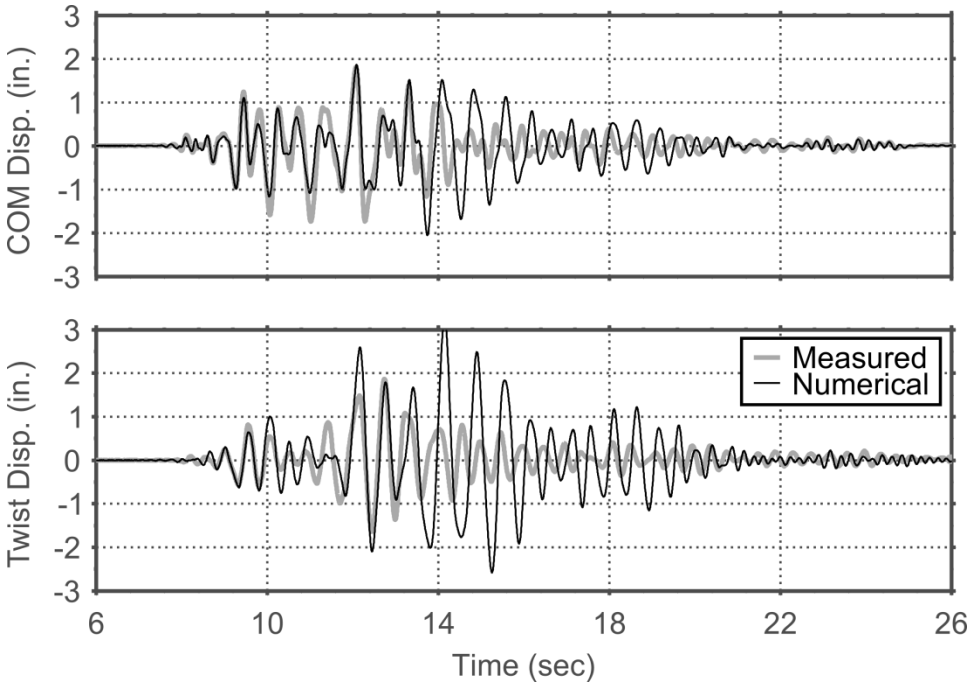

Figure 9.20 Center of mass and twist displacement histories for the 100% Design Level motion (Motion 16)

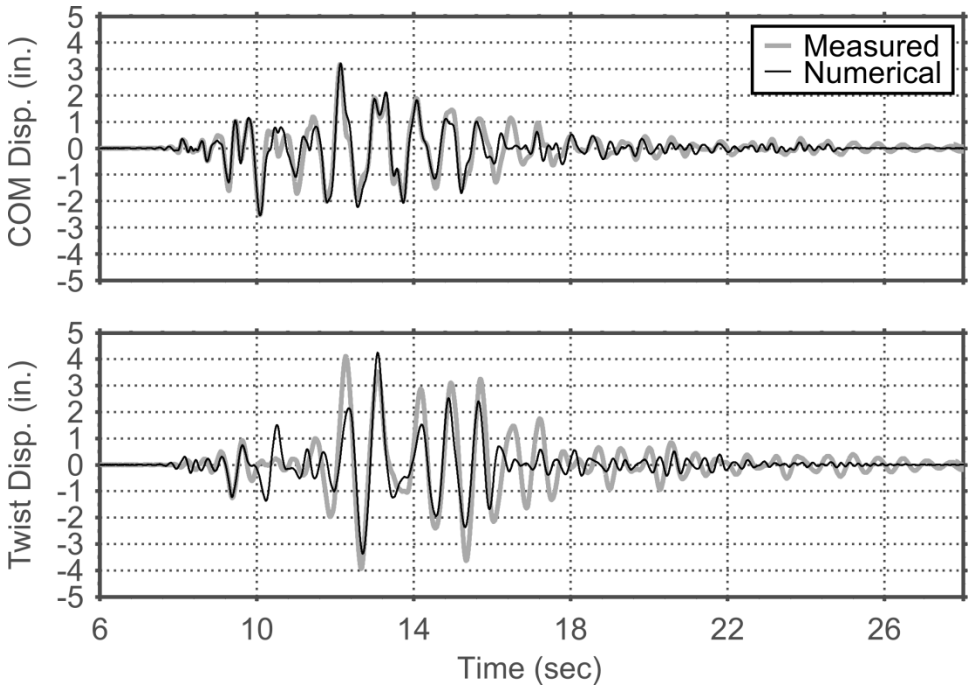

Figure 9.21 Center of mass and twist displacement histories for the 133% Design Level motion (Motion 17)

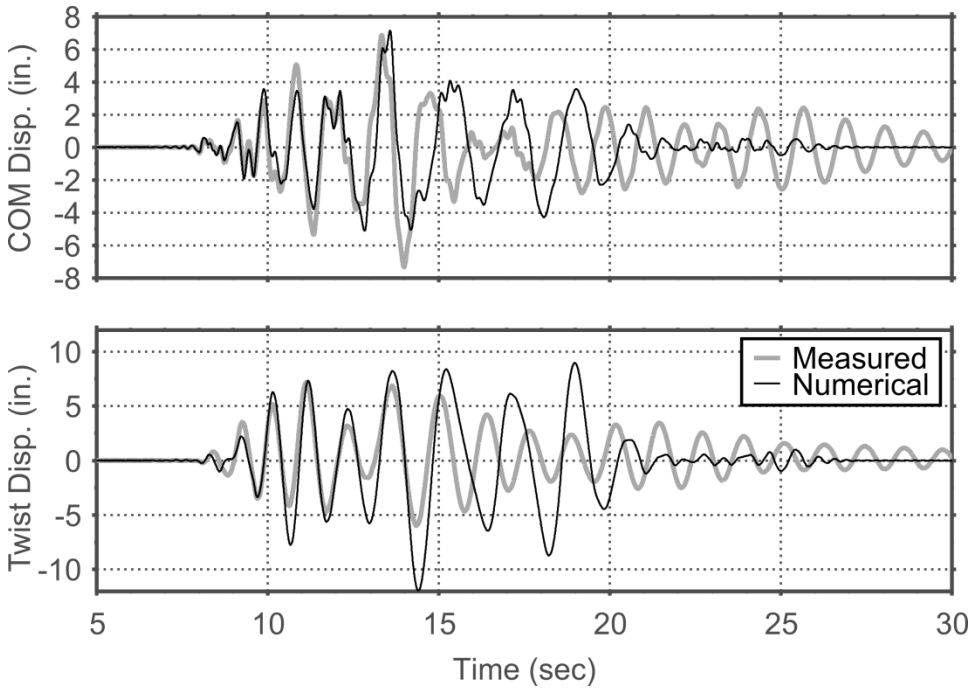

Figure 9.22 Center of mass and twist displacement histories for the 221% Design Level motion (Motion 19)

The maximum measured COM and twist displacements during the high-amplitude motions are shown in Figure 9.23. The maximum center-of-mass and twist displacements for the high amplitude motions prior to the 221% Design Level motion (Motion 19) are well predicted by the model, except during the 100% Design Level motion (Motion 16), where the twist displacement of the bridge specimen was over predicted by almost a factor of two.

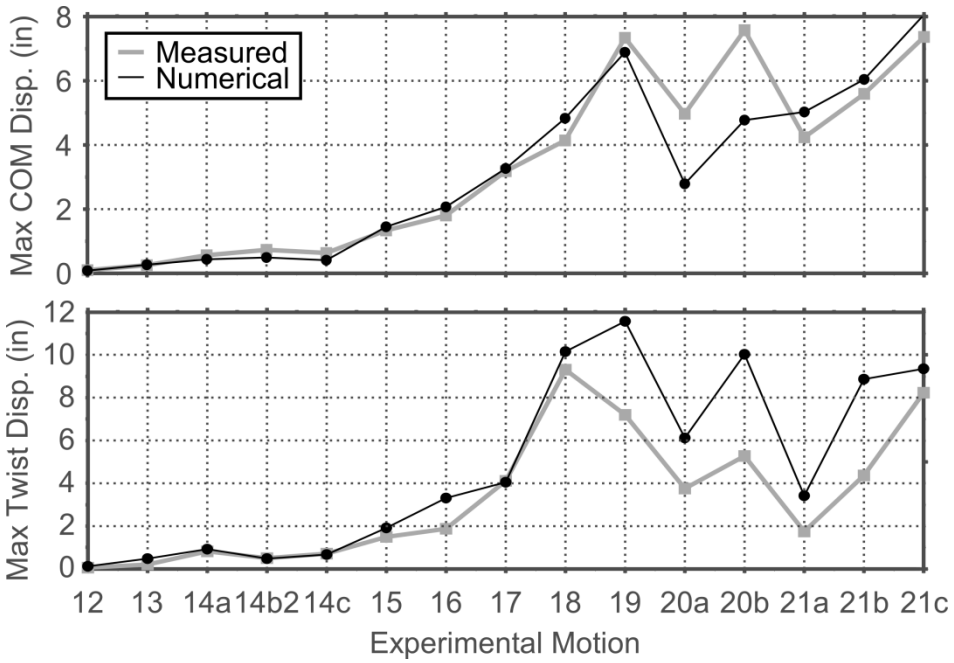

Figure 9.23 Maximum COM and twist displacement during high-level coherent motions

In the numerical model during the 177% Design Level motion (Motion 18), 75% and 33% of the deformed bar reinforcement fractured in bents 1 and 3, respectively. This increased the asymmetry in stiffness and strength of the bridge, leading to large twist displacements in the model during the 221% Design Level motion (Motion 19).

9.7 Influence of Fatigue Parameters on Model Response

As described in Section 9.6, the behavior of the bridge specimen throughout the high amplitude motions is highly influenced by the fracture of deformed bar reinforcement and thus, the chosen fatigue parameters used in the model.

To investigate the influence of the fatigue parameters on the bridge response, a parametric study was performed, varying the shape of the Coffin Manson curve, and thus the number of deformed bar reinforcement fractures during the high-amplitude, coherent motions. Table 9.2 shows the values of the fatigue parameters selected for the parametric investigation. For all of these models, *ConcreteCM* was used in the rocking sections.

Table 9.2 Parametric Study for Coffin-Manson Fatigue Parameters

Variation	Fatigue ductility coefficient	Fatigue ductility exponent
-10%	0.0716	-0.403
0 %	0.0795	-0.448
+10%	0.0875	-0.493

Figure 9.24 compares the number of deformed bar fractures in the three bents during the high amplitude coherent motions for opposite extremes of the parametric investigation. The labels in the figure indicate the specific case in the parametric study. Increasing the fatigue ductility coefficient and decreasing the fatigue ductility exponent (+10%/-10%) corresponds to delaying reinforcement fracture from the original model ("0%/0%). Conversely, decreasing the fatigue ductility coefficient and increasing the fatigue ductility exponent (-10%/+10%) corresponds to accelerating reinforcement fracture.

The total number of bars crossing a rocking interface in each bent was 24 (two columns times two rocking interfaces with six bars each). Also included are the fracture estimates from

Mantawy and Sanders (2016) who investigated the experimental fractures of the longitudinal reinforcement during the shaking table tests.

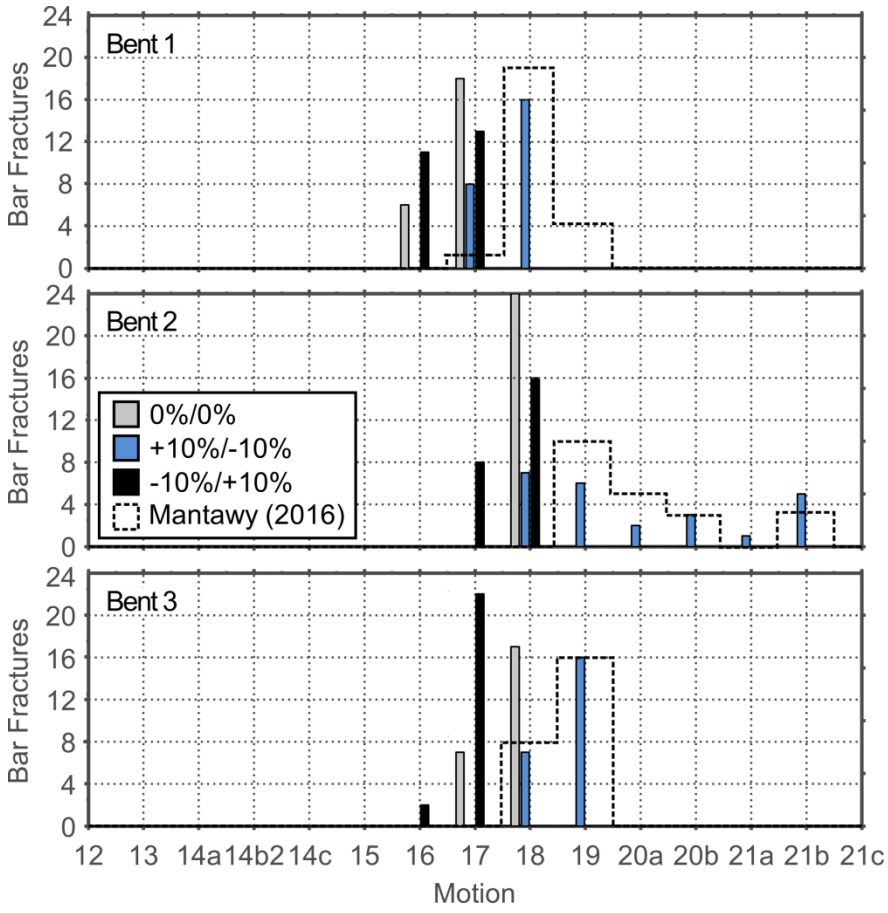

Figure 9.24

Bars generally fractured first in Bent 1, then Bent 3 and finally Bent 2. The progression of fractures in the model with parameters meant to delay bar fracture was most similar to the estimates of Mantawy and Sanders (2016).

Figure 9.25 shows the center of mass and twist displacements of the bridge model during the 221% Design Level motion (Motion 19) for opposite extremes of the parametric investigation.

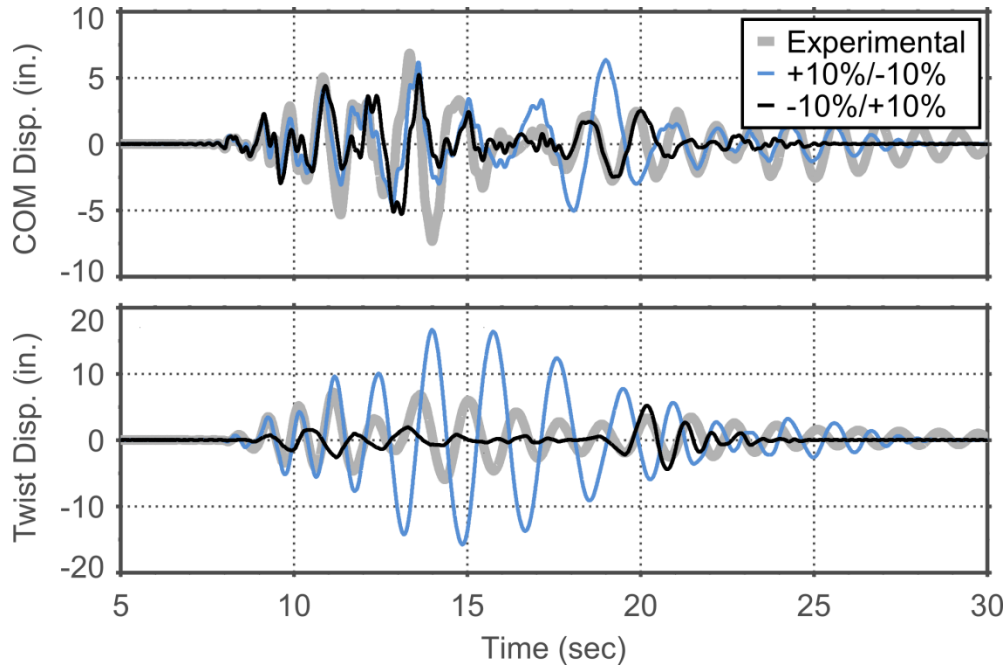

Figure 9.25

The Twist displacements in the model with parameters meant to delay bar fracture (+10%/-10%) were much larger than those in the model with fatigue parameters meant to accelerate it (-10%/+10%). In the model with fatigue parameters meant to delay bar fracture, all of the bars had fractured in Bent 1 and only 7 bars had fractured in bents 1 and 2 by the start of 221% Design Level motion (Motion 19). This pattern of fracturing of the reinforcement led to an increase in the asymmetry of strength and stiffness in the bridge, which led to large twist displacements. In contrast, the model with fatigue parameters meant to accelerate bar fracture had all of the bars in the bridge fracture prior to the 221% Design Level motion (Motion 19). This made the bridge more flexible, but did not significantly alter the asymmetry of strength and stiffness of the bridge. This led to smaller twist displacements.

9.8 Conclusions

A column modeling approach for pre-tensioned, rocking columns was implemented in OpenSees for both the subassembly and shaking table tests. The following conclusions were drawn from a comparison of the measured responses and those predicted by the models.

Concrete Constitutive Behavior. Using the concrete constitutive model with early reloading in compression (*ConcreteCM*) predicted the cross-over drift ratios more accurately than did the concrete model that lacked that feature (*Concrete04*).

Effective Depth of the Column Concrete. The force-displacement behavior of the numerical models was found to vary with the effective depth of the column concrete used in the zero-length elements. This value was calibrated in both the subassembly and shaking table models, and found to be roughly half of one column diameter.

Influence of fatigue parameters. Both the center-of-mass and twisting displacements of the pre-tensioned rocking bridge during the high amplitude motions were highly dependent on the number and location of deformed bar reinforcement fractures during the experimental program. Small variations to the fatigue parameters were found to have a large influence on the behavior of the numerical model. Further investigation into the effect of the fatigue model on the behavior of the pre-tensioned bridge can be found in Mantawy and Sanders (2016), who developed a modeling approach specifically to investigate reinforcement fracture during the shaking table tests.

CHAPTER 10: SUMMARY AND CONCLUSIONS

A new precast, pre-tensioned bridge substructure system has been developed. The system accelerates construction by using precast columns and cap beams, reduces residual seismic displacements by pre-tensioning the columns with partially unbonded tendons to create a rocking system, and eliminates seismic damage to the column concrete by armoring the ends of the columns. The system is the built on previous research at the University of Washington over the past decade.

The column-to-cap beam and column-to-foundation connections of the new system are similar to previously tested connections [Davis et al. 2012, Haraldsson et al. 2013]. The columns are outfitted with steel shoes at the connection interface that both protect the column concrete and promote rocking by providing a natural crack plane. Column longitudinal reinforcement is locally debonded at the connection interface to prevent premature bar fracture, a damage state that was observed in previous tests of the pre-tensioned column concept.

To validate this concept, subassembly tests were conducted by Schaefer et al. (2014a) and Kennedy (2015). The results of these tests informed a series of shaking table tests on a two-span, quarter-scale bridge. The bridge was constructed with precast, pre-tensioned columns and precast cap beams, and was designed to have strength and geometry similar to those of a previously-tested bridge built with cast-in-place construction methods [Johnson et al 2008]. The experimental programs were similar enough to allow direct comparison between the two tests.

10.1 Achievement of Performance objectives

The subassembly and shaking table experiments were used to assess the effectiveness of the new bridge system in meeting three key objectives:

Accelerated Construction. Connections similar to those used in the proposed system, but without pre-tensioning, have been successfully tested in the laboratory and constructed in the field [Khaleghi et al. 2012]. The addition of pre-tensioning causes no alterations to the column-to-spread footing connection and only minor alterations to the column-to-cap beam connection. In the shaking table tests, the use of precast components and connection details allowed the precast, pre-tensioned bridge to be constructed in the laboratory environment in 20% of the time needed for the conventional cast-in-place bridge that had been tested in 2005 [Johnson et al 2008].

Elimination of Residual Displacements. The columns in the subassembly tests exhibited good re-centering when the transverse load was removed, returning to 1% of vertical even after excursions to drift ratios exceeding 10%. The residual drifts were consistently smaller in shaking table tests of the precast, pre-tensioned bridge than in the conventional cast-in-place bridge. During the 221% Design Level motion (Motion 19), the residual drift ratio in the conventional, cast-in-place bridge reached 0.5%, and the extensive damage required removal of the added inertial mass blocks. By end of testing, the maximum residual drift was 1.7% in Bent 3. In contrast, the residual drift in the precast, pre-tensioned bridge never exceeded 0.4% despite its being subjected to an additional series of high-intensity, near-field ground motions that caused peak drifts of more than 12%.

Suppression of Concrete Damage. The steel shoes eliminated structural concrete spalling, both in the subassembly tests and the shaking table tests. The only damage to the column

concrete in the subassembly tests was cosmetic and could likely be avoided by a minor change in geometry. The only cracks that formed in the precast, pre-tensioned bridge were during the 221% Design Level motion (Motion 19); they were few in number (half of the columns never cracked) and never exceeded hairline width. In the precast, pre-tensioned bridge, the grout at the interface suffered some crushing, but it could have been repaired by injection without the need to close the bridge. In contrast, every column in the conventional cast-in-place bridge sustained both extensive cracking and major spalling during the shaking table tests, starting during the 67% Design Level motion (Motion 15).

10.2 Deformation Behavior

These tests offered insight into the deformation behavior of the bridge.

Maximum Displacement Demands. During the shaking table tests, the maximum drift ratios of the pre-tensioned bridge were essentially identical to the cast-in-place bridge through the 100% Design Level motion (Motion 16). After this motion, the peak drift ratios were higher in the pre-tensioned bridge due to the fracture of longitudinal reinforcement and the yielding of prestressing strands.

Concentration of Column Deformations at the Connection Interface. The behavior of the pre-tensioned specimens was dominated by the rigid-body rotation of the columns as evidenced by the rotations measured at the precast joints, and the strains in the prestressing tendons and deformed bar reinforcement.

Exceptional Ductility. In the subassembly tests, no significant reduction in lateral strength was observed even to drift ratios exceeding 10%. The moment-drift responses of the spread footing and cap beam subassemblies were remarkably similar despite the different connection detailing.

10.3 Detailing Considerations

These tests offered information with which to evaluate the details of the columns.

Effectiveness of Dowel Bar. The dowel bar that was included in the column-to-cap beam subassembly test to transfer shear forces from the column to the cap beam proved to be unnecessary. Friction was sufficient to transfer all of the column shear force to the foundation in the column-to-spread footing subassembly and shaking table tests.

Effect of Debonded Length of Deformed Bar Reinforcement. In the subassembly tests, the first reinforcing bar fractured at drift ratios of roughly 6% and 7% for the column-to-spread footing and column-to-cap beam subassemblies, respectively. This difference was consistent with the differences in debonded lengths of the longitudinal reinforcing, which were 16 and 24 bar diameters, respectively. In the shaking table tests, the reinforcement was debonded for a total of 24 bar diameters, which was similar to the value in the column-to-cap beam subassembly. Bar buckling first occurred in the conventional cast-in-place bridge at a drift ratio of 5.5% in Bent 3, but never occurred in the precast, pre-tensioned bridge, owing to the stiff confinement provided by the steel tube detail. The first bar fractures occurred at 7.8% and 5.6% drift ratio in the conventional and precast, pre-tensioned bridges respectively. It is likely that bar fracture in the precast, pre-tensioned bridge could be delayed by increasing the length of the deliberately debonded region of the bars.

Effect of Debonding Material. The material (steel vs PVC tubes) used to debond the longitudinal reinforcing bars did not affect the ability of the sleeve to suppress bar buckling, nor did it affect the drift ratio at bar fracture.

Effect of Initial Prestress in the Strands. The strands in the subassembly tests remained essentially elastic until a drift ratio of roughly 3%. This drift ratio is largely determined by the

initial stress in the strands, which in this case was 1,137 MPa (165 ksi), and by the column's length/diameter ratio. Because re-centering is promoted by the total prestressing force rather than the stress in any one individual strand, using a lower initial stress, with a corresponding large number of strands, would have delayed strand yielding even further.

Effect of Steel Confining Tube Thickness. The steel confining tubes used in the shake table test had a diameter-to-thickness ratio of 90. Bulging of the steel confining tube was first observed during the 177% Design Level motion (with maximum drift ratios of 9.2% and 6.0% in bents 1 and 3 respectively). Bulging could be likely delayed by using a thicker walled tube. The confining tubes used in the subassembly tests had a diameter-to-thickness ratio of 80 and remained elastic for the entire test protocol.

Strain Demands. For a design target drift ratio, the strains in the longitudinal reinforcing bars and the prestressing strands can be estimated well using rigid body kinematics

10.4 Design Procedure

These tests provided the basis with which to develop a design procedure aligning with the current AASHTO guidelines.

Performance Level and Deformation Limits. The life-safety minimum performance level mandated in the *AASHTO Guide Specifications for LRFD Seismic Bridge Design* (2015) limits the displacement capacity of the columns during a seismic event based on strains within the column section. This criterion is inappropriate for the new system, which can tolerate, without concrete damage, much higher ductility demands than can a conventional cast-in-place system. Performance levels higher than life-safety should therefore be considered, and suitable criteria must be established for defining them. Five performance levels were proposed for the pre-tensioned rocking system. They included fully operational, operational, limited damage, life

safety and near collapse. These performance levels were differentiated based on deformation limits corresponding to strand yielding, loss of prestress, reaching the rocking limit, and deformed bar reinforcement fracture.

Permissible Design Space. The permissible design space for proportioning the column reinforcement can be driven largely by the allowable tensile stress in the columns under service loads. For prestressed columns with unbonded tendons the *AASHTO LRFD Bridge Design Specifications* (2016) requires that columns must not decompress under Service IV loads. This requirement, rather than the required seismic performance, may control the size of the column and the required amount of deformed bar steel and prestressing steel reinforcement. In addition, the moments in the columns under Service IV loading could be controlled by temperature deformations imposed on the system under a temperature change that is uniform through the deck thickness. The requirement that the columns not decompress under these loads proves to be a critical constraint on optimizing the design of the columns for seismic performance.

Moment Rotation Analysis. The use of moment-rotation, rather than moment-curvature analyses to determine the inelastic response of the system is only a minor departure from current practice, and this change can easily be implemented in current software packages. The effective stiffnesses of the columns in the subassembly tests, found using this method, agreed well with experimental results.

10.5 Numerical Modeling

A column modeling approach for pre-tensioned, rocking columns was implemented in OpenSees for both the subassembly and shaking table tests. The major challenge in developing such a model is the representation of the rocking behavior of the prestressed columns.

Concrete Constitutive Behavior. Using a concrete constitutive model (*ConcreteCM*) with early reloading in compression more accurately predicted the force-displacement relationships and cross-over drift ratios than the concrete model that did not (*Concrete04*).

Effective Depth of the Column Concrete. The force-displacement behavior of the numerical models was found to vary with the effective depth of the column concrete. The effective depth is the length that relates strain to deformation. This value was calibrated in both models, and found to be roughly half of one column diameter for both the subassembly and shaking table tests.

Influence of fatigue parameters. Both the center-of-mass and twisting displacements of the pre-tensioned rocking bridge during the high amplitude motions depended on the number and location of deformed bar reinforcement fractures during the experimental program. Small changes to the fatigue parameters were found to have a large influence on the behavior of the numerical model. Further investigation into the effect of the fatigue model on the behavior of the pre-tensioned bridge can be found in Mantawy and Sanders (2016), who developed a modeling approach specifically to investigate reinforcement fracture during the shaking table tests.

REFERENCES

AASHTO (2011). "*AASHTO Guide Specification for LRFD Seismic Bridge Design*" 2nd ed., American Association of State Highway and Transportation Officials, Washington, D.C.

AASHTO (2012). "*LRFD Bridge Design Specifications*" 6th ed., American Association of State Highway and Transportation Officials, Washington, D.C.

Ameli, M.J., Parks, J.E., Brown, D.N., Pantelides C.P., (2015) "Seismic evaluation of grouted splice sleeve connections for reinforced precast concrete column–to–cap beam joints in accelerated bridge construction", *PCI Jo.*, Precast/Prestressed Concrete Institute, 60(2): 80-103.

Belleri, A. and Riva, P. (2012). "Seismic Performance And Retrofit Of Precast Concrete Grouted Sleeve Connections," *PCI Jo.* , pp. 97-109.

Berry, M. (2006). "Experimental Calibration of OpenSees Components Using the PEER Column Database". PhD thesis, University of Washington.

Berry, M.P. and Eberhard, M.O. (2007). "Performance Modeling Strategies for Modern Reinforced Concrete Columns." Pacific Earthquake Engineering Research Center Report, PEER 2007/7, University of California, Berkeley, July, 206 pp.

Billington, S.L., R.W. Barnes, and J.E. Breen (1999). "A Precast Segmental Substructure System for Standard Bridges," PCI Journal, Vol. 44, No. 4, August, pp. 56-73.

Billington, S.L., R.W. Barnes, and J.E. Breen (2001). "Alternate Substructure Systems for Standard Highway Bridges," ASCE Journal of Bridge Engineering, Vol. 6, No. 2, March/April, pp. 87-94.

Billington, S.L., and Yoon, J.K. (2004) "Cyclic Response of Precast Bridge Columns with Ductile Fiber-reinforced Concrete," *Jo. Bridge Eng.*, 9(4): 353-363.

Brown, W. (2008). "Bar Buckling in Reinforced Concrete Bridge Columns." MSCE Thesis, University of Washington, Seattle, WA.

Calvi, G.M., Kowalsky, M. (2013) "Displacement-Based Seismic Design of Bridges" *Structural Engineering International*. May 2013.112-121

Cheok, G. S., and Lew, H. S. (1991). "Performance of Precast Concrete Beam-to-Column Connections Subject to Cyclic Loading". *PCI Jo*., 36(3): 56–67.

Cheok, G. S., and Lew, H. S. (1993). "Model Precast Concrete Beam-to-Column Connections Subject to Cyclic Loading". *PCI Jo*., 38(4): 80-92.

Chou, C.-C. and Chen, Y.-C. (2006), Cyclic tests of post-tensioned precast CFT segmental bridge columns with unbonded strands. *Earthquake Eng. Struct. Dyn*., 35: 159–175. doi:10.1002/eqe.512

Christopoulos, C., Filiatrault, A., Folz, B. (2002). "Seismic response of self-centering hysteretic SDOF systems." Earthquake Engineering and Structural Dynamics, 31:1131-1150 (DOI: 10.1002/eqe.152)

Cohagen, L.S., Pang, J.B.K., Eberhard, M.O., and Stanton, J. F. (2008). " A Precast Concrete Bridge Bent Designed to Re-center after an Earthquake." Washington State Department of Transportation Report No. WA-RD 684.3, Washington State Department of Transportation, Washington, 2008.

Computers and Structures, Inc (2016) SAP 2000: Version 18.0.1. Walnut Creek, CA

Cousins, T.E., Johnston, D.W. and Zia, P. (1990)."Transfer and development length of epoxy coated and uncoated prestressing strand", *PCI Jo.*, Precast/Prestressed Concrete Institute, 35(4): 92-103.

Davis, P. M., Janes, T. M., Eberhard, M. O., and Stanton J. F., (2012). "Unbonded pre-tensioned columns for bridges in seismic regions." Pacific Earthquake Engineering Research Center Rep., Pacific Earthquake Engineering Research Center, Berkeley, CA.

Deslis, A. (2014) "Completing the ABC Package: Public Outreach Tactics" National Accelerated Bridge Construction Conference, Miami, United States

Dusenberry, K.T. (2015) "Lateral Slide of Historic Bridge in Washington State" National Accelerated Bridge Construction Conference, Miami, United States

ElGawady, M., Booker, A., and Dawood, H. (2010). "Seismic Behavior of Posttensioned Concrete-Filled Fiber Tubes." *Jo. Compos. Constr.*, 10.1061/(ASCE)CC.1943-5614.0000107, 616-628.

Elwood, K.J., Eberhard, M.O. (2009). "Effective stiffness of reinforced concrete columns", *ACI Str. Jo.*, American Concrete Institute, 106(4): 476-484.

FHWA (2009). "Connection Details for Prefabricated Bridge Elements and Systems", U.S. Department of Transportation, Federal Highway Administration.

FHWA (2011). "Accelerated Bridge Construction: Experience in Design, Fabrication and Erextion of Prefabricated Elements and Systems," U.S. Department of Transportation, Federal Highway Administration.

Finnsson, G. (2013). "Unbonded Pre-Tensioned Bridge Columns with Hybrid Fiber-Reinforced Concrete Shells", MSCE Thesis, University of Washington, Seattle, WA.

Guerrini, G., Restrepo, J., Massari, M., and Vervelidis, A. (2015). "Seismic Behavior of Posttensioned Self-Centering Precast Concrete Dual-Shell Steel Columns." *Jo. Struct. Eng.*, 141(4), 04014115.

Gulkan, P. and Sozen, M.A., (1974) " In-elastic Responses of Reinforced Concrete Structures to Earthquake Motions", *Proceedings of the ACI,* Vol. 71, No. 12, Dec., pp605-610.

Haber, Z., Saiidi, M., and Sanders, D. (2013). "Precast Column-Footing Connections for Accelerated Bridge Construction in Seismic Zones," Center for Civil Engineering Earthquake Research, Department of Civil and Environmental Engineering, University of Nevada, Reno, Nevada, Report No. CCEER-13-08, May 2013

Haraldsson, O.S. (2015) A" A Pre-Tensioned Bent System for Accelerated Bridge Construction in Seismic Regions" Ph.D. Thesis, University of Washington, Seattle, WA.

Haraldsson, O.S., Janes, T.M., Eberhard, M.O., and Stanton, J.F. (2013). "Seismic Resistance of Socket Connection between Footing and Precast Column," *Jo. Bridge Eng., ASCE,* 10.1061/(ASCE)BE.1943-5592.0000413

Hewes, J. T., and Priestley, N. (2002). "Seismic design and performance of precast concrete segmental bridge columns." Rep. No. SSRP-2001/25, Univ. of California at San Diego.

Hieber, D., Wacker, J., Eberhard, M.O., and Stanton, J. F. (2005a). "Precast Concrete Pier Systems for Rapid Construction of Bridges in Seismic Regions." Washington State Department of Transportation Report No. WA-RD-611.1, Washington State Department of Transportation, Washington, 2005.

Hieber, D., Wacker, J., Eberhard, M.O., and Stanton, J.F. (2005b). "State of the Art Report on Precast Concrete Systems for Rapid Construction of Bridges." Washington State Department of Transportation Report No. WA-RD-549.1, Washington State Department of Transportation, Washington, 2005.

Ishizuka, T., Hawkins, N. M., and Stanton, J. F., (1984) "Experimental Study of the Seismic Resistance of a concrete Exterior Column Beam Sub-assemblage Containing Unbonded Post-Tensioning Tendons," Dept. of Civil Engineering, University of Washington, May.

Japan Road Association: Design Specifications of Highway Bridges, Part V Seismic Design, 2002.

Jeong, H, Sakai, J. and Mahin, S.A. (2008). "Shaking Table Tests and Numerical Investigation of Self-Centering Reinforced Concrete Bridge Columns", Pacific Earthquake Engineering Research Center Report 2008/06.

Johnson, N., Ranf R., Saiidi, M., Sanders, D., Eberhard, M, (2008). "Seismic Testing of a Two-Span Reinforced Concrete Bridge," *Jo. Bridge Eng.*, ASCE March/April 2008, pp 173-182

Johnson, N., Saiidi, M., and Sanders, D. (2006). "Large-scale experimental and analytical seismic studies of a two-span reinforced concrete bridge system." Rep. CCEER-06-02, Civil Engineering Dept., Univ. Of Nevada, Reno, NV.

Kennedy, B. (2015). "Rocking Connection Between a Precast Bridge Column and Cap Beam", MSCE Thesis, Department of Civil and Environmental Engineering, University of Washington, Seattle, WA.

Kennedy, B. J. , Thonstad, T. , Eberhard, M. O., Stanton, J. F. (2014). "Cyclic Testing of an Unbonded Pre-tensioned Bridge Column with Rocking Detail: Capbeam Specimen", Network for Earthquake Engineering Simulation (distributor), Dataset, DOI:10.4231/D3HQ3S04M

Khaleghi, B., Schultz, E., Seguirant, S.J., Marsh, L.M., Haraldsson, O., Eberhard. M.O. and Stanton, J.F. (2012). “Accelerated Bridge Construction in Washington State: From Research to Practice.“ *PCI Jo.* 57(4), Fall, pp. 34-49.

Kowalsky, M. J. (2002),“A displacement-based approach for the seismic design of continuous concrete bridges“. *Earthquake Engng. Struct. Dyn*., 31: 719–747. doi:10.1002/eqe.150

Kumar P., Jen G., Trono W., Panagiotou M., Ostertag C. (2011). Self compacting hybrid fiber reinforced concrete composites for bridge columns, PEER Report No. 2011/106, Pacific Earthquake Engineering Research Center, University of California, Berkeley, CA.

Lehman, D.E., Moehle J.P. (1998). “Seismic performance of well-confined concrete bridge columns“. Technical Report 1998/01, Pacic Earthquake Engineering Research-Center.

Lehman, D. and Roeder, C. (2012). "Foundation connections for circular concrete-filled tubes." *Jo. of Constructional Steel Research*, 10.1016/j.jcsr.2012.07.001, 212-225.

Mander, J., Panthaki, F., and Kasalanati, A. (1994). ”Low-Cycle Fatigue Behavior of Reinforcing Steel.” J. Mater. Civ. Eng., 6(4), 453–468.

Mander, J. Priestley, M., and Park, R. (1988). “Theoretical Stress-Strain Model for Confined Concrete.” *Journal of the Structural Division ASCE 114(8)*, 1804-1826.

Manson, S.S. (1954) “Behavior of Materials Under Conditions of Thermal Stress” National Advisory Committee for Aeronautics. Report No. NACA-TR-1170

Mantawy, I., Thonstad, T., Sanders, D., Stanton, J., and Eberhard, M. (2016). "Seismic Performance of Precast, Pretensioned, and Cast-in-Place Bridges: Shake Table Test Comparison." *Jo. Bridge Eng.* , 10.1061/(ASCE)BE.1943-5592.0000934.

Mantawy, I.M. and Sanders, D.H.(2016) A“Assesment of an Earthquake Resilient Bridge with Pretensioned, Rocking Columns“ Center For Civil Engineering Earthquake Research,

Department Of Civil and Environmental Engineering, University of Nevada, Reno, Nevada, Report No. CCEER-16-03, May 2016.

Marsh, L.M., Wernli, M., Garrett, B.E., Stanton, J.F., Eberhard, M.O., and Weinert, M.D. (2011). NCHRP Report 698: "Application of Accelerated Bridge Construction Connections in Moderate-to-High Seismic Regions." Transportation Research Board, Washington, DC.

Marsh, L.M., Stringer, S.J. (2013) NCHRP Synthesis 440: "Performance-Based Seismic Bridge Design: A Synthesis of Highway Practice" Transportation Research Board, Washington, DC.

Mashal M. and Palermo A. (2014), "Quasi-Static Experimental Testing of Emulative and Low-Damage Seismic Technologies for Accelerated Bridge Construction in Seismic Areas", National Accelerated Bridge Construction Conference, Miami, United States

Matsumoto, E., Waggoner, M., Kreger, M., Vogel, J., and Wolf, L. (2008). "Development of a Precast Concrete Bent-Cap System. *PCI Jo., 53*(3), 74-99.

Miner, M. A., (1945) "Cumulative damage in fatigue." *Jo. of Applied Mechanics.*, 67, A 159-A 164.

Mole, A. (1994). "Seismic Response of Hybrid Connections in Precast concrete Frames", Master's Thesis, Department of Civil and Environmental Engineering, University of Washington, Seattle, WA.

Motaref, S., Saiidi, M., and Sanders, D. (2014). "Shake Table Studies of Energy-Dissipating Segmental Bridge Columns." J. Bridge Eng., 10.1061/(ASCE)BE.1943-5592.0000518, 186-199.

Moyer, M.J. and Kowalsky, M.J (2003) "Influence of Tension Strain on Buckling of Reinforcement in Concrete Columns" *ACI Struc. Jo.,* 100(1), 75-85

OpenSees Development Team (2012). Opensees: Open system for earthquake engineering simulations. Version 2.4.0, Berkeley, CA.

Osanai, Y., Watanabe, F., and Okamoto, S., (1996). "Stress Transfer Mechanism of Socket Base Connections with Precast Concrete Columns." *ACI Struct Jo.,* ACI, Chicago. IL. May-June, pp. 266-276.

Ou, Y.C., Tsai, M.S., Chang, K.C. and Lee, G. C. (2010). "Cyclic behavior of precast segmental concrete bridge columns with high performance or conventional steel reinforcing bars as energy dissipation bars". *Earthquake Eng. Struct. Dyn.,* 39: 1181–1198. 10.1002/EQE.986

Ozden, S., Ertas, O. (2007). "Behavior of Unbonded, Post- Tensioned, Precast Concrete Connections with Different Percentages of Mild Steel Reinforcement" *PCI Jo.,* 52(2) pp. 32-44

Palermo, A., Pampanin, S., and Marriott, D. (2007). "Design, Modeling, and Experimental Response of Seismic Resistant Bridge Piers with Posttensioned Dissipating Connections." J. Struct. Eng., 10.1061/(ASCE)0733-9445(2007)133:11(1648), 1648-1661.

Palmieri, L., Saqan, E., French, C. and Kreger M. (1996) "Ductile Connections for Precast Concrete Frame Systems". *ACI Special Publication,* ACI 162-13, pp. 313-356

Pang, J.B.K., Eberhard, M.O., and Stanton, J.F. (2010). "Large-Bar Connection for Precast Bridge Bents in Seismic Regions," *Jo. Bridge Eng., ASCE,* May-June, pp 231-239.

PEER, Pacific Earthquake Engineering Research Center, "PEER Strong Motion Database," http://peer.berkeley.edu/smcat/.

Phillippi, D. and Hegemier, G. (2013) "Use of Mechanical Couplers in Concrete Columns". AEI 2013: pp. 715-724. DOI: 10.1061/9780784412909.070

Popovics, S. (1973). "A numerical approach to the complete stress-strain curves for concrete." Cement and Conor. Res. , 3 (5), 583–599

Priestley M.J.N., and Park, R. (1987). “Strength and ductility of concrete bridge columns under seismic loading”. ACI Struct. Jo. 84(1), 61–76.

Priestley, M.J.N. and Tao, J. R. (1993) “Seismic Response of Precast Prestressed Concrete Frames With Partially Debonded Tendons”. *PCI Jo.*, 38(1): 58-69.

Priestley, M. J. N., F. Seible, and G. M. Calvi. (1996). Seismic Design and Retrofit of Bridges. John Wiley and Sons, New York, NY

Priestley, M.J.N. and MacRae, G. A. (1996) Seismic Tests of Precast Beam-to-Column Joint Subassemblages with Unbonded Tendons. PCI Journal, 64-80.

Priestley M.J.N., Calvi, M.C., and Kowalsky, M.J. (2007) Displacement-Based Seismic Design of Structures IUSS Press, Pavia, , 670 pp.

Ranf, R.T. (2007). “Model Selection for Performance Based Earthquake Engieering of Bridges”. PhD thesis, University of Washington.

Restrepo, J. and Rahman, A. (2007). "Seismic Performance of Self-Centering Structural Walls Incorporating Energy Dissipators." *Jo. Struct. Eng*., 10.1061/(ASCE)0733-9445(2007)133:11(1560), 1560-1570.

Restrepo, J., Matsumoto, E., and Tobolski, M. (2011). “Development of Precast Bent Cap Systems for Seismic Regions.” *NCHRP Report no 681*. Transportation Research Board, Washington, DC.

Schaefer, J., Kennedy, B., Stanton, J.F., Eberhard, M.O. (2014a). “Unbonded Pretensioned Bridge Columns with Rocking Detail”, Pacific Earthquake Engineering Research Center Report 2014.

Schaefer, J.A., Thonstad, T., Kennedy, B. J.,Eberhard, M. O., Stanton, J. F. (2014b). "Cyclic Testing of an Unbonded Pre-tensioned Bridge Column with Rocking Detail: Footing

Specimen 01", Network for Earthquake Engineering Simulation (distributor), Dataset, DOI:10.4231/D3G737473

Schoettler, M., Eberhard, M., Mahin, S., Mosalam, K., Ostertag, C., Panagiotou, M., Restrepo, J., Stanton, J., and Terzic, V., (2013). "Advancing the performance of bridge columns: Overview of a shake table test program". Proceedings of the 7th National Seismic Conference on Bridges & Highways. Paper No. 123, Oakland, CA.

Sideris, P., Aref, A., and Filiatrault, A. (2015). "Experimental Seismic Performance of a Hybrid Sliding–Rocking Bridge for Various Specimen Configurations and Seismic Loading Conditions." J. Bridge Eng., 10.1061/(ASCE)BE.1943-5592.0000742, 04015009.

Solberg, K., Mashiko, N., Mander, J., and Dhakal, R. (2009). "Performance of a Damage-Protected Highway Bridge Pier Subjected to Bidirectional Earthquake Attack." *Jo. Struct. Eng.*, 10.1061/(ASCE)0733-9445(2009)135:5(469), 469-478.

Stanton, J.F. and Nakaki, S.D. (2002) "Design Guidelines for Precast Concret Strucural Systems". PRESSS Report No. 01/03-09. Also published as UW Civil Engineering Report No SM02-02.

Stanton, J., Stone, W. C. and Cheok, G. S. (1997). Hybrid Reinforced Precast Frame for Seismic Regions. *PCI Jo.*, 42(2), 20-32.

Stanton, J., and McNiven, H. 1979. "The development of a mathematical model to predict the flexural response of reinforced concrete beams to cyclic loads, using system identification." Rep. No. EERC 79-02, Earthquake Engineering Research Center, Univ. of California, Berkeley, Calif.

Stephens, M.T. (2016) A" Design Expressions and Dynamic Evaluation of CFST Bridges Subjected to Seismic Hazards" Ph.D. Thesis, University of Washington, Seattle, WA.

Stone, W.C., Cheok, G.S. and Stanton, J.F. (1995). "Beam-Column Connections Subjected to Cyclic Loads". *ACI Str. Jo.,* Vol. 92(2), March-April, pp. 229-249.

Steuck, K., Stanton, J.F. and Eberhard, M.O. (2009). "Anchorage of Large-Diameter Reinforcing Bars in Ducts." ACI Str. Jo., July-August, pp 506-513.

Tazarv, M.. and Saiidi, M.S., (2014). "Next Generation of Bridge Columns for Accelerated Bridge Construction in High Seismic Zones," Center For Civil Engineering Earthquake Research, Department Of Civil and Environmental Engineering, University of Nevada, Reno, Nevada, Report No. CCEER-14-06, August 2014.

Thonstad, T., Mantawy, I., Stanton, J.F., Eberhard, M.O. and Sanders, D. (2015). "Shake Table Testing of a Two-Span Bridge Specimen with Unbonded, Pre-tensioned Rocking Columns", Network for Earthquake Engineering Simulation (distributor), Dataset, DOI:10.4231/D33B5W88M

Thonstad, T., Mantawy, I., Stanton, J.F., Eberhard, M.O. and Sanders, D.H. (2016) "Shaking Table Performance of a New Bridge System with Pre-Tensioned, Rocking Columns", *Jo. of Bridge Eng.* , 10.1061/(ASCE)BE.1943-5592.0000867.

Tobolski, M. J. (2010). "Improving the Design and Performance of Concrete Bridges in Seismic Regions". PhD thesis. University of California, San Diego, CA.

Tran, H.V. (2015). "Drilled Shaft Socket Connections for Precast Columns in Seismic Regions." Ph.D. Thesis, University of Washington, Seattle, WA.

Trono, W., Jen, G., Panagiotou, M., Schoettler, M., and Ostertag, C. (2014). "Seismic Response of a Damage-Resistant Recentering Posttensioned-HYFRC Bridge Column." *Jo. Bridge Eng.,* 10.1061/(ASCE)BE.1943-5592.0000692, 04014096.

Tsai W.T. (1988), “Uniaxial Compressional Stress-Strain Relation of Concrete”, *ASCE Jo. of Structural Engineering*, V. 114, No. 9, pp. 2133-2136

Vanek, C., Ryzhikov, V., Rudie, C. Poulson, J. (2014) “Slide-In-Replacement of the Skagit River Collapsed Span“ National Accelerated Bridge Construction Conference, Miami, United States

Varela, S., and Saiidi, M., “Dynamic Performance of Innovative Bridge Columns with Superelastic CuAlMn Shape Memory Alloy and ECC,” *Intl. Jo. of Bridge Eng.* 2(3), 2014, pp. 29-58.

Wacker, J., Hieber, D., Eberhard, M., and Stanton, J. (2005). “Design of Precast Concrete Piers for Rapid Construction of Bridges in Seismic Regions.” Washington State Department of Transportation Report No. WA-RD-629.1, Washington State Department of Transportation, Washington, 2005.

Walsh, K.Q., & Kurama, Y. C. (2012). Effects of Loading Conditions on the Behavior of Unbonded Post-tensioning Strand-anchorage Systems.” *PCI Jo.*, 57(1), 76-96.

Weinert, M.D. (2011). “Substructure Connections for Accelerated Bridge Construction in Seismic Regions”. MSCE thesis. University of Washington, Seattle, WA, 239 p.

White, S. and Palermo, A. (2016). "Quasi-Static Testing of Posttensioned Nonemulative Column-Footing Connections for Bridge Piers." *Jo. Bridge Eng.*, 10.1061/(ASCE)BE.1943-5592.0000872, 04016025.

WSDOT (2016). “*Bridge Design Manual (LRFD)*” Washington State Department of Transportation, Olympia, WA. Version M 23-50.16

Yamashita, R. and Sanders D. (2009) “Seismic Performance of Precast Unbonded Prestressed Concrete Columns” *ACI Str. Jo.*, Nov.-Dec., pp 821-830.

Appendix A: Material Properties

This appendix presents the measured material properties for the subassembly and shaking table test specimens. More detailed information on the material properties for the subassembly tests can be found in Schaefer et al. (2014a) and Kennedy (2015).

A.1 PreT-SF-ROCK

Table A.1 PreT-SF-ROCK concrete properties

	Compression strength (psi)	Modulus of rupture (psi)	Modulus of elasticity (ksi)
Day of Test	10273	673	5617

Table A.2 PreT-SF-ROCK reinforcement properties

	Yield strength (ksi)	Ultimate strength (ksi)
Continuous bars (No. 4)	66.1	88.2
Spiral wire (3 ga.)	86.3	96.0
Prestressing Strand	-	268.1

A.2 PreT-CB-ROCK

Table A.3 PreT-CB-ROCK concrete properties

	Compression strength (psi)	Modulus of rupture (psi)	Modulus of elasticity (ksi)
Day of Test	9030	909	4930

Table A.4 PreT-CB-ROCK grout compressive strengths

	Compression strength (psi)
Grout pad	6875
Central duct	9220
Rebar duct	9200

Table A.5 PreT-CB-ROCK reinforcement properties

	Yield strength (ksi)	Ultimate strength (ksi)
Continuous bars (No. 4)	73.1	107.3
Spiral wire (3 ga.)	86.3	96.0
Prestressing Strand	-	268.1

A.3 Shaking Table Specimen

A.3.1 Concrete Properties

Table A.6 Bent 1 concrete compressive properties

Day	Strength (psi)	Elastic Modulus (ksi)
1	1994	2508
2	4554	3725
3	6028	4161
4	6419	4414
5	7814	4816
6	6985	-
7	7431	5053
10	8808	4992
14	8889	5042
21	9892	5519
28	10267	5396
69	11016	5728
165 (Test)	10062	5806

Table A.7 Bent 2 concrete compressive properties

Day	Strength (psi)	Elastic Modulus (ksi)
1	2996	-
4	6197	-
7	7875	4910
16	8631	5020
28	9418	-
29	-	5355
62	10174	-
66	-	5568
133 (Test)	10259	5963

Table A.8 Bent 3 concrete compressive properties

Day	Strength (psi)	Elastic Modulus (ksi)
1	3007	-
3	6668	-
7	7067	-
28	8867	-
29	8672	4826
56	9390	5011
216 (Test)	9822	5605

Table A.9 Concrete tensile strength on day of test

Column	Average splitting tensile strength (psi)	Standard deviation (psi)
Bent 1	704	32
Bent 2	620	92
Bent 3	573	51

A.3.2 Grout Compressive Strength

Table A.10 Bent 1 grout pad compressive strength

Day	Strength (psi)
3	6850
10	8180
23	6970
43 (Test)	9500

Table A.11 Bent 2 grout pad compressive strength

Day	Strength (psi)
5	7240
11	7660
28	6710
48 (Test)	7800

Table A.12 Bent 3 grout pad compressive strength

Day	Strength (psi)
5	6880
10	8890
24	8410
44 (Test)	9770

Table A.13 Bent 1 duct grout compressive strength

Day	Compressive Strength (psi)	
	North Column	South Column
4	4500	5910
10	6180	9810
27	6070	6360
48 (Test)	6400	7830

Table A.14 Bent 2 duct grout compressive strength

Day	Strength (psi)	
	North Column	South Column
10	6410	4900
20 (Test)	7640	8560

Table A.15 Bent 3 duct grout compressive strength

Day	Strength (psi)	
	North Column	South Column
10	4840	5400
20 (Test)	8500	7120

A.3.3 Column Reinforcement

Table A.16 Column reinforcement properties

Bar Size	Yield Stress (ksi)	Ultimate Stress (ksi)	Elongation at Failure (%)
No. 3 (Continuous bars)	70.5	102	19.0
No. 4 (Discontinuous bars)	64.8	88.7	18.5
W2.9 (Spiral wire)	-	99.4	-
A882 Filled Epoxy Coated Strand	-	268.2	

Table A.16 Cantilever cap beam reinforcement properties

Bar Size	Yield Stress (ksi)	Ultimate Stress (ksi)	Elongation at Failure (%)
No. 3 (Skin steel)	74.5	107.9	12.3
No. 4 (Shear reinforcement)	71.2	107.0	12.6
No. 6 (Beam reinforcement)	67.1	91.2	18.9

Table A.16 Inverted-T cap beam reinforcement properties

Bar Size	Yield Stress (ksi)	Ultimate Stress (ksi)	Elongation at Failure (%)
No. 3 (Skin steel)	70.9	104.3	12.3
No. 4 (Shear reinforcement)	69.5	104.4	13.8
No. 6 (Beam reinforcement)	76.6	112	11.2

Appendix B: Shaking Table Specimen Drawings

This appendix presents the construction drawings for the shaking table test specimen described in Chapter 5 and the locations of the instruments during the tests. Detailed sensor lists, including sensor types and calibration constants can be found on the NEES data repository [Thonstad et. al 2015].

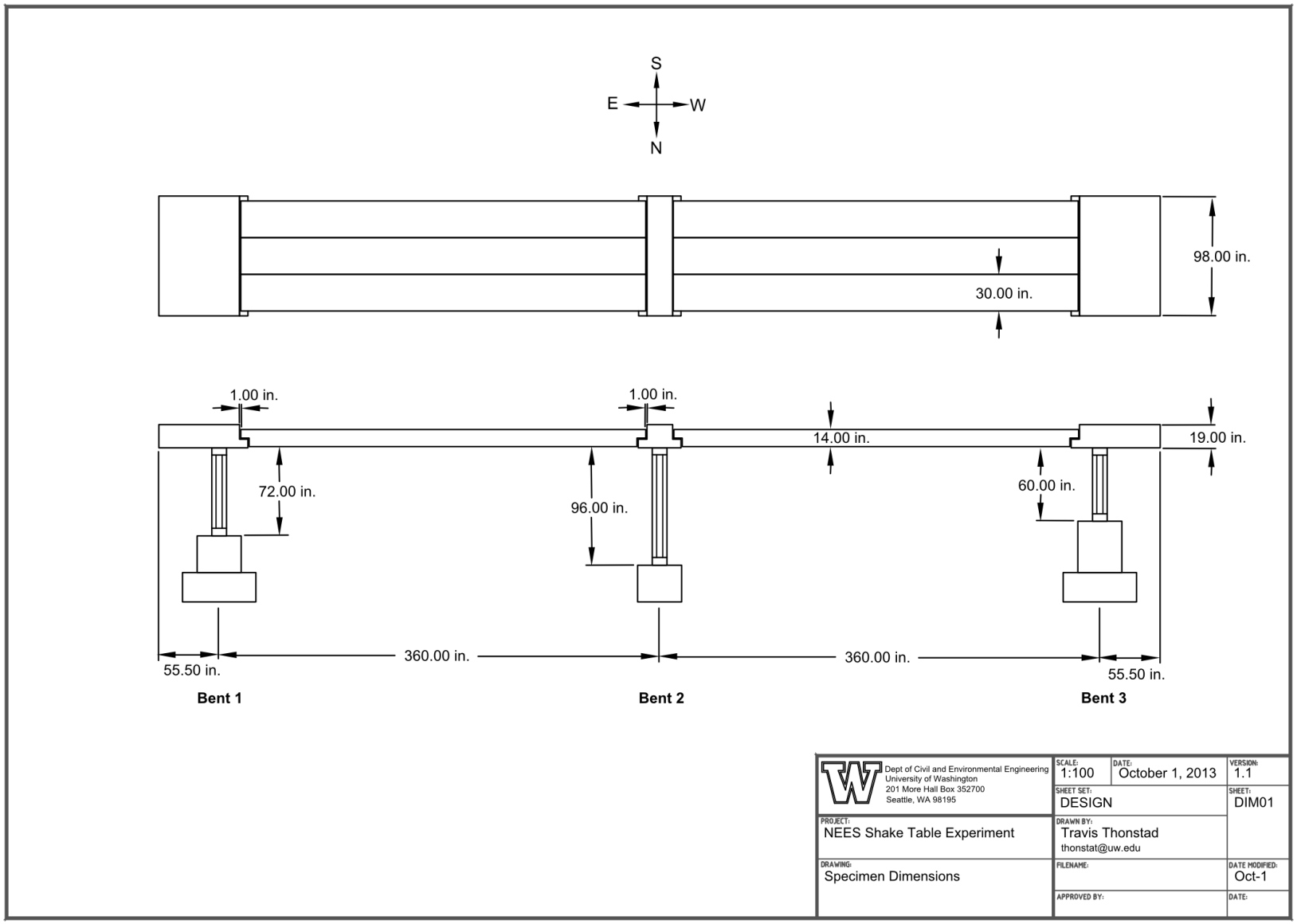

Figure B.1 Specimen dimensions

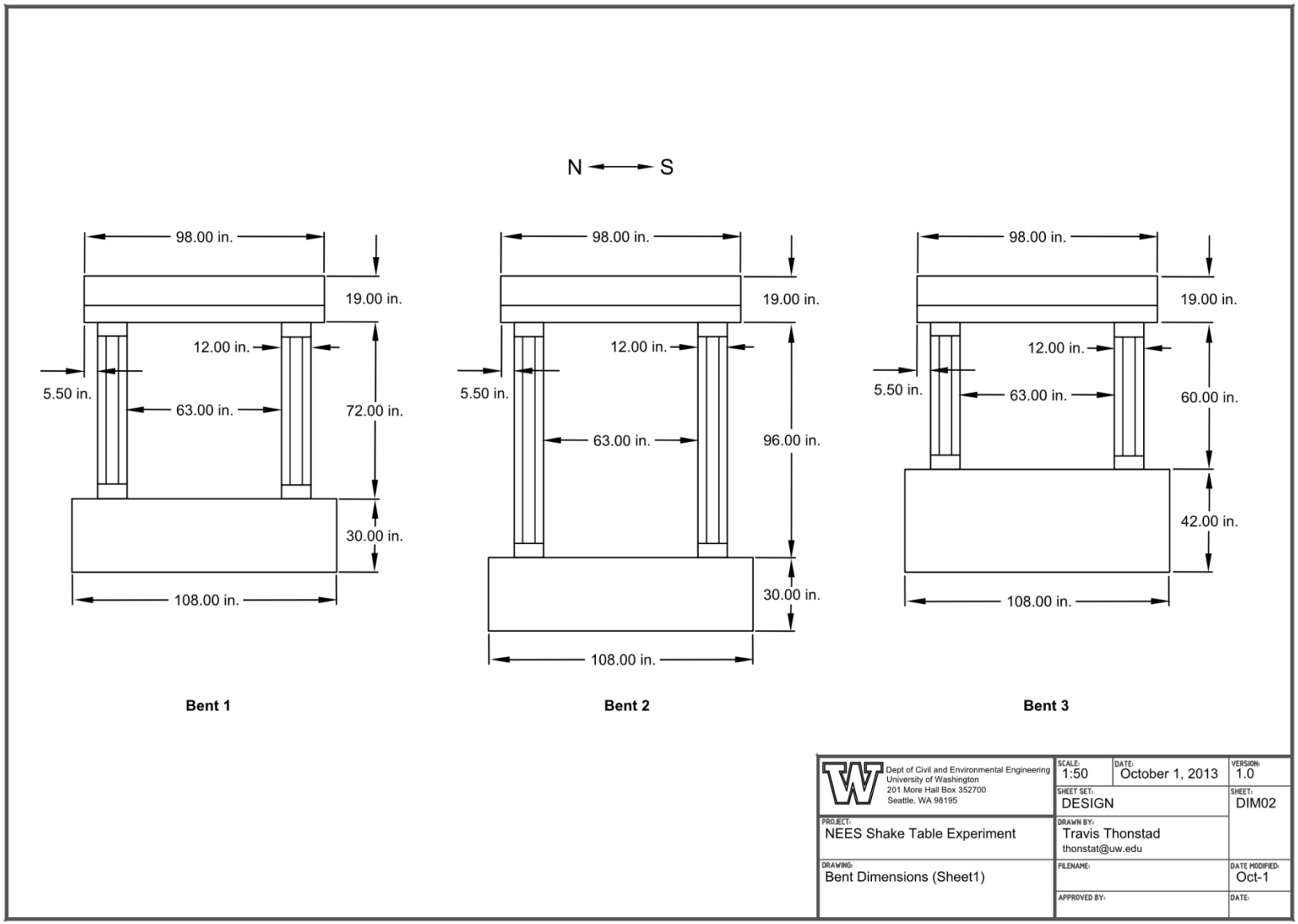

Figure B.2 Bent dimensions in transverse direction of the bridge

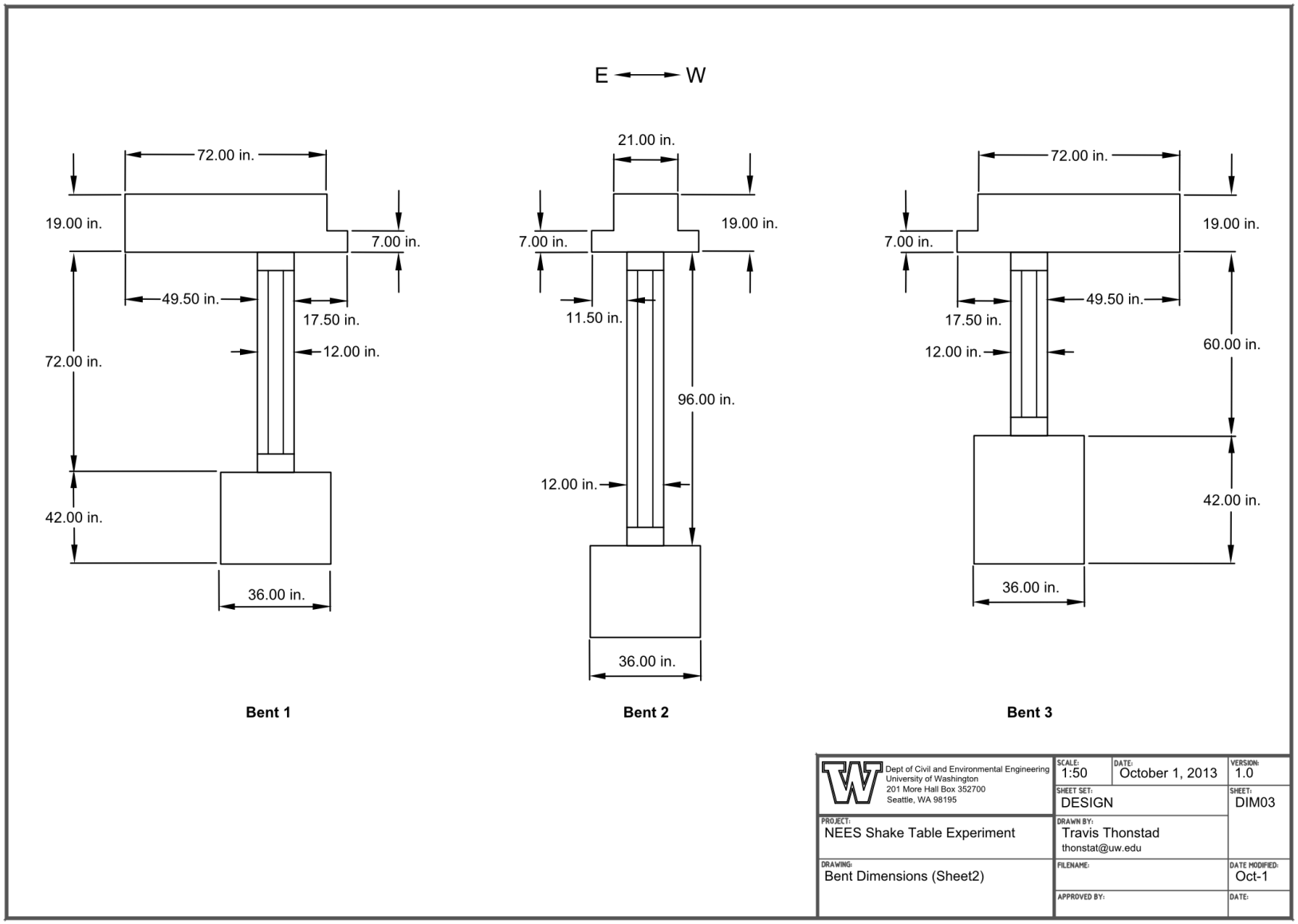

Figure B.3 Bent dimensions in the longitudinal direction of the bridge

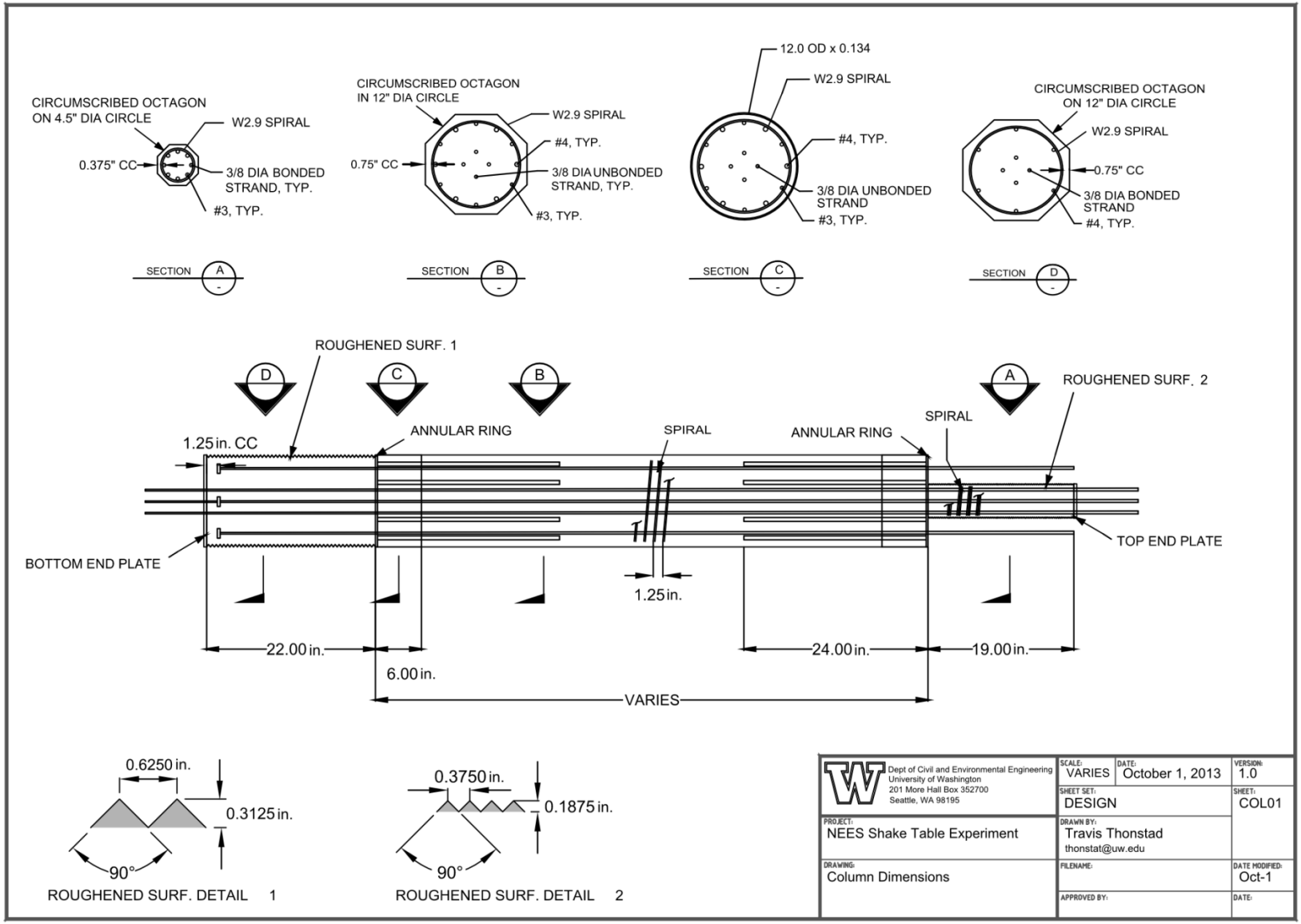

Figure B.4 Column reinforcement and details

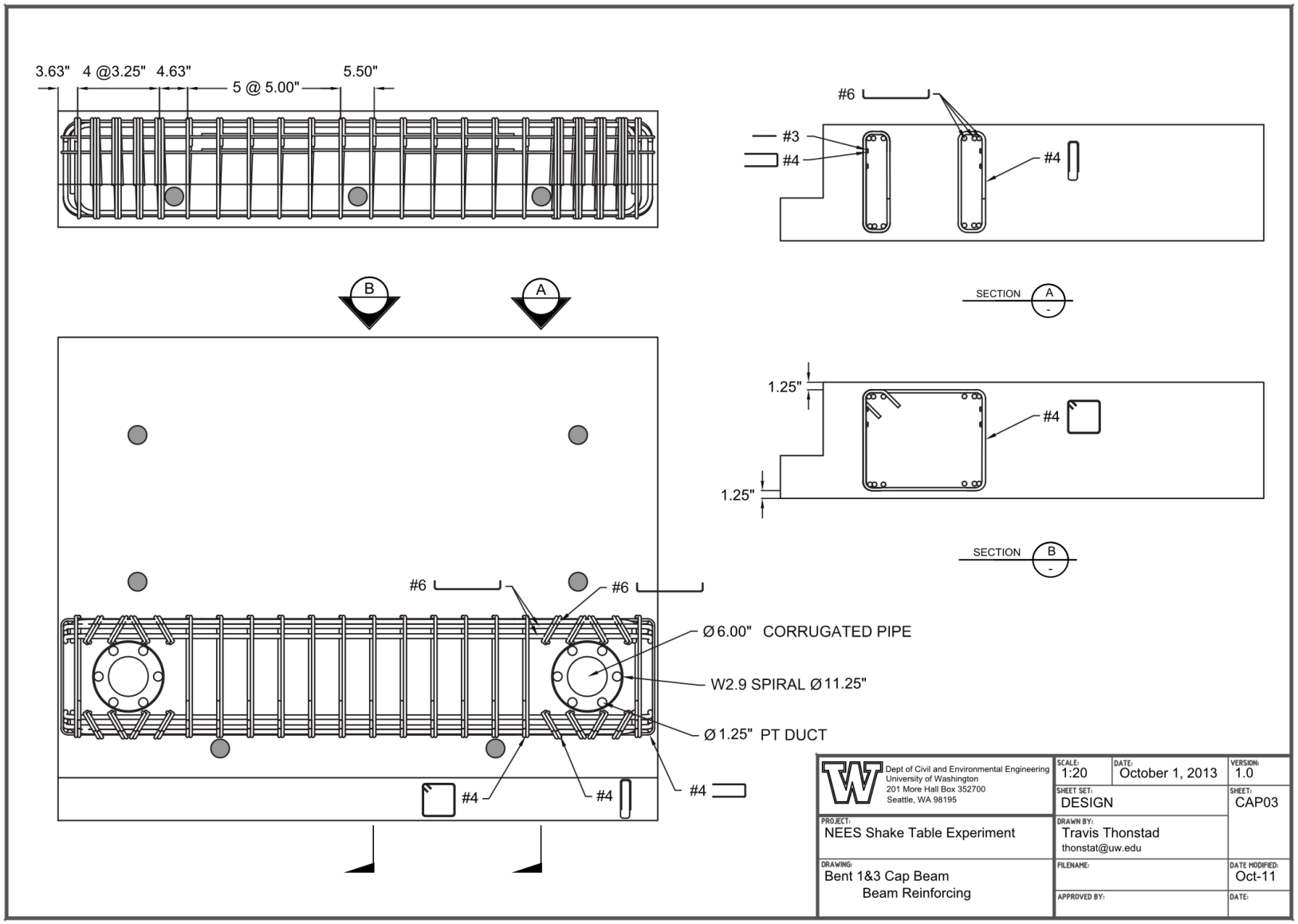

Figure B.5 Cantilever cap beam transverse beam reinforcement

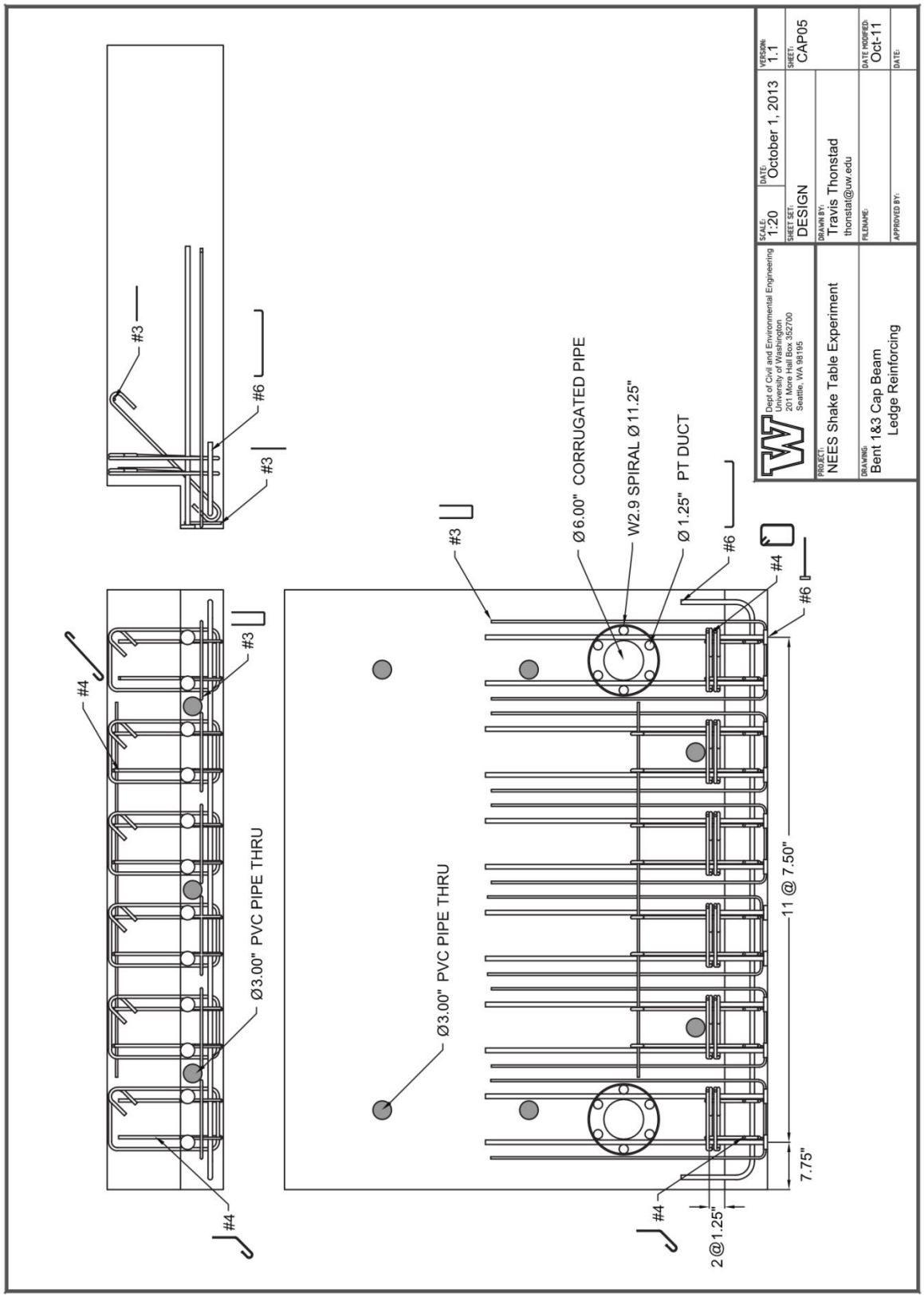

Figure B.6 cantilever cap beam ledge reinforcement

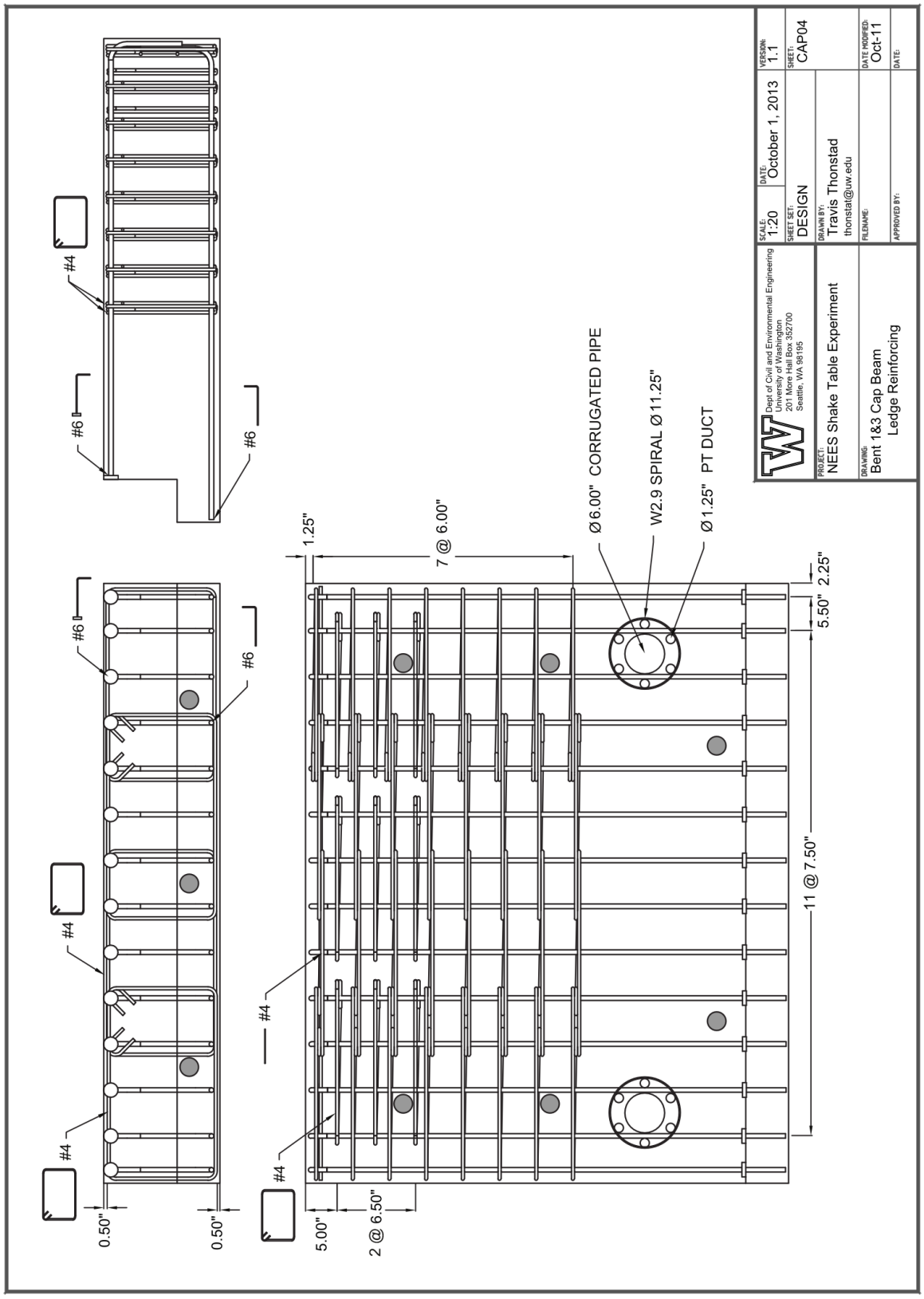

Figure B.7 Cantilever cap beam longitudinal beam reinforcement

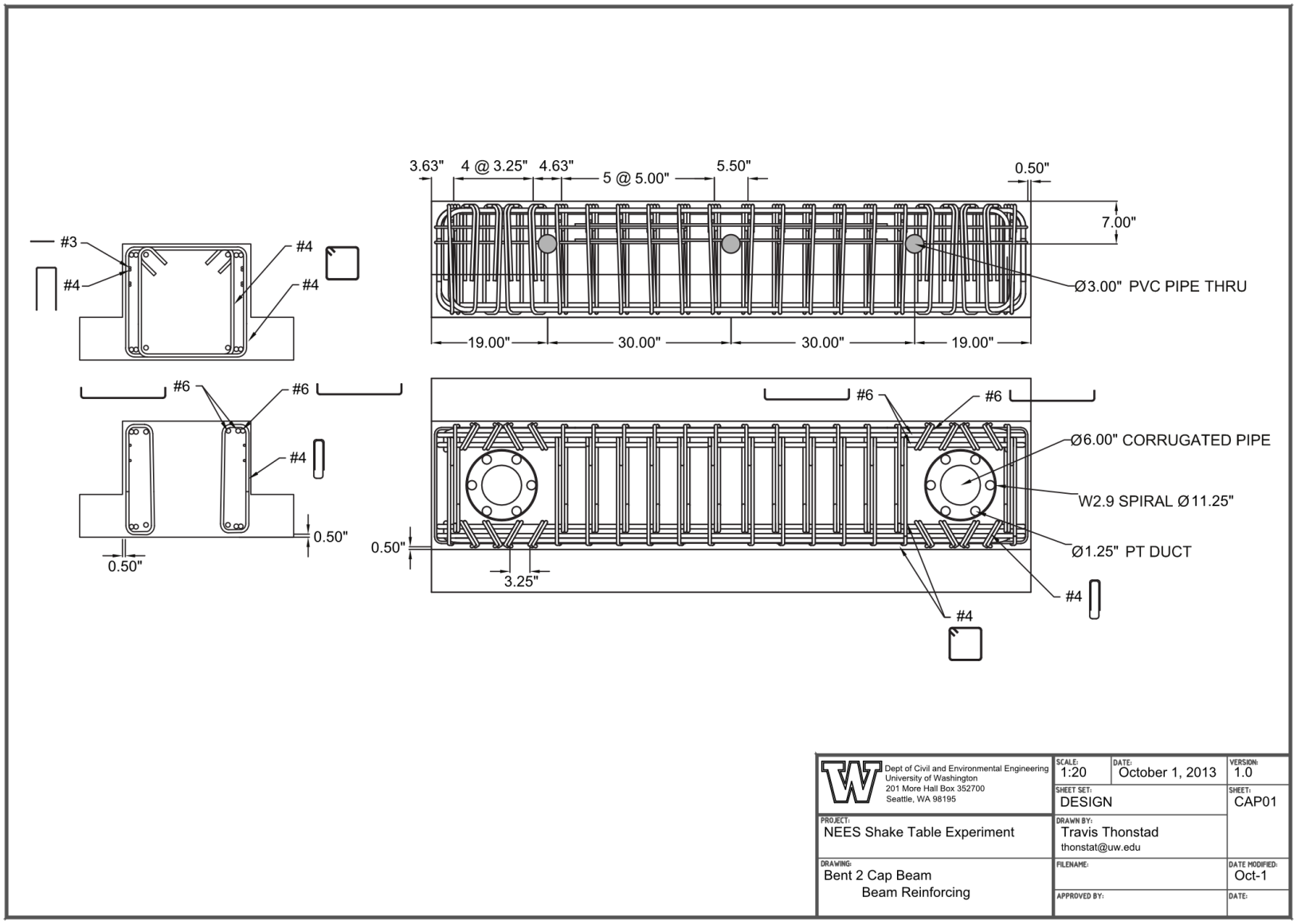

Figure B.8 Inverted-T cap beam transverse beam reinforcement

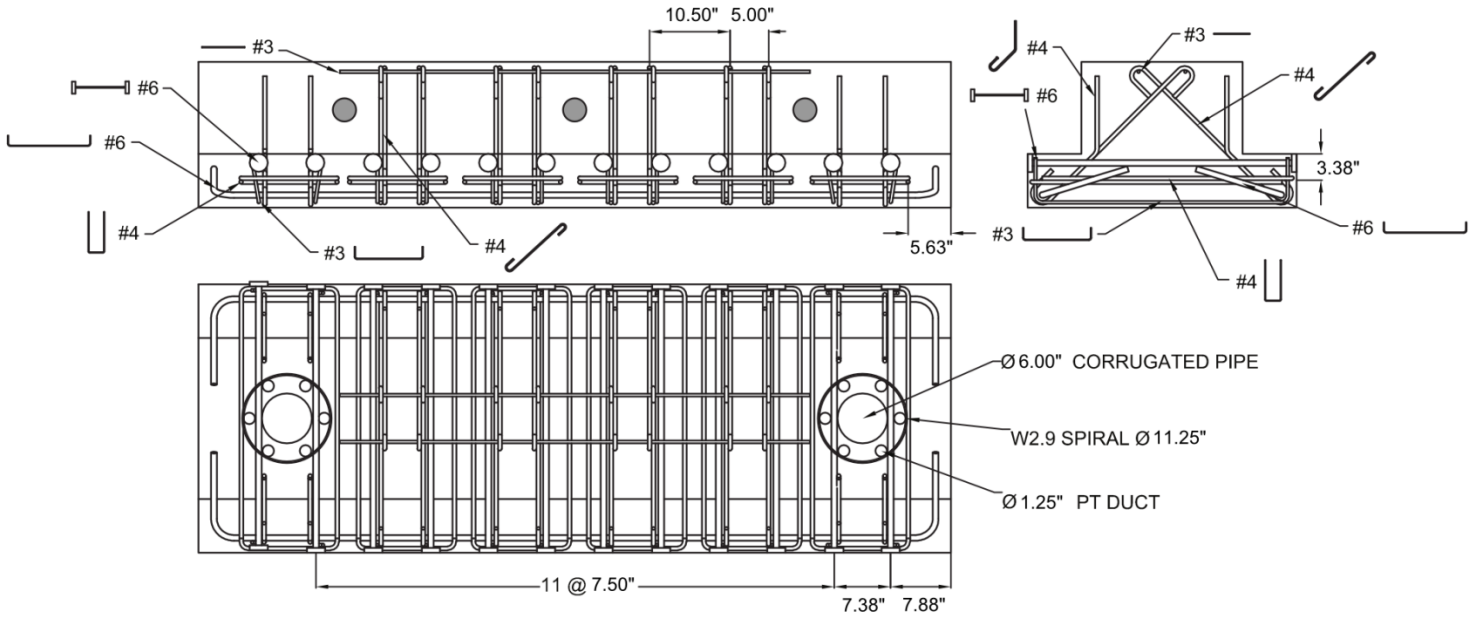

Dept of Civil and Environmental Engineering University of Washington 201 More Hall Box 352700 Seattle, WA 98195	SCALE: 1:20	DATE: October 1, 2013	VERSION: 1.0
	SHEET SET: DESIGN		SHEET: CAP02
PROJECT: NEES Shake Table Experiment	DRAWN BY: Travis Thonstad thonstat@uw.edu		
DRAWING: Bent 2 Cap Beam Ledge Reinforcing	FILENAME:		DATE MODIFIED: Oct-1
	APPROVED BY:		DATE:

Figure B.9 Inverted-T cap beam ledge reinforcement

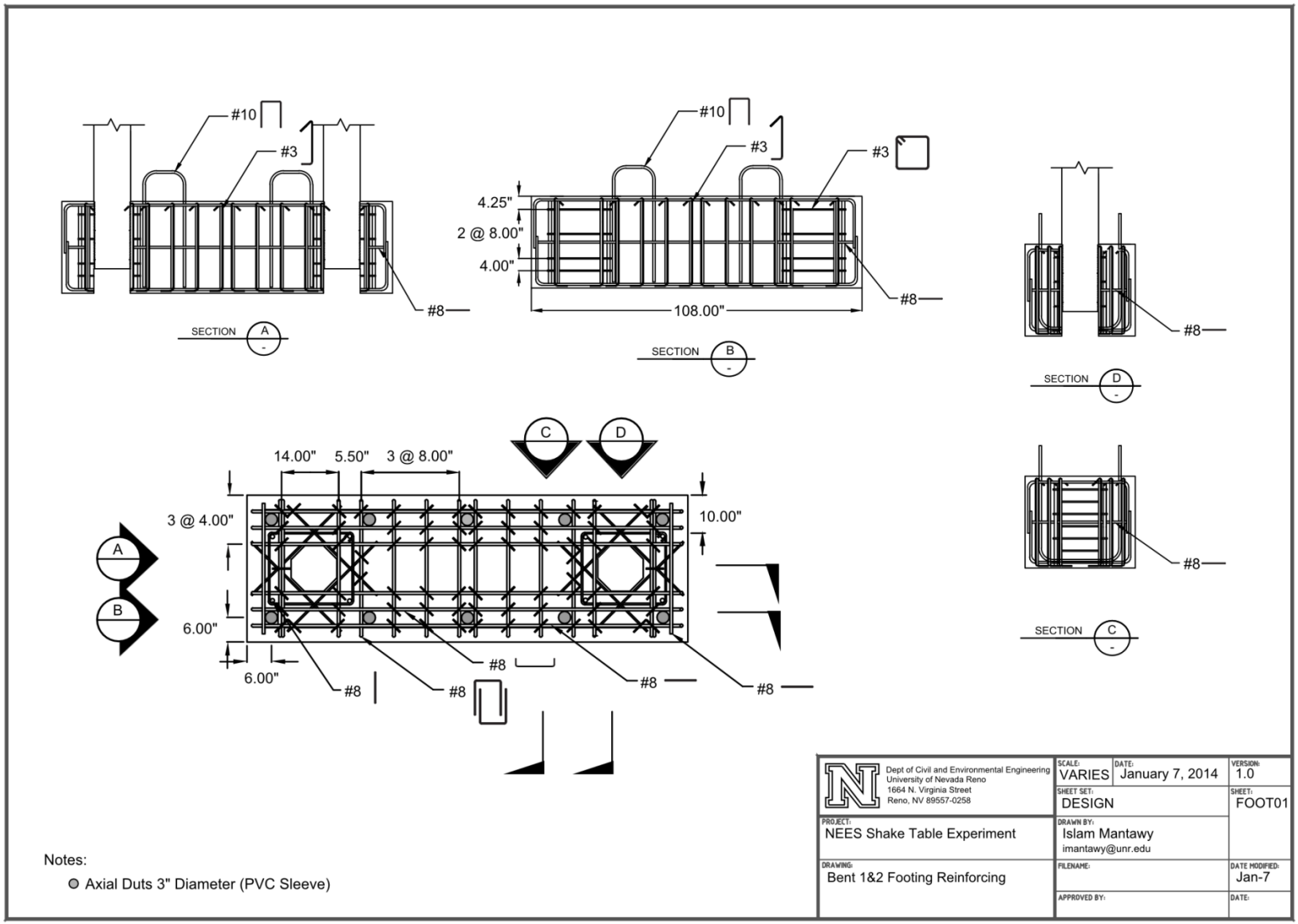

Figure B.10 Bent 1 and 2 footing reinforcement

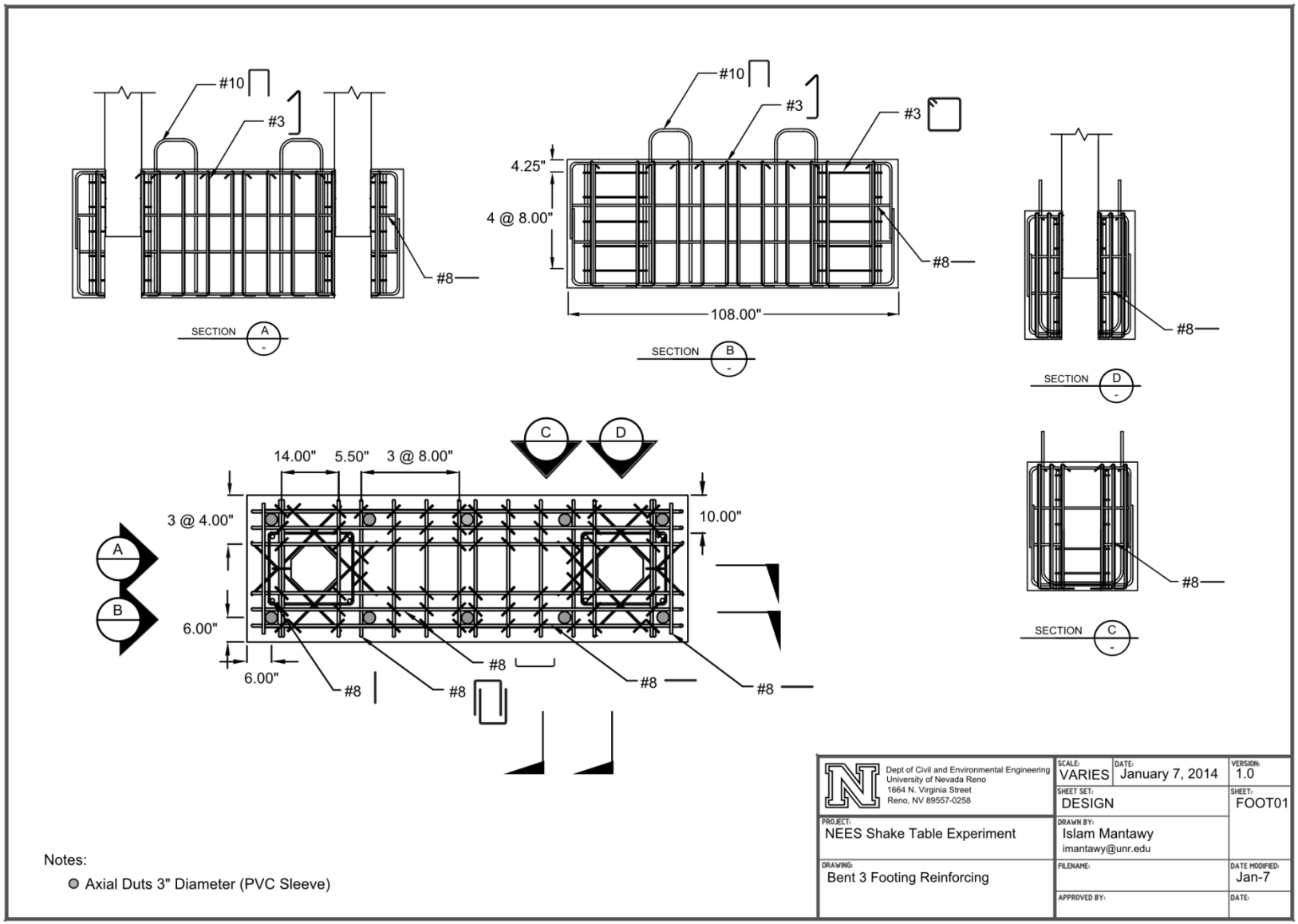

Figure B.11 Bent 3 footing reinforcement

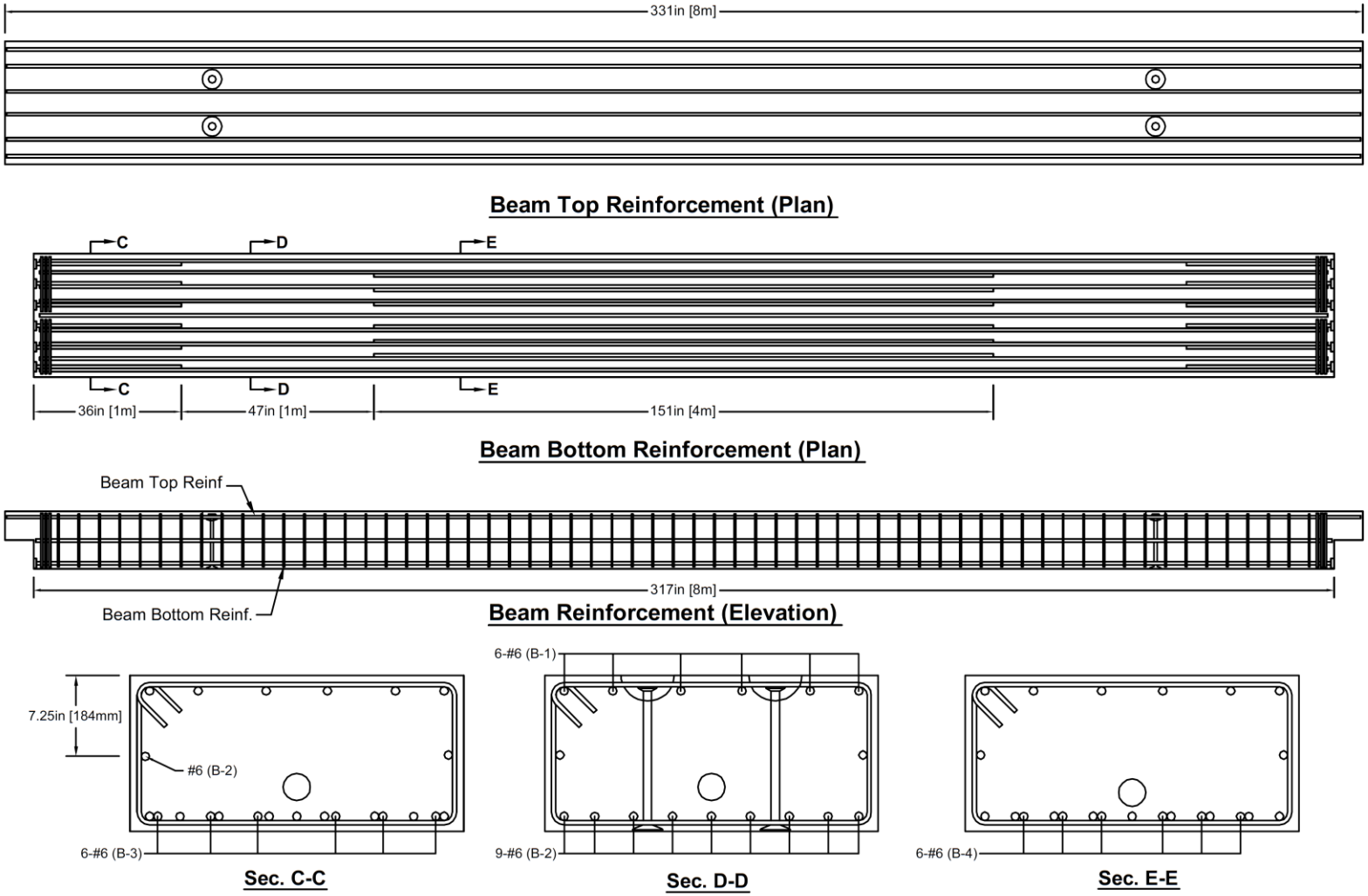

Figure B.12 Superstructure plank reinforcement (from Johnson 2006)

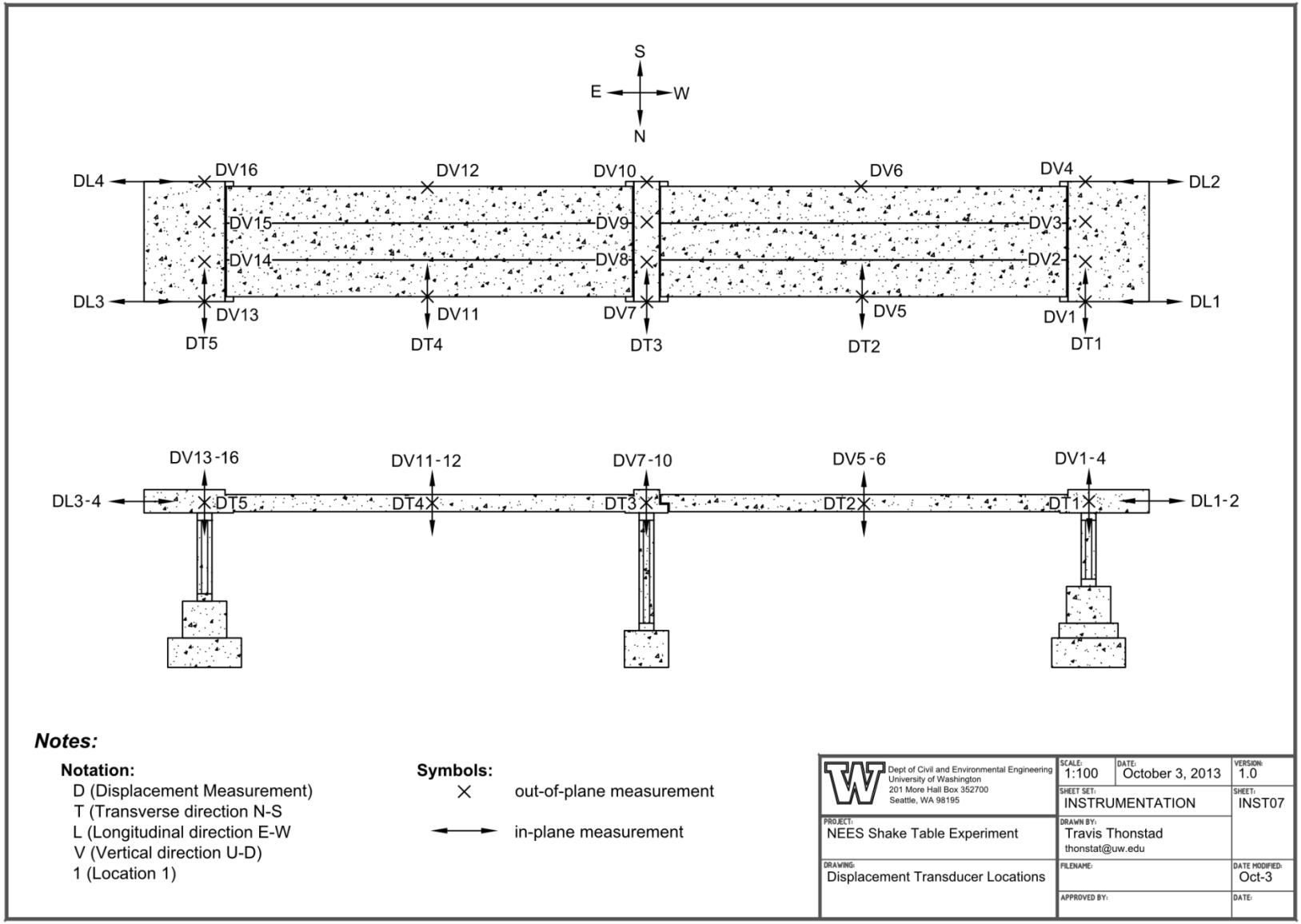

Figure B.13 Displacement transducer locations

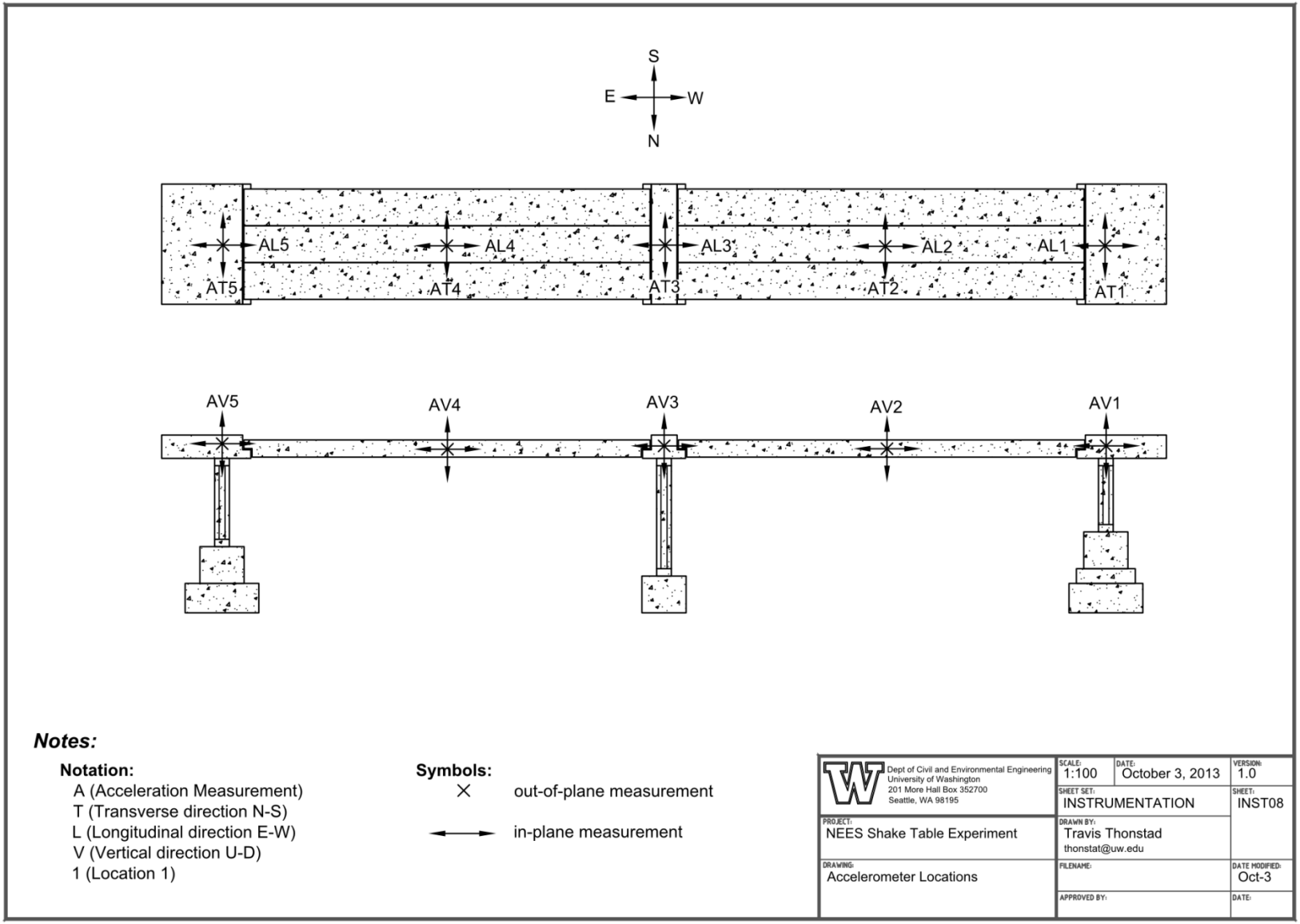

Figure B.14 Accelerometer locations

Instrument	A	B	C
1NTR1	3 - 5/8		2 - 3/4
1NTR2	3 - 1/8		2 - 1/2
1NTR3	2 - 7/8		2 - 1/2
1NTR4	3		2
1NTR5		6 - 1/8	2 - 3/4
1NTR6		5 - 13/16	2 - 5/8
1STR1	2 - 13/16		2 - 1/2
1STR2	2 - 7/8		2
1STR3	2 - 11/16		2 - 1/4
1STR4	2 - 7/16		2
1STR5		5 - 7/8	2 - 3/4
1STR6		6 - 5/8	2 - 3/4
1NBR1	3 - 3/16		2 - 1/2
1NBR2	3 - 3/8		2 - 1/2
1NBR3	3		2 - 1/4
1NBR4	2 - 3/4		2 - 1/4
1NBR5		6	2 - 1/2
1NBR6		5 - 7/8	2 - 1/4
1SBR1	3		2 - 1/4
1SBR2	3 - 1/8		2 - 1/4
1SBR3	3 - 1/16		2 - 1/8
1SBR4	3 - 1/16		2 - 1/8
1SBR5		6	3 - 1/8
1SBR6		5 - 9/16	3

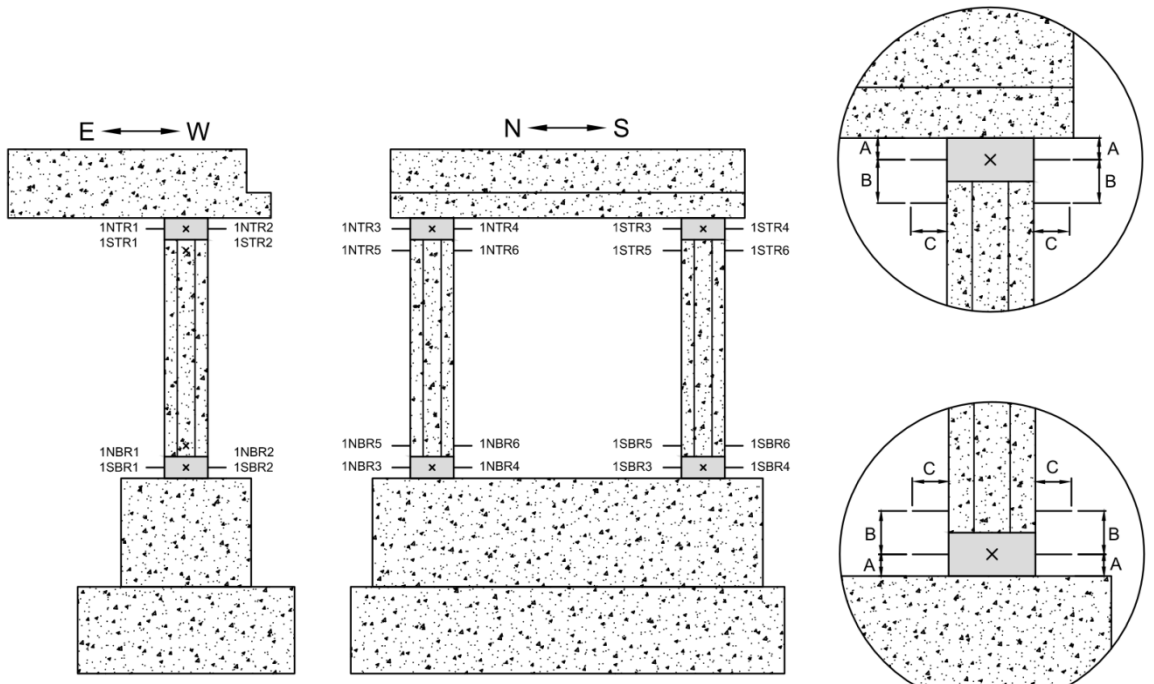

Notes:

Notation:
1 (Bent Number)
N (East Column)
T (Top of Column)
R (Rotation Measurement)
1 (Location 1)

Symbols:
× out-of-plane measurement
—— in-plane measurement

Dept of Civil and Environmental Engineering University of Washington 201 More Hall Box 352700 Seattle, WA 98195	SCALE: 1:40	DATE: October 1, 2013	VERSION: 1.1
	SHEET SET: INSTRUMENTATION		SHEET: INST01
PROJECT: NEES Shake Table Experiment	DRAWN BY: Travis Thonstad thonstat@uw.edu		
DRAWING: Bent 1 Curvature Rod Locations	FILENAME: Columns.dwg		DATE MODIFIED: Oct-1
	APPROVED BY:		DATE:

Figure B.15 Bent 1 rotation potentiometer locations

Instrument	A	B	C
2NTR1	3 - 1/8		1 - 3/4
2NTR2	3 - 1/8		2 - 1/4
2NTR3	3 -3/8		2 - 1/2
2NTR4	2 - 13/16		2
2NTR5		5 - 7/8	2 - 3/8
2NTR6		6 - 1/2	2 - 3/4
2STR1	2 - 5/8		2
2STR2	3		2
2STR3	3 - 1/2		2 - 1/8
2STR4	3 - 1/4		2
2STR5		5 - 5/8	2 - 1/2
2STR6		6	2 - 1/2
2NBR1	2 - 15/16		2
2NBR2	2 - 13/16		2
2NBR3	3 - 1/4		2 - 1/2
2NBR4	2 - 7/8		2 - 1/4
2NBR5		5 - 5/8	2 - 3/8
2NBR6		5 - 7/8	2 - 1/2
2SBR1	3 - 1/16		2 - 3/4
2SBR2	3 - 1/4		1 - 3/4
2SBR3	3 - 5/16		2 - 1/2
2SBR4	3 - 1/8		2 - 1/2
2SBR5		6	2 - 7/8
2SBR6		5 - 13/16	3

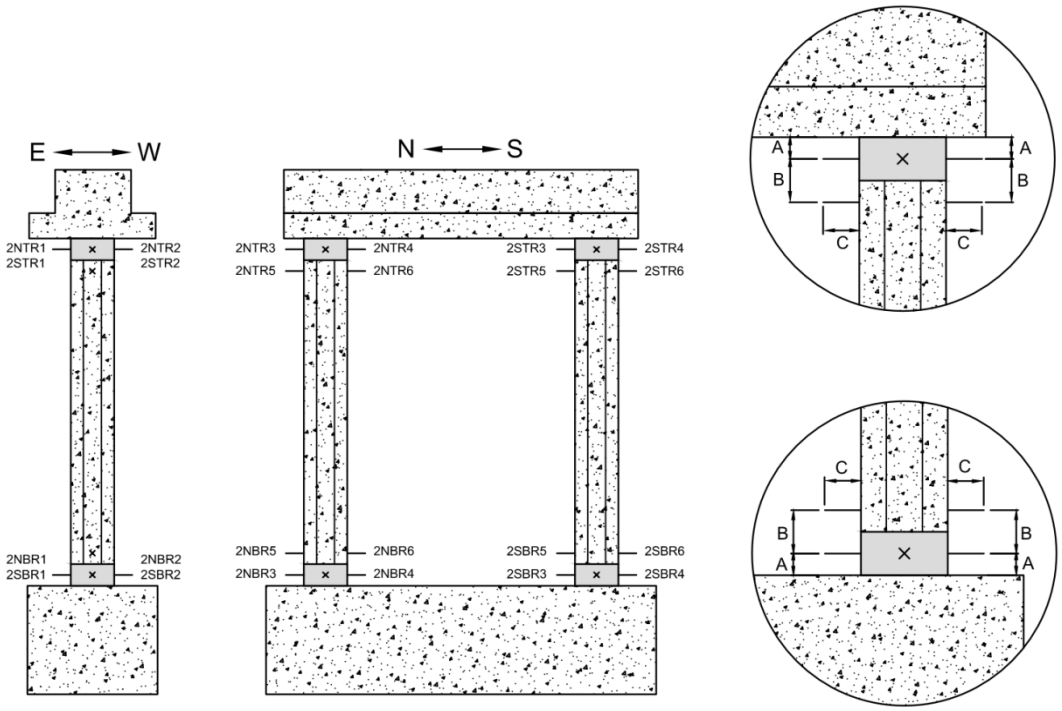

Notes:

Notation:
- 2 (Bent Number)
- N (East Column)
- T (Top of Column)
- R (Rotation Measurement)
- 1 (Location 1)

Symbols:
- × out-of-plane measurement
- —— in-plane measurement

Dept of Civil and Environmental Engineering
University of Washington
201 More Hall Box 352700
Seattle, WA 98195

SCALE: 1:40	DATE: October 1, 2013	VERSION: 1.1
SHEET SET: INSTRUMENTATION		SHEET: INST02
PROJECT: NEES Shake Table Experiment	DRAWN BY: Travis Thonstad thonstat@uw.edu	
DRAWING: Bent 2 Curvature Rod Locations	FILENAME: Columns.dwg	DATE MODIFIED: Oct-1
	APPROVED BY:	DATE:

Figure B.16 Bent 2 rotation potentiometer locations

Instrument	A	B	C
2NTR1	3 - 5/16		1 - 3/4
2NTR2	3 - 1/4		1 - 3/4
2NTR3	3 - 5/16		2 - 3/16
2NTR4	3 - 1/4		2 - 1/8
2NTR5		5 - 1/2	2 - 3/8
2NTR6		5 - 7/8	2 - 1/2
2STR1	3 - 1/4		1 - 7/8
2STR2	3 - 1/4		1 - 3/4
2STR3	3 - 3/8		2 - 3/16
2STR4	3 - 1/16		2 - 1/4
2STR5		6 - 1/8	2 - 3/8
2STR6		6 - 1/4	2 - 3/4
2NBR1	3 - 1/8		1 - 7/8
2NBR2	3 - 3/16		1 - 5/8
2NBR3	3		2 - 1/4
2NBR4	3 - 1/4		2 - 1/2
2NBR5		6 - 3/16	2 - 5/8
2NBR6		5 - 7/8	2 - 1/4
2SBR1	3 - 1/16		2 - 1/8
2SBR2	3 - 5/16		1 - 7/8
2SBR3	3		2 - 1/4
2SBR4	2 - 15/16		2 - 1/8
2SBR5		5 - 5/8	2 - 3/16
2SBR6		5 - 9/16	2 - 1/2

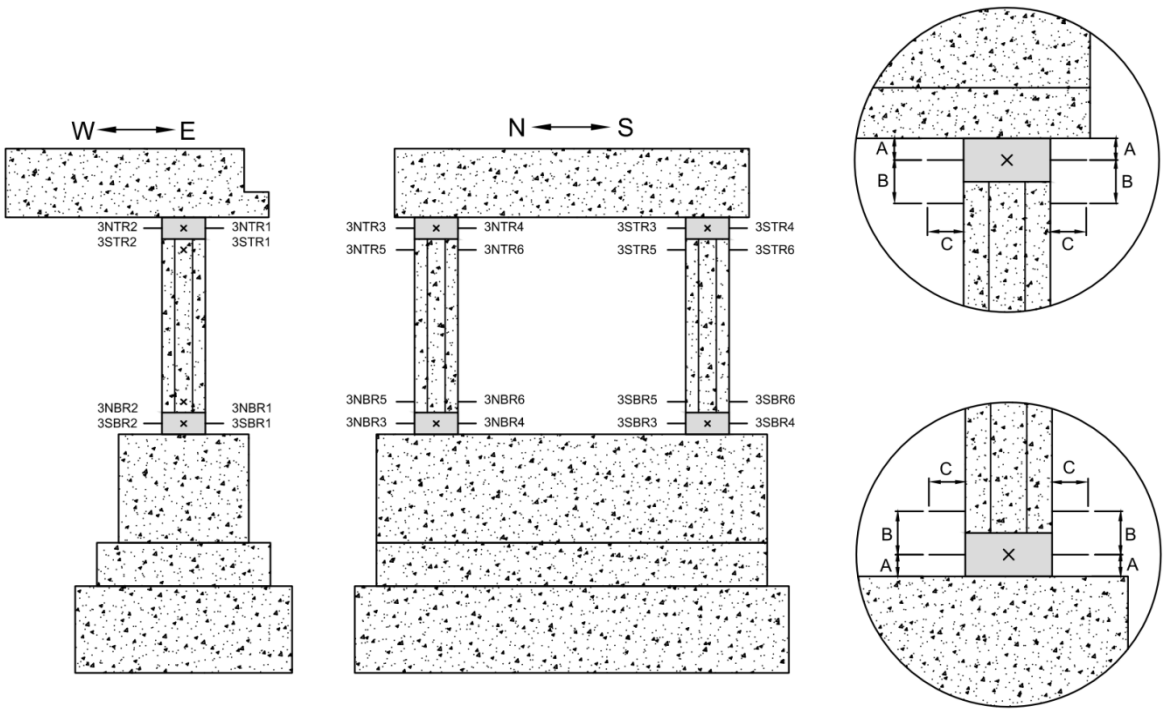

Notes:

Notation:
3 (Bent Number)
N (North Column)
T (Top of Column)
R (Rotation Measurement)
1 (Location 1)

Symbols:
× out-of-plane measurement
—— in-plane measurement

Dept of Civil and Environmental Engineering
University of Washington
201 More Hall Box 352700
Seattle, WA 98195

SCALE: 1:40	DATE: October 1, 2013	VERSION: 1.1
SHEET SET: INSTRUMENTATION		SHEET: INST03
PROJECT: NEES Shake Table Experiment	DRAWN BY: Travis Thonstad thonstat@uw.edu	
DRAWING: Bent 3 Curvature Rod Locations	FILENAME: Columns.dwg	DATE MODIFIED: Oct-1
	APPROVED BY:	DATE:

Figure B.17 Bent 3 rotation potentiometer locations

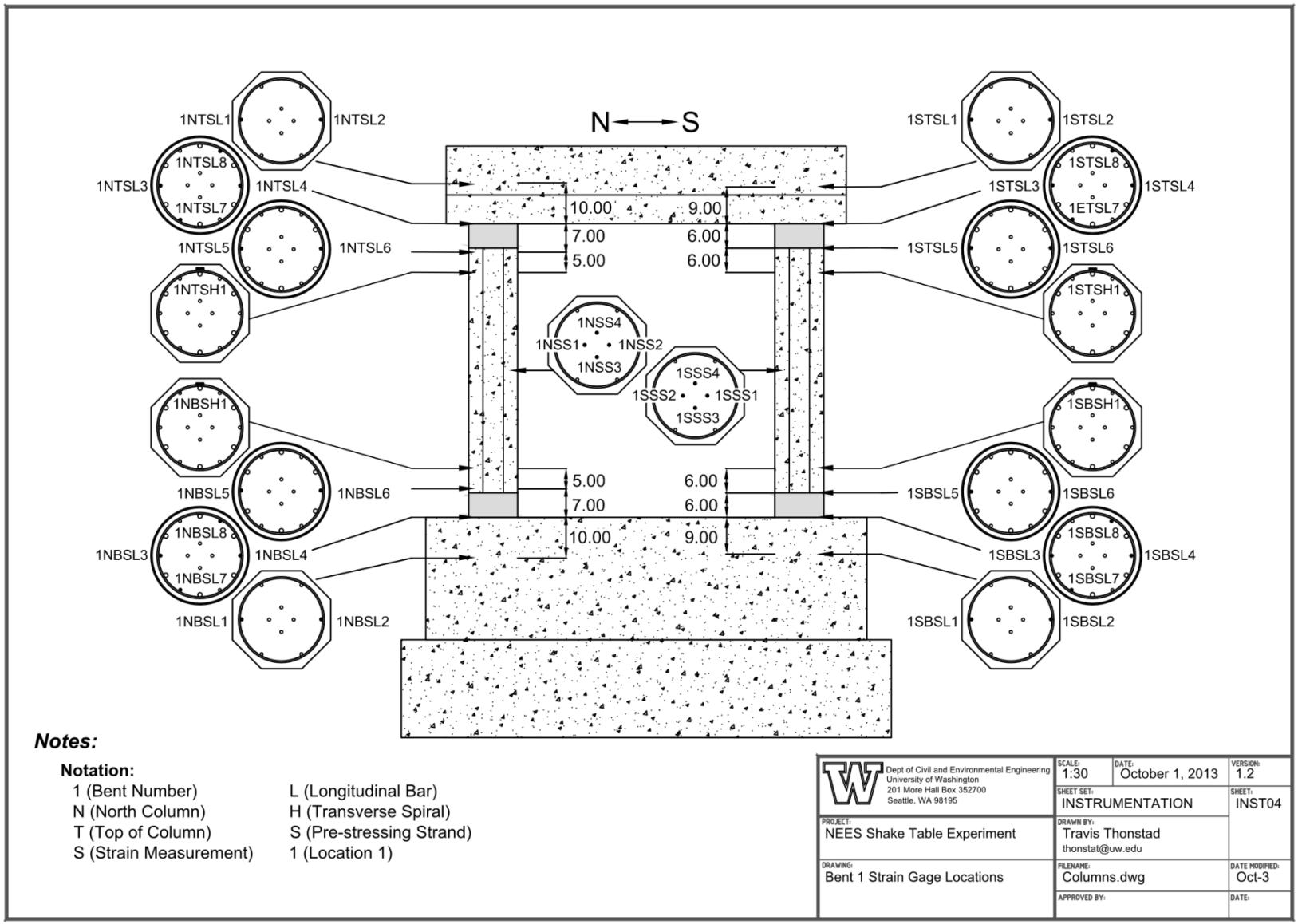

Notes:

Notation:

1 (Bent Number)	L (Longitudinal Bar)
N (North Column)	H (Transverse Spiral)
T (Top of Column)	S (Pre-stressing Strand)
S (Strain Measurement)	1 (Location 1)

Dept of Civil and Environmental Engineering University of Washington 201 More Hall Box 352700 Seattle, WA 98195	SCALE: 1:30	DATE: October 1, 2013	VERSION: 1.2
	SHEET SET: INSTRUMENTATION		SHEET: INST04
PROJECT: NEES Shake Table Experiment	DRAWN BY: Travis Thonstad thonstat@uw.edu		
DRAWING: Bent 1 Strain Gage Locations	FILENAME: Columns.dwg		DATE MODIFIED: Oct-3
	APPROVED BY:		DATE:

Figure B.18 Bent 1 strain gage locations

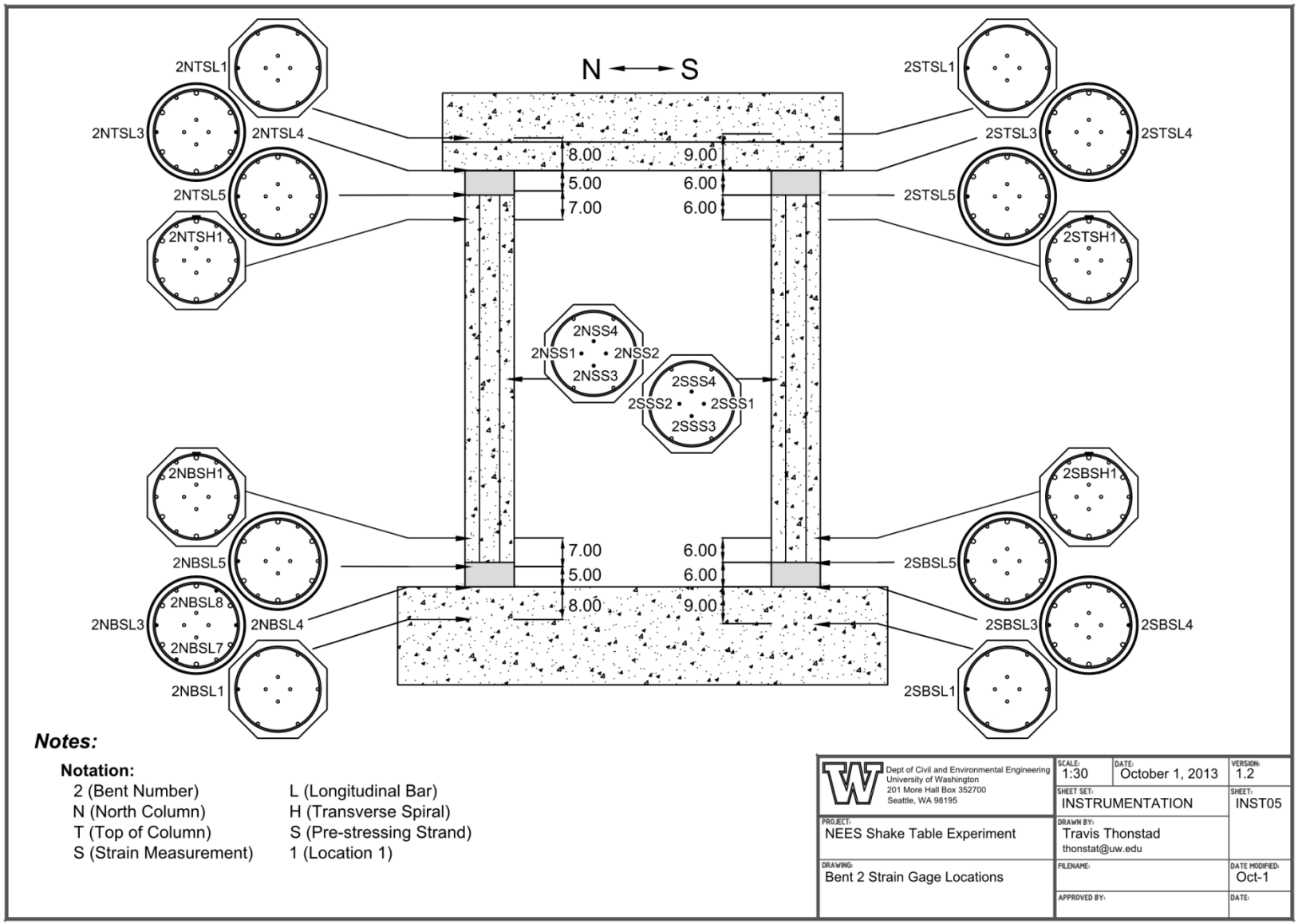

Figure B.19 Bent 2 strain gage locations

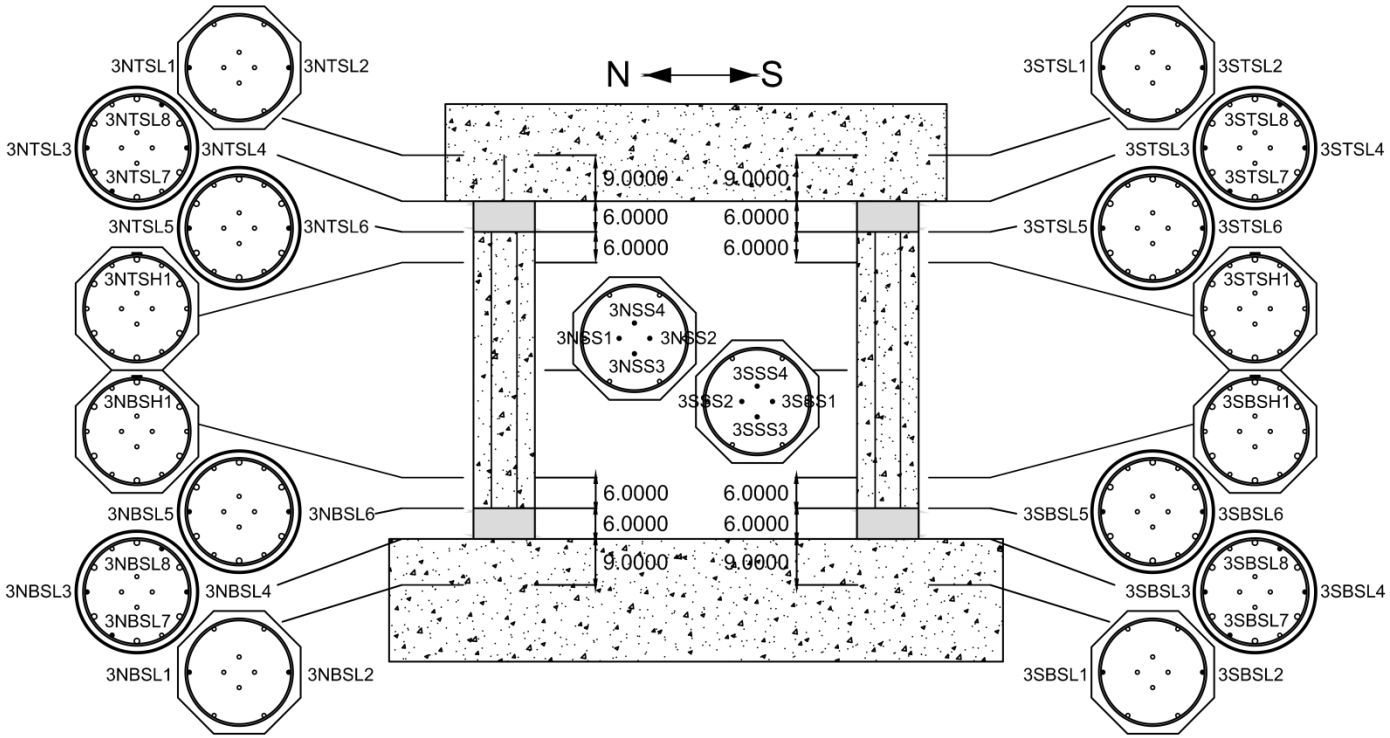

Notes:

Notation:

3 (Bent Number)	L (Longitudinal Bar)
E (East Column)	H (Transverse Spiral)
T (Top of Column)	S (Pre-stressing Strand)
S (Strain Measurement)	1 (Location 1)

Dept of Civil and Environmental Engineering University of Washington 201 More Hall Box 352700 Seattle, WA 98195	SCALE: 1:30	DATE: October 1, 2013	VERSION: 1.2
	SHEET SET: INSTRUMENTATION		SHEET: INST06
PROJECT: NEES Shake Table Experiment	DRAWN BY: Travis Thonstad thonstat@uw.edu		
DRAWING: Bent 3 Strain Gage Locations	FILENAME:		DATE MODIFIED: Oct-1
	APPROVED BY:		DATE:

Figure B.20 Bent 3 strain gage locations

Appendix C: AASHTO Displacement Based Design Example

In Chapter 8 a design methodology for pre-tensioned, rocking columns using the current AASHTO displacement based design procedure was proposed. This procedure is summarized in Figure C.1. Aspects of the procedure that are unique to pre-tensioned columns are highlighted in blue.

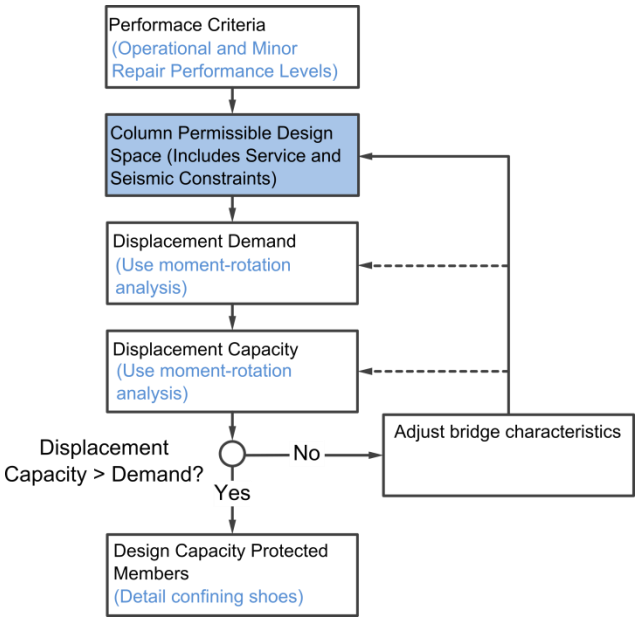

Figure C.1 Displacement Based Design Procedure

This Appendix uses this design procedure to redesign an existing bridge in the state of Washington, to demonstrating the procedure and discussing critical aspects of it. This example uses the finite element software SAP2000 [Computers and Structures Inc. 2015]. Although the bridge was originally designed for SDC C, the redesign of the bridge will instead consider the requirements of SDC D that include multi-modal response spectrum and incremental static analysis.

- Section C.1 Discusses the bridge geometry and the Design Level seismic hazard.
- Section C.2 Defines the Performance Criteria for the bridge
- Section C.3 Defines the Permissible Design Space for the columns
- Section C.4 Determines the displacement demand imposed on the bridge during the design level hazard using multi-modal response spectrum analysis in SAP2000.
- Section C.5 Determines the inelastic displacement capacity of several bridge substructures through incremental static, "pushover", analysis using SAP2000
- Section C.6 Describes detailing of the column ends
- Section C.7 Discusses how the final design and displacement demands would change if the requirement that the columns must not decompress under Service IV loads was ignored

C.1 Gold Creek Bridge

The Gold Creek Bridge located near mile post 55 on Interstate 90 in Washington State was selected as the prototype for the design. The bridge is shown in Figure C.2; an overview of the structure is shown in Figure C.3. The bridge has seven 155-ft. spans, with a longitudinal expansion joint at the end of the third span. The columns are conventional reinforced concrete, are 5 ft. in diameter, range in height from 21.4 to 23.0 ft., and are reinforced with 18 No. 11 longitudinal bars and No. 6 spiral at 3-in. on-center. A bridge of this length was selected to limit the influence of the abutments on the global response of the bridge.

Figure C.2 Gold Creek Bridge (from Stephens 2016)

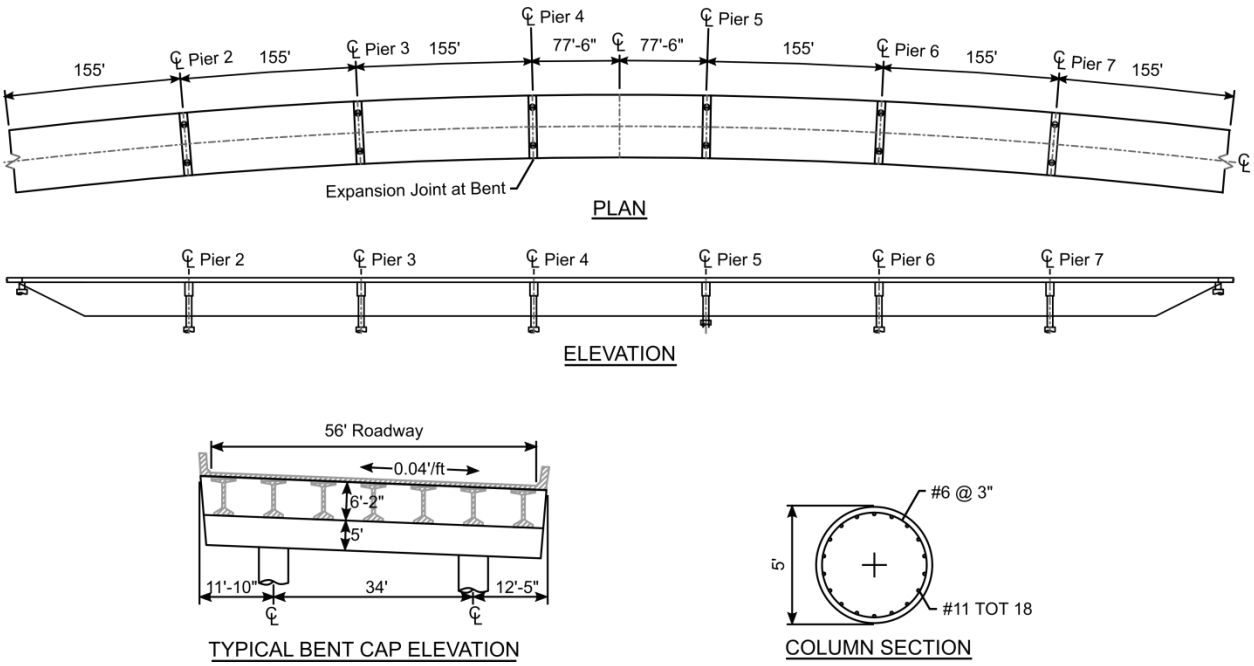

Figure C.3 Gold Creek Bridge overview (adapted from Stephens 2016)

The structure was originally designed using Seismic Design Category (SDC) C with Class D Soil. The seismic hazard with a 7% probability of exceedance in 75 years for the site is given in Table C.1.

Table C.1 Design level hazard

Hazard	PGA (g)	S_s (g)	S_1 (g)	F_a (g)	F_v (g)	S_{da} (g)	S_{DS} (g)	S_{D1} (g)
7% in 75 (SC D)	0.28	0.645	0.21	1.284	1.98	0.3472	0.8282	0.4158

C.2 Performance Objectives

The bridge was designed to meet the Operational performance level. It is expected that during the design level motion, both the strands and mild-steel reinforcement may yield, however neither will fracture and some prestress will remain in the columns to re-center the bridge. The deformation capacity of the column for this performance level is limited by the fracture strain of the longitudinal reinforcement, $\varepsilon_s < {\varepsilon_{su}}^R$, and the strain which corresponds to a loss of prestress in the strands, $\varepsilon_p < \varepsilon_{EE} + f_{pe}/E_p$. This performance objective implies that the structural properties of the bridge may be impacted due to the design level earthquake, however, no repair will be necessary and the bridge will still be able to withstand subsequent earthquakes without a significant loss of performance.

C.3 Permissible Design Space

In order to estimate the column diameter and to proportion the column reinforcement, both service and seismic design criteria were considered. These criteria lead to a permissible design space for the columns; the procedure for developing this design spaces is outlined in Figure C.4.

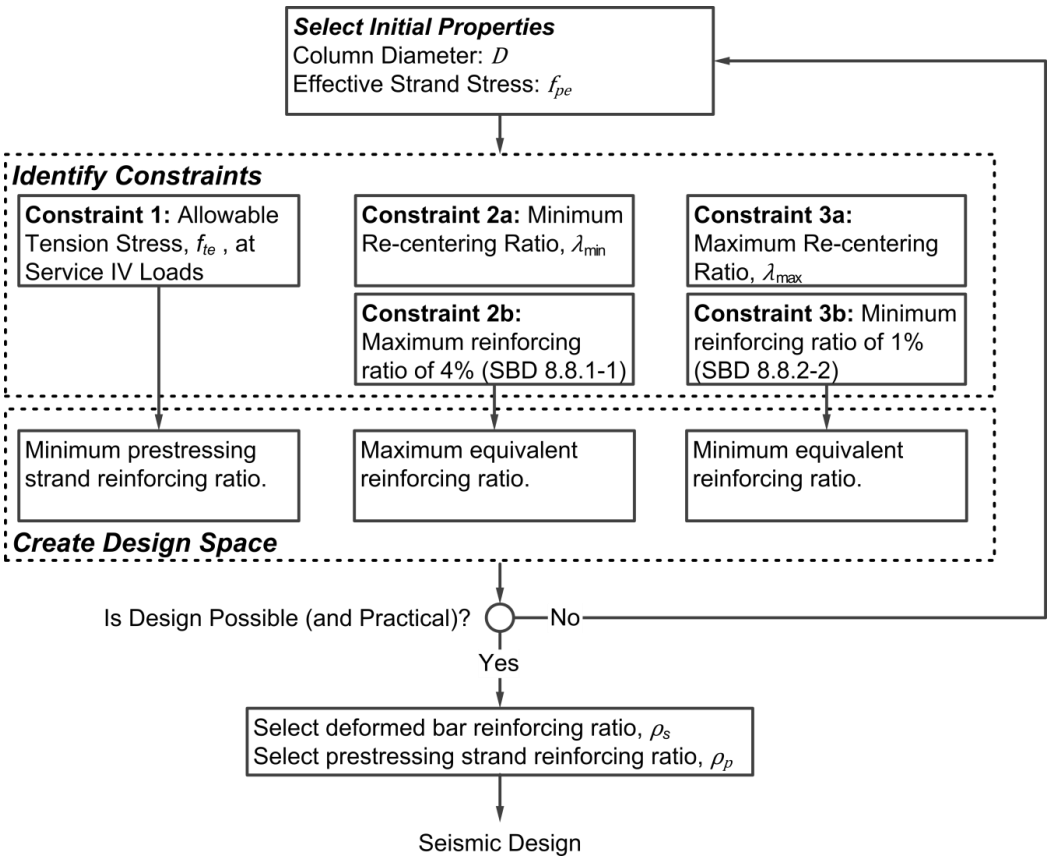

Figure C.4 Feasible design space flowchart

Two piers were analyzed under service loads to determine the required steel areas. Both the expansion pier (Pier 4) and the pier that will experience the greatest thermal induced moments (Pier 7) were chosen. The column geometry for both Piers is summarized in Table C.2. The bottoms of the columns were analyzed for decompression, where ingress of moisture is most probable and crack control is most critical.

Table C.2 Column dimensions

Material Strengths	Pier 4	Pier 7
Diameter	5 ft.	5 ft
Height	23 ft	21.4 ft
Cover	1.5 in.	1.5 in.

The service loads for the columns are shown in Table C.3. Both the axial load and moments were higher in the integral pier (Pier 7) than in the one containing the expansion joint (Pier 4). In addition, the Service IV column moments were largely controlled by the uniform temperature (TU) load case.

Table C.3 Service Loads (Bottom of column)

Load	Type	Pier 4			Pier 7		
		P (kips)	Mtrans (kip-ft)	Mlong (kip-ft)	P (kips)	Mtrans (kip-ft)	Mlong (kip-ft)
Dead load	DC	1649	80	10	1871	120	83
Overlay	DW	77	6	0	77	6	24
Wind	WS	±55	555	50	± 60	390	130
Temperature	TU	0	0	0	-12	0	1900
Creep	CR	0	0	0	-1	0	115
Shrinkage	SH	0	0	0	-1	0	115

C.3.1 Initial Properties

In this example, the column diameter was chosen to be 60 in. to match the existing structure. The effective stress in the strands was chosen to be 185 ksi (75% of the yield stress).

The material strengths for the reinforcement and concrete are shown in Table C.4. The reinforcement sizes used in this example are shown in Table C.5.

Table C.4 Material strengths

Material Strengths	
Concrete	$f'_c = 8$ ksi
Steel	$f_{sy} = 60$ ksi
Prestressing	$f_{py} = 245$ ksi
Confining Tube	$f_{ty} = 42$ ksi

Table C.5 Reinforcement dimensions

Material Strengths	Size	Db (in.)	Ab (in.2)
Longitudinal reinforcement	No. 11	1.41	1.56
Transverse reinforcement	No. 4	0.5	0.2
Prestressing strands	1/2"	0.5	0.153

C.3.2 Identify Constraints

The constraints on the design space are given in Table C.6. The allowable tension stress in the columns under Service IV loads is prescribed by Article 5.9.4.2.2 the *AASHTO LRFD Bridge Design Specifications* (2016), while the maximum and minimum re-centering ratios were selected based on engineering judgement. For context, the columns in the pre-tensioned bridge experiment described in chapters 5, 6 and 7 had re-centering ratios of roughly 2.5 and had residual drift ratios of less than 0.1% up to the 221% Design Level motion (Motion 19). This shaking table test specimen, however, lacked abutments, which would actively resist the re-centering forces produced by the columns in a real bridge structure.

Table C.6 Design constraints

Constraint	Symbol	Value
Allowable tension stress at Service IV	f_{te}	0 psi
Minimum Re-centering Ratio	λ_{min}	3
Maximum Re-centering Ratio	λ_{max}	6

In addition to these constraints, the *AASHTO Guide Specifications for LRFD Seismic Bridge Design* (2015) specifies a maximum and minimum reinforcing ratio, interpreted here to mean the effective reinforcing ratio, given in Equation C.1.

$$\rho_{equiv} = \rho_s + \rho_p f_{py}/f_{sy} \quad [C.1]$$

C.3.3 Define Design Space

These constraints lead to the design spaces shown in Figure C.5 for the expansion (Pier 4) and the integral (Pier 7) piers.

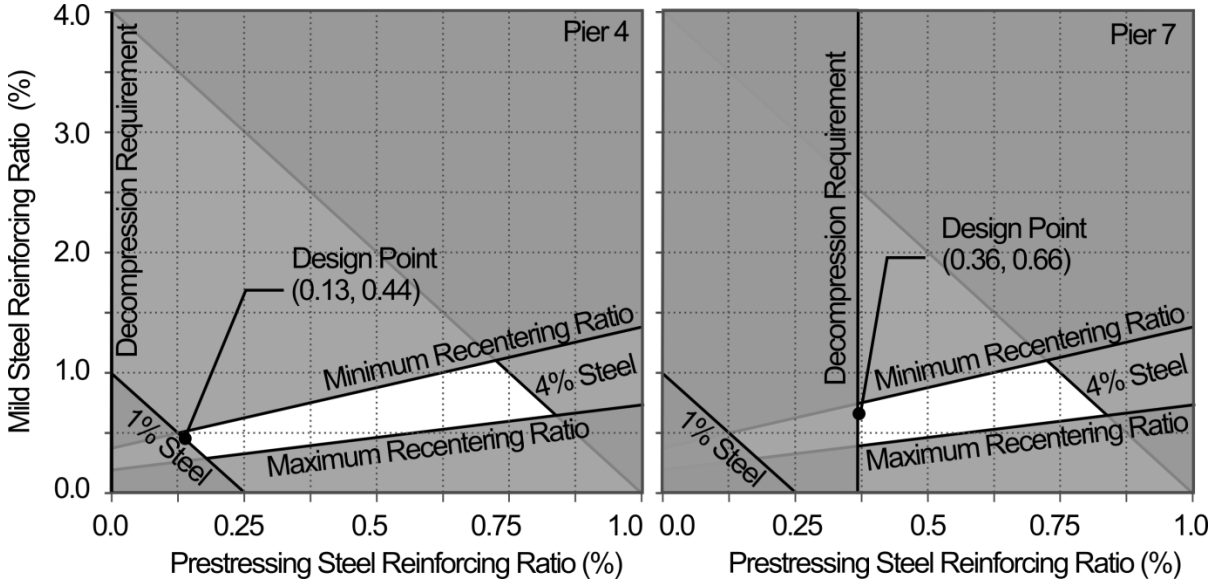

Figure C.5 Service load design space for Pier 4

The design of the integral pier (Pier 7) is largely controlled by the allowable tension stress under Service IV loads. The prescriptive minimum reinforcing is a redundant constraint in this case, since the decompression requirement drives the design. For the expansion pier (Pier 4), the opposite is true. Because no temperature or time-dependent loads act on the column, the decompression requirement becomes the redundant constraint.

C.3.4 Select Deformed Bar and Prestressing Strand Reinforcing Ratios

Independently minimizing the reinforcement for the columns in either pier leads to the designs shown in Figure C.6. In both cases, the number of mild steel bars was selected to produce symmetric section properties.

Using different column designs for each pier is impractical from a construction perspective. Therefore the cross-section determined for Pier 7 will be used for all of the columns of the bridge. This corresponds to the selected design point (0.36, 0.66) shown in Figure C.5. For the bar sizes shown in Table C.5, these reinforcing ratios lead to 12 reinforcing bars and 67 strands. This results in an equivalent reinforcing ratio for the columns of 2.1%.

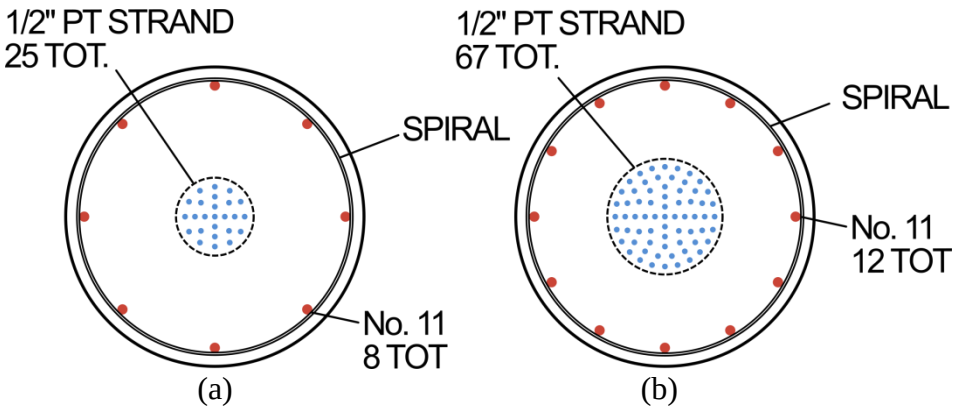

Figure C.6 Column cross sections for design point (a) Pier 4 (b) Pier 7

C.4 Determine Displacement Demand

The displacement demand during the design level motion for the chosen column size and reinforcing ratio was determined through multi-modal response spectrum analysis in SAP2000. The material properties for the bridge model are given in Table C.7.

Table C.7 Material properties

Material	Used For	Weight (pcf)	Strength (ksi)	Elastic Modulus (ksi)
Column concrete	Columns	165	8	5695.8
Crossbeam concrete	Crossbeams	145	4	3644
Superstructure concrete	Superstructure	165/155	9.6/4	5105.3*
Column steel	Columns	490	60	29000

*Composite property for girder-deck system

The locally debonded length of the reinforcement was chosen to be 21 bar diameters (30 in.). This implies that bar fracture should occur at a drift ratio of approximately:

$$\left(\frac{\Delta}{H}\right) = \frac{\varepsilon_{su}^{R} L_{s,unb}}{(d-c)} \approx \frac{(0.06)(21d_b+8d_b)}{(0.95D-0.1D)} = 4.8\% \qquad \text{[C.2]}$$

where $\frac{\Delta}{H}$ is the drift ratio of the column, $\varepsilon_{su}^{R}$is the reduced ultimate strain of the deformed bar reinforcement, $L_{s,unb}$ is the effective unbonded length of the reinforcement including the effects of strain penetration, d is the distance from the compressive face of the column to the reinforcement, and c is the neutral axis depth at the particular drift ratio.

Since this drift ratio is much larger than the expected deformation during the design level event, the chosen debonded length is assumed sufficient. This value should be assessed at the particular axial load, during the displacement capacity procedure. If the displacement capacity of the columns is found to be insufficient, one possible adjustment to the bridge characteristics could be this unbonded length.

The rotational stiffness of the cross section, k_r, was determined through moment rotation analysis under the service level axial load. This quantity is defined as the secant stiffness of the sections moment-rotation relationship at first bar yield. The moment rotation curve for the Pier 7 cross-section is shown in Figure C.7.

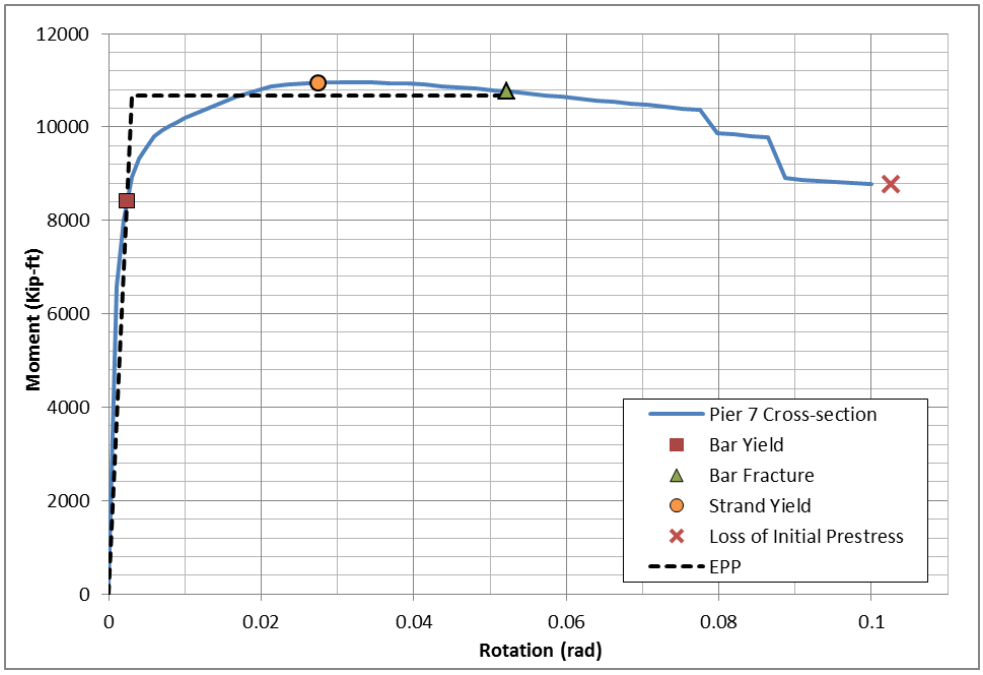

Figure C.7 Moment rotation curve for the Pier 7 cross-section

The resulting rotational stiffness of the section was determined to be, $k_r = 3.61 \times 10^6$ kip-ft/rad. The effective stiffness of the columns, using this value and the gross moment of inertia of the octagonal column section, was computed using Equation C.2.

$$\frac{I_{eff}}{I_g} = \frac{1}{1+(3\,E_c\,I_g)/(a\,k_r)} \qquad [C.2]$$

The ratio of the effective to the gross moment of inertia was found to be 35%. Table C.8 presents the section properties used in the SAP2000 model for both the columns as well as the cap beams and superstructure elements.

Table C.8 Frame section properties

Frame Sections	A_g (in^2)	I_{eff}/I_g	$I_{eff\text{-}33}$ (in^4)	$I_{eff\text{-}22}$ (in^4)	Av_{eff} (in^2)	J_{eff}/J_g	J_{eff} (in4)
Column	2673	0.35	222549	222549	2340	0.2	250103
Crossbeam	12264	1.0	21784952	∞	10220	1.0	∞
Superstructure*	12247	1.0	11925014	505646165	∞	1.0	∞

*Composite properties for girder-deck system

An overview of the bridge centerline model is shown in Figure C.8. The superstructure was modeled using displacement-based elastic beam column elements; each span was subdivided into four elements. Superstructure mass was lumped at the nodes, and the service axial loads were applied directly to the tops of the column elements. Rigid offsets were used to connect the superstructure centerline to the cap beams and the cap beam centerlines to the columns. The columns were modeled using single displacement-based beam column elements and were fixed at the base. Each column was subdivided into three elements.

The abutments were modeled as rollers, free to rotate and to translate in the longitudinal direction of the bridge, but restrained in the transverse direction by elastic springs. The *Washington State Bridge Design Manual* [WSDOT 2016] allows the transverse abutment stiffness to be modeled as 50% of the elastic transverse stiffness of the adjacent bent with approval. Modeling the abutments as either completely free or fixed in the transverse direction leads to unrealistic displacements at the abutments. Since precise modeling of the abutments was not the focus of this design example, the transverse abutment stiffness was taken as 50% of the adjacent bent stiffness in determining the design level displacement demands for the bridge.

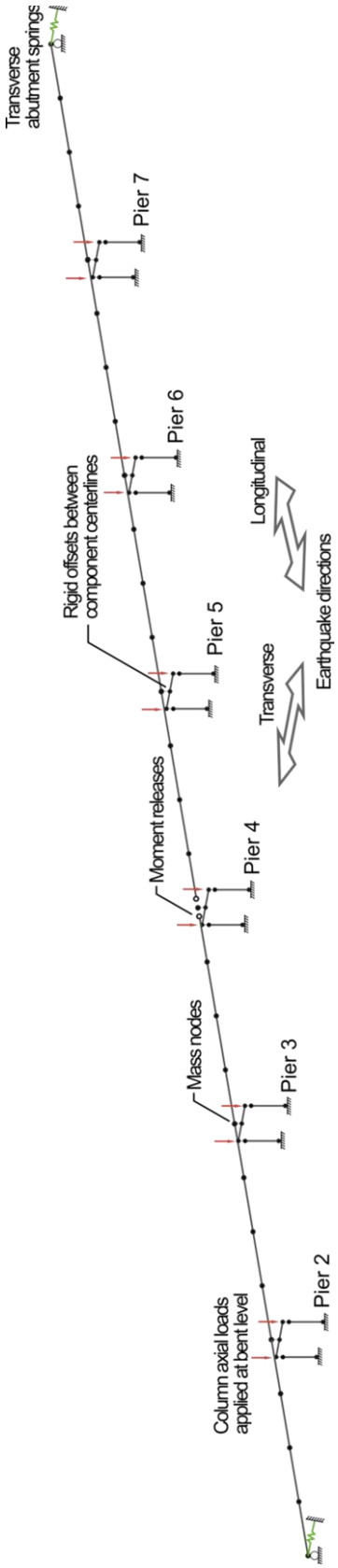

Figure C.8 SAP2000 elastic model overview

The periods of the first three modes of vibration in the longitudinal and transverse direction of the bridge are given in Table C.9, along with their modal mass participation ratios.

Table C.9 Fundamental modes and mass participation ratios

Mode	Period (s)	Mass Participation Ratio
Transverse 1	0.516	0.974
Transverse 2	0.489	0.013
Transverse 3	0.413	0.052
Longitudinal 1	0.680	0.895
Longitudinal 2	0.496	0.044
Longitudinal 3	0.437	0.049

The displacement demands determined from the elastic analysis were multiplied by a short period amplification factor, R_d, to obtain the design displacement demand in the orthogonal directions. The short period amplification factor was determined using Equation C.3 from Article 4.3.3 of the AASTHO SDC. The computed amplification factors are given in Table C.10.

$$R_d = \begin{cases} \left(1 - \frac{1}{\mu_D}\right)\frac{T^*}{T} + \frac{1}{\mu_D} \geq 1.0 & \frac{T^*}{T} > 1.0 \\ 1.0 & \frac{T^*}{T} \leq 1.0 \end{cases} \quad [C.3]$$

where $T^* = 1.25\,T_s$, μ_D is the displacement ductility (assumed to be 3 for the design level hazard)., and T_s determined form Article 3.4.1

Table C.10 Short period amplification factor

Direction	T (sec)	T^* (sec)	μ_D	R_d
Transverse	0.516	0.628	3	1.144
Longitudinal	0.680	0.628	3	1.0

The amplified displacement demands at each pier during the design level hazard in the longitudinal and transverse direction are shown in Table C.11. The total displacement demands

at each Pier, found by combining the displacement demands in the two orthogonal directions, are also shown in Table C.11.

Table C.11 Displacement demand from response spectrum analysis

	Transverse Direction		Longitudinal Direction		100%-30% Combo.	
Location	U_{long} (in.)	U_{trans} (in.)	U_{long} (in.)	U_{trans} (in.)	U_{long} (in.)	U_{trans} (in.)
Pier 1 (Abut)	0.00	1.59	2.66	0.00	2.66	1.82
Pier 2	0.04	2.09	2.30	0.01	2.31	2.39
Pier 3	0.03	2.14	2.29	0.01	2.30	2.45
Pier 4	0.00	1.70	1.58	0.00	1.58	1.95
Pier 5	0.04	2.21	2.22	0.01	2.23	2.54
Pier 6	0.02	2.32	2.42	0.00	2.43	2.66
Pier 7	0.06	2.02	2.21	0.01	2.23	2.32
Pier 8 (Abut)	0.00	1.40	2.62	0.00	2.62	1.60

C.5 Determine Displacement Capacity

The displacement capacity of the bridge was assessed using incremental static, or "pushover", analysis. Each frame of the bridge was assessed separately in the longitudinal direction (See Figure C.9), and a single "typical" pier was analyzed in the transverse direction.

In order to perform the inelastic pushover analysis, hinge properties must be established for the columns. These hinge properties were determined by performing a series of moment rotation analyses for the chosen column cross-section at different levels of axial load.

Five axial load levels were chosen up to 40% of the crushing capacity of the column concrete. At each level of axial load, the plastic moment and rotation capacities were determined. The plastic rotation capacity is defined here as the rotation to cause first bar fracture. For other column geometries and performance levels, other strain limits may apply. The resulting column hinge properties are shown in Figure C.10.

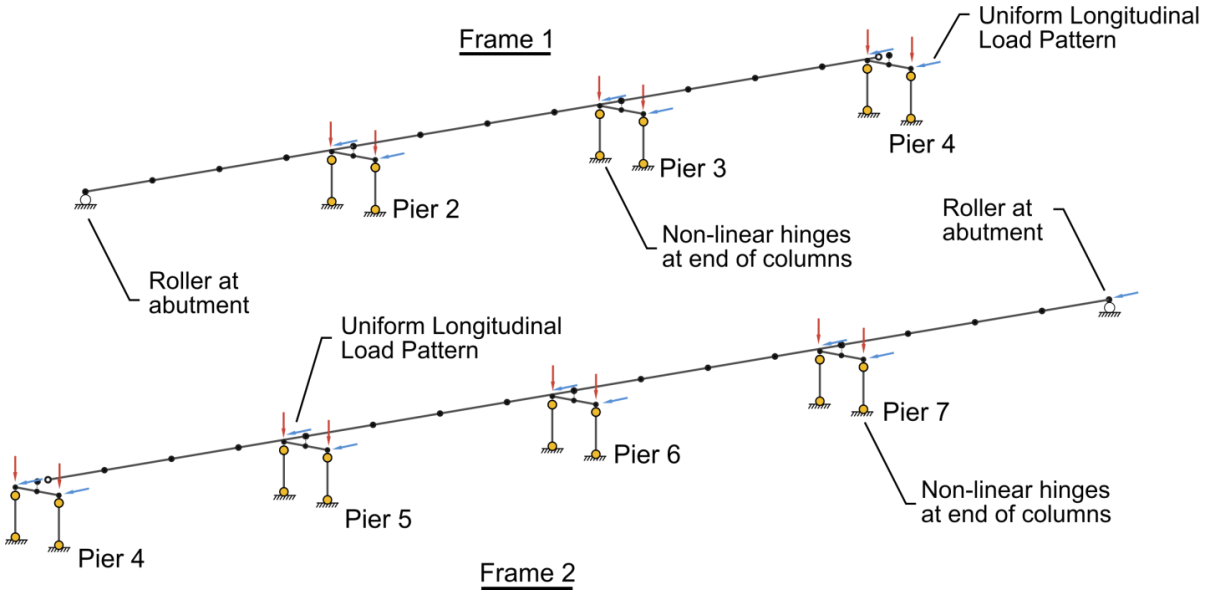

Figure C.9 Frames for longitudinal pushover analysis

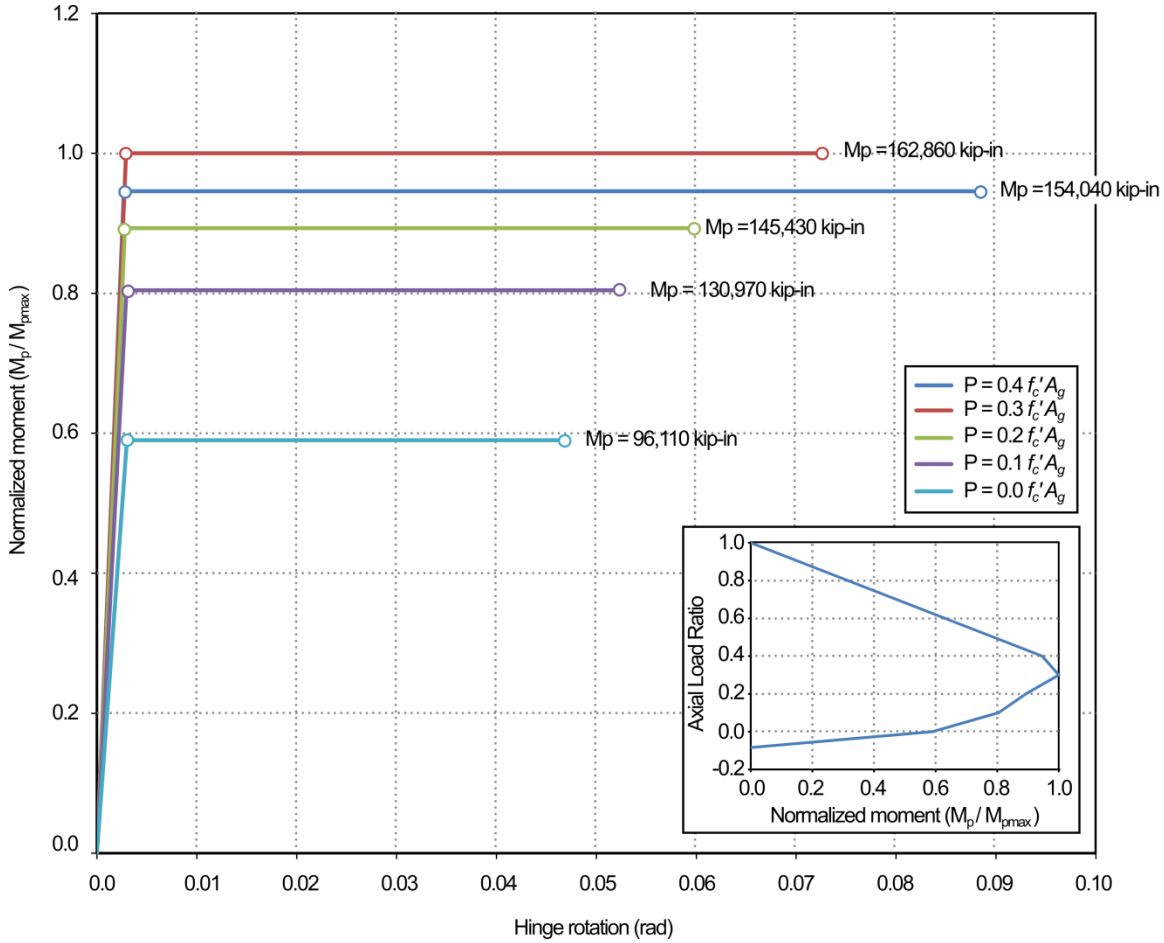

Figure C.10 Nonlinear column hinge properties for incremental static analyses.

The results of the pushover analyses for each of the bridge subassemblies are given in Table C.12.

Table C.12 Displacement capacity determined by push-over analyses

	Yield Displacement (in.)	Displacement Capacity (in.)
Frame 1 Longitudinal	1.52	16.18
Frame 2 Longitudinal	1.51	16.24
Bent Transverse	1.32	14.89

C.5.1 Capacity Check

The largest displacement demand in either orthogonal direction is 2.66 inches. Given the displacement capacity of the bents are close to 15 inches in the transverse direction, the bridge design is found to be satisfactory.

A summary of the axial loads, plastic rotations and ductility demands at the design level displacements of the bridge subassemblies are given in Table C.13, Table C.14, and Table C.15.

Table C.13 Frame 1 Longitudinal ductility demands during design event displacement

Location	P @ Yield (kip)	Mp (kip-in)	θ_YI	θ_PD	μD
Trailing Lower (Pier2)	-3716	142472	0.0028	0.0040	2.4
Trailing Upper (Pier2)	-3703	142994	0.0029	0.0021	1.7
Middle Lower (Pier3)	-3982	144424	0.0028	0.0022	1.8
Middle Upper (Pier3)	-3971	145576	0.0028	0.0039	2.4
Leading Lower (Pier4)	-	-	-	-	-
Leading Upper (Pier4)	-	-	-	-	-

Table C.14 Frame 2 Longitudinal ductility demands during design event displacement

Location	P @ Yield	Mp	thetaYI	thetaPD	muD
Trailing Lower (Pier4)	-	-	-	-	-
Trailing Upper (Pier4)	-	-	-	-	-
Middle Lower (Pier5)	-3750	144093	0.0028	0.0045	2.6
Middle Upper (Pier5)	-3750	144088	0.0028	0.0027	2.0
Middle Lower (Pier6)	-3842	144803	0.0028	0.0048	2.7
Middle Upper (Pier6)	-3841	144794	0.0028	0.0039	2.4
Leading Lower (Pier7)	-3944	145587	0.0028	0.0044	2.6
Leading Upper (Pier7)	-3946	145599	0.0028	0.0026	1.9

Table C.15 Typical Pier Transverse ductility demands during design event displacement

Location	P @ Yield	Mp	thetaYI	thetaPD	muD
Trailing Lower	-2425	133887	0.0029	0.0055	2.9
Trailing Upper	-2350	133309	0.0030	0.0052	2.8
Leading Lower	-4831	152412	0.0029	0.0049	2.7
Leading Upper	-4844	152511	0.0029	0.0044	2.6

In this case, because the hazard is low, the ductility demands meet the maximum ductility provision of 6.

C.6 Column End Detailing

The detailing of the column ends was based on the detailing of the columns in the shaking table and subassembly tests. Figure C.11 shows the details of the ends of the columns. Only detailing considerations unique to the precast, pre-tensioned columns are described here.

The target diameter-to-thickness ratio of the confining tubes was 80. This led to a 0.75 in. wall thickness for the tubes. The tubes were extended half of one column diameter, or 30 in., into the clear height of the columns. The annular end plate thickness was taken as twice the tube thickness, or 1.5 inches. The inner hole diameter for the annular endplate, based on the number of strands and the required spacing between strands, was 30 in.. The debonding material selected

for the No 11 continuous bars was 1-1/2 in. schedule 40 PVC pipe with an outside diameter of 1.9 inches. Therefore the required diameter of the holes in the annular end plate for the continuous reinforcement was 2 in.

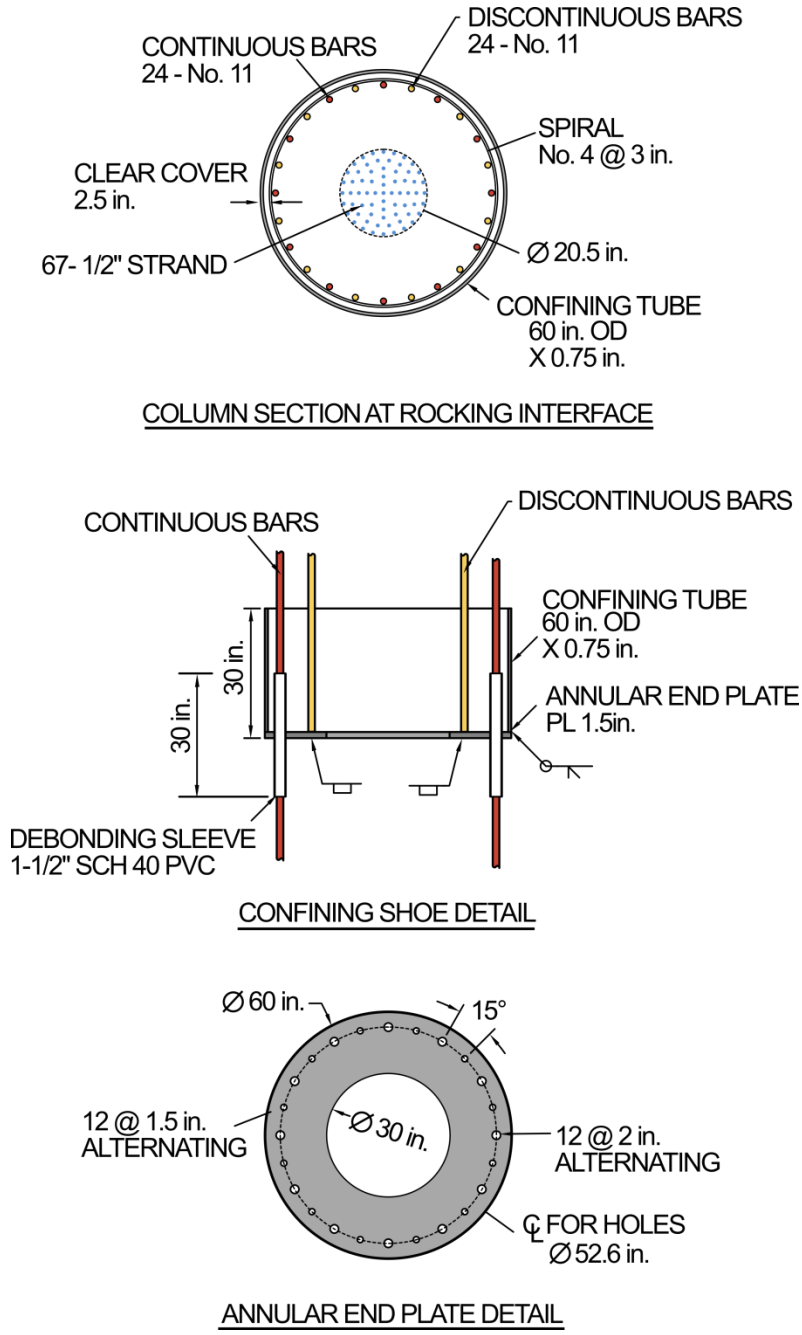

Figure C.11 Column end detailing

The minimum allowable spiral reinforcement ratio, specified in Article 8.6.5 of the *AASHTO Guide Specification for LRFD Seismic Bridge Design* (2016), is 0.5% for SDC D. Using No. 4 reinforcing bars as spiral, this requires a longitudinal spiral spacing of 3 inches.

The minimum development length of reinforcing steel for SDC D is given by Article 8.8.4 of the *AASHTO Guide Specification for LRFD Seismic Bridge Design* (2016). For No. 11 bars, this led to a development length of 27 inches. The discontinuous bars were extended 1.5 times this length, or 42 in. above the height of the confining tube. The total length of the discontinuous bars was therefore 72 inches.

C.7 Discussion

In the above example, the amount of deformed bar reinforcement and prestressing strand was largely determined by the criterion that the columns must not decompress under Service IV loads. The intention of this provision is to protect the column reinforcement from corrosion.

If one were to ignore this criterion, and instead protect the strands against corrosion in some other fashion, the column cross section in Figure C.12b could be used. This leads to a more economical column design and only a small increase in the displacement demands. These increases are shown in Table C.16, which compares the displacement demand of the two designs shown in Figure C.12. In both cases, the displacement capacities of the columns are much larger than the demands.

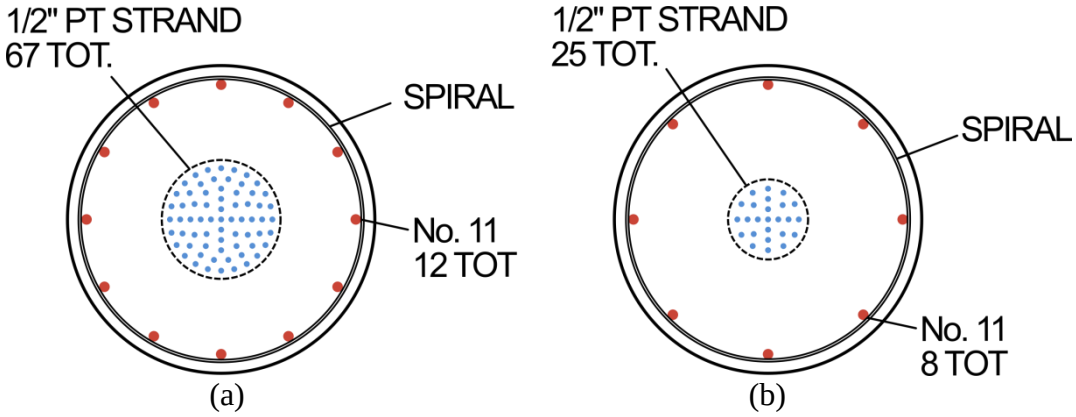

Figure C.12 Design of Pre-tensioned column cross-sections (a) with Service IV requirements (b) without Service IV requirements

Table C.16 Displacement demands for columns designed with and without decompression criterion.

Location	With Service IV Requirements		Without Service IV Requirements		Difference	
	U-long (in.)	U-trans (in.)	U-long (in.)	U-trans (in.)	U-long	U-trans
Pier 2	2.31	2.39	3.64	2.72	57%	14%
Pier 3	2.30	2.45	3.62	3.53	57%	44%
Pier 4	1.58	1.95	2.41	3.67	53%	88%
Pier 5	2.23	2.54	3.51	4.19	57%	65%
Pier 6	2.43	2.66	3.79	3.87	56%	46%
Pier 7	2.23	2.32	3.53	2.76	58%	19%